Exploring Longterm Spectral Variations in Blazars: A Detailed Study of 3C 279 and 4C 31.03

A thesis submitted to the University of Calicut, Kerala

for the award of the Degree of

DOCTOR OF PHILOSOPHY

in **PHYSICS**

under the Faculty of Science

by

AMINABI T

Department of Physics

University of Calicut

Kerala, India

July 2025

Dedication

Dedicated to the woman who gave me the gift of life, ***Fathima Patharakkal****, my beloved mother! And to* ***Aahil*** *and* ***Ahraz****, to whom I had the privilege of gifting life!*

CERTIFICATE

This is to certify that the thesis entitled "**Exploring Longterm Spectral Variations in Blazars: A Detailed Study of 3C 279 and 4C 31.03**" submitted to the Department of Physics, University of Calicut by **Mrs. Aminabi T** in partial fulfilment of the requirements for the award of the degree of **Doctor of Philosophy** is the original work carried out by her under my supervision and guidance at the Department of Physics, University of Calicut. No part of this thesis has been included previously for the award of any other degree, either in this university or any other institution. The thesis has been checked for plagiarism, using the **iThenticate** software, at the CHMK library, University of Calicut and the similarity index is found within the permissible limit. Also certified that the corrections suggested by the adjudicators have been incorporated in this revised thesis.

Supervisor:
Dr. C D Ravikumar
Professor
Department of Physics
University of Calicut

DECLARATION

*I hereby declare that the thesis titled "***Exploring Longterm Spectral Variations in Blazars: A Detailed Study of 3C 279 and 4C 31.03***" is an authentic record of research work carried out by me at the Department of Physics, University of Calicut under the supervision of Dr. C D Ravikumar. No part of this thesis has been included previously for the award of any other degree, either in this university or any other institution. The thesis has been checked for plagiarism, using the* **iThenticate** *software, at the CHMK library, University of Calicut and the similarity index is found within the permissible limit.*

Date:

Aminabi T
Research scholar
Department of Physics
University of Calicut

Acknowledgement

The journey of completing this thesis has been a transformative experience for me filled with challenges, growth, and a lot of learning. I am grateful to God for the faith and perseverance through which I have been able to overcome the hurdles and reach this significant milestone. There are some individuals who deserve special mention for their unwavering guidance, encouragement, and belief in my abilities, without whom this accomplishment would not have been possible.

First and foremost, I wish to express my deepest gratitude to my advisor, Prof. C. D. Ravikumar for the invaluable experiences and insights I gained during my association with him. His guidance and support have been pivotal at every stage of my research journey. I am particularly grateful for the remarkable freedom he provided, allowing me to explore my intellectual curiosity and cultivate critical thinking skills as an independent researcher. His exceptional ability for critical thinking and the constructive critiques he provided throughout my research have been invaluable advantages in shaping the quality of my work. I deeply appreciate his meticulous effort in reviewing and correcting my entire thesis. His remarkable writing skills and attention to detail have greatly enriched the clarity and presentation of my work, and I am truly fortunate to have benefited from his guidance.

I would also like to express my heartfelt gratitude to my collaborator, Dr Sunder Sahayanathan, who has been a true guide and mentor throughout my research journey. It was under his insightful guidance that I was introduced to the research problem that became the foundation of my work. His constant support, deep knowledge, and invaluable advice have been instrumental in navigating the complexities of my research and bringing it to completion. Beyond the guidance, he offered unwavering emotional support during challenging times. His ability to

connect with us on a personal level, and the kindness, created a bond that I will always cherish.

I would like to express my heartfelt gratitude to Dr. Vaidehi S. Paliya for his tremendous support and invaluable guidance, particularly in mastering data analysis methods in γ-ray astronomy. His interactions have always been a source of encouragement and rejuvenation for me. Dr. Paliya possesses an exceptional ability to inspire enthusiasm and a keen interest in tackling new research challenges, which has profoundly impacted my approach to science. I am deeply grateful for the many lessons I have learned from him, both academically and personally.

I am deeply thankful to Dr. Zahir Shah for his constant support and all the helpful suggestions and ideas he shared during the toughest times of my research. I needed expert advice in various contexts. His humble attitude and simplicity made him easy to approach.

I am deeply grateful to the University of Calicut for providing me with the opportunity to pursue my research and for the excellent facilities made available in the Department. I extend my heartfelt thanks to the current Head of the Department, Prof. Mohammed Shahin Thayyil, as well as the former HODs, Prof. Vinodkumar and Prof. P.P. Pradyumnan, for their invaluable assistance in ensuring that all official formalities were smoothly handled. I would also like to sincerely thank the non-teaching staff in the Department for their unwavering help and support throughout my journey.

Research is a collaborative journey, and having good companions along the way makes it immensely easier and more enjoyable. At this moment, I want to express my heartfelt gratitude to my friends in research, with whom I shared not only my academic concerns but also moments beyond the realm of research. I am especially thankful to Baheeja, my fellow researcher, for the countless hours we spent together. We shared everything that came our way, and her unwavering support was like a grounding force for me. Her presence undoubtedly helped ease many of my challenges.

I would also like to extend my appreciation to my other research teammates Zahoor Malik, Aqib Zahoor, and Amal for all the engaging discussions, joyous moments, and laughter we shared. Being a part of this group has truly been a privilege, and I feel fortunate to have been among such wonderful companions.

My gratitude also goes to my friends at the University of Calicut, particularly Sravan Das, Shabeeba, and Jamshias, whose companionship brought joy to my research journey and helped me endure the most difficult times. I fondly remember my hostel mates and friends Parvathy, Swapna, and Jinu for the beautiful memories we created together in the hostel and on campus. I will cherish these moments at the University and the hostel for the rest of my life.

Being a wife and a mother of two, my research journey was far from easy. Balancing research and personal life is a challenge, not just for the individual but for the entire family. I consider my family to be my greatest asset, my better half, Suneer, and my children, Aahil and Ahraz. Their deep understanding, patience, and unwavering pride in me have been my pillars of strength throughout this journey. If they had taken even a single step back, I am certain I would not have been able to complete my thesis. During a significant part of my research, I was away from them, yet they managed everything so gracefully without ever making me feel guilty. Their love and support were my driving force, and I owe them my deepest gratitude. At this significant milestone in my life, I extend my heartfelt gratitude to my beloved parents, Fathima and Mammed Koya, for their unwavering support, immense efforts, and boundless patience that have shaped me into the person I am today. I am deeply thankful to my wonderful sisters, Aysha and Anwara, for their constant love and companionship throughout my journey.

Finally, I would like to express my appreciation to all those individuals who, with their small acts of kindness, thoughtful gestures, or even a simple smile, brightened my days and brought happiness into my life during this incredible journey. Your support, no matter how small, has been invaluable, and I will forever cherish it.

Publications

1. **Aminabi Thekkoth**, C. Baheeja, S. Sahayanathan, and C. D. Ravikumar, "Gamma-ray variability and multi-wavelength insights into the unprecedented outburst from 4C 31.03," *Journal of High Energy Astrophysics*, vol. 42, pp. 115–128, June 2024. https://doi.org/10.1016/j.jheap.2024.04.005. arXiv: 2404.09137 [astro-ph.HE].

2. **Aminabi Thekkoth**, S. Sahayanathan, Z. Shah, V. S. Paliya, and C. D. Ravikumar, "Understanding the broad-band emission process of 3C 279 through long term spectral analysis," *Monthly Notices of the Royal Astronomical Society*, vol. 526, no. 4, pp. 6364–6380, December 2023. https://doi.org/10.1093/mnras/stad3094. arXiv: 2310.06819 [astro-ph.HE].

3. Aminabi Thekkoth, V. S. Paliya, C. Baheeja, S. Sahayanathan, and C. D. Ravikumar, "Investigating the multi-wavelength counterpart of the galactic plane γ-ray source 4FGL J0133.0+5930," (Under preparation).

4. P. N. Naseef Mohammed, **Aminabi Thekkoth**, C. Baheeja, S. Sahayanathan, V. S. Paliya, and C. D. Ravikumar, "Deciphering the multi-wavelength flares of the most distant very high-energy (>100 GeV) γ-ray emitting blazar," *Journal of High Energy Astrophysics*, vol. 47, p. 100365, July 2025. https://doi.org/10.1016/j.jheap.2025.100365. arXiv: 2502.01150 [astro-ph.HE].

5. C. Baheeja, **Aminabi Thekkoth**, S. Sahayanathan, C. D. Ravikumar, and N. Bhatt, "Long term multi-wavelength spectral variations of blazar S5 0716+714," *Publications of the Astronomical Society of Australia*, vol. 41, e103, 2024. https://doi.org/10.1017/pasa.2024.106.

Conference Presentations

1. **Fermi Summer School**, University of Delaware, USA, 28 May 2024 - 7 June 2024 – delivered an oral presentation titled *"Study on the unprecedented gamma-ray outburst from 4C 31.03"*

2. **Young Astronomer's Meet 2024**, Christ University, Bangalore, India, 6 March 2024 - 9 March 2024 – delivered a presentation titled *"Unravelling the very first major gamma-ray outburst from 4C 31.03"*

3. **IUCAA-sponsored 3-day Southern Regional Astronomy Meeting on research in astronomy: opportunities and challenges**, Rajagiri College, Cochin, India, 17 February 2023 - 19 February 2023 – delivered a presentation titled *"Understanding the spectral variations in Flat Spectrum Radio Quasars"*

4. **IUCAA-sponsored 4th National Conference on High Energy Emission from Active Galactic Nuclei**, Farook College, Kozhikode, India, 12 August 2022 - 14 August 2022 – delivered an oral presentation titled *"Understanding the Broadband emission process in 3C 279"*

5. **Theoretical Aspects of High Energy Emission from AGN**, University of Kashmir, Srinagar, India, 6 July 2021 – delivered an invited talk titled *"Probing the flux behavior of 3C 279 through Broadband correlation study"*

6. **41st Annual Meeting of Astronomical Society of India 2023**, IIT Indore, India, 1 March 2023 - 5 March 2023 – Presented a poster *"Identifying break/curvature in the GeV spectrum of 3C 454.3"*

7. **40th Annual Meeting of Astronomical Society of India 2022**, IIT Roorkee and ARIES Nainital, India, 25 March 2022 - 29 March 2022 –

Presented a poster *"Probing flux behaviour of 3C 279 through Broadband Correlation study"*

Contents

Preface

This thesis explores the multi-wavelength variability of blazars using two *Fermi* bright sources 3C 279 and 4C 31.03. Blazars are a subclass of active galactic nuclei (AGN) characterized by the relativistic jets that are pointed towards the observer. Much of the research on blazars have focused on the spectacular and strong flares exhibited by the sources in various energy bands. However, blazars are chaotically variable sources and their light curves feature both major and minor flares, the latter being more common. Therefore, a long-term study based on spectral and timing analysis is as essential as studies focused on individual flares of a source.

In Chapter 1, a general introduction to blazars is provided, including a detailed discussion of their unique properties. This chapter also presents a comprehensive description of the particle acceleration and radiative processes underlying the broadband emission of blazars. Chapter 2 introduces the space telescopes Fermi-LAT, Swift-XRT, and UVOT, along with the standard procedures for data reduction and analysis.

Chapter 3 focuses on a correlation/regression study of various spectral parameters of the narrowband spectra of the blazar 3C 279, used as a case study. It begins with a brief introduction to 3C 279, outlines the sample selection and data analysis methods, and discusses the results alongside their scientific interpretations. The primary conclusion of this study is that long-term spectral variations at low energies are mainly caused by changes in the spectral index, while variations at high energies are attributed to changes in the break energy of the underlying particle spectrum. These break energy variations are also reflected in the external Compton (EC) peak energy shifts, as evidenced by the observed γ-ray index values around 2. Systematic broadband SED modeling confirms that the EC peak energy shift can be caused either by variations in the break energy or by changes in the target photon

field.

Chapter 4 examines the first major γ-ray outburst exhibited by the blazar 4C 31.03 after a prolonged quiescent phase. This chapter begins with an introduction to the source, followed by a temporal analysis of its γ-ray light curves and the corresponding inferences. It also provides a detailed description of broadband SED modeling performed for three epochs. The study concludes that the production of γ-rays in 4C 31.03 likely occurs beyond the broad-line region (BLR) and notes a significant spectral transition of the source during the γ-ray outburst.

In Chapter 5, a flux distribution study for 3C 279 and 4C 31.03 is presented. For 3C 279, this study spans γ-ray, X-ray, and optical/UV bands using observations collected over 14 years. For 4C 31.03, the analysis is limited to the γ-ray spectrum due to the scarcity of X-ray and optical/UV data.

The final chapters of the thesis summarize the research conducted and provide recommendations for future studies.

List of Tables

List of Figures

Physical Constants

Parsec	pc = 3.086×10^{16} m
Solar Mass	$M_{\odot} = 1.989 \times 10^{30}$ kg
Solar Luminosity	$L_{\odot} = 3.826 \times 10^{33}$ erg/s
Velocity of light	c = 2.999×10^{8} m s^{-1}
Boltzmann Constant	$k_b = 1.38 \times 10^{-23}$ J/K
Planck's Constant	$h = 6.626 \times 10^{-34}$ Kg/s

Abbreviations

AGN	Active Galactic Nucleus
BL Lacs	BL Lacertae objects
BLR	Broad line region
CCD	Charge coupled device
EC	External Compton
FGL	Fermi Gamma-ray LAT
FSRQ	Flat spectrum radio quasars
HST	Hubble Space Telescope
IC	Inverse Compton
IR	Infrared
LAT	Large Area Telescope
SED	Spectral energy distribution
SMBH	Super massive black hole
SSC	Sychrotron self Compton
UVOT	Ultra-violet Optical Telescope
XRT	X-ray Telescope
3C	Third Cambridge Catalog

Chapter 1

Introduction

1.1 Active Galactic Nucleus: Star or Galaxy?

The sky has remained a mystery to humankind for ages. At night, it transforms into an eternal beauty, illuminated by countless stars, planets, moons, and the distant glow of galaxies each one carrying some stories to be told. Yet there are millions of exotic objects in the universe that remain shrouded in mystery. Active galactic nuclei (AGNs) are one such mystery. AGNs are extra-galactic sources associated with the nuclei of certain galaxies known as active galaxies. In these type of galaxies, energy arises from a central region that is extremely small compared to the galaxy as a whole, yet outshining the entire brightness of the host galaxy. This peculiar feature gives rise to the name 'Active galactic nucleus'. The Figure 1.1 shows the picture of an active galaxy Mkn 501 with its extremely bright center, imaged by Hubble space telescope. Today we know that AGNs are the most enigmatic sources in the universe powered by supermassive black-holes (SMBH) with masses in the range $10^{6-11} M_{\odot}$ at their centre.

AGN was first identified in 1908 by EA Fath at Lick Observatory when he noticed that the galaxy NGC 1068 had an unusual optical spectrum,

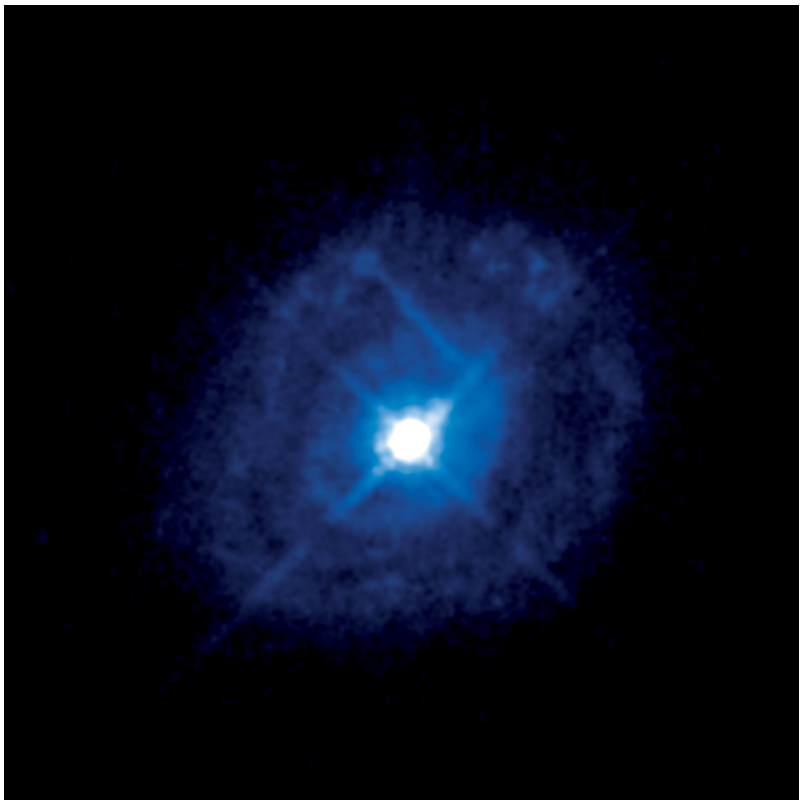

Figure 1.1: The image of the galaxy Markarian 509 from the NASA/ESA Hubble Space Telescope. The bright object at the center that appears like a star, is an active galactic nucleus. Credit: NASA, ESA, J. Kriss (STScI) and J. de Plaa (SRON)

similar to that of a gaseous nebula (Campbell, 1908). In 1943, Carl Seyfert also observed a similar kind of optical spectrum for six spiral galaxies having point-like central brightness profiles with broad emission lines. He confirmed that these objects form a distinct class of galaxies, now known as Seyfert galaxies (Seyfert, 1943). In late 1950s, with the revolution in radio astronomy that happened after the Second World War, the first radio sky surveys were performed and several catalogs were published. In 1963, Schmidt realized that 3C 273, a faint star-like object with a jet, has a high redshift and is associated with an optical counterpart (Schmidt, 1963). Later, it was realized that 3C 273 is actually a nuclear region of

a galaxy having brightness 100 times the host galaxy. Such objects were later named as quasi-stellar objects or Quasars and was categorized as one AGN subclass.

Energy Budget and Eddington Luminosity

The energy content of AGN is in the order of 10^{60} ergs and initially, it was attributed to a series of supernovae explosions occurring at the center of the galaxy (Burbidge 1959). The idea that SMBHs could account for the energy budget of AGNs was first put forward by Hoyle & Fowler (1963) and later by Salpeter (1964) and Lynden-Bell (1969).The theory of supermassive black holes remains consistent with the AGN energetics to date. The maximum amount of energy generated by the release of the gravitational potential energy, when a matter with mass m falls into a black-hole of mass, $M_{\rm BH}$ and Schwarzschild radius $R_s = 2GM_{\rm BH}/c^2$, is

$$E_{\rm max} = \frac{mc^2}{2}$$

This mechanism is highly efficient, as it can extract nearly 50% of the rest mass energy from the infalling material.

However, there is still a limit to the energy output of an AGN as the high radiation pressure exerted by the ions and electrons opposes the gravitational pull of the black-hole. The thermodynamic equilibrium between the gravitational force of a supermassive black-hole and the radiation pressure set a limit on the maximum amount of energy that can be liberated from an object. The maximum luminosity, that can be achieved from a thermodynamically balanced system is known as Eddington Limit, $L_{\rm Edd}$, given by

$$L_{\rm Edd} = \frac{4\pi c\, G M_{\rm BH}}{\kappa}, \tag{1.1}$$

where κ is the opacity of the environment surrounding the black-hole. For a spherically symmetric radiating object κ can be approximated as σ_T/m_p. σ_T is the Thomson scattering cross section and m_p is the proton mass. The Eddington luminosity can be expressed in terms of solar mass and luminosity as

$$L_{\text{Edd}} \approx 3 \times 10^4 \frac{M_{BH}}{M_\odot} L_\odot \tag{1.2}$$

Components of an AGN

AGNs are generally assumed to be consisting of the following components:

- SMBH: AGNs are powered by SMBHs with mass $10^{6-11} M_\odot$ at their center. The black-hole is believed to be spinning with some definite angular momentum, nevertheless, there is no constrained estimation of the spin.

- Accretion disk: In the process of accretion of matter into the SMBH, the high angular momentum of the gas and dust causes it to evolve towards a radiatively efficient thin disc. The disk luminosity will be primarily proportional to the rate of accretion of mass falling into the black-hole.

$$L_d \propto \frac{dm}{dt} c^2 \tag{1.3}$$

- X–ray corona: It is a hot layer sandwiching the accretion disc consisting radiatively active viscous regions in the inner sides of the disk.

- Broad line region (BLR): Sub-parsec region from the black-hole with many small clouds moving rapidly at ~ 3000 km s^{-1}. These clouds absorb about 10 percent of the radiation from the disk and re-emit it as broadened lines, hence the name Broad-line region (BLR).

- Torus: This is a dense molecular region at parsecs distance from the black-hole. It absorbs a fraction of the radiation produced by the disk and re-emit it in the infrared energies.

- Narrow line region: Another region of relatively less dense clouds ($10^3\,\mathrm{cm}^{-3}$) at large distance $\sim$ 100 parsec from the central core. These clouds are moving with lowe velocities ($\sim$ 300 $\mathrm{km\,s}^{-1}$) and are responsible for the narrow lines in the spectrum.

- The relativistic jets: These are magnetically collimated, bipolar outflows of plasma at relativistic speed from the central engine. These relativistic jets can extend up to Mpc scales beyond the host galaxy dimension.

How do we look at an AGN?

A key property of AGN is its observational diversity. Since the central region of AGN is anisotropic, the orientation effect is widely regarded as the main reason for this diversity (Antonucci, 1993). In general, AGNs fall into two physically distinct categories, radio-loud and radio-quiet (Wilson & Colbert, 1995). This classification is based on their ratio of luminosity at 5GHz to that in optical B-band (4850Å). Radio-loud AGNs, characterized by large-scale jets, have this ratio greater than 10 and are associated with elliptical galaxies. Radio quiet AGNs are associated with spiral galaxies and their ratio of radio to optical luminosity is less than 10 (Shastri et al., 1993). Based on this criterion, only 10% of AGNs were identified as radio-loud and this is still an unresolved dichotomy. Different subclasses within radio loud/quiet can be unified based on the viewing angle. The Unified model by Urry & Padovani (1995) categorizes radio-loud AGNs based on the viewing angle and the nature of optical and radio spectra. According to

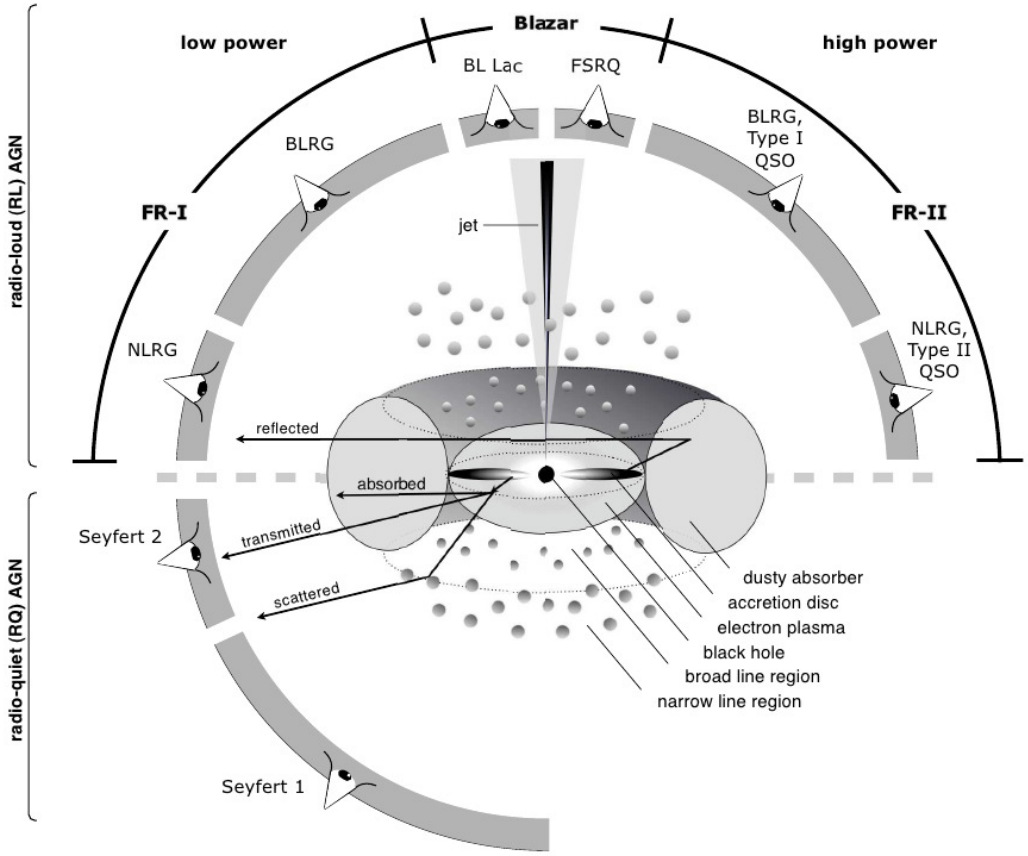

Figure 1.2: A schematic representation of how different classes of radio-loud AGNs emerge with the variation in the viewing angle of the observer. Image courtesy:Singh (2013)

this hypothesis, if the jet is directed towards the observer at smaller viewing angles ($< 10°$), the central core and the broad line region will be visible. This orientation gives blazar subclass and at larger inclinations, we can observe radio galaxies with large-scale jets.

1.2 Blazars

The term 'Blazar' was first proposed in 1978 by combining the words BL Lac objects and Optically violent variable quasars (OVV) (Angel & Stockman, 1980). Blazars represent the subclass of AGNs with one of two

the relativistic jets pointed at the observer. Their broad-band spectral energy distribution is characterized by rapid variability, blue-shifted line spectrum, and a high degree of polarization. Blazars are the most luminous objects in the universe and almost 70% of known extra-galactic γ-ray sources are blazars (Cerruti, 2020). The non-thermal continuum of blazars extends from radio to very-high-energy (VHE) γ-rays and is distinguished by two broad humps. The peak of the first radiative component falls in infrared to X-rays and the second in the energy range from MeV–TeV (Fossati et al., 1998). The Figure 1.3, depicts the broadband SED of 3C 454.3, a brightest blazar. Since the jet is moving towards the observer, the relativistic effect has three immediate consequences in the observed emission of blazars.

- Considering a blazar and a radio galaxy at same distance and with same intrinsic flux, the emission from the blazar will be several times brighter than that from radio galaxy since the observed flux density, F_ν of blazars will be translated from the jet's frame to observer's at scales as $\delta^3 F'_{\nu'}$, where $\delta = \dfrac{1}{\Gamma(1-\beta\cos\theta)}$ is the relativistic Doppler factor.

- The plasma moving in the jet will appear to be moving with velocities greater than c in the observer's frame. The apparent superluminal velocity is given by $\beta_{\rm app} = \dfrac{\beta\sin\theta}{1-\beta\,\cos\theta}$.

- As a result of time dilation, the flux variability time in the observer's frame will be shorter compared to the variability time scales in the jet's frame. A flare with a time scale of an hour in the jet's frame will likely be compressed into a minutes-long flare in the observer's frame (Lister et al., 2013).

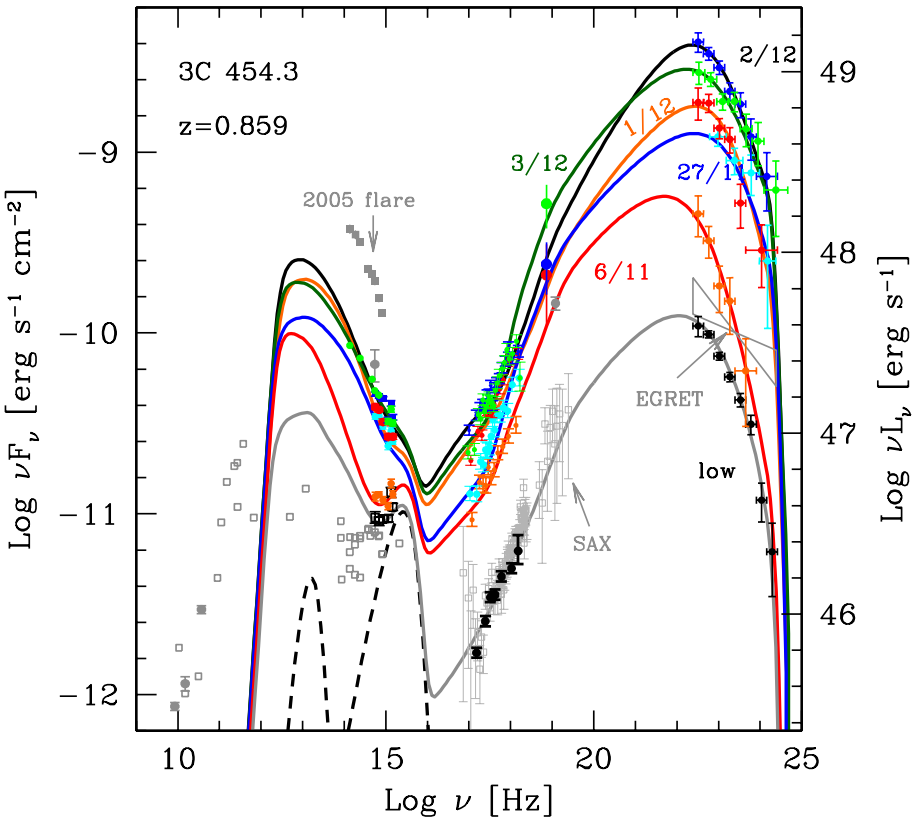

Figure 1.3: The SED of the blazar 3C 454.3 showing the double humb feature spnning from radio to γ-ray energies. The different colours in the figure represents observed SEDs corresponding to various epochs (Bonnoli et al., 2010).

1.2.1 Blazar sequence

Blazars typically come in two varieties: BL Lacertae objects (BL Lacs), and Flat-Spectrum-Radio-Quasars (FSRQs). FSRQs are with strong emission lines in the optical spectrum having EW greater than $5A^{\circ}$ while the opposite is true for BL Lac objects (Ghisellini et al., 1998). This classification is easy but does not depend on the source's actual physical state. As an alternative, Ghisellini et al. (2011) proposed FSRQs are the blazars with $L_{\rm BLR} > 10^{-3} L_{\rm Edd}$ and BL Lacs are the others.

However, there is a more physical concept that classifies this phenomenology known as blazar sequence (Fossati et al., 1998; Ghisellini

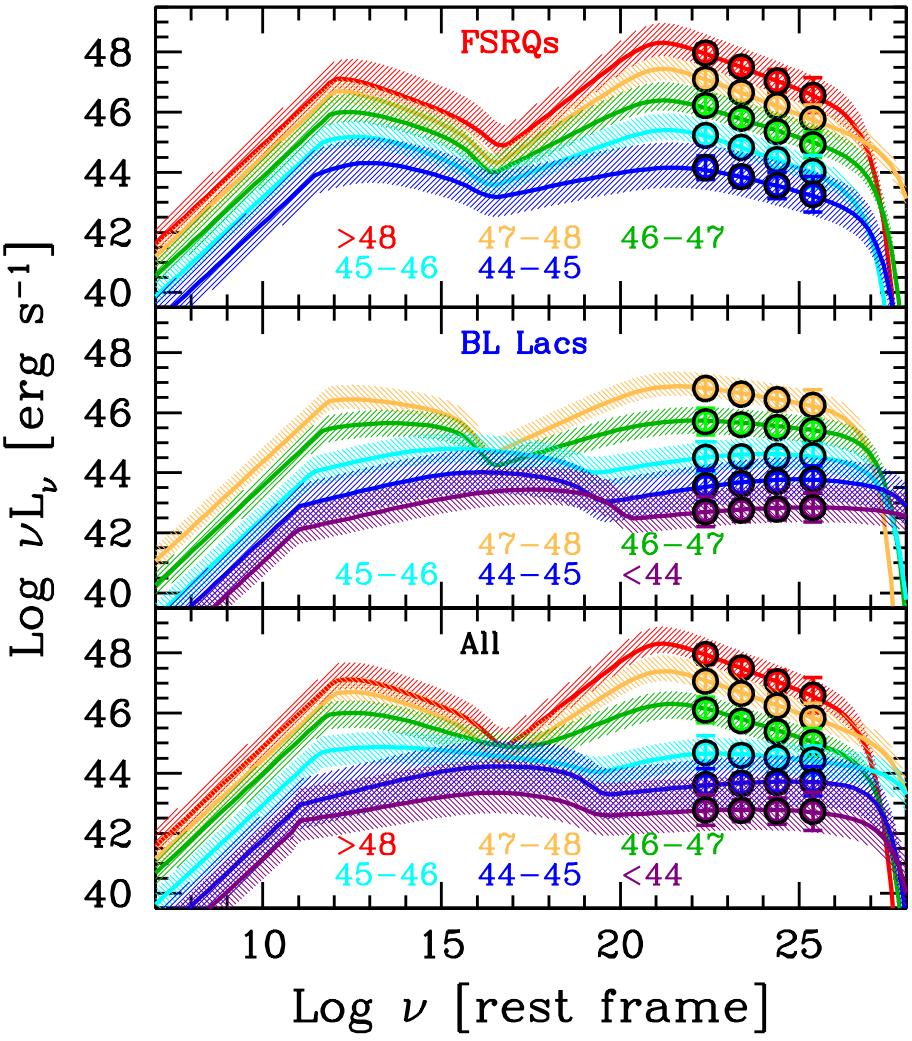

Figure 1.4: The phenomenological sequence revisited by Ghisellini et al. (2017). The sample is divided on the basis of γ–ray luminosity expressed in logarithms as indicated by the labels inboxed. The spectral shape of FSRQs remains almost same across the luminosity divisions, and shows variations for the Compton dominance. BL Lacs, significantly exhibit trends as in the primary blazar sequence.

et al., 1998). Blazar SEDs exhibit a continuity trend with the bolometric luminosity as i) become redder with increasing luminosity, i.e. SED peaks at low frequencies, (ii) Compton dominance ($P_{\rm IC}/P_{\rm sync}$), the ratio of powers of inverse Compton SED to synchrotron component, increases with luminosity, and iii) The γ-ray slope becomes softer while X-ray slope becomes harder

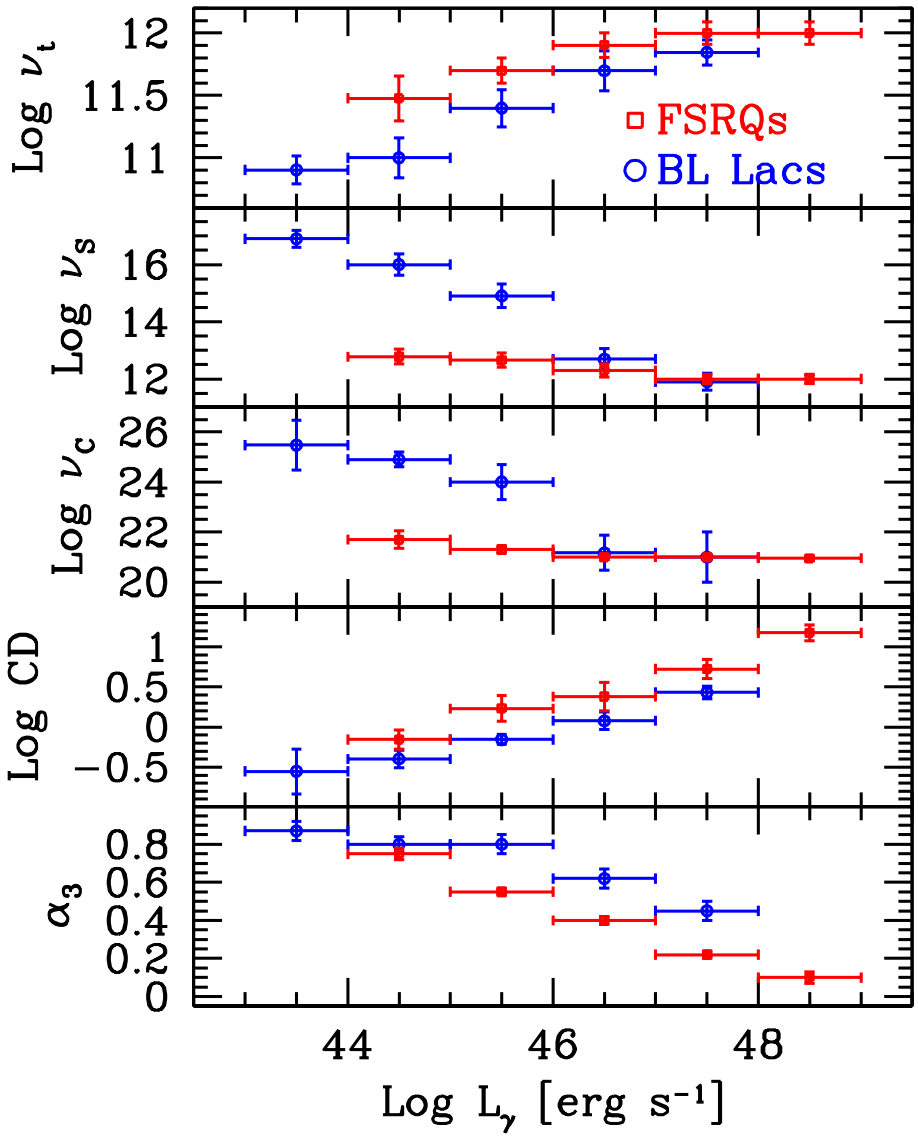

Figure 1.5: From top to bottom: low cut-off frequency due to self absorption ν_t, synchrotron SED peak frequency ν_s, high energy peak frequency ν_C, Compton dominance CD, and slope of SED before high energy peak α_3 as a function of the γ–ray luminosity in the LAT band Ghisellini et al. (2017).

with luminosity. FSRQs are the most luminous class with the lowest peak frequency and within BL Lacs, the sequence in the increasing order of peak frequency is LBL (low energy peak BL Lac) → IBL (intermediate energy peak BL Lac) → HBL (high energy peak BL Lac) → EHBL (extreme high energy peak BL Lac). However, the number of blazars considered for this study was 162 with only 33 detected in γ-rays by EGRET and they are the brightest γ-ray blazars. To compensate for this, Ghisellini et al. (2017) revisited the original sequence using the 3rd Fermi catalog of AGNs (Ajello et al., 2017). The revisited sequence with sample of 747 blazars is shown in Figure 1.4. The main findings of this study include i) All blazars do form a sequence as in the original and ii) When considering FSRQs and BL Lacs separately, FSRQs align with the sequence in the case of Compton dominance and the spectral slope at X-rays. They do not become redder with luminosity. Whereas, BL Lacs do form a sequence in all three cases (Figure 1.5)

1.2.2 Spectral energy distribution of Blazar

In the observed broadband SED of blazars, the component from radio to optical/X-ray is well established as synchrotron emission from relativistic electrons in the jet (Sahayanathan & Godambe, 2012; Rybicki & Lightman, 1986) (see Section 1.3.2 for synchrotron process). The origin and the location of high- energy emission (X-ray to TeV) emission is yet a matter of debate. There are two theoretically different approaches referred to as leptonic and hadronic models that explain the high energy SED of blazar (Cerruti, 2020; Böttcher et al., 2013; Boettcher, 2010). In leptonic scenarios, the population of relativistic leptons namely electrons and positrons are responsible for the entire radiative output while protons are assumed to be cold and contribute only toward the kinetic output of the jet. The high

energy SED is produced by inverse Compton scattering of soft photons either the synchrotron photon in the jet and/or the photon fields external to the jet (Sikora et al., 1994; Dermer & Schlickeiser, 1994a) (section 1.3.3). The emission mechanisms in these circumstances are named synchrotron self-Compton (SSC) and external Compton processes (EC) respectively. The X-ray emission from FSRQs is generally considered as SSC, while a dominant contribution of EC is required to address the γ-ray emission (Sahayanathan & Godambe, 2012; Shah et al., 2017). Sometimes, the combination of two or more EC components (eg: EC-disk or EC-BLR) provides a better fit to the γ-ray spectrum of these sources (Finke & Dermer, 2010). In BL Lac objects, the high energy SED is dominantly SSC, while there are exceptions. An additional EC of low luminosity disk photon and BLR gives more plausible parameters compared to pure SSC in the case of LBLs. Furthermore, the SEDs of IBLs S5 0716+714 and OJ 287 are well addressed by synchrotron+SSC+EC model (Madejski et al., 1999; Böttcher & Bloom, 2000).

The hadronic models assume the presence of relativistically accelerated protons in the blazar jets. Then the high-energy emission from blazar is dominated by proton-synchrotron emission, π° decay photons, and the out coming emissions from pair cascades (Mücke & Protheroe, 2001; Aharonian, 2000; Cerruti et al., 2011; Begelman et al., 1990). The solution involving the proton synchrotron process is the true hadronic model and others involving proton-photon interactions and subsequent pion decays are termed as lepto-hadronic. In the simplest lepto-hadronic model, the higher energy SED is still dominated by SSC and the emission from the secondary particles emerges in X-rays and the TeV regime is explained with photo-meson interactions (Böttcher et al., 2013; Cerruti et al., 2011). The main advantage of the lepto-hadronic model is that it can directly

predict the neutrino emission as secondary particles emerging from the processes. To date, there is no consensus on whether the leptonic or hadronic model better describes the SED of blazars. Leptonic models are a great success in this realm providing parameters close the minimum energy state of the source. However, in the case of TeV minute scale variability, instances of mismatch between steep optical-UV synchrotron spectrum and a relatively flat γ-ray spectrum, and the steepening of γ-ray spectrum due to Klein-Nishina effects, the leptonic models become inadequate. Even for a single source, the higher energy SED cannot always be explained by the leptonic or hadronic model alone. For example, the multi-wavelength SED of quasar 3C 279 is well fitted with a leptonic model involving synchrotron, SSC and EC emission processes (Paliya, 2015), whereas the VHE spectrum is better attributed to proton synchrotron model (Petropoulou & Mastichiadis, 2012) especially the TeV orphan flare happened in 2018 (Sunanda & Moharana, 2023) and Paliya et al. (2016) used lepto-hadronic processes to model the hard γ-ray flare in 2013. The contemporary detection of a VHE neutrino from IceCube-170922A, associated with the blazar TXS 0506+056 confirms the presence of hadronic processes happening in blazar jets and further asserts blazar as a cosmic-ray and neutrino source (IceCube Collaboration et al., 2018; Sunanda et al., 2022). The future multi-messenger observations including neutrino and gravitational waves together with the electromagnetic data can provide breakthroughs in the realm of extreme very high energy emission from blazars.

1.2.3 Blazars through multi-wavelength observations

Electromagnetic radiation is the major probe to understand the physical processes in blazars. The advancements that happened in multi-wavelength

astronomy facilitated huge advancements in our knowledge of the underlying non-thermal processes responsible for the emission in relativistic jets. Since blazar emission is prominent across the entire electromagnetic spectrum, it has been the primary target of interest for all multi-wavelength campaigns till date. Some exmaples for the major radio surveys on large samples of blazars are very long baseline interferometry (VLBI) surveys, single-dish observations, the 2 cm-survey program, Owens Valley Radio Observatory (OVRO) observations, and the Monitoring of Jets in AGNs with VLBA Experiments (MOJAVE) (Boccardi et al., 2017; Kellermann et al., 1998; Beasley et al., 2002; Lister et al., 2011). The MOJAVE program imaged 400 AGNs jets with the multi-epoch VLBA data at 15 GHz over a period of 25 years show a one-sided core-jet structure scenario for almost all blazars (Lister et al., 2011, 2016). Superluminal motion is usually observed in radio images with apparent speeds within $\sim 0.03c - 40c$ (Blandford et al., 2019).

Blazars are the dominant emitters in the extra-galactic γ-ray sky and have been monitored ever since the beginning of γ-ray astronomy. In the third EGRET (Energetic Gamma Ray Experiment Telescope) catalog, out of the 271 sources detected, 93 are blazars (Hartman et al., 1999). Now there are more than 3500 blazars in the latest 4FGL-DR3 catalog by Fermi γ-ray Space Telescope (Abdollahi et al., 2022). The fastest moving components observed in the radio images of almost all jetted sources were detected by Fermi, and this asserts the strong correlation between γ-ray luminosity and bulk Lorentz factor (Blandford et al., 2019). While Fermi can measure even up to 20 TeV energy range, the VHE emission from blazars up to 100s of TeV is monitored by several ground-based Imaging Atmospheric Cherenkov Telescopes (IACTs). High Energy Stereoscopic System (H.E.S.S.), Major Atmospheric Gamma Imaging Cherenkov Telescopes (MAGIC), Very

Energetic Radiation Imaging Telescope Array System (VERITAS), Major Atmospheric Cherenkov Experiment Telescope (MACE), and Cherenkov Telescope Array Observatory (CTAO) are the major IACT instruments. Recently, the Large-Sized Telescope (LST) at CTAO detected the quasar OP 313 with redshift 0.997 above 100 GeV. This is the first time discovery of VHE emission from a distant AGN. OP 313 becomes the farthest AGN and the second farthest astrophysical object ever detected at very high energies (Cortina & LST collaboration, 2023).

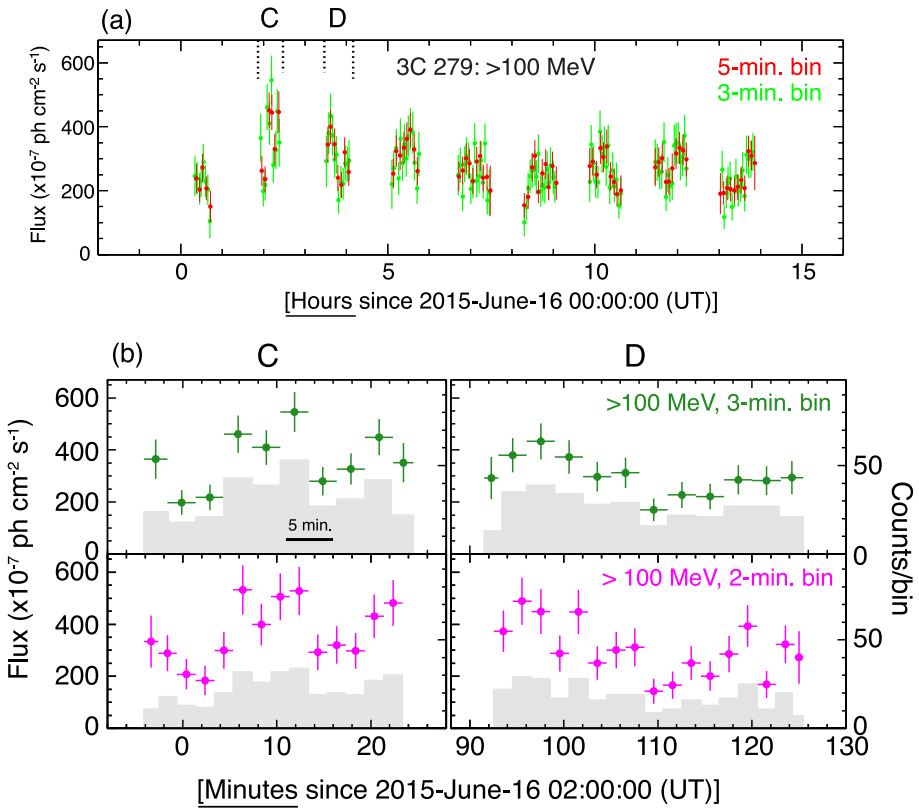

Figure 1.6: Light curves of 3C 279 above 100 MeV during the flare in 2015 June (a) 5 min (red) and 3 min (green) time binning (b): Enlarged images of epochs C and D. The fluxes are denoted by points and the histograms depicts the counts (right axis) detected within 8° radius around 3C 279 for each bin. Image credit: (Ackermann et al., 2016).

Flux variability time-scale in blazars ranges from a few minutes to decades. In recent years, γ-ray astronomy has matured and progressed

far beyond to utilize source variability time scales down to a few minutes. Fermi-LAT observed a giant outburst from the FSRQ 3C 279 on 2015 June 16 with a flux doubling within a time scale of almost 3 minutes (figure 1.6) (Ackermann et al., 2016). (Shukla et al., 2018) also reported a rapid GeV flare from CTA 102 within times of $\sim$ 5 minutes (Shukla et al., 2018). A rapid variability of 4 minutes is observed for the blazar PKS 2155-304 (Aharonian et al., 2007) and 1.5 hours for the source PKS 1510-089 (H. E. S. S. Collaboration et al., 2021) at VHE energy. The hour time-scales variability is observed sources MKN 501, 3C 273, and S5 0716+714 (Albert et al., 2007; Rani et al., 2013; Geng et al., 2020). Variability within less than a day at low energies is also observed for blazars. S5 0716+714 has shown intra-day variability in radio band and optical bands (Tripathi et al., 2024; Zhang et al., 2012; Gupta et al., 2012).

The rapid variability observed in blazars hints at extreme jet conditions based on light crossing time arguments like very compact emission regions located at a few hundred Schwarzschild radii away from the black-hole (Rieger, 2019b). The fastest variability timescale (τ) is often employed to constrain the physical size of the γ-ray emission region as

$$R \leq \frac{c\,\tau\,\delta}{1+z}\,, \tag{1.4}$$

where τ is characteristic time for fastest flux doubling/halving, δ is the Doppler factor and z is the redshift of the source. Conversely, must be located at a significant distance from the central black hole, as GeV γ-rays generated near the black hole can be absorbed by low-energy photons originating from the disk and broad-line region (BLR). The condition for the transparency of γ-rays produced from an emission region of size R (equation 1.4) against the pair absorption by the low energy photon fields can be utilized to set a lower-limit on the jet Doppler factor (Dondi &

Ghisellini, 1995a). For a γ-ray photon of energy $\epsilon = E/mc^2$ to be detected, the optical depth for the $\gamma - \gamma$ absorption in the emission region will be minimum, i.e. $\tau_{\gamma-\gamma} < 1$. Using the expression for the optical depth, $\tau_{\gamma-\gamma}$ in terms of the observational parameters, we can obtain the lower-limit on Doppler factor as

$$\delta \geq \left[\frac{\sigma_T \, d_L^2 \, (1+z)^2}{4 \, \tau \, m_e c^4} \epsilon \, f_x\right]^{\frac{1}{6}}, \tag{1.5}$$

where σ_T is the Thomson scattering cross section, d_L is the luminosity distance, and f_x is the X-ray flux observed simultaneously with the γ-ray events. The TeV flaring within a few minutes yields a Doppler factor > 50, typically more than the usual range of 10-35 observed from superluminal motion. The emission region size constrained through rapid variability may not be consistent with that derived through multi-wavelength SED modeling. The variability studies, usually performed in the context of high-flaring events remain inadequate to probe the exact nature of the emission scenarios since the flares are usually interpreted in terms of the interaction with shocks that propagate down the jet. In the context of variability, it is also essential to study the more frequent minor flares in the long-term lightcurves (Rieger, 2019b).

The lightcurves spanning months to years are usually referred as long-term light curves. Lightcurves with more than 10 years of data are available for blazars in optical and radio bands. In the X-ray band, some major blazars like MKN 421, 3C 279, MKN 501, 3C 454.3, PKS 1510-089 are monitored over more than a decade by Swift telescope onboard. Blazars are also monitored by other X-ray instruments like Chandra, XMM-Newton, and NuSTAR. Fortunately, Fermi-LAT with its scanning mode provides a surfeit of continuous γ-ray observations for almost all blazars detected.

The long-term multi-wavelength lightcurves are effective tools for analyzing the correlated variability and studying the connection between different wavebands, the underlying physical process behind the variations, and the possible periodicities in the light curves. The Discrete Correlation Function (DCF) can be utilized to study the cross-correlation between the lightcurves in different energy bands. Blazars show both correlated flares and time lags in the multi-wavelength lightcurves. Prince (2020b) showed a correlated variability with zero time lag between γ-ray and X-ray lightcurves of 3C 279 during the period 2017-2018. A strong correlation and zero time lag of γ-ray flares with optical or X-ray flares indicate its co-spatial origin, whereas a definite time lag its opposite. Moreover, under the leptonic scenario, a strong correlation between γ-ray flares with optical and X-ray flares is expected (Rajput et al., 2020). Besides correlated, orphan flares (no detected counterparts in other energy bands) are often observed in blazar multi-wavelength light curves. Liodakis et al. (2019) found that about 50% of the optical flares of blazars had no GeV counterparts and about 20% of γ-ray flares had no optical counterparts in a sample of 178 blazars. The orphan γ-ray flares may hint at the hadronic signatures in the high-energy emission process (Rajput et al., 2020).

The narrow band spectrum of blazars can be approximated with a simple power-law model. Nevertheless, the spectra falling on the peak of the SED deviate from a power-law. The synchrotron peak in HBLs/EHBLs falls in the X-ray energy range (0.3-50 keV) and the spectrum at this energy is convex shaped and shows a positive curvature (Massaro et al., 2004). The X-ray spectrum of HBLs is often better explained by a log-parabolic function indicating the same distribution for the underlying particle distribution. Such a particle distribution indicates an acceleration scenario where the probability of acceleration is energy dependent in a way

that the most energetic particles are less probable to get accelerated. We can also constrain the SED peak energy from a narrow band spectrum described by a log-parabolic function (Massaro et al., 2004). In FSRQs, the X-ray spectrum sometimes falls near the transition region between the synchrotron and inverse Compton dominated regions in the SED. Similarly, in many of the IBLs and LBLs, the soft X-ray spectrum switches between synchrotron and IC emissions. In these cases, we can model the transition region and obtain the value of energy at which the dominant emission mechanism changes (see Section 3.3.1 chapter 3). Besides, we can constrain the minimum particle energy $\gamma_{\rm min}$ from this value (Jagan et al., 2021). The Fermi observations revealed a clear spectral break at GeV energies in the spectrum of some FSRQs and low energy peaking BL lacs (Abdo et al., 2010d; Cerruti et al., 2013; Kang et al., 2021). Several phenomena such as Klein-Nishina effects, intrinsic break in the particle spectrum, internal absorption of γ-ray photons, and addition of two or more EC components are used to interpret the GeV spectral break (Finke & Dermer, 2010; Liu & Bai, 2006; Poutanen & Stern, 2010).

One of the peculiar properties of blazars is that their spectral index or peak energy exhibits a positive or negative correlation with the flux. Correspondingly, the positive correlation of index/peak energy with flux is termed as "softer or bluer when brighter", and the anti-correlation is known as "harder or redder when brighter" trends. Figure 1.7 shows the "softer or bluer when brighter" trend exhibited by the X-ray spectrum of HBL MKN 421. These trends are observed for many blazars in X-ray, optical, and γ-ray spectra (Pandey et al., 2017; Bhatta et al., 2018; Kapanadze et al., 2020; Shah et al., 2019). The harder when brighter trend indicates the dominance of soft electrons' contribution to the flux enhancement, while a steeper spectrum in a high flux state suggests the opposite (Bhatta

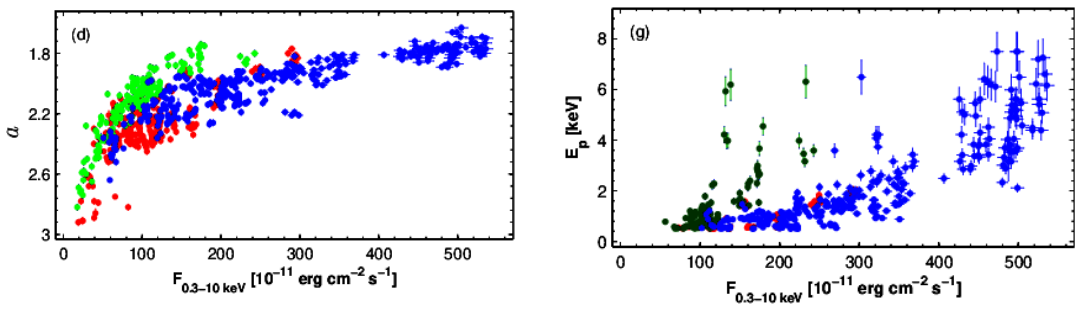

Figure 1.7: Correlation shown by the unabsorbed 0.3–10 keV flux with (left) the spectral index, a, and (right) the synchrotron SED peak energy E_p for the source MKN 421 respectively (Kapanadze et al., 2020).

et al., 2018). The blazars with steeper spectral indices are found to be more variable also (Bhatta & Dhital, 2020; Bhatta et al., 2018). The flux variability can be caused by circumstances such as increased injection of accelerated particles, release of energy over a large volume capable of producing effective acceleration, and big flares (Hayashida et al., 2015). The flux variations can also be due to extrinsic effects such as variations in the Doppler factor induced by the changes in the viewing angle (Bhatta, 2017). The relation between flux and index or peak energy is found to be varying during different periods and the overall nature of correlation between the flux and spectral state in blazars is somewhat uncertain.

1.3 Radiative Processes in Astrophysics

1.3.1 Scattering of a photon by an electron

The classical picture of the scattering of a photon by an electron can be illustrated as when an electromagnetic wave is incident on a charged particle, the electric and magnetic components of the wave exert a Lorentz force on the particle. Consequently, the particle gets accelerated and emits radiation. The particle absorbs energy from the incident radiation and re-emits it again

as radiation. This classical non-relativistic scenario is termed as Thomson scattering where the initial energy of the photon $\epsilon_i = h\nu$ is very much less than the rest mass energy $m_e c^2$ of the electron. This is an elastic or coherent scattering process as there is no change in the energy of the charged particle and the photon before and after scattering. i.e.

$$\epsilon_i = \epsilon_f,$$

where ϵ_f is the photon energy after scattering. The probability of a photon getting absorbed by an electron can be quantified by the differential scattering cross section given by

$$\frac{d\sigma}{d\Omega} = \left(\frac{e^2}{m_e\, c^2}\right) \frac{1}{2}(1 + \cos^2\theta), \tag{1.6}$$

where θ is the angle between incident and scattered radiation. The total cross-section can be obtained by integrating the equation 1.6 over the solid angle. The total scattering cross section associated with the scattering of a photon by an electron in the classical limit is known as Thomson scattering cross section, σ_T.

$$\sigma_T = \frac{8\pi}{3} \left(\frac{e^2}{m_e\, c^2}\right)^2 \tag{1.7}$$

It is numerically equal to $6.65 \times 10^{-25}\,\mathrm{cm}^{-2}$ and the quantity $e^2/m_e c^2$ is called classical electron radius r_0 ($2.8 \times 10^{-13}\,\mathrm{cm}$). Quantum mechanical treatment is required when the photon energy is comparable to electron rest mass energy, and the scattering in this limit is known as Compton scattering (Compton, 1923). The change in the energy of the photon in

Compton scattering is given by

$$\Delta\lambda \;=\; \frac{h}{m_e\,c}(1-\cos\theta), \tag{1.8}$$

and the energy of the photon after scattering, ϵ_f is related to energy before scattering ϵ_i as

$$\epsilon_f \;=\; \frac{\epsilon_i}{1+\frac{\epsilon_i}{m_e\,c^2}\,(1-\cos\theta)} \tag{1.9}$$

In the limit $\epsilon_i \ll m_e\,c^2$, this will turn as classical and ϵ_i will be equal to ϵ_f. However, at photon energies ϵ_i much greater than $m_e c^2$, the scattering becomes deeply inelastic and the scattering cross section decline fast from the value of σ_T (Klein & Nishina, 1928). This is known as Klein-Nishina effect and the differential scattering cross section in this limit ($\epsilon_i > m_e\,c^2$) is given by

$$\frac{d\sigma}{d\Omega} \;=\; \frac{3}{16\pi}\,\sigma_T\,\left(\frac{\epsilon_f}{\epsilon_i}\right)^2\,\left(\frac{\epsilon_i}{\epsilon_f}+\frac{\epsilon_f}{\epsilon_i}-\sin^2\theta\right) \tag{1.10}$$

The total cross section $\sigma_{\rm KN}$ can be obtained by integrating the equation (1.10) over the solid angle.

$$\sigma_{\rm KN} \;=\; \frac{3\sigma_T}{4}\,\left[\frac{1+x}{x^3}\,\left(\frac{2x(1+x)}{1+2x}\;-\;\ln(1+2x)\right)+\frac{\ln(1+2x)}{2x}\;-\frac{1+3x}{(1+2x)^2}\right] \tag{1.11}$$

where $x \;=\; \epsilon_i/m_e c^2$. At the classical limit, $\epsilon_i \ll m_e c^2$ or $x \ll 1$, $\sigma_{\rm KN}$ can be approximated as

$$\sigma_{\rm KN} \approx\; \sigma_T\,\left(1-2x+\frac{26x^2}{5}+..\right) \tag{1.12}$$

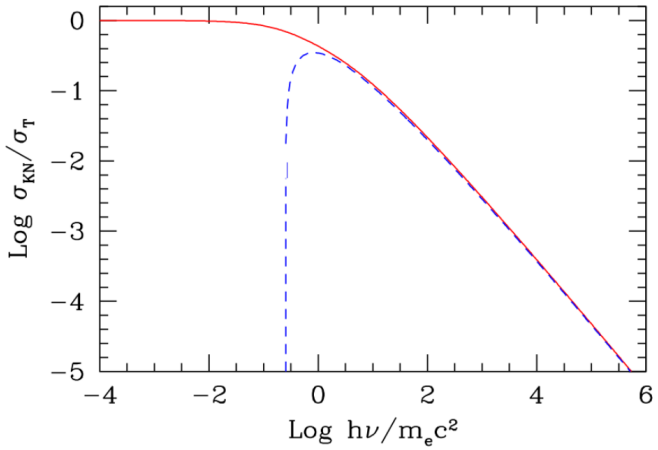

Figure 1.8: The plot showing variation of $\sigma_{\rm KN}/\sigma_T$ with energy in log. The plot is taken from Condon & Ransom (2016). It is clear from the Figure that $\sigma_{\rm KN}$ drops off significantly at higher energies. The dashed curve represents the approximate solution at higher energies given by the equation (1.13)

At the asymptotic limit $\epsilon_i \gg m_e c^2$ or $x \gg 1$ (the extreme Klein-Nishina), the cross-section is approximately

$$\sigma_{\rm KN} \approx \sigma_T \frac{3}{8x}\left(\ln 2x + \frac{1}{2}\right) \tag{1.13}$$

The decaying of scattering cross section $\sigma_{\rm KN}$ in the Klein-Nishina scattering is shown in Figure 1.8. This can make a signature cutoff in the observed γ-ray spectrum of blazars where the γ-rays are produced from the inverse Compton scattering of low-energy photons as discussed in the section 1.3.3.

1.3.2 Synchrotron

All accelerated charged particles emit radiation known as bremsstrahlung. When the acceleration is produced by magnetic field, the emission is termed as magneto-bremsstrahlung. In the astrophysical context, sources are extremely magnetized, capable of providing acceleration to charged particles up to relativistic energies and the magneto-bremsstrahlung emitted by these

particles is commonly known as synchrotron radiation. The most prominent particles taking part in the emission processes are the lightest ones (electrons, positrons). The power of emitted radiation by a non-relativistic particle is given by Larmor's equation,

$$P = \frac{2}{3}\frac{q^2\,a^2}{c^3}, \tag{1.14}$$

where q is the charge and a is the acceleration of the particle. The synchrotron radiation is omnipresent in the field of AGNs especially blazars, as it completely describes the emitted radiation from radio to optical/X-ray wavelengths in these objects.

Using fundamental principles of electrodynamics, we can write the equation of motion of an electron (relativistic) moving with a velocity $\vec{v}$ and Lorentz factor $\gamma = (1 - v^2/c^2)^{-\frac{1}{2}}$ in a magnetic field $\vec{B}$ as

$$F = \frac{d}{dt}(\gamma m_e \vec{v}) = \frac{e}{c}\,(\vec{v} \times \vec{B}) \tag{1.15}$$

From the property of cross product of vectors, it is clear that the acceleration will be along the direction perpendicular to that of the motion of electron and the field. The magnitudes of the components of electron's velocity, $v_{\parallel}$ and $v_{\perp}$ are constant, and the particle will execute a helical motion with constant radius r_g and pitch angle α with respect to the direction of the field $\vec{B}$ (Condon & Ransom, 2016). The component of $\vec{a}$ perpendicular to the direction of $\vec{B}$ is given by

$$a_{\perp} = \frac{eBv\sin\alpha}{\gamma mc} \tag{1.16}$$

The radius of gyration of electron, r_g can be found from $a_\perp = v_\perp^2/r_g$.

$$r_g = \frac{\gamma m_e c^2 \beta \sin\alpha}{eB} \tag{1.17}$$

The frequency of gyration or the fundamental frequency of synchrotron radiation from a single electron is the inverse of the time required to complete one orbit and is given by

$$\nu_B = \frac{v \sin\alpha}{2\pi r_g} = \frac{\nu_L}{\gamma}, \tag{1.18}$$

where ν_L is the Larmor frequency (gyration frequency of non-relativistic particle), given by

$$\nu_L = \frac{eB}{2\pi\gamma m_e c} \tag{1.19}$$

In the case of synchrotron, the radiated power in the electron's rest frame can be obtained by modifying the Larmor equation 1.14,

$$P' = \frac{2e^2 (a'_\perp)^2}{3c^3} \tag{1.20}$$

Applying the Lorentz transformations $a_\perp = a'_\perp/\gamma^2$, $P' = P$, and substituting for $a_\perp$ and using equation 1.7, we can obtain the equation for the synchrotron power emitted by a single electron in the lab frame as (Rybicki & Lightman, 1986; Ghisellini, 2013; Condon & Ransom, 2016)

$$P = 2\,\sigma_T\, c\, \beta^2 \gamma^2\, U_B \sin^2\alpha \tag{1.21}$$

Where U_B is the magnetic field energy density defined by

$$U_B = \frac{B^2}{8\pi}. \tag{1.22}$$

Average synchrotron power

In astrophysical environments like relativistic jets, the electrons are multiply scattered by the magnetic field fluctuations and other charged particles. Consequently, their pitch angles gradually become random and isotropic (Rybicki & Lightman, 1986). Thus the average synchrotron power per electron from an ensemble of electrons having the same energy and an isotropic distribution of pitch angle α, can be obtained by averaging $\sin^2\alpha$ over all the pitch angles.

$$\langle \sin^2\alpha \rangle \;=\; \frac{1}{4\pi}\int_0^{4\pi} \sin^2\alpha \, d\Omega \;=\; \frac{2}{3}$$

Thus the average synchrotron power per single electron is

$$\langle P \rangle \;=\; \frac{4}{3}\sigma_T \, \beta^2 \, \gamma^2 \, c \, U_B \tag{1.23}$$

The synchrotron spectrum from a single electron

To an observer from the earth, the synchrotron radiation appears at frequencies higher than ν_B although the electrons emit at a single frequency. The electrons emit isotropically in their co-moving frames. However, due to aberration effects, the radiation will be strongly beamed and confined in a narrow cone of angular width $\sim 2/\gamma$ along the direction of the observer. Thus the observer will see the radiation only from a tiny fraction, $1/(\pi\gamma)$ of the electron's total circular orbit at the time when the latter is pointing almost directly to the observer (Figure 1.10). i.e., although the relativistic electron emits photons all along its orbit, it will shoot or direct along the observer's direction only for the time, $\Delta t' = 1/\gamma\omega_B$, where $\omega_B = 2\pi\nu_B$, the angular frequency of the radiation (Ghisellini, 2013; Condon & Ransom, 2016). This is the time of emissions in the electron's frame whenever the

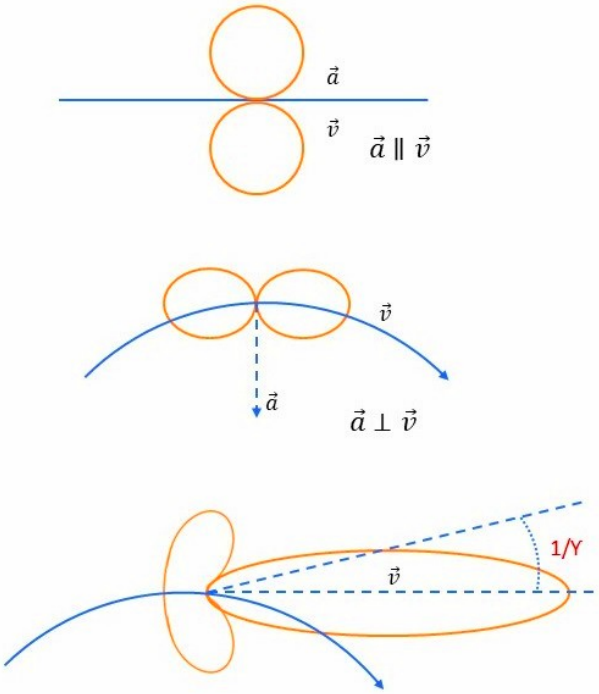

Figure 1.9: a) Radiation patterns of electrons with velocities: relativistic (top), mildly relativistic (middle), and relativistic (bottom) (Ghisellini, 2013).

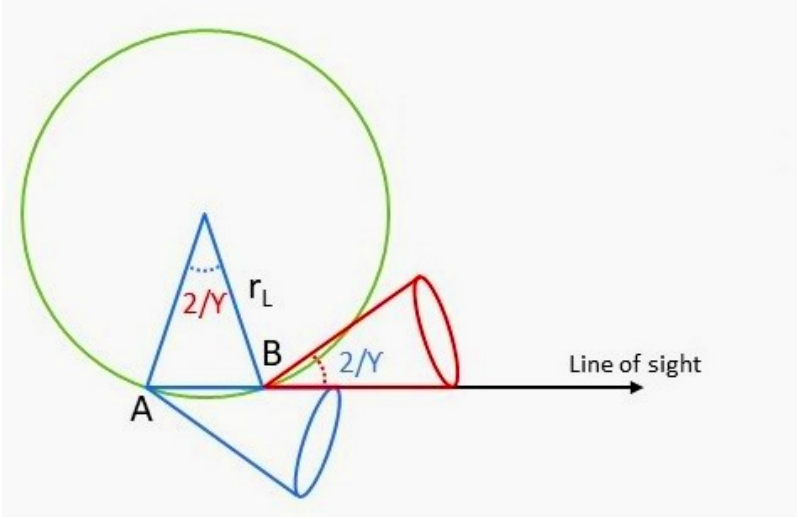

Figure 1.10: The orbit of an electron with 90° pitch angle will be a circle with radius r_L, and the observer will see the radiation when the beaming cone points towards the observer (Ghisellini, 2013).

observer sees the radiation. Since the electron is relativistic, the observer sees the radiation in the form of pulses in much shorter time intervals given by

$$\Delta t \, = \, \frac{1}{\gamma^3 \omega_B} \tag{1.24}$$

Thus one can find that the observed frequency of synchrotron radiation gets increased by a factor of γ^3 in the observer's frame of reference (Rybicki & Lightman, 1986).

$$\nu_s \, = \, \gamma^3 \nu_B \qquad \text{or} \qquad \nu_s \, = \, \gamma^2 \nu_L \tag{1.25}$$

The observed synchrotron spectrum, $P(\nu)$ will be the Fourier transform of the time series of the short pulses and can be expressed as given by (Ghisellini, 2013)

$$P(\nu) = \frac{\sqrt{3} e^3 B \sin\alpha}{mc^2} \left[\left(\frac{\nu}{\nu_c} \right) \int_{\nu/\nu_c}^{\infty} K_{5/3}(y) dy \right] \tag{1.26}$$

where $\nu_c \, = \, \frac{3}{2} \nu_s \sin\alpha$ is the cutoff frequency and $K_{5/3}(y)$ is the modified Bessel function. The frequency dependence is contained in the function in the square bracket of the equation 1.26 which peaks at frequency $\nu \sim 0.29\nu_c$. At low frequencies, the spectrum can be well approximated with a power-law of slope 1/3 and it decays exponentially at higher frequencies.

$$P(\nu) \, \propto \begin{cases} \left(\dfrac{\nu}{2\nu_c} \right)^{\frac{1}{3}} & \nu \ll \nu_c \\ \dfrac{\nu}{\nu_c} \, \exp(\frac{-\nu}{\nu_c}) & \nu \gg \nu_c \end{cases} \tag{1.27}$$

Synchrotron spectrum from a non-thermal distribution of electrons

The simplest functional form for the accelerated particle distribution in AGNs and blazars is a power-law represented as

$$N(\gamma)\, d\gamma \;=\; K\gamma^{-p}\; cm^{-3}; \qquad \gamma_{\rm min} < \gamma < \gamma_{max} \tag{1.28}$$

where $\gamma_{\rm min}$ and γ_{max} are the minimum and maximum of the Lorentz factor of the particles and K is the normalization factor.

The total synchrotron emissivity from a power-law distribution of electrons can be estimated as $1/4\pi$ times the integral of the power emitted by a single electron times the $N(\gamma)$ across all γ.

$$\epsilon_s(\nu) \;=\; \frac{1}{4\pi}\int_{\gamma_{\rm min}}^{\gamma_{max}} P(\nu)N(\gamma)d\gamma \tag{1.29}$$

The spectral index of the total synchrotron spectrum must be greater than 1/3, the slope of the single particle spectrum. One can find from equation 1.29 that,

$$\epsilon_s(\nu) \;\propto\; K\, B^{(p+1)/2}\, \nu^{-(p-1)/2} \tag{1.30}$$

Thus, it is interesting to notice that a power-law particle distribution gives out a power-law photon spectrum for which the spectral index, α is related to the particle index as

$$\alpha \;=\; \frac{p-1}{2}$$

The total synchrotron flux from a homogeneous optically thin source of volume V and size R at a distance of d_L can be obtained from emissivity $\epsilon_s(\nu)$ as

$$F(\nu) \;=\; \frac{V}{d_L^2}\,\epsilon_s(\nu) \propto \frac{R^3}{d_L^2} K\, B^{1+\alpha}\, \nu^{\alpha} \tag{1.31}$$

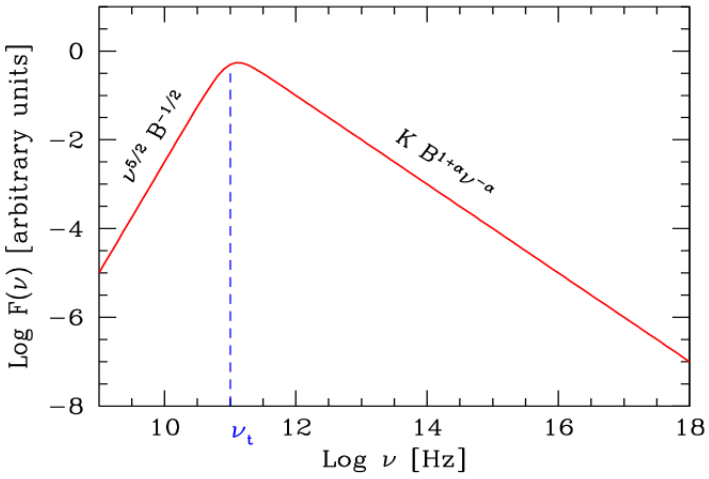

Figure 1.11: The synchrotron spectrum from a partially self-absorbed source. ν_t is the frequency at which the optical depth, τ becomes unity.

Synchrotron self absorption

According to equation (1.31), the spectrum of an optically thin (optical depth $\tau \ll 1$) is proportional to $\nu^{-\alpha}$, and according to this one would expect a continuously rising spectrum at low frequencies. However, the observed spectrum shows a falling off at low energies due to the absorption of synchrotron photons by the electrons in the emission region. This phenomenon is known as synchrotron self absorption and the low frequency spectrum (Radio wavelength) decay more rapidly with an index of -5/2, independent of that of the particle distribution as given by (Condon & Ransom, 2016),

$$I_\nu \propto \nu^{5/2}\, B^{-1/2} \tag{1.32}$$

The Figure 1.11 shows the synchrotron spectrum of a partially absorbed source.

1.3.3 Inverse Compton scattering

When the electrons that scatter the photons become relativistic, the opposite of Compton scattering can happen, in which the photon can gain energy from the electron and the process is known as inverse Compton scattering. Since the electrons are relativistic, one must apply the Lorentz transformations between the observables measured from electron's rest frame K′ and from the lab frame K. The photon energies in K and K′ are related as,

$$\epsilon'_{i,f} \;=\; \epsilon_{i,f}\gamma(1-\beta\cos\phi_{i,f}) \tag{1.33}$$

where $\phi_{i,f}$ are the angles between electron and photon directions and i and f suffixes represent quantities before and after collisions. The transformation equation for $\phi_{i,f}$ can be written following the relativistic aberration formula as,

$$\cos\phi'_{i,f} \;=\; \frac{\cos\phi_{i,f}-\beta}{1-\beta\cos\phi_{i,f}} \tag{1.34}$$

Using equation 1.34, the relation for photon energies can also be written as

$$\epsilon'_{i,f} \;=\; \frac{\epsilon_{i,f}}{\gamma(1+\beta\cos\phi'_{i,f})} \tag{1.35}$$

In the lab frame, K, the incoming photons are isotropically distributed concerning a moving electron with velocity, v and hence half of the photons must have ϕ_i between π and $\pi/2$. Hence from equation 1.34, the value for $\cos\phi'_i$ will be $-\beta$ when $\phi_i = \pi/2$. This means that for relativistic electrons with $\beta \simeq 1$, most of the photons are in head-on scattering in K' as shown in Figure1.12.

In **Thomson regime:** for $\epsilon'_i \ll mc^2$, $\epsilon'_i = \epsilon'_f$ Following equations 1.33

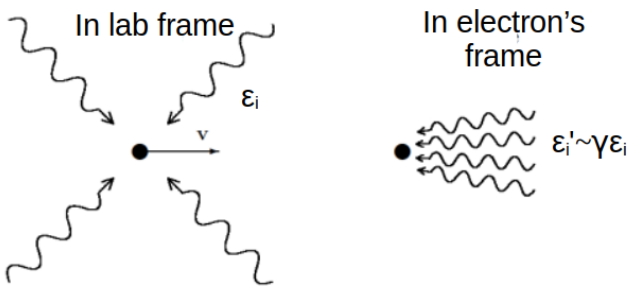

Figure 1.12: left) In the lab frame K, incoming photons are isotropically distributed with energy $\sim \epsilon_i$ about an electron with velocity v. right) In electron's frame K′, the incoming photons are significantly anisotropic and with respect to electron, they are nearly head-on, and their typical energies are boosted by a factor γ. Image courtesy: Frank M. Reiger

and 1.35, we can get

$$\frac{\epsilon_f}{\gamma(1+\beta\cos\phi'_f)} = \epsilon_i\,\gamma(1-\beta\cos\phi_f) \tag{1.36}$$

substituting for ϕ'_f using equation 1.34, and simplifying, we can obtain the energy of the scattered photon in the lab frame as,

$$\epsilon_f = \epsilon_i \frac{(1-\beta\cos\phi_i)}{(1-\beta\cos\phi_f)} \tag{1.37}$$

The maximum energy transfer occurs when the collision is head-on and the photon is scattered along the direction of electrons ($\cos\phi_i = \pi$ and $\cos\phi_f = 0$). i.e. the maximum energy transfer in Thomson limit is given by

$$\epsilon_{f,max} = 4\gamma^2\epsilon_i \tag{1.38}$$

In **Klein-Nishina regime:** $\epsilon'_i \gg mc^2$ and the maximum amount of energy transfer can be obtained by using the energy conservation in lab frame K as

$$\epsilon_{f,max} \leq \epsilon_i + \gamma m_e c^2 \tag{1.39}$$

Energy loss rate per single electron in the Thomson limit

In the Thomson limit, the energy of the scattered photon is much greater than the incident photon in the lab frame. Hence the rate of energy loss of electron would be equal to the rate of energy gain of scattered photon (Blumenthal & Gould, 1970; Ghisellini, 2013). i.e.

$$-\frac{dE_e}{dt} = \frac{d\epsilon_f}{dt}$$

The power emitted by the electron $-\frac{dE_e}{dt}$ is an invariant quantity, hence,

$$-\frac{dE_e}{dt} = \frac{d\epsilon'_f}{dt'} = \epsilon'_f \frac{dN'}{dt\prime} \tag{1.40}$$

Here $\dfrac{dN}{dt}$ is called the rate of scattering[1]. Let n be the number density of photons with energy $\epsilon = h\nu$ moving with velocity v and ϕ is the angle between photon and electron directions. For a mono-directional photon distribution, the scattering rate can be given by

$$\frac{dN}{dt} = \int \sigma_T \, v_{\rm rel} \, dn = \int \sigma_T \, c \, (1 - \beta \cos\phi) \, dn,$$

where $v_{\rm rel}$ is the relative velocity of the photon with respect to the electron. The average rate of energy loss per single electron in the Thomson limit can be written as (Blumenthal & Gould, 1970)

$$-\frac{dE_e}{dt} = \frac{4}{3} \sigma_T \, c \, \beta^2 \, \gamma^2 \, U_{\rm ph} \tag{1.41}$$

where $U_{\rm ph} = 4/3 \int \epsilon_i \, dn$ is the energy density of the isotropic photon gas (Ghisellini, 2013; Blumenthal & Gould, 1970).

[1]number of scattering per unit time per electron. Here the primed quantities are measured from electron's rest frame and unprimed are from the lab frame.

Following equations 1.21 and 1.41, one can find that the ratio of synchrotron power $P_{\rm sync}$ to the inverse Compton power $P_{\rm com}$ radiated from a single electron is equal to the ratio of magnetic field energy density U_B to the target photon field energy density $U_{\rm ph}$. i.e.

$$\frac{P_{sync}}{P_{com}} = \frac{U_B}{U_{\rm ph}} \tag{1.42}$$

The mean energy of the Compton scattered photon can be expressed as

$$-\frac{dE_e}{dt} = \langle \epsilon_f \rangle \frac{dN}{dt}, \tag{1.43}$$

where $\frac{dN}{dt}$ is the scattering rate and using equation 1.41, the average energy of scattered photon for isotropic field can be expressed as (Blumenthal & Gould, 1970)

$$\langle \epsilon_f \rangle = \frac{4}{3}\gamma^2 \langle \epsilon_i \rangle, \tag{1.44}$$

where $\langle \epsilon_i \rangle = U_{\rm ph}/n$ is the mean energy of the photon gas before scattering.

Total inverse Compton scattering spectrum

In general, the rate of total energy loss per single electron can be computed from the equation given by (Blumenthal & Gould, 1970).

$$-\frac{dE}{dt} = \int (\epsilon_f - \epsilon_i) \left(\frac{dN_{\gamma,\epsilon}}{dt\, d\epsilon_f} \right) d\epsilon_f \tag{1.45}$$

Here in all cases, ϵ_i can be neglected compared to ϵ_f. The quantity in the second bracket in RHS of the equation is the Compton scattered spectrum from the scattering an isotropic density segment, $dn = n(\epsilon)d\epsilon$ having energies within $d\epsilon$ by electrons of energy $\gamma m_e c^2$. The total Compton spectrum from a distribution of electrons can be computed from integrating

the spectrum overall electron energies, γ of the particle spectrum $N(\gamma)d\gamma$, and overall photon energies ϵ (Blumenthal & Gould, 1970).

$$\frac{dW}{dtd\epsilon_f} = \iint N(\gamma)d\gamma \left(\frac{dN_{\gamma,\epsilon}}{dtd\epsilon_f}\right) d\epsilon \tag{1.46}$$

Considering the simplest case, a power-law distribution for electron, $N(\gamma)d\gamma = K\gamma^{-p}d\gamma$, the total spectrum produced by the scattered photons with energy ϵ_f by the relativistic distribution of electrons in Thomson limit is given by (Blumenthal & Gould, 1970)

$$\frac{dW}{dtd\epsilon_f} = \pi\, r_0^2\, c\, K 2^{p+3} \frac{p^2+4p+11}{(p+3)^2(p+1)(p+5)} \epsilon_f^{-(p-1)/2} \times \int \epsilon^{(p-1)/2} n(\epsilon)\, d\epsilon \tag{1.47}$$

Remembering the equation for synchrotron spectrum at this point (equation 1.31), we can say that both synchrotron and inverse Compton spectrum at Thomson regime will have the same spectral slope of $(p-1)/2$ for the same power-law particle distribution of index p.The total inverse Compton scattering spectrum in the Klein-Nishina limit is obtained by the equation,

$$\frac{dW}{dt\, d\epsilon_f} = \pi\, r_0^2\, c\, K\, (m_e c^2)^{p+1} \epsilon_f^{-p} \times \int \frac{d\epsilon}{\epsilon} n(\epsilon) \left(\ln \frac{\epsilon\, \epsilon_f}{(mc^2)^2} + C(p)\right) \tag{1.48}$$

Here $C(p)$ is a parameter close to unity. Since the Klein-Nishina cross-section declines fast very high energies, the spectrum in this regime will be much soft.

1.3.4 Hadronic Processes

Hadronic processes represent the unique category of phenomena that share the presence of a primary population of accelerated protons in the relativistic jets. The primary hadronic process is the proton synchrotron

emission in which the relativistic protons in the jet radiate in the magnetic field. However, the actual physical conditions needed for accelerating protons to relativistic energies are exotic and are entirely different from those for electrons. The proton synchrotron spectrum will also be a power-law with index $\alpha = (p-1)/2$ for a power-law injection of protons with same particle distribution index p as that of electrons. The peak energy of this emission falls in the range 10-100 GeV, and is observed usually for the high energy SED of HBLs[2] (Cerruti, 2020).

Protons in the jet can also interact with the low-energy photon fields. Unlike electrons, the dominant proton photon interaction is the photo-meson production and the Bethe–Heitler pair production rather than inverse Compton scattering. The photo-meson production involves the formation and decaying of pions (π) during the interaction of protons (p) with photons (γ). The $*$ indicates the excited state.

$$\begin{aligned} p + \gamma &\rightarrow p^* + \pi^0 \\ p + \gamma &\rightarrow n + \pi^+ \\ p + \gamma &\rightarrow p^* + \pi^+ + \pi^- \end{aligned} \tag{1.49}$$

The threshold photon energy, ϵ_γ in the proton frame required to produce pions must be greater than $m_\pi c^2 + (m_\pi/2m_p) c^2 \simeq 145$ MeV. The pions

[2]assuming parameters $\gamma_{max} = 10^9$, B = [10G,100G] and δ = [10,50]

formed through the above reactions can decay as

$$\begin{aligned} &\pi^0 \rightarrow 2\gamma \\ &\pi^+ \rightarrow \mu^+ + \nu_\mu \rightarrow e^+ + \nu_e + \overline{\nu}_\mu + \nu_\mu \\ &\pi^- \rightarrow \mu^- + \overline{\nu}_\mu \rightarrow e^- + \overline{\nu}_e + \nu_\mu + \overline{\nu}_\mu \end{aligned} \tag{1.50}$$

An interesting feature of photo-meson interaction is the production of neutrinos as secondary particles that can escape from the emission region without suffering any form of absorption. The Bethe–Heitler pair-production is the interaction represented by the equation

$$p + \gamma \rightarrow p' + e^+ + e^- \tag{1.51}$$

The minimum energy required for a proton to initiate the Bethe–Heitler reaction is lower than that for the photo-meson production by a factor of $m_e/m_\pi \simeq 0.004$. Hence this is the dominant proton-photon interaction at low energies (originates in X-rays). The photo-meson production, on the other hand takes over at high energy where the energy of the proton exceeds the threshold of $\simeq 145$ MeV.

1.3.5 Particle acceleration mechanisms in Blazars

The origin of cosmic rays has been an unresolved issue in Astrophysics since its discovery by V. Hess in 1911. The presence of energetic particles in the cosmic rays hints highly efficient acceleration mechanisms present in our galaxy as well as other parts of the universe. Supernova remnants were initially considered the best candidates for the acceleration of particles from the cosmos. However, the presence of synchrotron radiation

from extra-galactic sources like AGN confirms them as effective particle accelerators. Further, with the advent of γ-ray astronomy, the detection of GeV and TeV photons became possible and these types of sources are now remarked as capable of accelerating particles even protons up to ultra relativistic energies. In an astrophysical scenario, the particles gain energy from the repeated interactions with the magnetic structures embedded in a shock, called magnetic mirrors.

Fermi acceleration processes

In the scenario of astrophysics, the magnetic mirrors are typically Alfven waves or magnetized clouds. The pioneering physicist Enrico Fermi realized that the scattering of particles by the Alfven waves can impart efficient energization (Fermi, 1949, 1954). For example, let us consider the interaction of a particle with velocity $\vec{v} = (-v\cos\theta, -v\sin\theta)$ with a mirror moving with a velocity V along the x-axis such that $\theta = 0$ specifies a head-on collision. Consider P_x as the momentum of the particle along the direction of V and E as the energy of the particle. Writing Lorentz transformation equations for energy and momentum of the particle before scattering in lab and mirror frames (with prime) as,

$$E' = \gamma\,(E - V P_x) \qquad \text{and} \qquad P'_x = \gamma\,(P_x - \frac{V\,E}{c^2}) \tag{1.52}$$

Assuming an elastic process in the co-moving frame of the mirror, the final momentum P_{x1} and energy E_1 of the particle are given by

$$E'_1 = E' \qquad \text{and} \qquad P'_{x1} = -P'_x \tag{1.53}$$

The transformation equation for E_1 is

$$E_1 \;=\; \gamma(E'_1 + V P'_{x1})$$

Using equations 1.52 and 1.53, we can write the expression for the energy of the particle after scattering in the lab frame as

$$E_1 = [E - 2V\frac{E}{c^2}v_x + 2V^2\frac{E}{c^2}] \tag{1.54}$$

The fractional energy change, $\frac{E_1 - E}{E}$ is given by

$$\frac{\Delta E}{E} = \frac{2V}{c^2}(v\cos\theta + V), \tag{1.55}$$

where $v_x = -v\cos\theta$. The head-on ($\cos\theta = 1$) collisions lead to a gain in energy and are statistically more probable than the opposite. Averaging the energy gain over an isotropic distribution of velocities, one gets as

$$\langle\frac{\Delta E}{E}\rangle = \frac{8}{3}\frac{V^2}{c^2} \tag{1.56}$$

This process is referred to as the second-order Fermi mechanism since the energy gain is proportional to $(V/c)^2$. However, it is not considered as a very efficient mechanism for the acceleration since typically $V \ll c$.

The acceleration process can be highly efficient if all the collisions are head-on. In that case, the average would be on all $\cos\theta > 0$ and the energy gain will be dominated by the first-order term in the equation 1.55. Such acceleration scenarios are known as Fermi first-order mechanisms. For example, the Diffusive Shock Acceleration (DSA), where particles are frequently reflected back and forth across a shock front undergoing multiple head-on collisions. Suppose a strong non-relativistic shock wave propagates through the plasma such that the velocity of upstream is much higher than the downstream velocity as viewed from the shock frame. Hence in the restframe of upstream/downstream, the plasma is always approaching towards the particle and the it will always experience head-on collisions

while crossing the shock. Thus the particles gain energy whenever it crosses the shock front (Rieger et al., 2007; Blandford & Ostriker, 1978; Krymskii, 1977; Bell, 1978).

In addition to the first and second-order Fermi processes, there is one more mechanism known as shear acceleration (Rieger et al., 2007). It is a special kind of second-order acceleration in which particles get accelerated when they cross a gradual shear flow of plasma carrying magnetic turbulent structures. As the particle travels through the shear flow, it encounters scattering centers with varying local velocities, and the gain in energy of the particle will be proportional to,

$$\frac{\langle \Delta E \rangle}{E} \propto \left(\frac{\partial u_z}{\partial x} \right)^2 \tau^2, \tag{1.57}$$

where $\frac{\partial u_z}{\partial x}$ is the relative velocity of the scattering centers along the motion of the particles and τ is the average scattering time (Rieger et al., 2007).

Bell's argument for the accelerated particle distribution

Generally, the Fermi acceleration processes produce a particle distribution that does not depends on the nature of the acceleration process. This argument can be easily illustrated using Bell's approach (Bell, 1978). Let n_0 be the number of particles having initial energy E_0, injected into a typical acceleration zone. E is the instantaneous value of particle's energy and $G = \Delta E/E$ is the fractional energy gain per cycle (Caprioli, 2023). If l is the probability of the particle being advected downstream, then $1 - l$ will be the probability of leaving the acceleration zone. After one cycle, the number of particles in the acceleration zone will be $n_0 l$ with energy GE_0. Hence after k steps, there will be $n_k = n_0\, l^k$

number of particles with energy $E_k = E_0 G^k$. Taking k as

$$k \;=\; \ln(n_k/n_0)/\ln l \;=\; \ln(E_k/E_0)/\ln G$$

we obtain,

$$\ln(n_k/n_0) \;=\; Q\,\ln(E_k/E_0),$$

where $Q \;=\; -\ln l/\ln G$. Or we can write as

$$n_k \;=\; n_0 \left(\frac{E_k}{E_0}\right)^{-Q} \tag{1.58}$$

Here Q can be considered as the index of the energy spectrum for the total number of particles in the acceleration zone. For a non-relativistic shock, Q is given by $3/(\kappa - 1)$, where κ is the compression ratio of a shock, which is proportional to the ratio of velocities of upstream to downstream (Bell, 1978; Caprioli, 2023). Here we can also notice that Fermi acceleration processes generally yield a non-thermal power-law particle distribution.

1.3.6 One zone Leptonic model for Blazar SED

In this theoretical framework, the electrons in the jet are assumed to be accelerated to relativistic energies through Fermi processes, while the protons are considered as cold, and contribute only to the total jet's kinetic momentum (Celotti et al., 1997; Ghisellini & Tavecchio, 2009a). The accelerated electrons emit synchrotron radiation in an optically thin plasma (Beckmann & Shrader, 2012). The relativistic electrons also upscatter the soft photon fields to X-ray and γ-ray energies through SSC and EC processes. The ambient external photon fields are,

- Thermal photons from the accretion disk.
- Bright line emissions and the re-emitted accretion disk photons from

the BLR The prominent line emission from BLR is the Ly-α emission and the emission from BLR can be approximated as a Planckian spectrum peaked at 10.2 eV (corresponding to the Ly-α frequency), with a characteristic temperature of $\sim$ 42000K.

- The thermal IR photon field in the Torus. This can be well described by a black-body with a temperature of 1000 K.

This Section describes a one-zone leptonic model by Sahayanathan et al. (2018) that is utilized in the theoretical modeling of broadband blazar SEDs discussed in this thesis. The model incorporates synchrotron, SSC, and EC emission processes, and the numerical code is loaded in XSPEC (Arnaud, 1996) for performing a systematic fitting. Levenberg-Marquardt algorithm is used for the parameter estimation. The model assumes a homogeneous distribution of electrons in a spherical blob of plasma with radius R, moving down the jet with a bulk Lorentz factor Γ and at a viewing angle θ with respect to the observer. The model assumes a broken power-law distribution for the electrons accelerated to relativistic energies.

$$N(\gamma)\,d\gamma = \begin{cases} K\,\gamma^{-p}\,d\gamma & \text{for} \quad \gamma_{\rm min} < \gamma < \gamma_b \\ K\,\gamma_b^{q-p}\gamma^{-q}\,d\gamma & \text{for} \quad \gamma_b < \gamma < \gamma_{\rm max} \end{cases} \quad {\rm cm}^{-3} \tag{1.59}$$

where γ is the electron energy in $m_e c^2$ units and the $\gamma_{\rm min}$ and $\gamma_{\rm max}$ are respectively the minimum and maximum of the available electron energy. K is the normalization constant of the particle distribution and γ_b is the break energy. p and q are the particle indices at low ($\gamma_{\rm min} < \gamma < \gamma_b$) and high ($\gamma_b < \gamma < \gamma_{\rm max}$) energies respectively. The break energy γ_b of a particle distribution is a particular energy within the range $[\gamma_{\rm min}, \gamma_{\rm max}]$ at which the rate of radiative cooling becomes equal to the rate of particles' escape from the emission region. The magnetic field associated within

the emission blob is represented by the parameter B. In this approach, the target photon field energy density at the emission blob undergoing external Compton scattering process is expressed as a fraction (f) of the corresponding black-body energy density.

$$U_{\rm target} = f\, U_{\rm BB} \tag{1.60}$$

where, $U_{\rm BB} = \dfrac{4\sigma_B}{c} T^4$ is the black-body energy density at specific temperature T.

The flux observed at a frequency $\nu_{\rm obs}$ in a direction $\Omega_{\rm obs}$ with the observer is estimated from the emissivities of synchrotron and inverse Compton processes, after correcting for Doppler and cosmological effects (Begelman et al., 1984; Dermer, 1995).

$$F_{\rm obs}(\nu_{\rm obs}) = \frac{\delta^3(1+z)}{d_L^2} V j_{\rm rad}\left(\frac{1+z}{\delta}\nu_{\rm obs},\, \phi_{\rm obs}\right) \quad {\rm erg/cm^2/s/Hz} \tag{1.61}$$

where, d_L is luminosity distance, δ is the Doppler factor, z the redshift of the source, V the emission region volume, $j_{\rm rad}$ is analytical approximations of the emissivities corresponding to synchrotron, SSC, and EC processes, and $\phi_{\rm obs}$ the azimuthal angle of the observer. The approximated solutions for the resultant fluxes observed at earth corresponding to these processes are

given by Sahayanathan et al. (2018) as a function of the source parameters.

$$F^{\rm syn}_{\rm obs}(\nu_{\rm obs}) \approx \begin{cases} \mathbb{S}(z,p)\,\delta^{\frac{p+5}{2}} B^{\frac{p+1}{2}} R^3 K \nu_{\rm obs}^{-\left(\frac{p-1}{2}\right)} \\ \qquad\qquad\qquad\qquad \text{for} \quad \nu_{\rm obs} \ll \delta\,\gamma_b^2 \nu_L/(1+z) \\ \mathbb{S}(z,q)\,\delta^{\frac{q+5}{2}} B^{\frac{q+1}{2}} R^3 K \gamma_b^{q-p} \nu_{\rm obs}^{-\left(\frac{q-1}{2}\right)} \\ \qquad\qquad\qquad\qquad \text{for} \quad \nu_{\rm obs} \gg \delta\,\gamma_b^2 \nu_L/(1+z) \end{cases} \tag{1.62}$$

$$F^{\rm ssc}_{\rm obs}(\nu_{\rm obs}) \approx \begin{cases} \mathbb{C}(z,p)\,\delta^{\frac{p+5}{2}} B^{\frac{p+1}{2}} R^4 K^2 \nu_{\rm obs}^{-\left(\frac{p-1}{2}\right)} \log\left(\frac{\gamma_b}{\gamma_{\rm min}}\right) \\ \qquad\qquad\qquad\qquad \text{for} \quad \nu_{\rm obs} \ll \delta\,\gamma_b^4\,\nu_L/(1+z) \\ \mathbb{C}(z,q)\,\delta^{\frac{q+5}{2}} B^{\frac{q+1}{2}} R^4 K^2 \gamma_b^{2(q-p)} \nu_{\rm obs}^{-\left(\frac{q-1}{2}\right)} \log\left(\frac{\gamma_{\rm max}}{\gamma_b}\right) \\ \qquad\qquad\qquad\qquad \text{for} \quad \nu_{\rm obs} \gg \delta\,\gamma_b^4\,\nu_L/(1+z) \end{cases} \tag{1.63}$$

$$F^{\rm ec}_{\rm obs}(\nu_{\rm obs}) \approx \begin{cases} \mathbb{E}(z,p)\,\delta^{p+3} U_* \overline{\nu}_*^{\frac{p-3}{2}} R^3 K \nu_{\rm obs}^{-\left(\frac{p-1}{2}\right)} \\ \qquad\qquad\qquad\qquad \text{for} \quad \nu_{\rm obs} \ll \delta\,\Gamma\gamma_b^2\,\overline{\nu}_*/(1+z) \\ \mathbb{E}(z,q)\,\delta^{q+3} U_* \overline{\nu}_*^{\frac{q-3}{2}} R^3 K \gamma_b^{q-p} \nu_{\rm obs}^{-\left(\frac{q-1}{2}\right)} \\ \qquad\qquad\qquad\qquad \text{for} \quad \nu_{\rm obs} \gg \delta\,\Gamma\gamma_b^2\,\overline{\nu}_*/(1+z) \end{cases} \tag{1.64}$$

All the quantities in the above equations with suffix 'obs' are measured from observer's frame, and with $*$ represents AGN frame. The rest of the quantities are measured from the emission region frame Here $\mathbb{S}$, $\mathbb{C}$ and $\mathbb{E}$ are functions involving physical constants, redshift and particle index. U_* and $\overline{\nu}_*$ are the energy density and the frequency of target photon field.

The model consists of 12 free parameters K, $\gamma_{\rm min}$, $\gamma_{\rm max}$, γ_b, δ, B, R, $\overline{\nu}_*$ and U_* which makes it difficult to converge the fit due to the

limited number of data points available from multi-wavelength observations. An estimate for the upper limit of the emission region size, R and the minimum jet Doppler factor ($\delta_{\rm min}$) can be estimated numerically using γ-ray observational results (Abdo et al., 2010c; Foschini et al., 2011; Dondi & Ghisellini, 1995b) (Section 1.2.3). Moreover, the observed synchrotron peak frequency, $\nu_{\rm sp}$ is related to γ_b as

$$\nu_{\rm sp} = \left(\frac{\delta_D}{1+z}\right)\gamma_b^2\,\nu_L \tag{1.65}$$

where ν_L is Larmor frequency. Similarly, the SSC peak frequency, $\nu_{\rm sscp}$ is expressed in terms of γ_b as

$$\nu_{\rm sscp} = \left(\frac{\delta_D}{1+z}\right)\gamma_b^4\nu_L \tag{1.66}$$

Henceforth, a fair guess on the break energy γ_b can be made using the above relations provided one has good information about the synchrotron and IC peak frequencies. The EC peak frequency, $\nu_{\rm ecp}$ is related to the jet Doppler factor and the target photon field frequency, $\overline{\nu}_*$ as

$$\nu_{\rm ecp} = \left(\frac{\delta_D\Gamma}{1+z}\right)\gamma_b^2\,\overline{\nu}_* \tag{1.67}$$

The target photon field frequency $\overline{\nu}_*$ can be estimated from the target photon energy density approximated as a blackbody at temperature T (equation 1.60). The magnetic field energy density (U_B) in terms of electron energy density (U_e) and equipartition relation is given by

$$U_B = \eta U_e \tag{1.68}$$

where, $U_B = \frac{B^2}{8\pi}\,\mathrm{erg/cm^3}$ is the magnetic field energy density and

$$U_e = m_e c^2 \int_{\gamma_{\rm min}}^{\gamma_{\rm max}} \gamma N(\gamma) d\gamma\,\mathrm{erg/cm^3}$$

is the energy density in the particle distribution. The parameter η is the equipartition factor and a value of 1 indicates the equipartition condition which allows us to obtain a minimum jet power solution (Pacholczyk, 1970). Using the values of U_e and η, we can obtain an approximate value of the magnetic field.

In this chapter, we provided a detailed overview of blazars, focusing on their physical and observational properties across the electromagnetic spectrum. We also examined the dominant radiative processes that govern their emissions, along with a theoretical framework for modeling the broadband spectral energy distribution of blazars. These discussions set a back stage for the subsequent chapters of this thesis. In the following chapter, we delve into the multiwavelength observations and data analysis, laying the groundwork for a comprehensive understanding of the results presented in this study.

Chapter 2

Multiwavelength Data and Analysis

2.1 Multiwavelength Astronomy

We all know that the electromagnetic spectrum is the arrangement of radiations in the order of their wavelengths/frequencies. Different types of celestial objects emit radiation at some specific wavelengths that can tell us about the temperature and energy of the source according to Wien's displacement law: $\lambda_{\max} T = 3 \times 10^6 \,\mathrm{nm}\, K$. Here, $\lambda_{\max}$ is the wavelength corresponding to the maximum intensity, that can be emitted from a black body at an equilibrium temperature, T (Bhagwan et al., 2015). This situation holds good in star-like objects which emit radiation like a blackbody. However, in the case of more complex objects like quasars and AGNs, this is not the case. The non-thermal continuum emission from these sources extend the entire electromagnetic spectrum and cannot be described by a single characteristic temperature. The emitting particles in such objects define a non-Maxwellian distribution. To fully understand such objects, it is essential to look into multi-wavelengths or even other messengers like neutrinos or gravitational waves. These multi-wavelength

or multi-messenger information can provide a more comprehensive view of the source's properties. Different wavelengths reveal different layers of information of the object. To illustrate this further, the image of Centaurus A galaxy in different wavelengths and a combined image is shown in Figure 2.1. The X-ray image in the Figure 2.1 reveals Centaurus A's highly energetic central region around the supermassive black hole which is accreting gas and dust in to it. Looking in optical we can see the light from the stars in the galaxy though it is heavily obscured by thick dust lanes around the galactic edge. In IR, the same dark dust region looks bright and stars seem dimmer, where as radio does not show the galaxy itself, but reveals the jets of materials ejected out at larger distances from the center. It is not until we combine all the pieces of information together, we get a complete knowledge of what object really Centaurus A is. An astronomer looking in a single wavelength can only grasp a piece of puzzle. It is crucial for any research in observational astronomy to leverage the diverse multi-wavelength resources for bringing significant progress in science.

In the following sections, we provide the details of the multi-wavelength instruments or telescopes pertinent to this study. This includes a brief overview of the instruments, mode of operation, data structure, as well as the general methods of data reduction and analysis.

2.2 Fermi γ-ray telescope

The Fermi γ-ray Telescope is an international space observatory by NASA that observes the sky in gamma-rays, the most energetic form of light (Thompson & Wilson-Hodge, 2022; Atwood et al., 2009). The mission was launched as the Gamma-ray Large Area Space Telescope (GLAST) from Cape Canaravel air station. Shortly after the launch, the

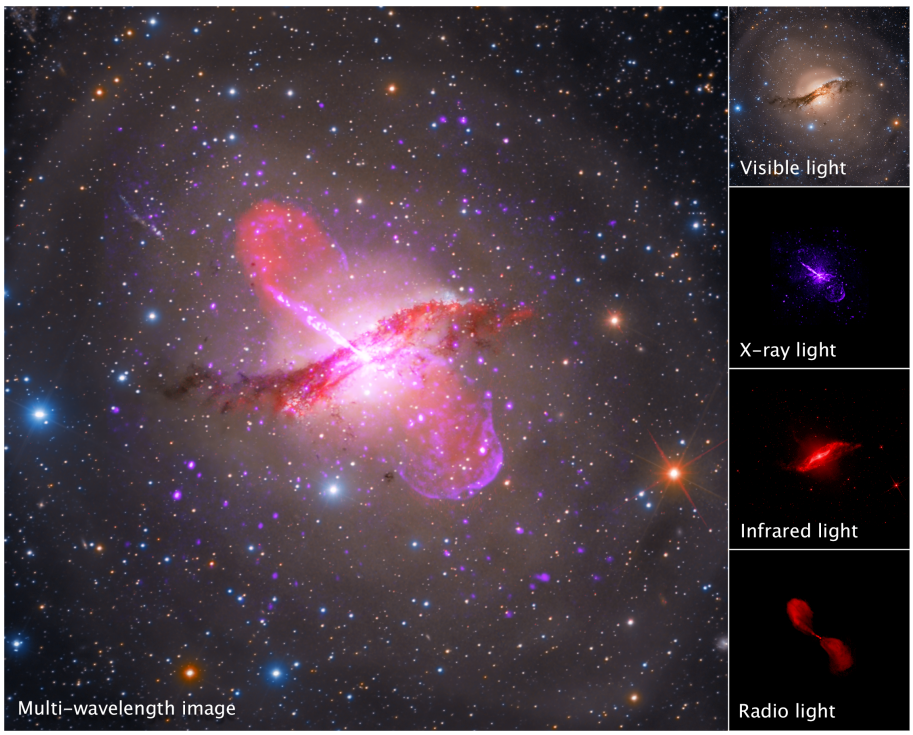

Figure 2.1: left) A multiwavelength picture of Centaurus A obtained by combining the images in the right panel. right) Images collected by Hubble (visible), Chandra (X-ray), Spitzer (IR), and Very Large Array (Radio) telescopes. Image courtesy:`https://webbtelescope.org/contents/media/images/2021/015/`

observatory has been renamed in honor of Enrico Fermi (1901-1954), a pioneer in high-energy physics. The prime goal of the mission was to explore the highly dynamic gamma-ray sky particularly above 1 GeV, where the historic mission EGRET's sensitivity was poor. The scientific objectives of Fermi includes, investigating the origins of tremendous energies far beyond anything possible on Earth, achieving new breakthroughs in understanding of Dark matter, and to answer long lasting questions in the realm of gamma-ray bursts, pulsars, solar flares and more.

Fermi has two payloads, namely the Large Area Telescope (LAT) covering 20 MeV to 2 TeV energy range, and the Gamma-ray Burst Monitor (GBM), that detects and localizes gamma-ray bursts (GRBs) providing the

spectral and temporal information in 10 keV–25 MeV energy band. GBM also sends triggers to the LAT for a burst in progress. Fermi has an orbital period of 90 minutes and covers the entire sky in every 3 hour alternating between two orbits at $\pm 50^{\circ}$[1].

2.2.1 Large Area Telescope (LAT)

The Large Area Telescope is the prime instrument of Fermi that detects gamma-rays in the energy range 20 MeV to 2 TeV. It has an effective area > 8000 cm^2 and a point source sensitivity of $< 6 \times 10^{-9}$ phs cm^{-2} s^{-1} at energies greater than 100 MeV. Unlike the optical and radio instruments, the gamma-rays cannot be focused, but can be scattered and absorbed in the matter. Above 10 MeV energy, pair conversion is the most efficient energy loss mechanism for gamma-rays. LAT uses this technique to detect gamma-rays (Atwood et al., 2009) The LAT has an array of 16 tracker (TKR) modules consisting of silicon strip detectors, coated on top with Tungsten convertor foil that convert gamma-rays in to pairs. The tracker can also measure the direction of incident gamma-rays. The bottom part of the LAT is occupied by 16 calorimeter (CAL) modules made of CsI(Tl) performing adequate energy measurements of the pairs in the LAT energy band (Atwood et al., 2009). A schematic representation of the components and working is illustrated in Figure 2.2.

The charged cosmic ray particles can also create e^+/e^- pairs when they strike on the LAT. These pairs are much larger in counts and exceeds those produced by preferred gamma rays by factors of $10^2 - 10^5$. This can result a potentially overwhelming background inside the LAT. Hence an anti-coincidence detector (ACD), consisting of scintillator tiles is installed over the hardware of LAT. ACD detects such events and issue a veto signal.

[1] `https://fermi.gsfc.nasa.gov/ssc/observations/types/post_anomaly/`

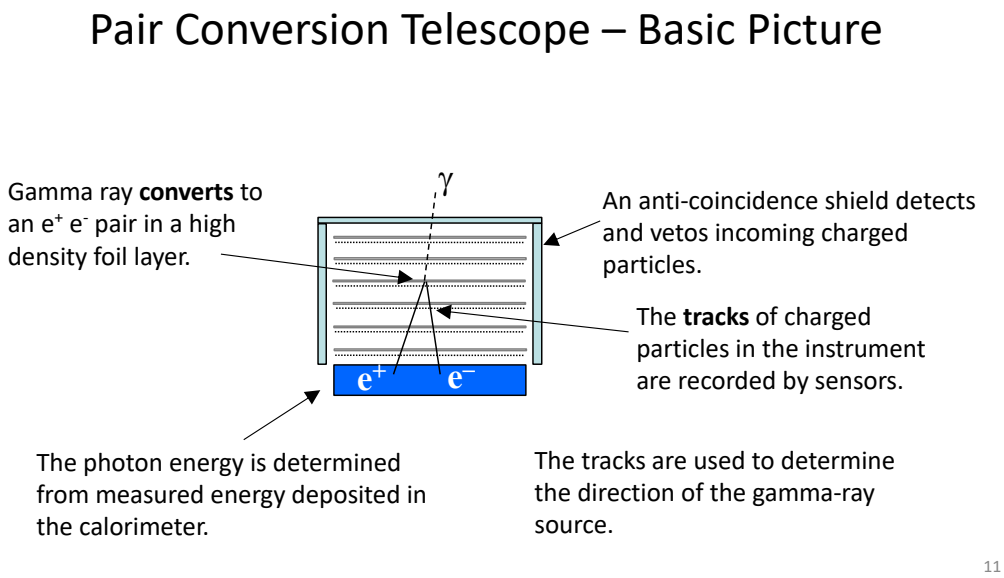

Figure 2.2: Schematic diagram of LAT instrument (Hays, 2023).

LAT data and Instrument Response Function (IRF)

The Level-1 data processing in LAT involves reconstructing the events from the hits on the parts of the LAT, identifying the type of each event, and characterizing the event's physical parameters like direction and energy (Atwood et al., 2009; Ackermann et al., 2012). The event-level analysis software has been updated periodically to incorporate the improvements in the understanding of LAT and its orbital environment. Since launch, there have been four major data releases or Passes from the LAT team, with Pass 8 is the latest release (Atwood et al., 2013). A Pass means a version of the Fermi LAT data package with instrument simulation, reconstruction code, event selection, IRFs, systematic uncertainties, and isotropic templates. The LAT response function describes the response of the instrument to the arrived gamma-ray photon of given energy and direction in the instrument coordinates. The LAT team classifies the events in to different classes based on the quality of event reconstruction, defined in terms of different

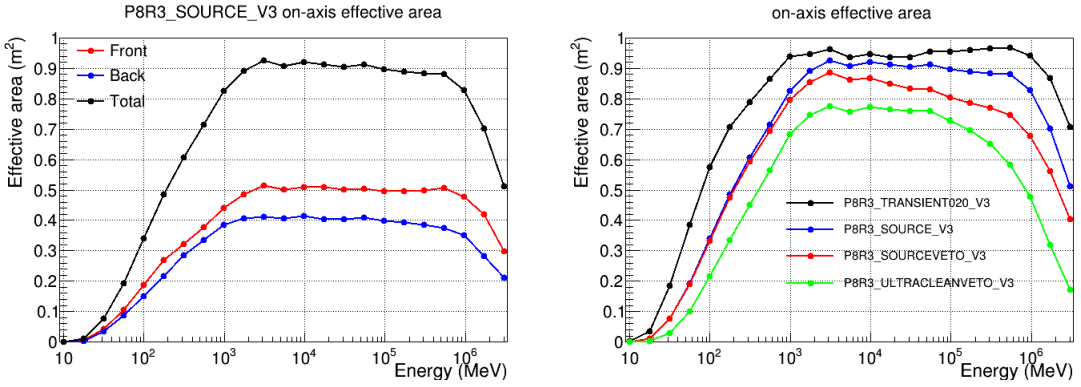

(a) (b)

Figure 2.3: (a): The effective area as a function of energy for normal incidence photons (θ=0), (b): comparison of the on-axis effective area (Total) as a function of the energy for different P8R3_V3 event classes. `https://www.slac.stanford.edu/exp/glast/groups/canda/lat_Performance.htm`

parameters. *transient* class have the most background contamination, then *source*, *clean*, and the *ultraclean* with least background (Ackermann et al., 2012). Each event class is defined by a set of event types and has a corresponding set of response functions which are unique to the particular class. Based on the conversion type, the events are partitioned into FRONT and BACK conversion types. Additionally, Pass8 categorizes data into partitions based on the quality of position reconstruction (PSF0, PSF1, PSF2, PSF3) and energy reconstruction (EDISP0, EDISP1, EDISP2, EDISP3). Each datum is divided into quartiles, ranging from the lowest quality quartile (PSF0, EDSP0) to the best quality quartile (PSF3, EDISP3) (Atwood et al., 2013; Ackermann et al., 2012). The IRFs are provided for each combination of event class and type and further details can be found in `https://fermi.gsfc.nasa.gov/ssc/data/analysis/documentation/Cicerone/Cicerone_LAT_IRFs/IRF_overview.html`.
As an example, the Figure 2.3 shows how the effective area parameter of P8R3_V3 response function varies with different event types and classes.

2.2.2 LAT Data Analysis

Data structure

The LAT observation for any source mainly consists of two types of data files: photon file and spacecraft file. The photon file carries information of photons such as energy, position, quality of event reconstruction, which are required for the science analysis. On the other hand, the spacecraft file contains spacecraft position and orientation information for 30 second intervals. Additionally, the spacecraft file also carries the information about the time period when the spacecraft passes the South Atlantic Anomaly (SAA). The LAT data over a user defined region in sky (10-15 degree) can be downloaded from data access website.

Prerequisites

- Software: The Fermi Science Support Center (FSSC) and the LAT instrument team collaboratively developed a suite of python based instrument specific tools named *Fermi Science tools* for public use. This software is distributed and maintained by the FSSC. More details for the installation can be found in the FSSC Data Analysis webpage[2].

- Instrument Response Functions (IRF): The fermitools can access appropriate IRF files at the time of running the analysis.

- Diffuse emission models: The LAT detects point sources in the background of the bright diffuse emission from our galaxy and other extra galactic sources. Hence for the accuracy of the analysis, it is crucial to model the galactic diffuse emission and the isotropic emissions from all other gamma-ray sources. The templates for

[2]`https://fermi.gsfc.nasa.gov/ssc/data/analysis/`

galactic diffuse and isotropic emission used for P8R3 data are *gll_iem_v07.fits* and *iso_P8R3_SOURCE_V3_v1.txt*.

- Input model file: The sources in the LAT catalogs are defined as either PointSource or a DiffuseSource each of which are modeled with a spectral model and a spatial model. The LAT spectral models for point sources are defined in cm^{-2} s^{-1} MeV^{-1} while for diffuse sources, the fluxes are described in cm^{-2} s^{-1} MeV^{-1} sr^{-1}. The spatial model used for a point source is *SkyDirFunction*, which describes a position in the sky. An XML model file containing the spatial and the spectral description of all the sources of interest, is necessary for performing spectral fitting using LAT data.

Analysis description

The tutorial for the data analysis can be found in the FSSC webpage `https://fermi.gsfc.nasa.gov/ssc/data/analysis/scitools/`. The first step in the process of data preparation is to apply some selection cuts on the data using the fermitool *gtselect*. The data selection recommendations based on event type and classes for the analysis of different types of sources can be found from the link[3]. Additionally, the data set has to be constrained in time frame of the analysis, energy range and position in the sky. The selection cut on position is done by defining a region of interest (ROI) centered at the ra and dec of the target. The size of the ROI is usually set same or smaller than size of the region selected for data extraction. The maximum zenith angle is set as 90 degrees to exclude Earth's limb events that may result in elevated background levels.

After the *gtselect*, the *gtmktime* script is used to update the Good Time

[3] `https://fermi.gsfc.nasa.gov/ssc/data/analysis/documentation/Cicerone/Cicerone_Data_Exploration/Data_preparation.html`

Intervals (GTI) extension in the photon file. The Good Time Interval is the intervals of time when the data quality is good. The GTI extension in the photon files contains a list of these GTIs. The *gtmktime* tool reads the spacecraft data, and creates a set of GTIs based on the specified cuts and then recombine this with the existing GTIs in the event file after incorporating the user defined logical expression. The tool excludes all time outside this new set of GTI in the output file. The most comment filter expression used is "DATA_QUAL == 1 && LAT_CONFIG == 1". The option "ROIcut=yes" is used to exclude times where ROI is beyond the field of view.

The LAT IRF depends on the inclination angle of the direction of the source with the z-axis of the instrument. Hence the number of photons of a specific intensity that are detected from a source depends on how long the source is at various inclination angles over the course of an observation. Hence, it is essential to compute the accumulated time, known as *livetime* in which the LAT could actively record the events from a particular source. The *gtltcube* tool computes the *livetime* as a function of the angle of inclination and location on the sky for a specified period of observation using the spacecraft file.

An exposure map is simply an accounting of the exposure at each position in the sky, that we need for background modeling. The *gtexpmap/gtexpcube2* tool compute the exposure map for the case of unbinned/binned analysis (2.2.2). The LAT point spread function is broad especially at low energies (68% of the counts will fall within 3.5 degrees around the source at 100 MeV). As a consequence, the PSF tails of nearby sources will overlap significantly with the emission from the target source. In order to obtain a more accurate fit, the user has to fit all the nearby point sources and the diffuse components simultaneously, and this will

require the selection of an ROI, that is several times larger than the PSF size at the *gtselect* level. Again due to the large PSF of the LAT, sources from well outside the ROI can also affect the sources we are analyzing. To correct for this, we must create an exposure map over a region that includes sources up to 10 degrees beyond the ROI. This defines another region known as "Source Region" much larger in size, several PSF length scales, centered about the ROI. The exposure map created over a particular region is unique to a particular ROI defined. The input source model file for the *gtlike* should also include all of the sources in the Source Region.

LAT data are fitted using maximum likelihood method in which the likelihood function is defined in terms of the expected photon distribution for a given source model defined by a set of parameters. *gtdiffrsp* tool pre-computes the expected photon distribution by convolving the source model and the instrument response functions. The *gtlike* tool performs unbinned and binned likelihood spectral fitting of the LAT data. Likelyhood fitting can be performed in two statistics, binned and unbinned (2.2.2). User can also choose from various optimization algorithms to converge the fit including 'DRMNFB', 'NEWMINUIT', 'MINUIT', 'DRMNGB', and 'LBFGS'.

Likelihood fitting of Fermi-LAT data:

The likelihood method was introduced to photon-counting experiments by Cash Cash (1979) and maximum likelihood method was initially applied for the estimation of parameters in the analysis of EGRET data (Mattox et al., 1996). Likelihood function is generally defined as the probability of obtaining an observed data from a given input model with a set of parameters (Cash, 1979). In this case, the input model is the distribution of gamma-ray sources on the sky including their intensity and spectra. To

analyze LAT data, a likelihood function suitable to the data has been constructed, and then the best fit parameters have been estimated after maximizing the likelihood function. Assume that LAT data is binned in to many bins and each bin contains a small number of counts. The observed number of counts in each bin is assumed to be a Poisson distribution. Let m_i be the expected number of counts in the i^{th} bin of the data and is a function of the assumed model. Then the probability for n_i counts to occur in the i^{th} bin is given by

$$P_i = \frac{m_i^{n_i} e^{-m_i}}{n_i!}. \tag{2.1}$$

By definition, likelihood will be the product of all P_is.

$$L = \prod_i \frac{m_i^{n_i} e^{-m_i}}{n_i!} \tag{2.2}$$

The parameter space can be quite large when a number of sources are involved. The spectral parameters of all sources of interest must be fitted simultaneously. As mentioned earlier, LAT likelihood tools provide a choice optimizer to maximize the likelihood efficiently. Fitting involves repeated calculation of likelihood for different sets of parameters until a value sufficiently near the maximum is obtained. The optimizer provides hints to the choice of new trial parameter sets for converging the fit efficiently. The parameter uncertainties are estimated from the variation of the likelihood in the vicinity of the maximum value obtained.

The likelihood spectral fitting provides the best fit parameter values and their uncertainties. However, we cannot obtain the goodness of fit directly from this method. Also the fitting procedure does not involve fitting of spatial coordinates. The space localization is done by performing a grid search to find out the maximum likelihood over a grid of locations. The maximization of likelihood at a particular position is quantified through

the quantity called Test Statistic (TS), a monotonic function of likelihood. The TS is defined as

$$TS = -2\ln\left(\frac{L_{\max,0}}{L_{\max,1}}\right) \tag{2.3}$$

where $L_{\max,0}$ is the maximum likelihood value for a model without a source (the 'null hypothesis') and $L_{\max,1}$ is the maximum likelihood value for a model with source at a specified location. Maximizing TS on a grid is equivalent to maximizing the likelihood on a grid and the square root of the TS is approximately considered as the detection significance for a given source. The concept of TS can also be employed for comparing the suitability of any two spectral models for a particular source. For example, if the value defined by,

$$-2\ln\left(\frac{L_{\max,1}}{L_{\max,2}}\right) = TS(model2) - TS(model1) \tag{2.4}$$

where, $L_{\max,1}$ and $L_{\max,2}$ are the maximum likelihood values corresponding to model 1 and 2 respectively, yields a large positive value, then model 2 can be inferred as a better choice than model 1.

Unbinned and binned Likelihood

Likelihood fitting of LAT data can be performed in two methods: Unbinned and binned analysis. In the unbinned method, each photon is taken separately and the script computes response for each photon. This approach is the most effective one where photons are sparse. For example, in the case of time series analysis with short time bins and at high energies (> 10 GeV) where the number photons is a few. However, for large time period analysis including bright background sources (such as the Galactic plane), the unbinned analysis is asymptotically slow and binned likelihood method is the preferred one. In this approach, the data is binned in space

and energy while the instrument response is averaged over space and energy.

2.3 Swift Gamma-Ray Burst Telescope

Swift is a pioneering space observatory in the multiwavelength field with it's major science goal being the study of the origin as well as after glow emissions of gamma-ray bursts (GRBs). Swift was launched into a low-Earth orbit on November 20, 2004. The Swift telescope payload has 3 instruments observing in γ-ray, X-ray and optical/UV bands.

Burst Alert Telescope (BAT):

The Burst Alert Telescope (BAT) has a large field-of-view (2 steradians) and act as a sensitive instrument for providing critical GRB triggers. BAT detects signals in the hard X-ray and soft γ-ray energies between 15-150 keV. It can alert a detection within seconds and idenitifies 100 GRBs annually.

2.3.1 X-ray Telescope (XRT):

The XRT is a focusing X-ray telescope with an effective area of 110 cm^2 at the energy range 0.3–10 keV and an angular resolution of 18 arcseconds at 1.5 keV. This instrument utilizes a grazing incidence Wolter 1 telescope having 23.6× 23.6 arcmin field of view to focus X-rays. XRT helps Swift to localize GRB positions with an accuracy of few arcseconds within 100 seconds burst. The detection sensitivity is 2×10^{-14} erg cm^2 s^{-1} in 10^4s (Citterio et al., 1996; Burrows et al., 2005; Hill et al., 2000). XRT is intended to study the X-ray counterparts of GRBs by measuring the fluxes, spectra, and lightcurves, starting from 20-70 seconds after the burst and continuing to weeks. The Figure 2.4 shows the schematic representation of the major components of X-ray telescope and the plot of effective area

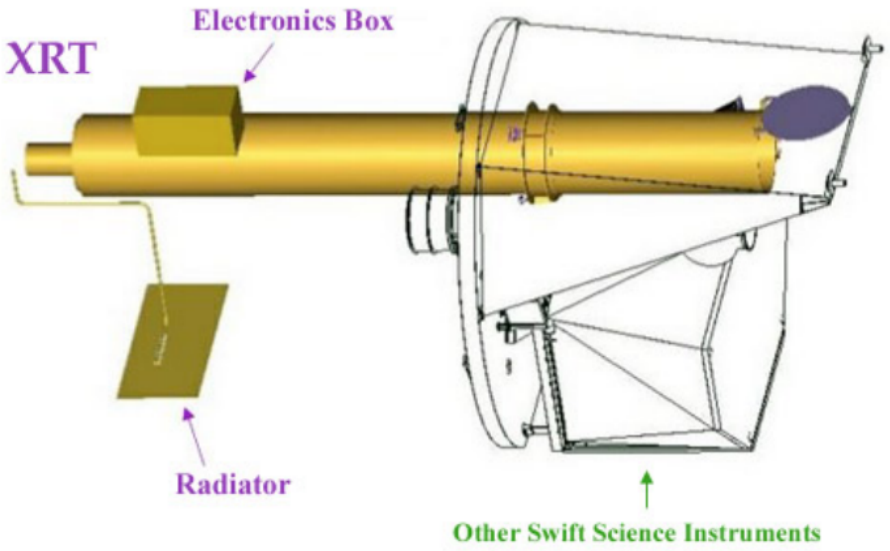

Figure 2.4: The schematic diagram of the XRT instrument.`https://swift.gsfc.nasa.gov/about_swift/xrt_desc.html`

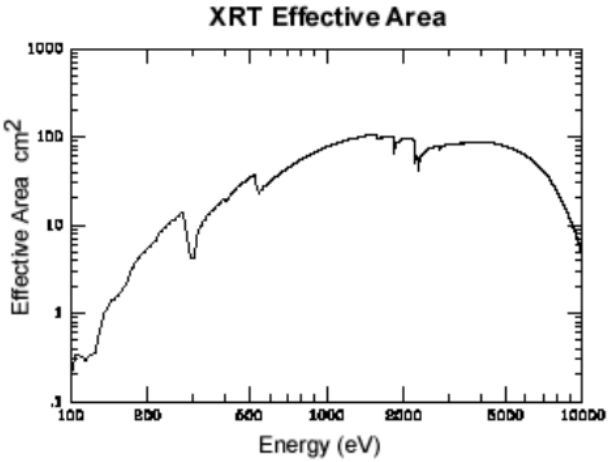

Figure 2.5: The plot of effective are as a function of energy. Image credit: `https://swift.gsfc.nasa.gov/about_swift/xrt_desc.html`

with energy. The XRT has the following operating modes (Burrows et al., 2005).

- Imaging mode: This is a normal imaging exposure and readout method where photons are being allowed to pile up. There is no event recognition in the onboard processing. The CCD operates likes an optical one in this mode of operation.

- Photodiode (PD) mode: This mode is used to produce accurate timing information for very bright sources producing high speed light curves with a time resolution of 0.14 ms.

- Windowed timing (WT) mode: This mode is used to obtain high resolution timing (2.2ms) with 1-D position information and spectroscopy. However, this mode is restricted to the central 8 arcminutes of the field of view.

- Photon-counting (PC) mode: It is the most common mode of operation of the X-ray CCD. It provides full imaging and spectroscopic resolution. Even though, the time resolution is only 2.5 seconds. The instrument is operated in this mode at very low fluxes (below 1 mCrab).

XRT data reduction

The Swift Data Center (SDC) at NASA/GSFC performs the pipeline processing using Level 0/1 software and produces standard format FITS event files. The Level 2/3 software for generating high level scientific data products is called the XRT Data Analysis Software (XRTDAS), a set of FTOOLS comes in collaboration with HEASOFT package available at HEASARC/NASA/GSFC webpage. The HEASOFT software

package can be downloaded from the HEASARC software site[4]. To analyze the data, the calibration database (CALDB) for the Swift and individual instruments must be accessible as a local installation or user can access remotely. The Swift calibration files for all instruments can be downloaded from `https://heasarc.gsfc.nasa.gov/docs/heasarc/caldb/swift/` and can be installed following instructions in the page [5]. Though the level 2 cleaned event lists are generated by the SDC processing, it is recommended that users should run the pipeline on level 1 data to ensure that the most recent version of the processing scripts is being used. The generation of cleaned event files mainly involves two steps: calibration and screening. The criteria of calibration are different for different modes. This stage involves identification of bad pixels, transformation of coordinates, time tagging, reconstruction of the events, and elimination of piled up frames as well as partially exposed pixels. The screening uses the GTIs obtained from the housekeeping parameters and conditions on the quantities related to attitude and orbit. Further selections are applied on the GRADE and the STATUS columns. All these tasks are implemented in the script *xrtpipeline*. This tool uses files available in the 'auxil' and 'xrt' directories of the downloaded observation to perform the screening and filtering of the events.

The ftool *xrtproducts* is used to extract high level science products, like spectra, light curves and images for PC, WT, and PD modes. The user can specify a region of arbitrary shape for the extraction of products through an ASCII file with .reg extension. The most common is a circular region centered around the source defined in sky coordinates. It is highly recommended to take a substantially larger region in a source free field

[4] `https://heasarc.gsfc.nasa.gov/lheasoft/download.html`
[5] `https://heasarc.gsfc.nasa.gov/docs/heasarc/caldb/caldb_install.html`

than that for the source as the background. *xrtproducts* also generates the ancillary response files (ARF) needed for the spectral analysis together with the spectrum and lightcurves.

The Swift-XRT data products generator

This online facility creates ready-to-publish light curves, spectra, images in the X-ray, and positions of any point source in the Swift-XRT field of view (Evans et al., 2009; Goad et al., 2007). The fully calibrated output products are corrected for instrumental artifacts such as pile up and bad pixels on the CCD. The spectra available from this tool are automatically fitted with a power-law. However, user can download the spectral files as a tar archive including responses and background spectra. The downloaded spectra can be analyzed with different models after loading it on platforms like XSPEC. More details can be found at the page Swift-XRT data products generator available at the link[6].

2.3.2 UV/Optical Telescope (UVOT):

The UVOT makes Swift a complete multi-wavelength facility by providing simultaneous ultraviolet and optical coverage (170-650 nm) in a $17' \times 17'$ field. UVOT comprises a 30 cm modified Ritchey-Chretien UV/optical telescope spatially aligned with the X-ray Telescope (Roming et al., 2005). UVOT operates in a similar mode to typical X-ray telescopes using photon counting detectors. The UVOT usually takes images and can also obtain spectra of GRB afterglows during the pointed follow-up observations.

UVOT takes data in three different modes: image mode, event mode, and image & event mode. There are 6 broadband filters associated with

[6] `https://www.swift.ac.uk/user_objects/docs.php`

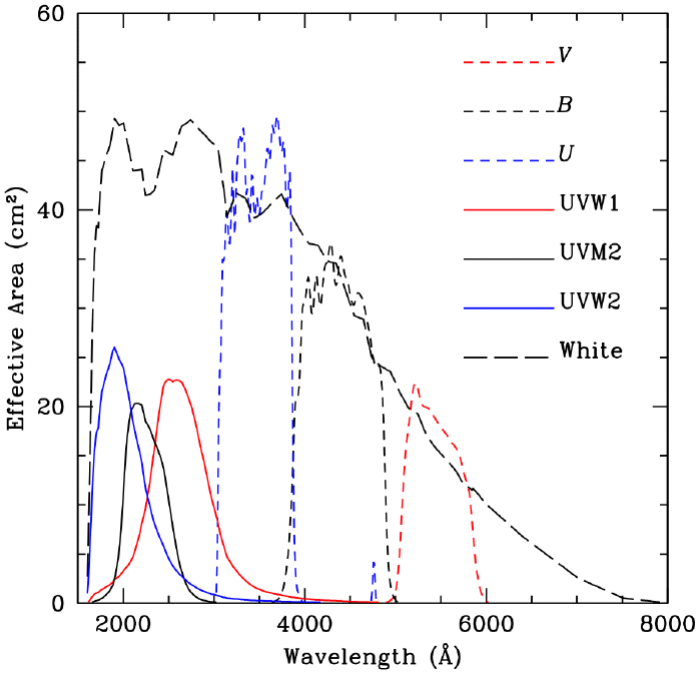

Figure 2.6: The plot of effective are as a function of wavelength for all the 6 UVOT filters. The dashed black curve shows the cumulative effective area. Image credit: `https://www.swift.ac.uk/analysis/uvot/filters.php`

image mode comprising 3 UV (UVW2, UVM2, UVW1) and 3 optical (U, B, V) filters. Their central wavelengths in Ångström are 1928, 2246, 2600, 3465, 4392, and 5468 respectively (Figure 2.6). Unlike the XRT data, UVOT data reduction generally starts with Level 2 sky images. However, calibration files are needed for further analysis (Kuin et al., 2015). Some of the most common UVOT tools for the Level 2 image reduction are listed below. More details can be found online at `https://www.swift.ac.uk/analysis/uvot/`.

- Before beginning the analysis, user has to check that all images are correctly aligned to the World Co-ordinate System (WCS). This can be done by looking the value of keyword 'ASPCORR' in the image header using ftool *fkeyprint*. If 'ASPCORR = DIRECT', then the

images are already correctly aligned. If not, one has to run the task *uvotskycorr* twice to get that corrected[7].

- *uvotsource*: This tool is used to preform the aperture photometry on the UVOT sky image files. The recommended size of the aperture around the source is 5 arcseconds for all filters and it is always preferable to define a background region several times larger than the source extraction region. The resulting FITS file provides the information of coincidence-corrected count rate, magnitude and flux density in erg $cm^{-2}\,s^{-1}\,A^{-1}$ and in mJy with 1-σ error [8] along with the significance of source detection.

- *uvotimsum*: This tool is employed to sum the extensions within an image in order to study faint sources. Additionally, the ftool *fappend* can be applied to sum the output FITS files of *uvotimsum* from different observations.

- *uvot2pha*: The uvot spectral points corresponding to each filter can be obtained in the form of pha files after running the tool *uvot2pha*. The response matrices can be accessed through the CALDB database. This tool will create source and background spectra with response files that can be grouped and loaded in XSPEC.

- *uvotproduct*: This tool creates level 3 science products from the level 2 images after combining images until significant detections are achieved. The script generates a plot of the light-curve in all available filters for a particular observation, together with the corresponding FITS file and a text file containing a report of the output.

[7] `https://www.swift.ac.uk/analysis/uvot/`
[8] in the case of 3-σ source detection otherwise "Background threshold"-σ upper limits

2.3.3 Advanced analysis methods

The data reduction procedures mentioned in previous sections yields science products such as sky images, spectra, and lightcurves. We can perform advanced analysis on these products for detailed studies. The spectra obtained can be fitted and studied with various functions in platforms like XSPEC (Arnaud, 1996). This allows us to explore different spectral parameters and study the spectral evolution of the source. Additionally, the spectral points can also be plotted and modeled using many third party software available to bring breakthrough results. For example, the broad-band spectral energy distribution (SED) of the interested sources can be obtained from the spectra generated by the standard pipelines. Then these SEDs can be studied using user defined models. On the other hand, researchers can do the systematic SED modeling of blazars and AGNs using free softwares such as *JetSet*, *AGNpy*, and *GAMERA* (Tramacere, 2020; Hahn, 2016; Nigro et al., 2022). The systematic study of SEDs provides hints on the physics behind the emission processes. The lightcurves are often used for further statistical analysis to understand the nature of emission processes and the temporal behaviour of the source. Bayesian blocks, histograms, power spectrum, correlation functions are some of the tools that are commonly used in such studies. There are various other software packages that are helpful in analyzing astronomical data like *astropy*[9], *gammapy*[10], *lmfit*, *emcee*[11], and *PyAstronomy*[12].

[9] `https://www.astropy.org/`
[10] `https://gammapy.org/`
[11] `https://lmfit.github.io/lmfit-py/examples/example_emcee_Model_interface.html`
[12] `https://pyastronomy.readthedocs.io/en/latest/`

Chapter 3

Understanding the Broadband Emission Process of 3C 279 through Long term Spectral Analysis

3.1 Introduction

3C 279 is one of the well-studied FSRQs with redshift, z=0.539 (Lynds et al., 1965) and the first one to be detected at GeV/TeV energies. This source was studied extensively in gamma-rays by *EGRET* during different flux states. With the advent of Fermi, 3C 279 has been monitored continuously at MeV-GeV energies revealing a series of extreme flaring events (Ackermann et al., 2016; Hayashida et al., 2012, 2015; Paliya, 2015; Shah et al., 2019). The broadband SED of 3C 279 is characterized by two broad peaks with the low-energy component peaking at IR and the high-energy component peaks at MeV energies. The γ-ray spectrum of 3C 279 in the energy range 0.1-10 GeV is significantly curved since the high energy SED of the source peaks in this energy band (Ackermann

et al., 2016). Hence a log-parabolic function represents the γ-ray spectrum better than a power-law during a flare (Roy et al., 2021; Zhang et al., 2021; Larionov et al., 2020). The source also undergoes considerable changes in the spectral parameters along with the flux variations, for instance, during the 2018 flare, variation in the peak energy was positively correlated with the gamma-ray flux showing a 'bluer when brighter' trend (Shah et al., 2019). The spectral curvature at the peak energy also showed a positive correlation with the flux. The soft X-ray and optical band, on the contrary, follow a simple power law with relatively harder X-ray spectral index (Zhang et al., 2021; Prince, 2020a). During a flare the X-ray hardness increases with the flux showing a 'harder when brighter' behaviour (Abdo et al., 2010b; Yoo & An, 2020). Besides these, studies using longterm multiwavelength lightcurves have shown that the gamma-ray and X-ray fluxes were correlated in 3C 279; nevertheless, no significant correlation is observed between optical and gamma-ray energy bands (Prince, 2020a; Larionov et al., 2020).

One of the striking features of 3C 279 is its flux variability observed within timescales down to minutes (Ackermann et al., 2016; Paliya, 2015). Such rapid variability demands a very compact emission region located well within the broad line emitting region of the quasar (Joshi et al., 2013; Narayan & Piran, 2012). However, the location of the emission region inferred from the broadband SED modelling contradicts this since the γ-ray emission is better interpreted as EC-IR process demanding an emission site beyond the BLR (Sikora et al., 2009; Paliya et al., 2016).

The broadband SEDs of blazars, and 3C 279 in particular, have been reasonably well understood through broadband spectral modelling using synchrotron, SSC, and EC emission processes (Błażejowski et al., 2000; Sahayanathan & Godambe, 2012; Shah et al., 2017; Shah et al., 2019).

However, the temporal behaviour of the source at different energy bands in connection with these emission models is not addressed in detail. Such a study, besides refining the emission models, has the potential to identify the origin of the flaring mechanism. In this work, we performed a detailed analysis of optical–X-ray–gamma-ray spectral behavior of 3C 279 spanning from 2008 to 2022. Since the spectra at these energies are interpreted by different emission processes, we carried over a correlation study between the best fit parameters of the individual spectral fittings to identify the plausible reasons for the observed flux variations. Further, we also performed a statistical broadband spectral fit using synchrotron and inverse Compton emission processes for two epochs with simultaneous *Swift*, *Nu*STAR and *Fermi* observations to investigate the emission processes.

3.2 Observations and Data Reduction

3C 279 is one of the well-studied FSRQs thanks to the wealth of observations at different energy bands. To study its spectral behavior at optical/UV, X-ray, and γ-ray energy bands, we performed a detailed analysis of the source using longterm observations by Swift-UVOT, Swift-XRT, and Fermi-LAT telescopes on board. We also supplement these with the simultaneous Nu-STAR observations of the source at hard X-rays available for two epochs.

3.2.1 Fermi-LAT Observations

In this work, we have analyzed the Fermi-LAT observation of 3C 279 spanning the time period 2008 – 2022 (MJD 54693-59754) in the energy range 0.1-300 GeV. A 10° circular region centered at RA=194.0415,

Dec= -5.7887 was chosen as Region of interest (ROI) to download the data[1]. We used the *Fermitools* software version 2.2.0 for the data analysis. First, we performed the preferred selection cuts in the event data on region, time, energy interval, and type using standard criteria recommended for Pass 8 data. The '*gtmktime*' tool was applied on the event files to update good time intervals based on the spacecraft parameters. A livetime and exposure maps were created using '*gtltcube*' and '*gtexpmap*' respectively. The binned likelihood method was performed to fit the data over the whole time interval using standard templates gll_iem_v07 and iso_P8R3_SOURCE_V3_v1 for the galactic diffuse and extragalactic isotropic background emissions. All the γ-ray sources within 20-degree radius circle from the center were considered in the analysis and their spectral shapes were adopted from the 4FGL catalog. The parameters of all sources lying within the ROI were kept free while that of the sources outside ROI were fixed to their catalog values. The significance of γ-ray detection from all the positions was quantified using the test statistic defined as, $TS = 2\log(\mathcal{L})$ where $\mathcal{L}$ is the ratio of maximum likelihood value with the source at a particular position to that without the source in that position. A larger TS indicates a higher probability for the source to be at the position. The spectral parameters of all sources for which TS<25 were then kept frozen. The output file thus obtained was used as the input sky model in further analysis.

We obtained longterm γ-ray lightcurves of 3C 279 for two types of binning, a constant time interval (3 day) and the adaptive binning. The adaptive binning is a new technique for the lightcurves, in which bin widths are estimated by setting a constant relative uncertainty on the flux (Lott et al., 2012; Sahakyan et al., 2022). Unlike the constant time bin method, which smooths out the minute scale variability, this method

[1] `https://Fermi.gsfc.nasa.gov/ssc/data/access/lat/12yr_catalog`

is more suitable for studying highly variable sources, especially during the flaring periods. The adaptive time bins for a 20% constant relative flux density were obtained following the steps in the documentation[2]. The optimum energy for estimating the adaptive time bins was computed as 157 MeV. The same was chosen as the minimum energy, E_{min} for estimating fluxes in the adaptively binned lightcurve. The unbinned likelihood analysis was adopted for obtaining lightcurves in the case of adaptive as well as 3 day binning criteria. We chose the power-law2 function[3] to model the γ-ray spectrum of 3C 279 and used an iterative approach for the likelihood fit to obtain convergence in fit. Initially 'DRMNFB' optimizer was used and all the sources with TS<9 were deleted once found no convergence in trial runs. Additionally, all the parameters other than the norm for sources with TS between 9 and 50 were kept frozen in such cases. All the final fits were optimized using 'Newminuit' method.

3.2.2 Swift Observations

In the X-ray and optical/UV bands, a total of 491 observations were available for 3C 279 up to 59754 MJD. We obtained the Swift X-ray spectra from the automated online tool *'Swift-XRT data products generator'* (Evans et al., 2009). All the obtained spectra were rebinned to 20 minimum counts in each energy bin and fitted with a absorbed power-law in XSPEC (Arnaud, 1996). To account for the attenuation of X-rays by the hydrogen atoms, the neutral hydrogen column density was set at $n_H = 2.24 \times 10^{20}\, cm^{-2}$ (Pian et al., 1999). The unabsorbed integrated flux in the energy range of 0.3-10 keV and spectral index were determined from the best fit results. For the present work, we considered only those spectra which were well fitted

[2] `https://www.slac.stanford.edu/~lott/ABM_mult_P8.tar.gz`
[3] `https://fermi.gsfc.nasa.gov/ssc/data/analysis/scitools/source_models.html`

with a power-law (reduced chi-square between 0.6 and 1.8). Additionally, we rejected some spectra due to very low exposure periods and a very low number of energy bins. After these reductions, we were left with 326 X-ray spectra and the fit details are given in Table 3.1.

All the available UVOT observations for 3C 279 were downloaded from the HEASARC archive. We followed the standard procedures of data reduction given by the tutorial[4] for obtaining spectral files. For each observation, the images over all the extensions were summed up using the *uvotimsum* tool for every filter. A circle of radius 6 arcsec centered at the source was chosen to extract the source counts while, for the background estimation, we used a circle of radius 20 arcsec from a source-free region near the target. For all the observations, the spectral products corresponding to each filter were then obtained using *uvot2pha* tool. For the spectral fit, we considered only those *UVOT* observations for which the images are available in atleast 3 filters. The selected optical/UV spectra were then fitted using XSPEC with an absorbed power-law model. The integrated fluxes were corrected for galactic extinction after fixing the value of the parameter E(B-V) magnitude to 0.025 (Schlafly & Finkbeiner, 2011a). For some observations, we included an additional 3% systematic error in order to obtain the reduced chi-square less than 2. Those observations with reduced chi-square larger than 2 even after adding 3%systematic error are not considered in the present work. Similarly, we also rejected those observations whose power-law spectral fit resulted in a reduced chi-square of less than 0.6 as this indicates the over estimation of the best-fit parameters. Finally, we were left with 189 *UVOT* observations and the details are given in Table 3.2.

For the combined optical/UV–X-ray spectral analysis, some of the

[4]https://Swift.gsfc.nasa.gov/analysis/threads/uvot_thread_spectra.html

Table 3.1: Table showing results of power-law fitting of Swift-XRT observations. From left to right: Observation id, time in MJD, un-absorbed flux in the energy range 0.2–10 keV, spectral index, chi-square, and degrees of freedom. The entire tabular data is given the Table A.1 in the appendix.

Obs.Id	**Time in MJD**	**Flux** 10^{-11} **ergs cm**$^{-2}$ **s**$^{-1}$	**spectral index,** Γ_x	χ^2	**Dof**
000 35019001	53748.0	1.498 ± 0.057	1.517 ± 0.040	111.22	132.0
000 35019002	53749.0	1.414 ± 0.066	1.579 ± 0.052	70.27	96.0
000 35019003	53751.2	1.636 ± 0.202	1.397 ± 0.130	16.06	15.0
000 35019004	53752.0	1.592 ± 0.051	1.521 ± 0.033	178.63	179.0
000 35019005	53753.1	1.766 ± 0.061	1.545 ± 0.037	160.48	148.0

Swift observations are excluded since either UVOT or the XRT spectra were not available due to the selection criteria mentioned above. We were finally left with 170 *Swift* observations for which simultaneous optical–X-ray information was available. Similarly, for the simultaneous γ-ray analysis, we considered the adaptively binned *Fermi* spectrum which overlapped (at least partially) with the *Swift* observation epochs. This resulted in 260 simultaneous X-ray–γ-ray observations and 164 optical/UV–γ-ray observations. However, we have included all the selected observations for studying individual energy band.

3.2.3 NuSTAR Observations

We used two *Nu*STAR Observations (60002020002 and 60002020004) of 3C 279 which are publicly available and having simultaneous *Swift* observations for the broadband SED analysis. The data were downloaded from the archive and reduced using the standard pipeline techniques (software version v1.9.7)[5]. The *nupipeline* tool was used to filter the event lists from the downloaded observations. Then the tool *nuproducts* was

[5]`https://heasarc.gsfc.nasa.gov/docs/nustar/analysis/`

Table 3.2: Table showing results of power-law fitting of Swift-UVOT observations. Columns from left to right: 1 – Observation id, 2 – time in MJD, 3 – un-absorbed flux in the energy range 2–7 eV, 4 – spectral index, 5 – chi-square, and 6 – degrees of freedom. The entire data is given the Table A.2 in the appendix.

Obs.Id	**Time in MJD**	**Flux** 10^{-11} **ergs cm**$^{-2}$ **s**$^{-1}$	**spectral index,** $\Gamma_{o/uv}$	χ^2	**Dof**
000 30867007	54157.27	2.23 ± 0.04	2.777 ± 0.049	2.53	4.0
000 30867009	54266.79	1.07 ± 0.02	2.665 ± 0.046	5.12	4.0
000 30867017	54686.49	0.38 ± 0.02	2.149 ± 0.135	3.13	4.0
000 30867022	54695.6	0.45 ± 0.02	2.14 ± 0.114	4.65	4.0
000 30867024	54698.01	0.75 ± 0.02	2.164 ± 0.081	3.65	4.0

used to extract spectral products and response files for the two instruments FPMA and FPMB. To extract the source counts, we selected a circular region of 49 arcsecond radius centered at the source. Another circle of 60 arcsecond radius in a source-free region was selected as background region. Separate source and background region files were used for FPMA and FPMB observations. The obtained spectra were loaded in XSPEC and fitted with an absorbed power-law. The best fit photon power-law indices for the two observations are 1.73 ± 0.02 and 1.76 ± 0.01 with fit statistics (χ^2 (dof)) 529.42 (528) and 678.77 (737), respectively. The unabsorbed fluxes in 3-79 keV energies is used for the broadband spectral study (Section 3.4).

3.3 Multi-wavelength Analysis

In Figure 3.1, we show the multi-wavelength lightcurve of the source in γ-ray, X-ray, and optical/UV bands. It is evident from the multi-wavelength lightcurve that the source exhibits significant variability in all energy bands and the instances where the flux enhancements are not correlated. For example, we observe an optical/UV flux excess around the epochs

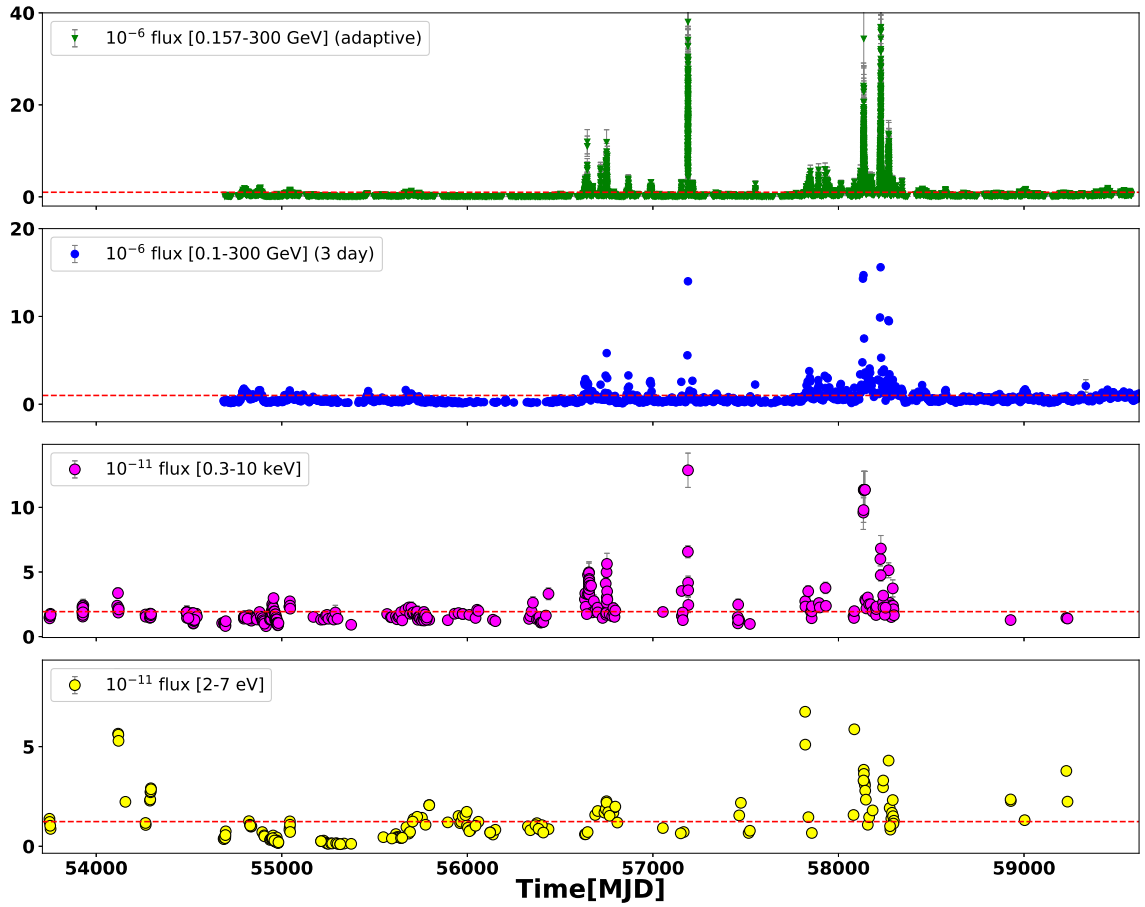

Figure 3.1: light curves of 3C 279 in γ-ray, X-ray and optical energies. The horizontal dashed lines represent the average flux. The X-ray and optical/UV fluxes are in units of $\mathbf{ergs\,cm^{-2}\,s^{-1}}$ and γ-ray fluxes are in units of $\mathbf{phs\,cm^{-2}\,s^{-1}}$. From top to bottom: panel 1 & 2 displays the γ-ray light curves using Fermi observations in the energy range 0.1-300 GeV with adaptive and 3 day binning respectively. panel 3: X-ray lightcurve using Swift-XRT observations, panel 4: optical/UV lightcurve using Swift-UVOT observations.

57827 and 59238; whereas, no significant flux enhancement is observed in X-ray and γ-ray bands. On the contrary, during epochs 56750 and 57188, flux enhancement is witnessed in γ-ray and X-ray energy bands with no such variation in optical band. The simultaneous SED during correlated and uncorrelated flares for certain epochs were already studied under synchrotron and inverse Compton emission models (Rajput et al.,

2020). Here, we considered all the observations of the source by Swift and Fermi telescopes during its entire period of operation till 59754 MJD. The γ-ray light curves were obtained for two different binning criteria. The top panel displays the lightcurve using adaptive binning technique whereas, the second from the top shows that with 3 day binning. The average flux over the entire period is shown as a horizontal line in all the light curves. The value of the average optical/UV flux estimated is $1.24 \times 10^{-11}\ erg\,cm^{-2}\,s^{-1}$ and that for X-ray emission is $1.93 \times 10^{-11}\ erg\,cm^{-2}\,s^{-1}$. The average γ-ray flux for 3C 279 was found to be $9.27 \times 10^{-7}\ phs\,cm^{-2}\,s^{-1}$. We used these values of fluxes to demarcate high and low states in the corresponding energy bands.

To investigate the relation between the optical, X-ray, and γ-ray energies, we studied the spectra at these energies using a power-law function. *Swift* being a pointing telescope, the individual observation period of 3C 279 spans mostly from 0.2 to 7 ks; whereas, due to the scanning mode of operation, the *Fermi*-LAT observations are continuous. The γ-ray spectra simultaneous to optical/UV and X-ray spectra were taken from the corresponding adaptive bins. The γ-ray spectrum of 3C 279 is generally curved and often modelled using a log-parabolic function. To verify whether the γ-ray spectrum from the selected bins (adaptive bins) show curvature, we estimated the test statistics for curvature, TS (curv) as TS (LP) - TS (PL), where TS (LP) is the TS obtained with log-parabola model and TS (PL) is that for power-law model. A large positive value of TS (curv) will indicate significant curvature in the spectrum (Prince, 2020a). Our study suggests that the γ-ray spectra are well represented by a power-law and the details of this study are given in Table 3.3. The integrated γ-ray flux is estimated by considering the best-fit power-law.

Table 3.3: Table showing Details of best fit parameter values of power-law fit of selected γ-ray observations (adaptive time bins) simultanoeus to Swift observtaions. Columns from left to right: 1 – Tstart in MJD, 2 – Tstop, 3 – integrated flux in the energy 0.157-300 GeV, 4 – spectral index, 5 – TS of power-law function, 6 – TS of log-parabola model, 8 – TS of curvature. Entire data is presented in the Table A.3 in the appendix.

Tstart MJD	Tstop MJD	Flux [0.1-300 GeV] 10^{-7}phs cm^{-2} s^{-1}	PL Index Γ_γ	TS(PL)	TS(LP)	TS(Curv)
54693.0	54696.0271	1.05 ± 0.50	2.00 ± 0.30	34.58	34.59	0.02
54693.0	54696.0271	1.05 ± 0.50	2.00 ± 0.30	34.58	34.59	0.02
54696.0271	54697.0139	6.20 ± 1.74	2.40 ± 0.28	57.42	57.42	0.0
54697.8665	54698.2684	8.90 ± 2.60	2.13 ± 0.23	72.46	72.46	0.0
54795.0751	54795.6055	15.33 ± 3.84	2.20 ± 0.21	110.21	110.21	0.0

3.3.1 Spectral Transition

The broadband spectral modelling of 3C 279 indicates that the optical/UV emission is by synchrotron process while the X-ray emission is due to Inverse Compton scattering (Sahayanathan & Godambe, 2012; Paliya, 2015). From the narrow band spectral fitting using power-law functions, we found that the optical/UV spectral index $\Gamma_{\rm o/uv} > 2$ and the X-ray spectral index $\Gamma_x < 2$ (Tables 3.1 & 3.2). This suggests the optical/UV emission falls on the decaying part of the synchrotron spectrum while the X-ray emission lies on the rising part of the IC spectrum (Sahayanathan & Godambe, 2012; Larionov et al., 2020). A combined spectral study can therefore probe the relation between these spectral components. Particularly, studying the transition energy variations, where the dominant emission shifts from synchrotron to IC, can investigate the changes in the dominance of these components during different flux states. To facilitate this, we performed a combined spectral fit of optical/UV and

X-ray observations using a broken power-law described as

$$\frac{df}{d\epsilon} = \begin{cases} f_0\,\epsilon^{-\Gamma_1} & \text{for } \epsilon \leq \epsilon_b \\ f_0\,\epsilon_b^{\Gamma_2-\Gamma_1}\epsilon^{-\Gamma_2} & \text{for } \epsilon \geq \epsilon_b \end{cases} \tag{3.1}$$

where Γ_1 and Γ_2 are the high and low-energy photon spectral indices respectively, ϵ_b is break energy, and f_0 is the normalization. The parameter ϵ_b can be treated as the transition energy and to obtain better constraints on it, we have fixed Γ_1 and Γ_2 to the best fit power-law indices of the corresponding optical/UV and X-ray spectrum. The best fit values of ϵ_b obtained from the broken power-law fitting of simultaneous observations of *Swift* UVOT and XRT are given in Table 3.4.

An improved estimation of the transition energy can be obtained by fitting the simultaneous optical/UV and the X-ray data with a double power-law function. If we consider the underlying electron distribution responsible for the broadband SED of 3C 279 to be a broken power-law, then the optical/UV emission can be attributed to the synchrotron emission from high energy electrons and the X-ray emission to the inverse Compton scattering from the low energy electrons. We define the double power-law function as

$$\frac{df}{d\epsilon} = f_0 \left[\left(\frac{\epsilon}{\epsilon_{\rm m}}\right)^{-\Gamma_{\rm syn}} + \left(\frac{\epsilon}{\epsilon_{\rm m}}\right)^{\Gamma_{\rm com}} \right] \tag{3.2}$$

Here, ϵ_m is the energy at which the synchrotron and IC fluxes are equal to f_0 while $\Gamma_{\rm syn}$ and $\Gamma_{\rm com}$ are the synchrotron and IC spectral indices respectively. The valley energy (ϵ_v) corresponding to minimum flux will be

$$\epsilon_v = \epsilon_m \left(\frac{\Gamma_{\rm syn}}{\Gamma_{\rm com}}\right)^{1/(\Gamma_{\rm syn}+\Gamma_{\rm com})} \tag{3.3}$$

Table 3.4: Table showing results of combined spectral fitting of XRT and UVOT spectra with the Broken power-law model. Columns from left to right: 1 – observation id, 2 – time in MJD, 3 – break energy ϵ_b (keV), 4 – chi-square, and 5 – Dof. The entire data is given in the Table A.4 of the appendix.

Obs Id	**Time** MJD	**Break energy,**ϵ_b keV	χ^2	**Dof**
000 30867009	54266.79	0.103 ± 0.005	40.09	50.0
000 30867022	54695.6	0.757 ± 0.166	21.44	19.0
000 30867024	54698.01	0.409 ± 0.134	21.53	21.0
000 30867028	54828.2	0.099 ± 0.008	13.62	23.0
000 30867031	54834.23	0.079 ± 0.007	13.82	18.0

and this can be treated as the transition energy. The double power-law model is added as a local model in XSPEC with f_0, $\Gamma_{\rm syn}$, $\Gamma_{\rm com}$ and ϵ_v as free parameters, and the combined spectral fits to optical/UV and X-ray data were performed. The results of the spectral fit are given in Table 3.5. In Figure 3.2 (a), we plot the transition energies obtained through a broken power-law (ϵ_b) and double power-law (ϵ_v) functions along with the identity line. We find the estimate of the transition energy obtained using either methods closely match. We also compare the optical/UV and X-ray power-law spectral indices with $\Gamma_{\rm syn}$ and $\Gamma_{\rm com}$ in Figures 3.2 (b) and (c), along with the identity line. It is evident from the figures that $\Gamma_{\rm syn}$ and $\Gamma_{\rm o/uv}$ reasonably matches; whereas $\Gamma_{\rm com}$ is relatively harder than Γ_x.

3.3.2 Correlation Analysis

Flux-index Correlation

In Figures 3.3 (a), (b), and (c), we show the scatter plots between the integrated fluxes at optical/UV, X-ray, and γ-ray energies respectively with their corresponding spectral indices. The dashed vertical line shows the corresponding average flux values in all the plots. A negative correlation

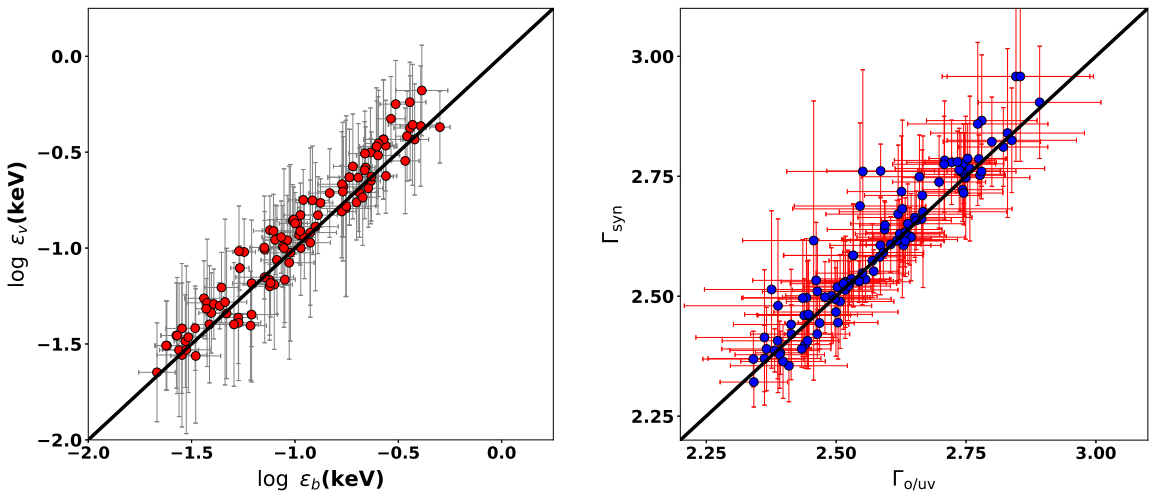

(a)

(b)

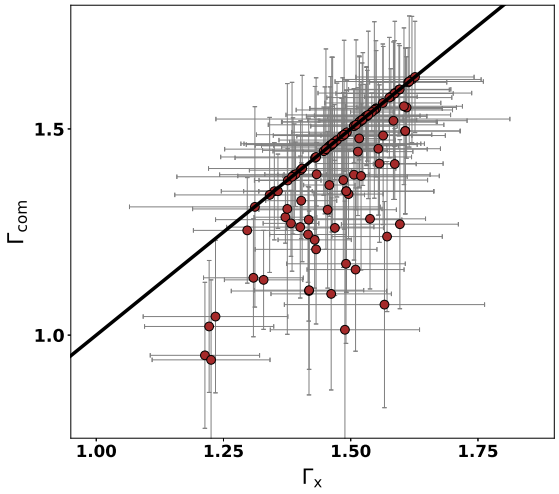

(c)

Figure 3.2: Scatter plots between the parameters obtained from broken power-law/power-law and double power-law fitting along with the identity line (black solid line). (a) The estimates of transition energy, ϵ_b and ϵ_v, (b) optical/UV indices $\Gamma_{\rm o/uv}$ and $\Gamma_{\rm syn}$, and (c) X-ray indices Γ_x and $\Gamma_{\rm com}$ respectively.

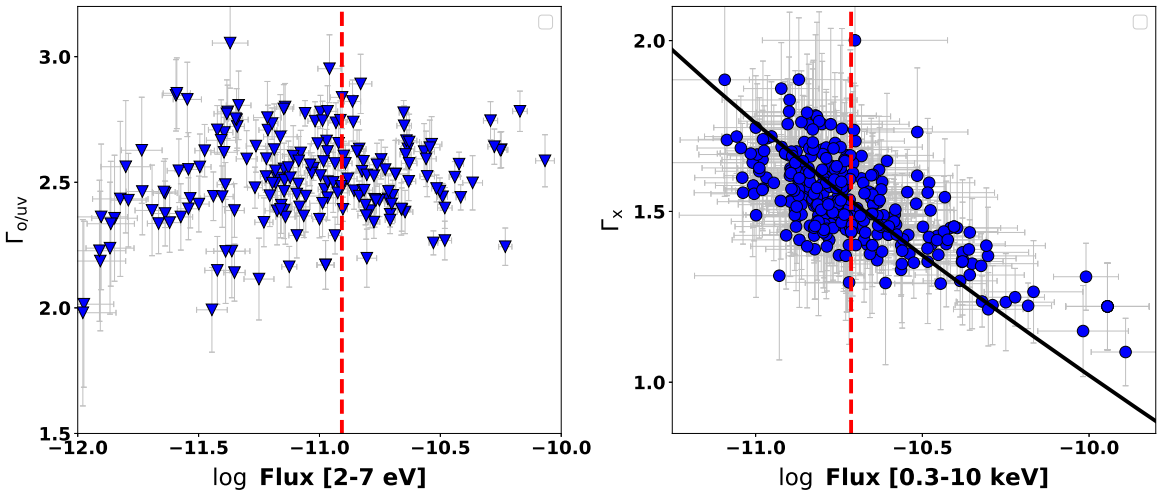

(a) (b)

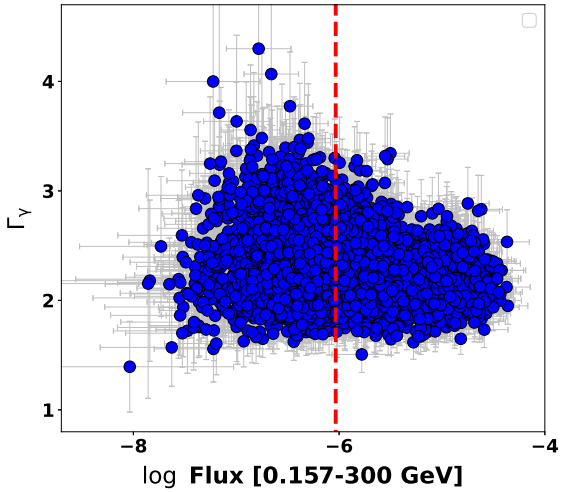

(c)

Figure 3.3: Scatter plots between integrated fluxes and photon indices. The vertical dashed lines represents the average value of corresponding fluxes in logscale. X-ray and optical/UV fluxes are in units of $\mathbf{ergs\,cm^{-2}\,s^{-1}}$ and γ-ray flux is in units of $\mathbf{phs\,cm^{-2}\,s^{-1}}$ (a) Optical/UV flux and index, (b) X-ray flux and index, the solid curve represents the integrated power-law function mentioned in Section 3.3.2. (c) γ-ray flux and index (adaptive binning).

Table 3.5: Table showing Details of Combined spectral fitting of XRT and UVOT specra with the Double power-law model. Columns from left to right: 1 – observation id, 2 – time in MJD, 3 – Photon index $< \epsilon_v$, 4 – index at $> \epsilon_v$, 5 – Transition Energy, ϵ_v, 6 – chi-square, and 7 – Dof. The entire data is presented in Table A.5 in the appendix.

ObsId	Time	$\Gamma_{\rm syn}$ ($\Gamma_{\rm o/uv}$)	$\Gamma_{\rm com}$ ($\Gamma_{\rm x}$)	ϵ_v	χ^2	Dof
	MJD			keV		
000 30867001	54113.0	2.761 ± 0.056	1.415 ± 0.086	0.428 ± 0.080	154.53	138.0
000 30867003	54118.22	2.606 ± 0.062	1.269 ± 0.205	0.563 ± 0.128	34.61	27.0
000 30867004	54119.22	2.630 ± 0.059	1.239 ± 0.182	0.576 ± 0.120	36.05	25.0
000 30867005	54120.18	2.625 ± 0.060	1.282 ± 0.170	0.472 ± 0.104	25.4	28.0
000 30867007	54157.27	2.752 ± 0.039	1.386 ± 0.141	0.172 ± 0.022	11.07	23.0

between the flux and indices indicates a "harder when brighter" trend while the reverse indicates a "softer when brighter" trend. Since we have considered the observations spanning over a decade, this study tells the general behavior of the source irrespective of its individual flaring states. It is evident from Figure 3.3 (a) and 3.3 (c), that no significant correlation was observed between optical flux and index as well as γ-ray flux and index. A Spearman rank correlation study between these quantities resulted in the correlation coefficient $\rho \approx 0.13$ with the null hypothesis probability $P \approx 0.06$ for the former, and $\rho = -0.09$ with $P \approx 0.28$ for the latter. However, a negative correlation with the $\rho = -0.64$ and $p < 0.001$ is obtained for the X-ray flux and index study. This suggests that the source generally shows a "harder when brighter" trend in X-ray. A "harder when brighter" trend may be evident in time periods around the flares in optical/UV and γ-ray energies. However, our longterm study indicates that this trend may not be the only possibility in these energy bands.

The negative correlation observed at X-ray energy also suggests that the enhancement in integrated flux may be predominantly due to the spectral hardening of the power-law function. The integrated flux in νf_ν

representation between the photon energies ϵ_1 and ϵ_2 will be:

$$\left(\frac{K\,\epsilon_0^{\Gamma}}{2-\Gamma}\right)\left(\epsilon_2^{2-\Gamma}-\epsilon_1^{2-\Gamma}\right) \tag{3.4}$$

Here, K is the normalization, ϵ_0 is the pivot energy and Γ is the spectral index. To verify our inference, we plotted the integrated flux against Γ for a constant K. With a proper choice of K, we find that the predicted line reasonably supports the 'harder when brighter' trend. However, the spread of the points around this line suggests, the variation in normalization is also responsible for the flux variation. The absence of any such correlation at optical/UV and γ-ray energies suggests significant variation in normalization may be responsible for the flux variations. Alternatively, this could also suggest that the source exhibits both "harder when brighter" and "softer when brighter" behaviors during different flaring states.

Index-index Correlations

If we consider the radiative loss origin of the broken power-law electron distribution, then the indices should be positively correlated (Kardashev, 1962; Baheeja et al., 2022). Since, $\Gamma_{\rm o/uv} > 2$ and $\Gamma_x < 2$ (Tables 3.1 & 3.2), these indices can relate to the high energy and the low energy power-law indices of the electron distribution. However, the Spearman correlation study between these two quantities obtained from the power-law fit suggested a poor correlation with $\rho \approx -0.23$ and $P \approx 0.002$. The scatter plot between $\Gamma_{\rm o/uv}$ and Γ_x is shown in Figure 3.4 (a). Interestingly, a moderate positive correlation with $\rho \approx 0.52$ and $P < 0.001$ is witnessed (figure 3.4 (b)) when the optical/UV and X-ray spectral indices are obtained from a double power-law function ($\Gamma_{\rm syn}$ and $\Gamma_{\rm com}$). However, the difference between the optical/UV and X-ray spectral indices are much larger than

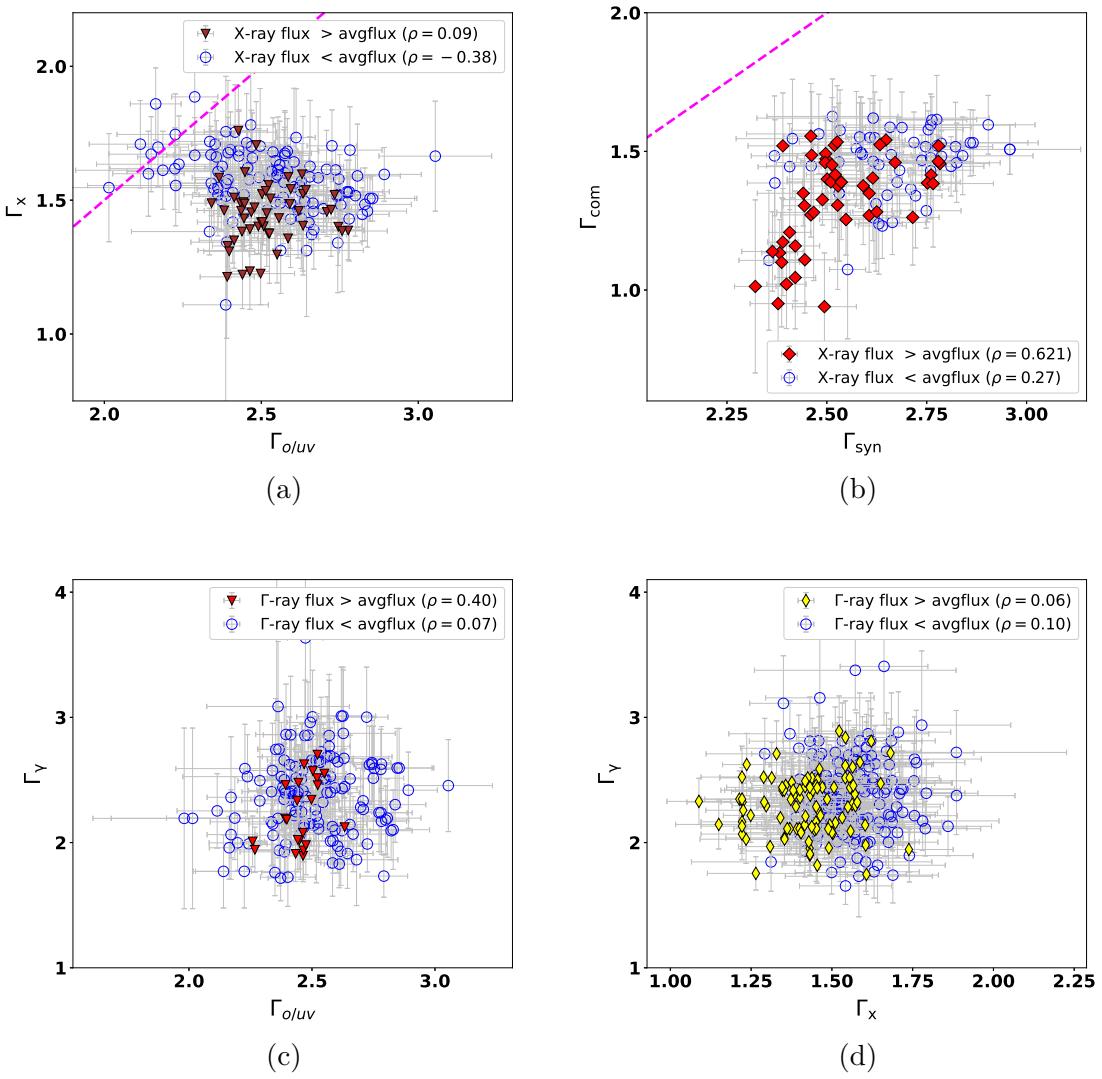

Figure 3.4: Scatter plots between the spectral indices obtained through power-law and double power-law spectral fitting to simultaneous optical/UV, X-ray and γ-ray spectra. (a) Optical/UV and X-ray spectral indices from simple power-law fit ($\Gamma_{\rm o/uv}$ & Γ_x). (b) The same from double power-law fit ($\Gamma_{\rm sync}$ & $\Gamma_{\rm com}$). The dashed line indicate the straightline '$X = Y + 0.5$'. It is evident from the figures, that the points deviate considerably from this line indicating an index difference > 0.5 as mentioned in Section 3.3.2. (c) Optical/UV and γ-ray power-law indices. (d) X-ray and γ-ray power-law indices. In all the subplots, filled shapes represent the states of high flux and open shapes the low flux states and the details of correlation coefficient ρ with respect to flux states have been inboxed in the plots.

0.5 and hence, cannot be interpreted in terms of radiative losses (Baheeja et al., 2022). Therefore, this study is inconclusive on the radiative cooling interpretation of the broken power-law electron distribution.

If the electron distribution responsible for the broadband emission is an outcome of multiple acceleration processes (e.g. stochastic and shock acceleration), then the resultant broken power-law indices will be governed by the corresponding acceleration rate (Sahayanathan, 2008). Under this scenario, it may happen that the power-law indices of the electron distribution (or the corresponding photon spectral indices) are not strongly correlated. Such a study may involve the exact description of the acceleration processes with a suitable choice of the magneto-hydrodynamic turbulence (Rieger et al., 2007; Rieger, 2019a) and is beyond the scope of present work.

We did not find any significant correlation between $\Gamma_{\rm o/uv}$ / Γ_x and the γ-ray spectral index Γ_γ. This result may indicate that the electron energies responsible for the emission at these photon energies are different. Probably, the electron population responsible for the γ-ray emission is falling close to the break energy. This is consistent with the range of Γ_γ which is spread around 2.

To study the spectral index behavior of the source during high and low X-ray flux states, we distinguish the points in the scatter plots in Figure 3.4 using filled shapes for high flux and open shapes for low flux. From the scatter plot between the indices obtained from power-law spectral fit of optical/UV and X-ray spectra, we find that during high flux states (filled shapes) the Γ_x is moderately harder and $\Gamma_{\rm o/uv}$ softer. However, no such behaviour is seen when the indices are obtained through a double power-law function (Figure 3.4 (b)). Similarly, in Figure 3.4 (c) and (d), we again divide the data points on the basis of average γ-ray flux with the filled/open

shapes indicating the high/low γ-ray flux. No definite trend is observed for the indices corresponding to high/low flux states of the γ-ray spectrum. The distribution of the filled data points is almost similar to that of the open ones with the values of Γ_γ spread around 2. The individual flares may exhibit either "bluer when brighter" or "redder when brighter" which is consistent with the absence of any definite pattern in the scatter plots (Figures 3.4 (c) and (d)). On the other hand, the X-ray indices during the γ-ray high flux show a mild hardness (figure 3.4 (c)) which is consistent with the "harder when brighter" trend mentioned earlier.

Flux-Flux Correlations

3C 279 is known to exhibit multi-wavelength flux correlations during its several major outbursts (Hayashida et al., 2015; Zhang et al., 2021; Hayashida et al., 2012; Patiño-Álvarez et al., 2018; Prince, 2020a; Paliya, 2015; Rajput et al., 2020). To study whether such correlations exist in its long term behaviour spanning over 14 years we performed a correlation test on the simultaneous fluxes at the optical/UV, X-ray, and γ-ray energies. Contrary to X-ray–γ-ray spectral indices, the γ-ray flux is well correlated with the X-ray flux, and the plot between these quantities is shown in Figure 3.5 (c). The Spearman rank correlation study resulted in $\rho = 0.72$ with $P < 0.001$.

The flux–index correlation study at X-ray energies suggests the flux variability is predominantly due to the change in the index, whereas at γ-ray energy no such correlation is observed. However, the range of index values suggests that the Compton SED peak may fall at this energy range. Hence, flux–index correlation at X-rays can also cause variation in flux at the low energy γ-rays if the same power-law electron distribution is responsible for the emission at both these energies.

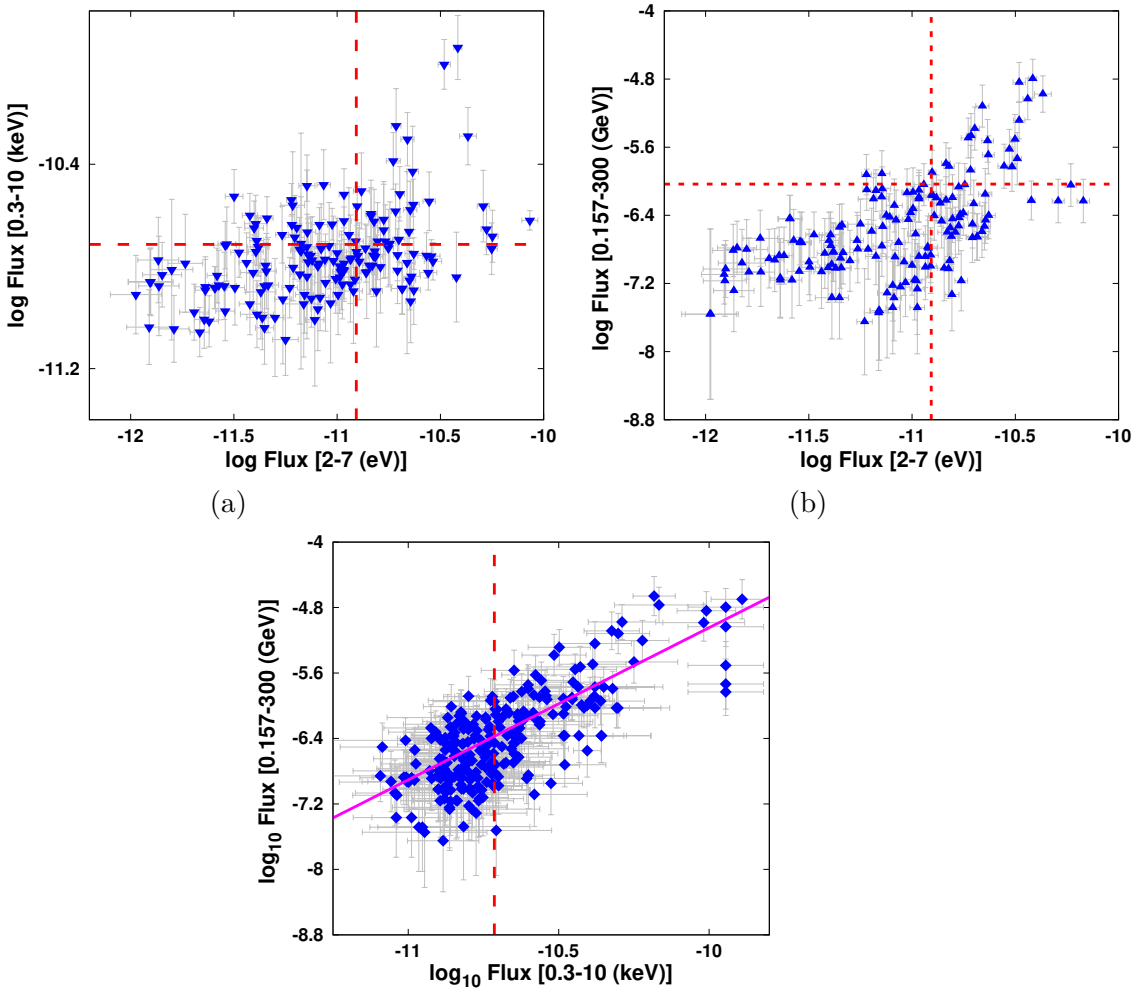

Figure 3.5: Scatter plots between the integrated fluxes of optical/UV (2-7 eV) , X-ray (0.3-10 keV) and γ-ray (0.157-300 GeV) spectra of 3C 279. (a) X-ray and optical/UV flux. (b) Optical/UV and γ-ray flux. (c) X-ray and γ-ray flux. The solid line represents the best-fit linear regression to this correlation. The dashed lines in all the plots represents the value of arithmetic average of the fluxes plotted on respective axis. The X-ray and optical/UV fluxes are in units of $\mathbf{ergs\,cm^{-2}\,s^{-1}}$ and γ-ray fluxes are in units of $\mathbf{phs\,cm^{-2}\,s^{-1}}$.

The observed correlation between the X-ray and γ-ray fluxes is also possible when the same radiative process is responsible for the emission at these energies. To understand this, we performed a linear regression analysis between the logarithm of the X-ray and γ-ray fluxes and obtained the best fit straight line as

$$\log F_{\gamma-\mathrm{ray}} = (1.9 \pm 0.1) \log_{10} F_{\mathrm{X-ray}} + (13.5 \pm 1.0) \tag{3.5}$$

with Q-value[6] of 0.87. A near quadratic dependence of the γ-ray flux on the X-ray flux disfavours this interpretation. Quadratic dependence between the X-ray and γ-ray fluxes is also observed for the BLLac type source MKN 421 (González et al., 2019; Kapanadze et al., 2018; Mastichiadis & Kirk, 1997; Goswami et al., 2020). The X-ray emission for this source is due to the synchrotron process and the quadratic dependence of γ-ray emission supports the SSC interpretation of the Compton spectral component (Błażejowski et al., 2005; Acciari et al., 2011). However, in the case of 3C 279, both the X-ray and the γ-ray emission are due to IC process. The broadband SED modeling of the source also associates the X-ray emission to the SSC process and the γ-ray emission to the EC process (Section 3.4).

A moderate correlation is also observed between the optical/UV and γ-ray fluxes with the Spearman rank correlation coefficient $\rho = 0.60$ and $P < 0.001$. Again, this correlation may be associated with the fact that the Compton peak falls in the γ-ray regime. If we consider a broken power-law electron distribution responsible for the broadband emission, then the enhancement in optical flux may be associated with the increase in the high energy (larger than the break energy) electron component. This would also affect the high energy γ-ray flux resulting in the observed correlation. However, the correlation may be suppressed due to orphan

[6]Q is known as the probability of fitting and the fitting can be accepted if the value of Q$<$ 0.1

flares often encountered in 3C 279 (Rajput et al., 2020; Paliya et al., 2021). We did not observe any significant correlation between optical/UV and the X-ray fluxes. The Spearman correlation study resulted in $\rho = 0.42$ and $P < 0.001$. This is consistent with the absence of a strong correlation between the corresponding spectral indices.

Correlation with Transition Energy

We identify the transition energy as the photon energy at which the dominance of the synchrotron or IC flux switches. This is obtained by fitting the optical/UV and the X-ray spectra with broken power-law and double power-law functions (Section 3.3.1). Consistently, we obtained two estimates of the transition energy, ϵ_b and ϵ_v, and studied the correlation of these quantities with the spectral indices and fluxes. Since the transition energy is very sensitive to the indices, even a minor change in the latter can vary the result considerably. We find both ϵ_b and ϵ_v are well correlated with the optical/UV flux though, the correlation is much stronger in the case of ϵ_v. The correlation results are $\rho = 0.73$ with $P < 0.001$ for ϵ_b and $\rho = 0.91$ with $P < 0.001$ for ϵ_v. We find no significant correlation of the transition energy with the optical/UV index and the correlation results are $\rho = -0.33$ with $P < 0.001$ in the case of ϵ_b and $\Gamma_{\rm o/uv}$ while $\rho = -0.39$ with $P < 0.001$ for ϵ_v and $\Gamma_{\rm syn}$.

The correlation results, in the case of transition energy with X-ray spectrum were contrary to that of optical/UV. We found that the transition energy is anti-correlated with the X-ray spectral index with $\rho = -0.72$ and $P < 0.001$ in the case of ϵ_v and $\Gamma_{\rm com}$. However, this correlation is found to be weak in the case of ϵ_b and Γ_x where we obtained $\rho = -0.14$ and $P = 0.07$. This is consistent with the variation observed between Γ_x and $\Gamma_{\rm com}$ (figure 3.2(c)). No significant correlation was observed between the

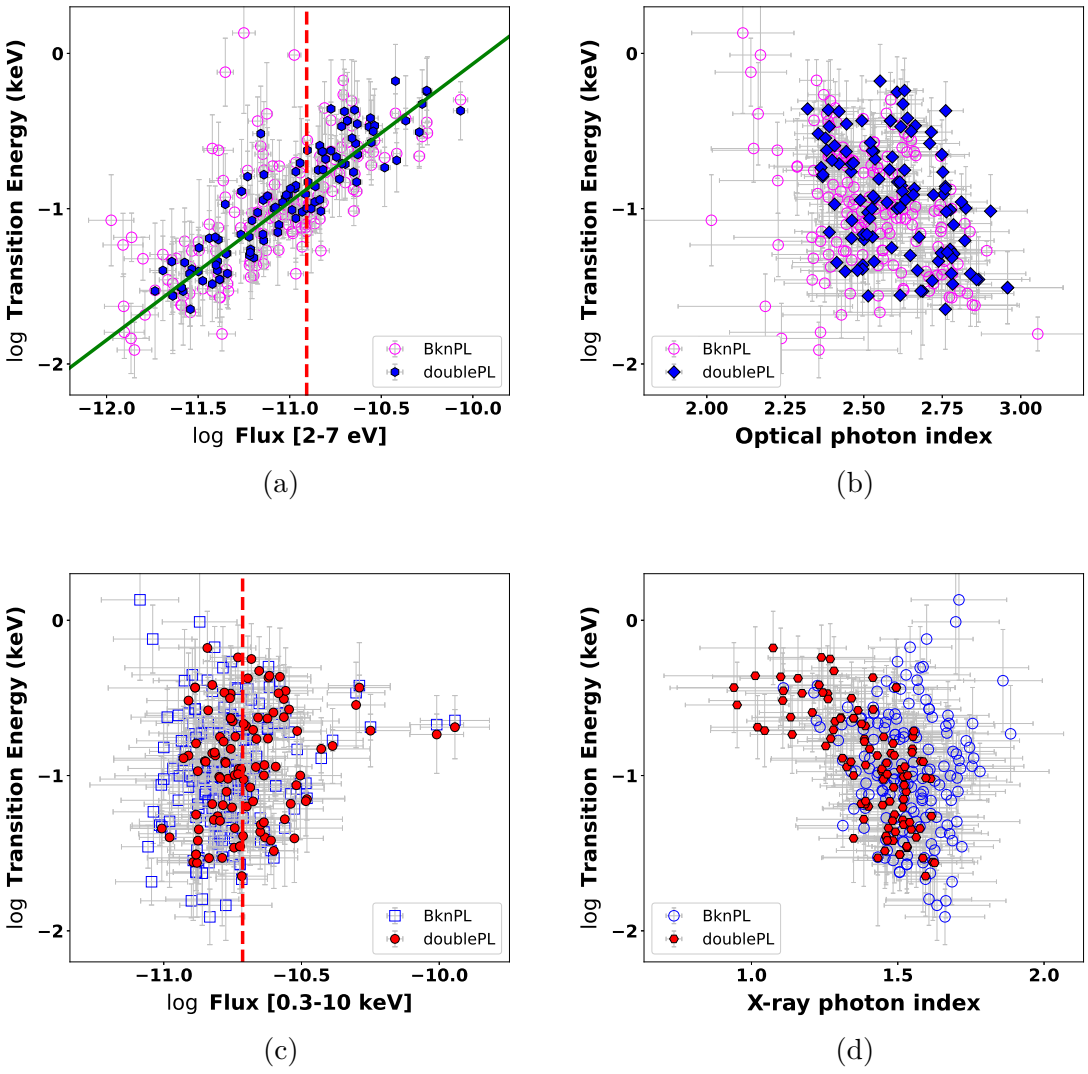

Figure 3.6: Scatter plots between transition energy and other parameters. (a) The variation of transition energy (ϵ_b/ϵ_v) with optical/UV flux (b) Transition energy (ϵ_b/ϵ_v) and $\Gamma_{\rm o/uv}/\Gamma_{\rm syn}$ (c) The variation of transition energy (ϵ_b/ϵ_v) with X-ray flux. (d) Transition energy (ϵ_b/ϵ_v) and $\Gamma_x/\Gamma_{\rm com}$. In all the plots, hollow shapes represent the parameters obtained from broken power-law (BknPL) and filled one show that from double power-law (doublePL).

transition energy and the X-ray flux. The correlation results are $\rho = 0.15$ with $P = 0.04$ in the case of ϵ_b while, $\rho = 0.20$ with $P = 0.03$ for ϵ_v with X-ray flux. The scatter plot between the transition energy and the flux/index is shown in Figure 3.6 with the vertical dashed lines in (a) and (c) denoting the average optical/UV and X-ray fluxes.

To understand the variability behaviour of the source depicted by these correlation studies with the transition energy, we performed a linear regression analysis between the quantities which showed a strong correlation. We were able to obtain an acceptable linear fit in the case of ϵ_v and $F_{2-7\mathrm{eV}}$ and the linear regression line obtained is given by

$$\log(\epsilon_v) \;=\; (0.89 \pm 0.04)\; \log(F_{\mathrm{o/uv}}) \;+\; (8.82 \pm 0.44) \tag{3.6}$$

with Q-value of 0.99. The near-linear dependence of the transition energy with the optical/UV flux supports that the flux variability at this energy band is mainly governed by the changes in the normalization. This inference is further asserted by the absence of any correlation between the transition energy and the optical/UV spectral index. The anti-correlation between the transition energy and the X-ray spectral index is consistent with the "harder when brighter" trend observed in the X-ray flux-index correlation. The lack of any appreciable correlation between the transition energy and the X-ray flux also supports the idea that the flux variations are mainly governed by the index changes in this band. If the broken power-law electron distribution responsible for the broadband emission is given by

$$N(E)\,dE = \begin{cases} K\,E^{-p_1}dE & \text{for } E \le E_b \\ K\,E_b^{p_2-p_1}E^{-p_2}dE & \text{for } E \ge E_b \end{cases}, \quad cm^{-3} \tag{3.7}$$

then extending our correlation/regression studies to the emitting electron

distribution, one can conclude that: *at low energy ($E < E_b$) the variations are mainly governed by the changes in index p_1, whereas at high energy ($E > E_b$) the variations can be due to the change in E_b.* Since the X-ray spectrum is governed by the low energy electrons, the changes in p_1 are consistent with the "harder when brighter" trend observed in the flux-index correlation and the anti-correlation observed between the transition energy and X-ray spectral index. Similarly, the transition energy-flux correlation observed for the optical/UV band is consistent with the change in normalization initiated by the variations in E_b. The change in E_b may also be consistent with the variation in γ-ray peak suggested by the range of Γ_γ. These results disfavour the radiative cooling interpretation of E_b and probably the broken power-law electron distribution may be an outcome of the acceleration process itself (Aharonian et al., 2003; Sahayanathan, 2008; Rieger et al., 2007). The details of all Spearman rank correlation studies discussed in this Section are also furnished in Table 3.6.

3.4 Broadband SED Analysis

The multi-wavelength correlation analysis between different spectral quantities (Section 3.3.2) suggests the optical/UV emission fall on the high energy end of the synchrotron SED. The X-ray and γ-ray energy bands fall on the Compton SED and the linear regression analysis suggests different emission processes to be active at these energies. Further, the γ-ray energy band falls around the peak of the Compton spectral component. To validate these findings, we performed a detailed spectral modelling of the simultaneous observation of the source using synchrotron, SSC and EC processes. For this, we selected two epochs with simultaneous observation by Swift, NuSTAR, and Fermi telescopes. Figure 3.7 shows the observed

Table 3.6: The details of correlation results found between different source parameters/quantities.

Parameters/quantities	ρ	P
$\Gamma_{\rm o/uv}$ and Flux [2-7 (eV)]	0.13	0.06
Γ_x and Flux [0.3-10 (keV)]	-0.64	< 0.001
Γ_γ and Flux [0.157-300 (GeV)]	-0.09	0.28
$\Gamma_{\rm o/uv}$ and Γ_x	-0.23	0.002
$\Gamma_{\rm o/uv}$ and Γ_γ	-0.03	0.68
Γ_x and Γ_γ	0.07	0.38
Flux [2-7 (eV)] and Flux [0.3-10 (keV)]	0.42	< 0.001
Flux [2-7 (eV)] and Flux [0.157-300 (GeV)]	0.60	< 0.001
Flux [0.3-10 (keV)] and Flux [0.157-300 (GeV)]	0.72	< 0.001
ϵ_b and Flux [2-7 (eV)]	0.73	< 0.001
ϵ_b and Flux [0.3-10 (keV)]	0.15	0.04
ϵ_b and $\Gamma_{\rm o/uv}$	-0.33	< 0.001
ϵ_b and Γ_x	-0.14	0.07
ϵ_v and Flux [2-7 (eV)]	0.91	< 0.001
ϵ_v and Flux [0.3-10 (keV)]	0.20	0.03
ϵ_v and $\Gamma_{\rm syn}$	-0.39	< 0.001
ϵ_v and $\Gamma_{\rm com}$	-0.72	< 0.001
$\Gamma_{\rm syn}$ and $\Gamma_{\rm com}$	0.52	< 0.001
$\Gamma_{\rm o/uv}$ and Γ_x (x-ray flux > average flux)	0.09	0.50
$\Gamma_{\rm o/uv}$ and Γ_x (x-ray flux > average flux)	-0.38	< 0.001
$\Gamma_{\rm syn}$ and $\Gamma_{\rm com}$ (x-ray flux > average flux)	0.62	< 0.001
$\Gamma_{\rm syn}$ and $\Gamma_{\rm com}$ (x-ray flux > average flux)	0.27	0.12
$\Gamma_{\rm o/uv}$ and Γ_γ (γ-ray flux > average flux)	0.40	0.06
$\Gamma_{\rm o/uv}$ and Γ_γ (γ-ray flux > average flux)	0.07	0.38
Γ_x and Γ_γ (γ-ray flux > average flux)	0.06	0.51
Γ_x and Γ_γ (γ-ray flux > average flux)	0.10	0.31

multi-wavelength SEDs along with the fitted models.

To model the SED, we considered a one-zone leptonic model by Sahayanathan et al. (2018) as described in Section 1.3.6 of chapter 1. The numerical model capable of producing flux for synchrotron, SSC, and EC spectra from the source parameters, was added as a local model in XSPEC and used to fit the broadband SED corresponding to the selected two epochs (56642–56649 MJD and 56649–56660 MJD). To reduce the number of free parameters, we assumed equipartition between the magnetic field and the electron energy densities (Burbidge, 1959; Kembhavi & Narlikar, 1999). The proton population, responsible for providing the bulk jet power, is assumed to be cold in the reference frame of the emission region and hence was not included in deriving the equipartition condition. The limited information available at optical/UV, X-ray and γ-ray energies does not let us to constrain all the parameters and hence the fit was performed only on four parameters namely, p, q, Γ and B. The rest of the parameters are frozen at their typical values or at a value that provides better fit statistics (χ^2). The values chosen for the frozen parameters are $\theta = 2\,\mathrm{deg}$. $\gamma_{\mathrm{min}} = 40$, $\gamma_{\mathrm{max}} = 10^7$, and $R \sim 10^{16}$ cm. The temperature of the external photon field is frozen either at 1000 K (EC-IR) or 42000 K (EC-BLR) depending upon the fit statistics. The parameter γ_b can be constrained with the knowledge of the photon frequencies at which synchrotron and SSC spectral component peaks (Sahayanathan et al., 2018).

$$\gamma_b = \sqrt{\frac{\nu_{\mathrm{ssc,peak}}}{\nu_{\mathrm{syn,peak}}}} \tag{3.8}$$

However, the available information at optical/UV and X-ray energies does not let us to obtain these peak frequencies. Nevertheless, since $\Gamma_{\mathrm{o/uv}} > 2$ and $\Gamma_x < 2$, this suggests that $\nu_{\mathrm{syn,peak}} < 2$ eV and $\nu_{\mathrm{ssc,peak}} > 79$ keV

corresponding to the minimum photon energy of optical observation and maximum photon energy of X-ray observation. A constraint on γ_b can then be obtained as $\gamma_b > 200$. The initial spectral fit was performed keeping γ_b as a free parameter with the above constraint satisfied. We find that the choice of γ_b as 750 for the epoch 56642–56649 MJD and 400 for the epoch 56649–56660 MJD provide better fit statistics. The fit is repeated with γ_b frozen at these values and the results are given in Table 4.6.

The γ-ray spectrum corresponding to the epoch 56642–56649 MJD is hard and this demanded the EC peak to fall at high energies to obtain a better fit. Consistently, we found EC-BLR provides a better fit to the SED with $\chi^2_{\rm red} = 1.58$ as compared to EC-IR ($\chi^2_{\rm red} > 10$). On the contrary, the γ-ray spectrum corresponding to the epoch 56649–56660 MJD is relatively soft and the EC peak frequency falls at lower energies. Through the SED fitting, we also noted that EC-IR interpretation of the γ-ray spectrum provides a better fit statistic ($\chi^2_{\rm red} = 1.5$) than EC-BLR ($\chi^2_{\rm red} > 10$) for this epoch. It can be argued that with a proper choice of γ_b, the γ-ray spectrum during these epochs can be explained under a single emission process (EC-IR or EC-BLR). However, this was not favoured by our initial fit to the SED when γ_b set as a free parameter. We found better fit statistics when γ_b is approximately equal to the values quoted in Table 4.6 along with mentioned target photon fields. Hence, the SED fitting for these two epochs indicates a significant variation in the target photon field (IR from the dusty environment and the Ly-α emission from BLR) and this suggests during different flaring epochs, the emission region can be located at different distances from the central black hole (Ghisellini & Tavecchio, 2009a). Interestingly, this analysis implies that the variation in the EC spectral peak of 3C 279 is associated with the change in the frequency of external photon field. To be consistent with our inference obtained from

the correlation study (Section 3.3.2), where the variation in Compton SED peak is attributed to the changes in γ_b, we interpret that the variations in Compton peak may be associated with the change in γ_b and/or the external photon field. The best-fit parameter values presented in Table 4.6 may vary moderately, if we relax the assumption of equipartition condition which banks upon the minimum total energy criterion of the source (Burbidge, 1959; Kembhavi & Narlikar, 1999). However, the imposed constraint on the equipartition does not affect our conclusion on the variation in the target photon field for the EC process. The reason for this being, the equipartition condition constrains the particle and magnetic field energy densities; whereas, the EC spectral component depends upon the particle distribution and the external photon field with no direct dependence on the jet magnetic field (Shah et al., 2017).

Table 3.7: Best fit values of the source parameters from the broadband SED fitting.

Name of parameter	Symbol	56642-56649	56649-56660
Particle index at low energy	p	1.96±0.13	1.00±0.27
Particle index at high energy	q	4.69±0.11	4.10±0.10
Bulk Lorentz factor	Γ	14.05±0.80	17.6±1.5
Magnetic Field (G)	B	1.60±0.04	1.52±0.03
Break Lorentz factor	γ_b	750	400
External photon energy density (erg cm^{-}3)	$U_{\rm target}$	7.06×10^{-3}	2.3×10^{-3}
Total jet power (erg s^{-1})	$P_{\rm jet}$	4.47×10^{45}	4.72×10^{45}
Total radiated power (erg s^{-1})	$P_{\rm rad}$	1.40×10^{43}	1.30×10^{43}
Doppler Factor	δ_D	21.6	25.5
	χ^2/Dof	27/17	24/16

3.5 Summary

We performed a detailed longterm spectral analysis of the FSRQ 3C 279 using simultaneous broadband observations of Swift-XRT, UVOT, and Fermi-LAT observations. The spectra at these energy bands can be individually fitted by a power-law and we found a clear "harder when brighter" trend at X-ray energy; however, no such behavior was witnessed in optical/UV and γ-ray energies. We also estimated the transition photon energy at which the dominance of the synchrotron and the inverse Compton spectral component switches. The transition energy is well correlated with the optical/UV flux and the X-ray spectral index but not with the other spectral parameters. This correlation study suggests that at X-ray energies the flux enhancement is mainly dominated by the variations in the spectral index while at optical/UV energies the flux variations are majorly caused by the changes in normalization. We also find a moderate correlation between the optical/UV and X-ray spectral indices; however, the linear regression analysis disfavoured the radiative loss origin of the broken power-law electron distribution responsible for the broadband emission. These study results let us conclude that multiple acceleration process may be responsible for the broken power-law electron distribution and the long term spectral variations are predominantly associated with the power-law index changes at lower energy ($E < E_b$) and the variation in break energy at higher energy ($E > E_b$). This is also consistent with the range of γ-ray spectral indices.

The broadband SED of the source was performed considering synchrotron, SSC, and EC processes for the two epochs with simultaneous observations by Swift, NuSTAR, and Fermi telescopes. Among the two selected epochs, the one with hard γ-ray spectrum (56642-56649 MJD)

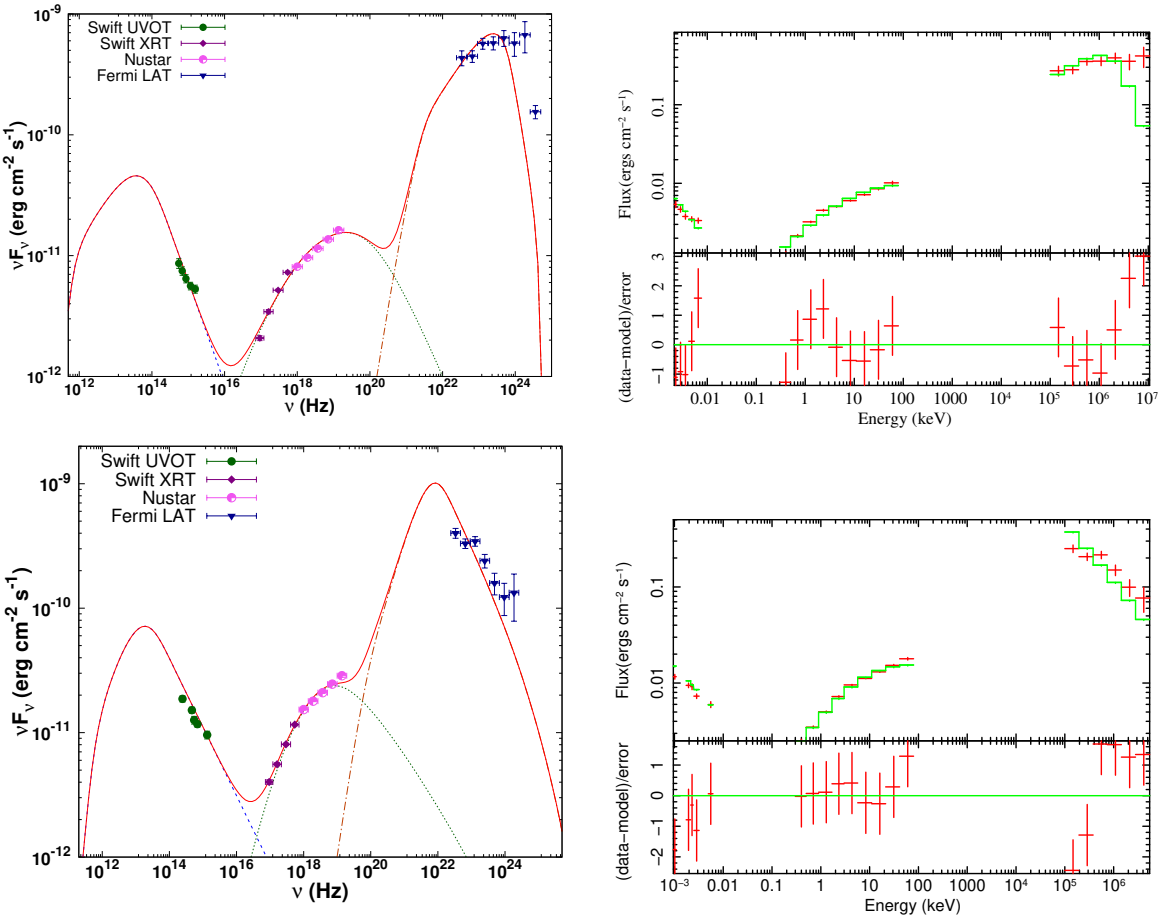

Figure 3.7: Figure showing the broadband SED fitting of 3C 279 during the time intervals 56642-56649 (top) and 56649-56660 (bottom). **Left**: Dashed curve represents the synchrotron, dotted curve shows SSC, and dashed dotted curve represents the EC-BLR/EC-IR components respectively. The solid curve shows the total best-fit model. **Right**: The plots of unfolded spectrum with residuals generated from XSPEC.

indicates EC-BLR origin for the γ-ray emission and the epoch with soft γ-ray spectrum (56649-56660 MJD) supports EC-IR emission process. Interestingly, these SED fits suggest that the variations in γ-ray peak may be associated with the change in target photon frequency. Combining this result with the conclusions drawn from the correlation study, we find that the variation in the peak of the γ-ray spectral component can be associated

with the changes in the break energy of the electron distribution and/or the temperature of the target photon field involved in the EC process.

Chapter 4

Gamma-ray variability and multi-wavelength insights into the unprecedented outburst from 4C 31.03

4.1 Introduction

Fermi-LAT is a γ-ray space telescope, that observes the cosmos in the energy range 20 MeV to 1 TeV. Recently, in January 2023, *Fermi*-LAT reported an enhancement in the γ-ray activity from the source 4C 31.03, consistent with the coordinates RA=18.2227 and DEC=32.1399 (Ciprini & Garrappa, 2023). 4C 31.03 is recognized as a flat spectrum radio quasar (FSRQ) with redshift z=0.603, (Wills & Wills, 1976) and is included in the *Fermi* 4FGL point source catalog with the identifier J0112.8+3208 (Abdollahi et al., 2020). This source is also historically known with other names such as, B2 0110+31, OC 317, and NRAO 62. Further, it is considered as a possible candidate for the study of neutrino emission from Blazars (Chang et al., 2022). This recent high γ-ray outburst

marks the first instance of such an extraordinary activity since its discovery. The daily average gamma-ray flux reported ($\sim 4 \times 10^{-6}$ phs cm^{-2} s^{-1}) is 60 times greater than the average value quoted in the 4FGL catalog. Contemporarily, the IceCube Collaboration conducted a search for possible muon neutrino events from the source and obtained an upper limit on the neutrino flux, with a 90% confidence level (Hori & IceCube Collaboration, 2023). After this flaring event, the source reverted back to its quiescent flux level within a few days. The source again underwent a major transition to the phase of high activity during June 2023 with a maximum flux of 4.9×10^{-6} phs cm^{-2} s^{-1} (Cutini, 2023). The variability aspects of this source has not been thoroughly studied before, despite continuous monitoring by *Fermi*-LAT since 2009.

The underlying mechanism for the high-energy (HE) emission and the location of the main emission region from the central blackhole still remain as open questions (Joshi et al., 2013). Identification of the target photon field for the EC process can provide hints about the location of the emission region in FSRQs (Joshi et al., 2013; Dermer et al., 2009). The knowledge of the shortest variability time (τ) has been often used to constrain the emission region size and its location in blazar jets. The light crossing time suggests the emission region size, R, is less than $c\,\delta\,\tau/(1+z)$, where, δ is the relativistic Doppler factor. If the emission arises from a homogeneous region, then $R > r_g$, where $r_g \sim \frac{GM}{c^2}$, is the Schwarzchild radius of the central blackhole. If ψ is the semi aperture angle of the conical jet, then the location of emission region from the central black hole would be $r \sim R/\psi$. The availability of continuous observations from *Fermi*-LAT presents a surfeit of data to search for the shortest time variability events. The minute scale variability suggests a compact emission region situated at sub-parsec scales within the broad line region (Dermer & Schlickeiser,

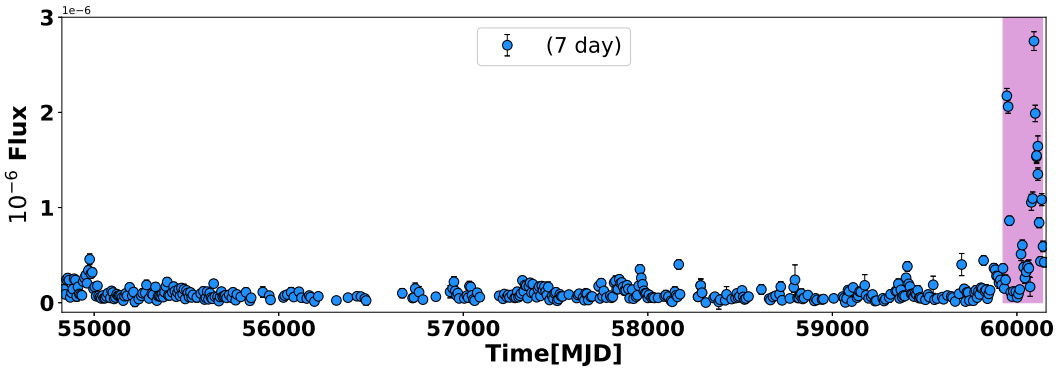

Figure 4.1: 7 day binned lightcurve of 4C 31.03 generated using *Fermi*-LAT observations from 54832 to 60152 MJD. The shaded time period represents the observed recent high activity epoch. The γ-ray fluxes are in the units of phs cm^{-2} s^{-1}.

1994b; Blandford & Levinson, 1995). Conversely, for the γ-rays to escape from the pair production losses with the ambient photon field (BLR), the emission region should be sufficiently far from the central engine (Dondi & Ghisellini, 1995b).

Modelling the lightcurve variability patterns as well as the spectral energy distribution (SED) are powerful tools for deciphering the underlying particle distribution and the physical processes responsible for the broadband emission. The multi-wavelength SED of 4C 31.03 during the quiescent phase has been previously modeled under hadronic scenario using proton synchrotron emission (Liodakis & Petropoulou, 2020). Due to the decade long quiescent phase, this source has been sparsely studied. In this chapter, a comprehensive study on the major γ-ray outbursts of 4C 31.03 using its variability patterns and multi-wavelength observations are presented. As mentioned before, up to authors' knowledge, this is the first study reporting the variability and multi-wavelength aspects of 4C 31.03.

4.2 Multiwavelength Observations and Data Reduction

4.2.1 γ-ray Observations

The *Fermi*-LAT observation in the energy range 0.1-500 GeV spanning the time interval 2009 - 2023 (MJD 54830-60160) was used in this work to study the γ-ray emission of 4C 31.03. A 10 degree circular region centered at RA=18.2227 and DEC=32.1399 was selected as the ROI for this analysis. We used the software package *Fermitools* version 2.2.0 for data reduction and analysis. The photon events were filtered and extracted the good time intervals (GTI) following standard criteria mentioned in the FSSC page[1]. The livetime cube and exposure map were generated using *'gtltcube' and 'gtexpmap'* tools. A circular region of radius 25 degree centered at the target was selected as the source region and exposure map was generated for the same. We optimized the ROI of all the sources of interest with models from the 4FGL catalog. An initial sky model for all the sources of interest was obtained after performing a binned likelihood analysis over the total observation. The parameters of the sources within the ROI were kept free while that of the other sources were frozen to their catalog values. We have also applied a selection, based on the value of test statistics, TS, such that the parameters of all sources for which TS (in the entire time interval) < 9 were kept fixed. The sky model thus acquired was used in the preparation of lightcurves and the γ-ray SEDs. We generated a 7 day binned global light curve of 4C 31.03 for the entire observation. The γ-ray lightcurves during the recent active phase were obtained with two time bin sizes, 0.5 and 1 day. We adopted the unbinned likelihood analysis for obtaining the light curves. The PowerLaw2 function was chosen to model

[1] `https://fermi.gsfc.nasa.gov/ssc/data/analysis`

the γ-ray spectrum of 4C 31.03 while generating the lightcurves. In order to obtain the fit convergence in each time bin, we made an iterative procedure: initially, the 'DRMNFB' optimizer was applied to fit in the individual time bins and whenever this fit failed to converge, we deleted all the sources with TS$<$ 5. In the final step, we performed the fit within all time bins after setting 'Newminuit' as the optimizer. We rejected those time bins that failed to converge in the final step.

4.2.2 Swift Observations

The Swift telescope also monitored the outburst of 4C 31.03 in the X-ray and optical/UV bands. To study the X-ray spectrum, we obtained the ready-to-use Swift-XRT spectra from the automated online tool Swift-XRT data products' generator (Evans et al., 2009). This tool automatically selects the source and background regions based on count rate and also performs the corrections for pile up and bad pixels. All the spectra were rebinned to 20 minimum counts in each energy bin using ftool 'grppha'. Then the spectra were loaded and fitted in the X-ray fitting platform XSPEC (Arnaud, 1996). The unabsorbed fluxes in the selected energy bins were estimated after setting the value of hydrogen column density to $n_H = 7.8 \times 10^{20}\, cm^{-2}$ (Kalberla et al., 2005). We also obtained the values of the photon indices and the unabsorbed integrated fluxes in the energy range 0.3-10 keV for each observation.

The UVOT observations were downloaded from the archive and reduced following standard procedures[2]. The images in all the available filters were summed over the extensions using the tool *uvotimsum*. A circular region of radius 6 arcsec was used to extract the source counts, while a 20 arcsec radius circle in the source free region was used for background

[2]`https://swift.gsfc.nasa.gov/analysis/threads`

estimation. For all observations, we also produced spectral products using the tool *uvot2pha* and these were fitted in XSPEC to estimate the total integrated flux in the energy range 2-7 eV. All the fluxes in each filter as well as the integrated fluxes were corrected for galactic absorption by fixing E(B-V)= 0.0503 for R_v=3.1 (Schlafly & Finkbeiner, 2011b). The results of the data reduction and analysis of Swift observations are presented in Table 4.1.

Table 4.1: The summary of the analysis performed for the Swift XRT and UVOT observations.

Swift-XRT						
state	Flux (ergs cm^{-2} s^{-1})	Photon Index (Γ/α)	Curvature (β)	χ^2/Dof		
Flare1	$(3.6 \pm 0.3) \times 10^{-11}$	2.8 ± 0.2	-0.6 ± 0.1	58.5/80		
Flare2	$(1.5 \pm 0.1) \times 10^{-11}$	1.40 ± 0.07	-	45.7/49		
Quiescent	$(5.6 \pm 0.4) \times 10^{-12}$	1.50 ± 0.1	-	42/35		
Swift-UVOT (Fluxes in phs cm^{-2} s^{-1})						
	V	B	U	UVW1	UVM2	UVW2
Flare1	3.8 ± 0.3	4.8 ± 0.3	3.7 ± 0.3	3.0 ± 0.2	2.1 ± 0.1	2.6 ± 0.2
Flare2	3.00 ± 0.07	3.70 ± 0.06	2.60 ± 0.05	1.96 ± 0.04	1.30 ± 0.03	1.50 ± 0.02
Quiescent	0.37 ± 0.01	0.43 ± 0.01	0.29 ± 0.01	0.23 ± 0.01	0.18 ± 0.01	0.20 ± 0.01

Table 4.2: The duration and peak time of the flares identified.

Flare	T_{start} MJD	T_{peak} MJD	T_{stop} MJD
1	59945.0	59948.0	59952.0
2	59953.0	59955.5	59960.0
3	60031.0	60032.0	60033.0
4	60071.0	60095.0	60123.0
5	60131.5	60134.7	60138.0

4.3 RESULTS AND DISCUSSION

4.3.1 γ-ray temporal analysis of 4C 31.03

In Figure 4.1, we show the 7-day binned γ-ray lightcurve obtained for the time duration 54832-60152 MJD. It is evident from the figure that the source 4C 31.03 has shown such pronounced activity (shaded region) for the first time since it's discovery. In this work, we imposed two conditions on all the lightcurves studied, which are : a) In each time bin, test statistics, TS$\geq$ 4 and b) uncertainty in flux, $\Delta F \leq 0.5\,F$. There are two reported instances during which the flux exhibited an extraordinary increase (Ciprini & Garrappa, 2023; Cutini, 2023). In order to achieve better resolution in time and to differentiate the rise and decay substructures in this unprecedented high activity period, we obtained 1 and 0.5 day binned lightcurves during the shaded region in Figure 4.1. The highest flux obtained is 4.8×10^{-6} phs cm^{-2} s^{-1} for one day binned and 6.9×10^{-6} phs cm^{-2} s^{-1} for 12 hour binned lightcurve. To have a systematic identification of the duration of flares, we employed an algorithm utilizing Bayesian blocks (Meyer et al., 2019; Wagner et al., 2022). This algorithm starts by identifying a block with higher flux than its preceding and succeeding blocks. It then proceeds in both directions from the peak, as long as sequentially lower blocks are found. The start/end of a flare is set by the flux exceeding/falling under

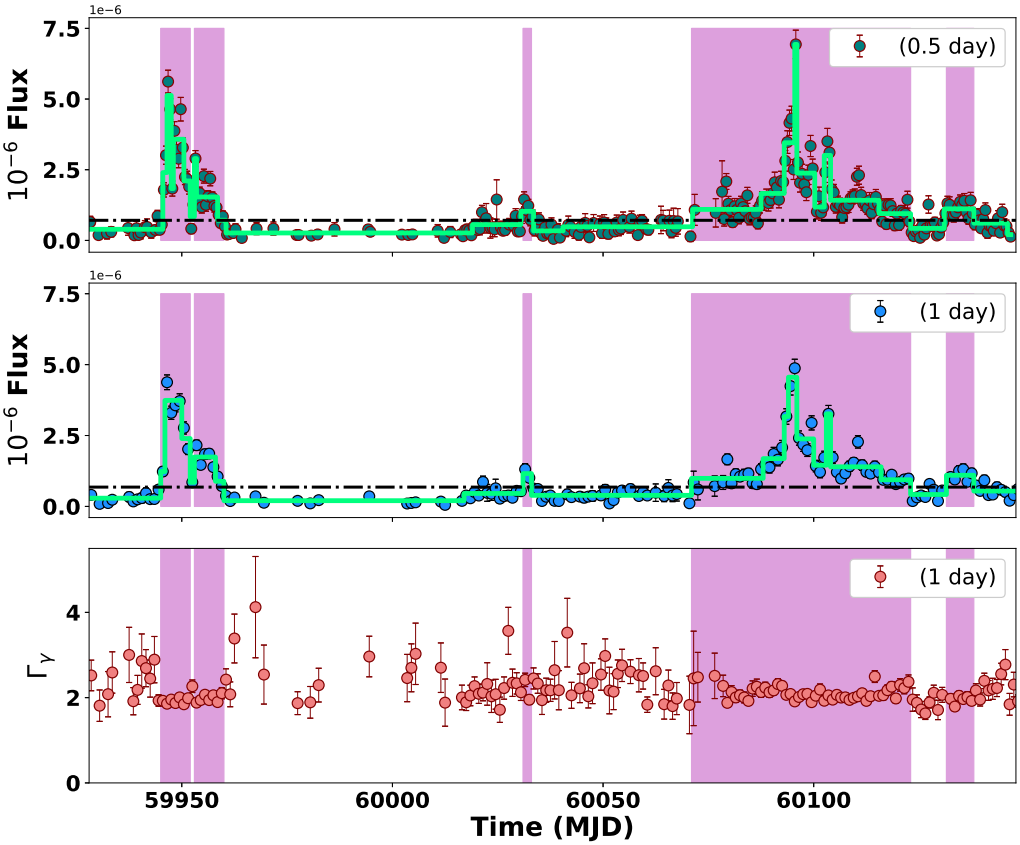

Figure 4.2: γ-ray lightcurve of 4C 31.03 spanning the time 59940-60152 MJD. Panels 1 & 2: 0.5 and 1 day binned lightcurves. Fluxes are in units of phs cm^2 s^{-1}. The solid line indicates the Bayesian blocks obtained while horizontal dashed line represents the average flux level. Bottom panel: photon index obtained from 1 day binned lightcurve. The shaded time periods represent the duration of flares as characterized from the HOP analysis.

a predefined flux level (average flux). This approach is referred to as the "HOP algorithm," and was first introduced by Eisenstein & Hut (1998). We identified five epochs of flaring in the 12 hour and 1 day binned lightcurves shown as the shaded regions in Figure 4.2. The top 2 panels display the 0.5 and 1 day binned lightcurves along with the Bayesian blocks respectively. In the bottom panel, we plotted the γ-ray photon index, Γ_γ, obtained from the 1 day binned lightcurve. It is apparent from the figure that

γ-ray spectrum shows a clear hardness during the flares. Out of all the identified flares, 3 time intervals (flares 1,2, and 4) corresponding to MJD 59945-59952, 59953-59960, and 60071-60123, show prominent activity. The other 2 epochs exhibit less significant activity, especially flare 3. The time periods corresponding to the beginning and the decay of flares as well as the period of maximum flux, are tabulated in Table 4.2. The Bayesian blocks and the HOP groups in this analysis were obtained using an open source python module provided by Wagner et al. (2022). Furthermore, the variation of Γ_γ around 2, during the flares hints that the external Compton peak falls in the *Fermi* energy range ($>$ 100 MeV).

Searching for the fastest γ-ray variability

To investigate the fastest flux doubling or halving time during the flares, we scanned the 0.5 day binned lightcurve using the equation:

$$F(t) = F(t_0)\, 2^{-(t-t_0)/\tau} \tag{4.1}$$

where $F(t)$ and $F(t_0)$ are the fluxes at consecutive times t and t_0 respectively and τ is the characteristic time scale. We further imposed a minimum 3σ significance level for the difference in flux at consecutive times (Foschini et al., 2013) for this analysis. The values of τ corresponding to the times at which the above condition has been satisfied are shown in Table 4.3. Our analysis shows variability time scales ranging from 5 to 18 hours, with the fastest flux decay between MJD 59951-59952 in a time scale of 5.5 ± 0.7 hours. Following the light travel arguments discussed in §5.1, the size of the emission region, R for a τ in the order of hours, will be roughly in the range $10^{15} - 10^{16}$ cm (Ghisellini & Tavecchio, 2009b; Dermer et al., 2009). An observed hour scale flux variability time usually indicates further shorter

cooling time scale for the emitting particle distribution. And it is worth mentioning that a cooling time scale lesser than one hour supports the BLR while more than 10 hour suggests the molecular torus as the location of γ-ray emission in blazars (Foschini et al., 2011).

Table 4.3: The summary of the short term variability analysis. t_0 and t_1 are the times in MJD; $F(t_0)$ and $F(t_1)$ are the fluxes in units of $\times 10^{-6}$) phs cm^{-2} s^{-1}; significance of difference in flux in σ; variability time scale τ; uncertainty in τ; nature of the flux variations, rise or decay.

t_0	t_1	$F(t_0)$	$F(t_1)$	Significance	τ (hour)	$\Delta\tau$ (hour)	R/D
59945.25	59945.75	0.6 ± 0.2	1.8 ± 0.3	3.8	7.2	1	R
59945.75	59946.25	1.8 ± 0.2	3 ± 0.3	3.0	16	0.6	R
59946.25	59946.75	3 ± 0.3	5.6 ± 0.4	5.1	13	0.5	R
59947.25	59947.75	4.6 ± 0.4	1.8 ± 0.3	6.1	9	0.6	D
59947.75	59948.25	1.8 ± 0.3	3.9 ± 0.3	4.9	11	0.6	R
59949.25	59949.75	2.9 ± 0.3	4.6 ± 0.4	3.3	17.6	0.5	R
59951.75	59952.25	1.9 ± 0.2	0.41 ± 0.08	4.7	5.5	0.7	D
59952.75	59953.25	1.3 ± 0.2	3 ± 0.3	4.5	10	0.7	R
59953.25	59953.75	2.9 ± 0.3	1.4 ± 0.2	4.3	11	0.7	D
59954.75	59955.25	1.2 ± 0.2	2.3 ± 0.2	3.4	13	0.7	R
59955.25	59955.75	2.3 ± 0.2	1.3 ± 0.2	3.0	14	0.8	D
60078.75	60079.25	0.8 ± 0.2	2.1 ± 0.3	3.6	8.2	1	R
60094.75	60095.25	4.3 ± 0.4	2.5 ± 0.3	3.2	15.4	0.6	D
60095.25	60095.75	2.5 ± 0.3	7 ± 0.5	7.2	8.2	0.6	R
60095.75	60096.25	7 ± 0.50	2.8 ± 0.4	6.7	9	0.5	D
60099.75	60100.75	2.5 ± 0.3	1.0 ± 0.2	3.7	18	2	D

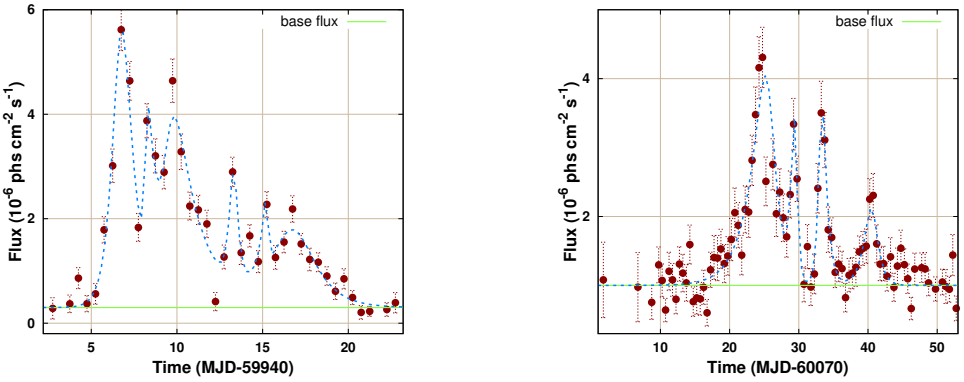

Figure 4.3: Plots showing the temporal profile fitting of the 3 prominent flares observed. The dashed curve represent the total best fit model and solid line is the base flux level chosen. Flare 1 and 2 fitted together (left). Flare 4 is plotted in the right panel.

Additionally, we performed a χ^2 minimization fitting of the subflares using exponential profiles represented by

$$F(t) = 2F_0 \left[\exp\left(\frac{t_0 - t}{T_r}\right) + \exp\left(\frac{t - t_0}{T_d}\right) \right]^{-1} \tag{4.2}$$

where T_r and T_d are the rise and decay times of subflares, respectively, and F_0 is the approximated amplitude of each subflare, measured at time t_0. We considered the epochs 59945-59960 and 60071-60123 including the three prominent flares 1, 2 and 4 as given in Table 4.2. All the fluxes were estimated above a constant base flux in the analysis. The plots of the lightcurve with the total best fit function are shown in Figure 4.3. In the analysis, flare 1 and 2 were fitted together since there is no much time gap between the flares compared to the lightcurve binning time (0.5 day). Certain sub-flares within the flare 1 and 2 contain only three data points and cannot be fitted with the equation 4.2. Hence the parameters of these subflares (2, 4, and 5) were kept fixed at their optimized values. These fixed parameters are given in Table 4.4 with suffix $*$. For the sub-flares

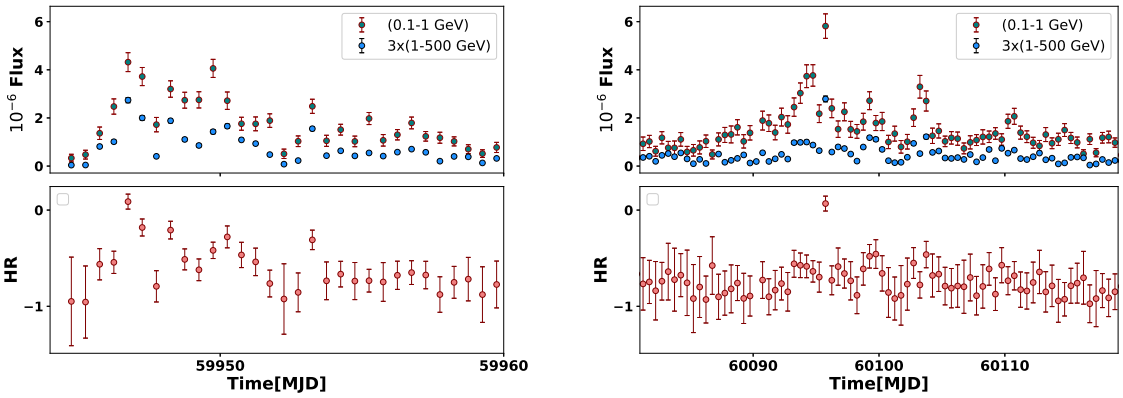

Figure 4.4: The γ-ray ligtcurves with 12 hour binning in the low (0.1-1 GeV) and high-energy (1-500 GeV) ranges are shown in the top panels. The high-energy light curve is scaled ($\times$ 3) to plot together. In the bottom panel, hardness ratio HR is plotted against time. Left) Flare 1 and 2 combined. Right) Flare 4.

with more than three data points we quote the standard errors. We also found the value of asymmetry ζ for each subflare from the expression, $(T_r - T_d)/(T_r + T_d)$. The flares with $\zeta < 0$ are known as fast rise and exponential decay (FRED) flares which are common in γ-ray lightcurves. Such flares support the scenario of an injection time scale faster than the radiative time scale (Meyer et al., 2019). However, in our analysis, very few sub-flares are found with $\zeta < 0$. Moreover, most of the sub-flares are slightly/moderately asymmetric since $|\zeta| < 0.7$ (Abdo et al., 2010a).

High and low-energy γ-ray lightcurves

The good test statistics (TS) for the fluxes during the 3 prominent flares made it possible to split the lightcurve into low-energy (0.1-1 GeV) and high-energy (1-500 GeV) divisions. In Figure 4.4, we show the lightcurves in these energy ranges plotted together (high energy lightcurve is scaled appropriately). In the bottom panel, we plotted the hardness ratio (HR)

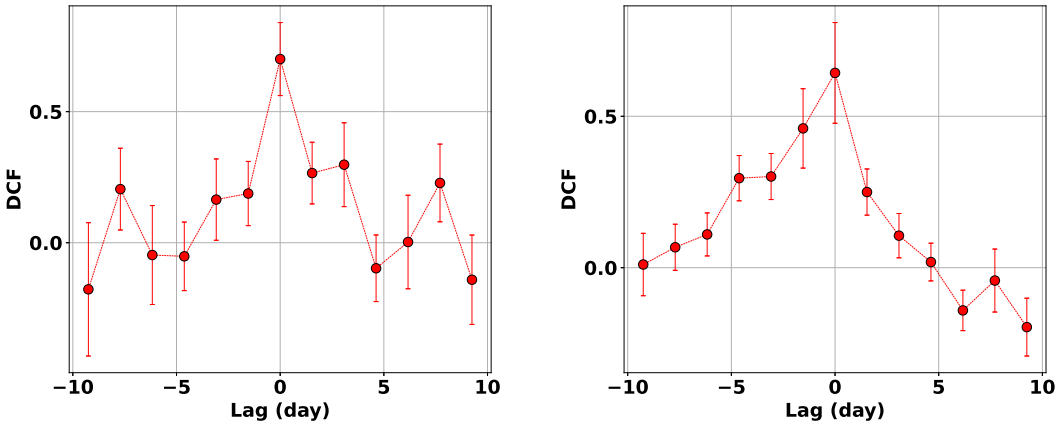

Figure 4.5: Discrete correlation function (DCF) is plotted across the lag in days measured as Time (100-500 GeV) - Time (0.1-100 GeV) lightcurves. Left) flare 1 and 2, Right) flare 4.

Table 4.4: The rise and decay times estimated from equation 4.2 for all the subflares. The peak flux F_0 is in units of ($\times 10^{-6}$) phs cm^{-2} s^{-1}.

t_0 (MJD)	F_0	T_r (day)	T_d (day)	ζ
Flare 1& 2:		$\chi^2_{\rm red}$=1.21	dof=28	
59946.75	5.2 ± 0.4	0.43 ± 0.04	0.59 ± 0.06	0.17
59948.20	2.3*	0.1*	0.5*	−0.7
59949.50	2.9 ± 0.3	0.37 ± 0.08	1.4 ± 0.2	0.59
59953.25	2.1*	0.21*	0.22*	0.02
59955.50	1.0*	0.34*	0.06*	0.7
59956.75	1.5 ± 0.2	1.2 ± 0.3	1.2 ± 0.2	0.001
Flare 4:		$\chi^2_{\rm red}$=1.8	dof=48	
60095.75	3.8 ± 0.3	2.2 ± 0.3	0.91 ± 0.20	-0.42
60099.50	2.2 ± 0.5	0.55 ± 0.20	0.30 ± 0.10	-0.31
60103.25	2.5 ± 0.5	0.40 ± 0.10	0.64 ± 0.10	0.26
60110.50	1.1 ± 0.3	1.0 ± 0.3	0.75 ± 0.30	-0.14

defined by,

$$HR = \frac{f_H - f_L}{f_H + f_L} \tag{4.3}$$

where f_H and f_L are the fluxes in the high and low energy bands respectively. The nature of variations in the low and high energy scenarios seems similar, however, during most of the epochs, the flaring is more intense in the low energy regime. This observation indicates that the recent active phase of 4C 31.03 is primarily caused by the low energy electrons in the particle spectrum. We also explored the time lag between the low and high energy γ-ray lightcurves using the Discrete Correlation Function (DCF) (Edelson & Krolik, 1988). A zero time-lag between these lightcurves is obtained suggesting an energy-independent evolution of the light curves or the underlying electron distribution. However, the cooling timescales of the emitting electron distribution at these photon energies are too short than the light curve binning of 12 hour used for the DCF analysis. For instance, the cooling time scale (equation 4.7 from §4.3.3) corresponding to ~ 0.5 GeV emission is ~ 7.3 hours and in case of ~ 20 GeV it is ~ 1 hour. Hence, the zero time-lag obtained through the DCF analysis indicates its inability to probe the energy-dependence of the electron cooling using 12 hour binned lightcurve.

γ-ray spectral variations

In order to study the γ-ray spectral transitions during the recent activity phase of 4C 31.03, we obtained the corresponding SEDs for the flares 1,2,4, and 5 (Section 4.3.1) using the *likeSED.py* module. The SED for flare 3 cannot be constrained due to low photon statistics. We also extracted the γ-ray SED during the epoch 59960-59975, when the

source is at a quiescent state. This SED is used later to compare the broadband SEDs during different activity states of the source (Section 4.3.3). The SEDs corresponding to these epochs were fitted independently using power-law (PL), log-parabola (LP), broken power-law (BPL), and power-law with an exponential cutoff (PLEC) models. The PL model was able to give an acceptable fit only during the quiescent state. The significance of curvature/break, ($TS_{\rm curv}$) of a spectrum can be estimated as TS (model of curvature/break) - TS (PL). According to this criterion, a spectrum shows significant curvature/break if $TS_{\rm curv} \geq 16$, as it indicates a 4σ level confidence (Prince, 2020b; Prince et al., 2021). The results of this analysis with the $\rm TS_{curv}$ values obtained are given in Table 4.5. The results of $TS_{\rm curv}$ test show that nearly all the flaring γ-ray spectra (flares 1, 2, and 4) exhibit a notable break, as BPL model provided better statistics in these cases. However, in the case of flares 1 and 4, the γ-ray spectra can also be well described by LP and PLEC models in addition to BPL (Table 4.5). In the case of flare 5, the results show that the spectrum can be described equally well by all the models. The plots of the γ-ray SEDs obtained along with the models are shown in Figure 4.6. The γ-ray spectrum becomes harder during the outburst as evident from the change in the value of the spectral index from 2.7 at quiescent state to 1.8 during flares.

The energy corresponding to the break in the spectra is found to be almost stationary and lies around 2 GeV. The GeV spectral break in Fermi bright blazars might be intrinsic in nature and can be attributed to the shape of the underlying particle distribution or the target photon spectrum (Kang et al., 2021; Lefa et al., 2012). The break/curvature in the γ-ray spectrum can also be caused by the pair absorption of GeV photons from the Ly-α line emission of the BLR. This will be the case only when the emission region lies within the BLR (Poutanen & Stern, 2010). However, Costamante

et al. (2018) investigated the external Compton scenario involving BLR photons in a sample of 106 *Fermi* bright FSRQs (including 4C 31.03) and suggested that the γ-ray spectra of such sources do not exhibit significant absorption effects, instead, γ-rays seems to be produced outside the BLR.

Highest photon energy

As mentioned above, the detection of photons with energy greater than 20 GeV is pivotal in the case of FSRQ type sources since the photons of such energy detected can plausibly indicate that the γ-ray production happens beyond the BLR (Liu & Bai, 2006; Costamante et al., 2018). We found the energies of the photons detected during the active state of 4C 31.03 which are positionally consistent with the source co-ordinates using the fermitool *gtsrcprob*. Three epochs were noticed at which photons with energy greater than 50 GeV have been detected from the source with more than 99% association probability. They are 51.3 GeV at 59946.76 MJD, 82.6 GeV at 59947.15 MJD, and 65.5 GeV at 60107.24 MJD.

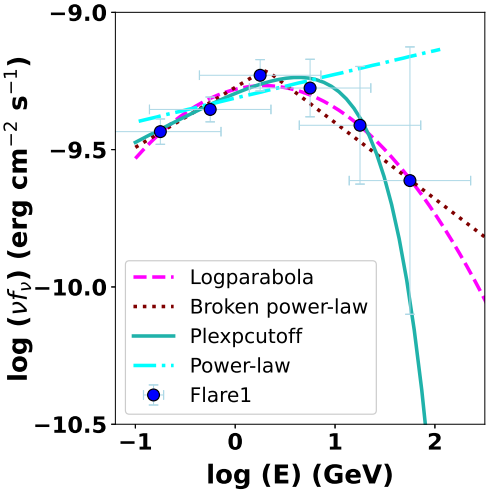

(a) Flare 1

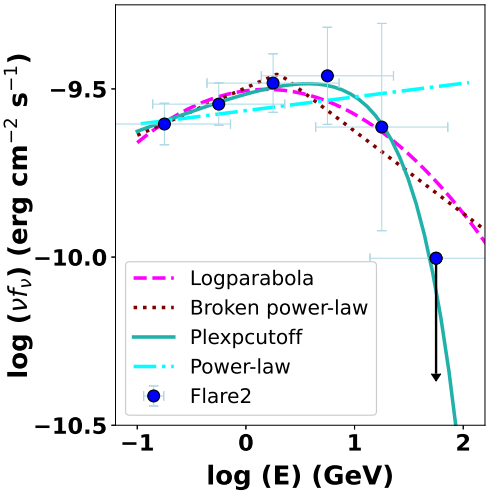

(b) Flare 2

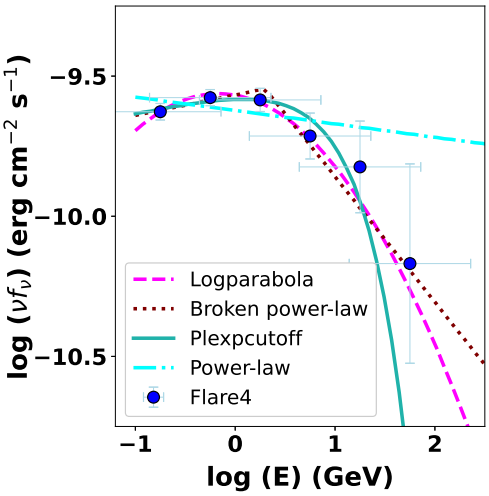

(c) Flare 4

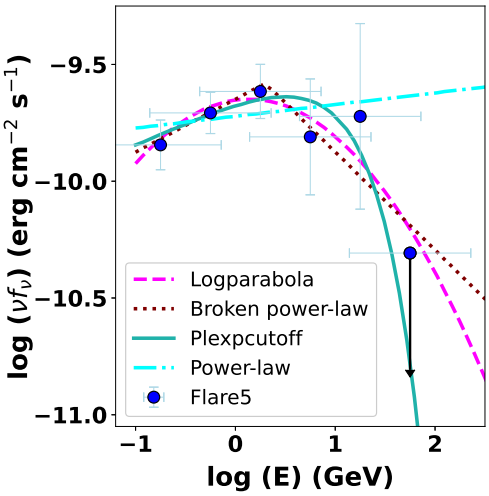

(d) Flare 5

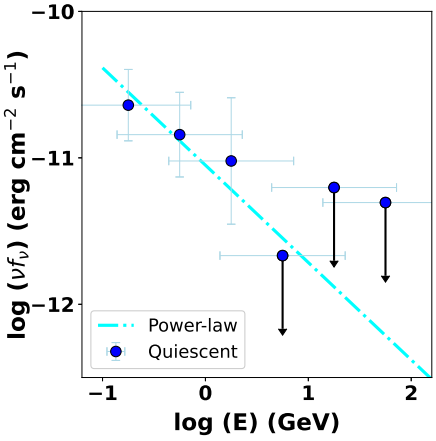

(e) Quiescent

Figure 4.6: Plots showing the γ-ray SEDs during different activity states along with the fitted spectral models. The details of models are inboxed in the plots.

Table 4.5: Results of γ-ray spectral analysis for the flaring and quiescent states.

Flare	$F_{0.1-300\mathrm{GeV}}$	PowerLaw			TS	$\mathrm{TS_{curv}}$
	(10^{-6} ph cm^{-2} s^{-1})	Γ				
1	2.6±0.08	-1.92±0.02			6682.16	
2	1.7±0.07	-1.96±0.03			3116.97	
4	1.6±0.03	-2.05±0.02			12894.82	
5	1.1±0.07	-1.95±0.04			1464.99	
Quiescent	0.16±0.02	-2.72±0.20			109.53	
		LogParabola				
		α	β			
1	2.4±0.08	1.81±0.03	0.07±0.01		6736.82	54.66
2	1.6±0.07	1.90±0.04	0.05±0.02		3125.17	8.19
4	1.5±0.03	1.94±0.02	0.08±0.01		13003.37	108.55
5	1.0±0.07	1.81±0.07	0.09±0.03		1468.75	4.75
		Broken PowerLaw		$\epsilon_{\mathrm{break}}$		
		Γ_1	Γ_2	(GeV)		
1	2.5±0.08	-1.78±0.03	-2.28±0.07	2.00±0.05	6725.74	43.58
2	1.6±0.07	-1.86±0.04	-2.24±0.10	2.00±0.07	3134.50	17.53
4	1.5±0.03	-1.92±0.02	-2.43±0.06	1.82±0.20	12965.38	70.56
5	1.0±0.07	-1.77±0.07	-2.42±0.17	1.99±0.03	1478.32	13.41
		Power-law with exponential cutoff		$\epsilon_{\mathrm{cutoff}}$		
		Γ_{plec}		(GeV)		
1	2.5±0.08	-1.80±0.03		22.0±5.0	6733.48	51.32
2	1.6±0.07	-1.88±0.03		30.0±0.8	3110.54	-6.43
4	1.5±0.03	-1.92±0.02		16.0±3.0	12915.87	21.07
5	1.0±0.07	-1.81±0.07		16.5±7.4	1461.22	-3.68

4.3.2 Constraints on the Doppler factor

The detection of γ-rays from blazars is often used to constrain various source parameters (Foschini et al., 2013; Tavecchio et al., 2010). The observed variability timescale (τ) coupled with the light travel time arguments can effectively constrain the emission region size as

$$R \leq \frac{c\,\tau}{1+z}\,\delta \tag{4.4}$$

where δ is the jet Doppler factor. Using this relation along with the pair production opacity of the γ-ray photons against the target X-ray photons, one can obtain a lower limit on the jet Doppler factor (Dondi & Ghisellini, 1995b; Abdo et al., 2010a). For a γ-ray photon of energy ϵ in $m_e c^2$ units and the target X-ray photon flux f_x, the minimum jet Doppler factor can be deduced as

$$\delta \geq \left[\frac{\sigma_T\, d_L^2\,(1+z)^2\, f_x\, \epsilon}{4\,\tau\, m_e\, c^4}\right]^{\frac{1}{6}} \tag{4.5}$$

where, σ_T is the Thomson scattering cross section and d_L is the luminosity distance. The highest photon energy detected during the time period of flares 1 and 2 is 82.6 GeV (Section 4.3.1) and the X-ray flux obtained in the energy range 0.3-10 keV during the flaring state is 2.915×10^{-11} erg/cm^2/s. Incorporating this values with shortest variability timescale of 5.5 hours (Section 4.3.1) in the above equation, we found the minimum jet Doppler factor during the flaring state as 17. Using this value in equation 4.4, the upper-limit on the emission region size R is estimated to be $\sim 10^{16}$ cm. For a similar value of the emission region size and the target X-ray photon flux 5.6×10^{-12} erg/cm^2/s corresponding to the quiescent state, the jet Doppler factor was found to be 13. Here, we used the highest photon energy as 26 GeV (detected during the quiescent state on 59960 MJD).

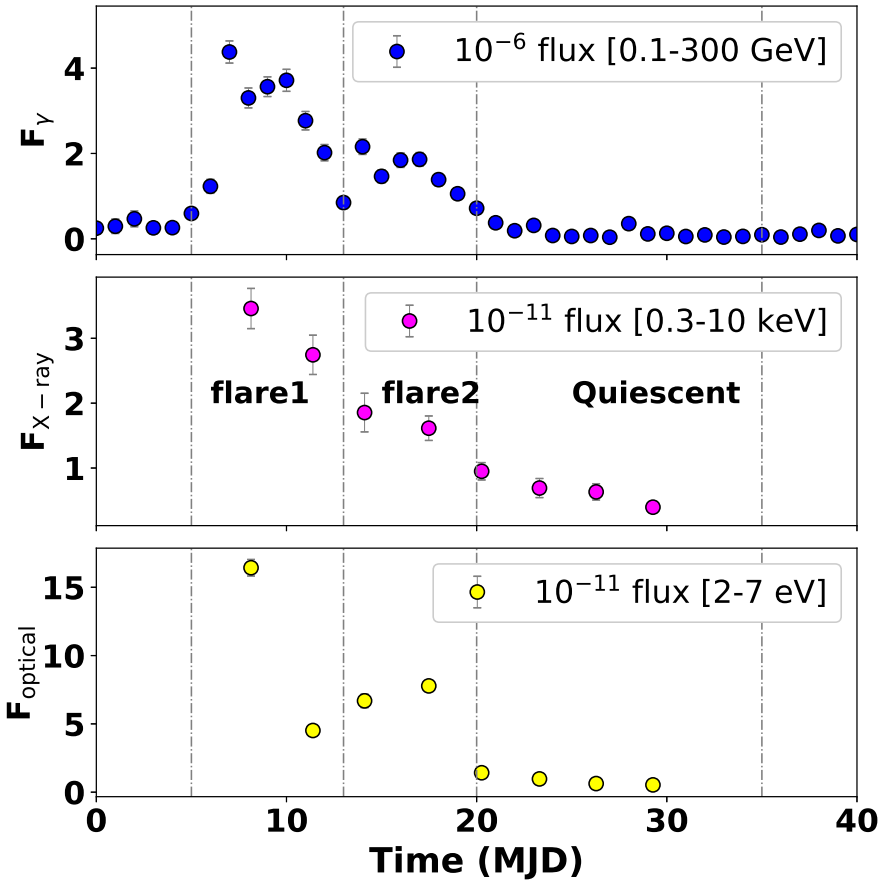

Figure 4.7: Figure showing the multi-wavelength fluxes of 4C 31.03 during MJD 59940-59965. From top to bottom: γ-ray flux (phs cm^{-2} s^{-1}), X-ray flux (erg cm^{-2} s^{-1}), and optical/UV flux (erg cm^{-2} s^{-1}). Time zero corresponds to 59940 MJD.

4.3.3 Broadband SED analysis

The broadband spectral modeling of the source with different emission processes can provide clues on the gamma-ray emission mechanism and the plausible location of the emission region in the blazar jet (Ghisellini & Tavecchio, 2009b; Cerruti, 2020). For this, we selected three epochs from the multi-wavelength light curve corresponding to two high activity states and a quiescent state. These epochs were also chosen based on the availability of the *Swift* observations and are shown in Figure 4.7. In Figure

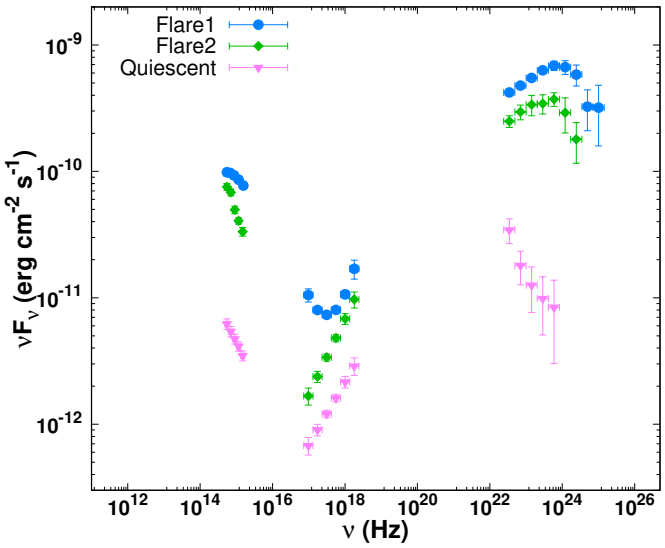

Figure 4.8: Plot showing all the 3 multiwavelength SEDs together.

4.8, we show the observed SEDs corresponding to these three flux states.

The broadband SEDs available at optical/UV, X-ray, and γ-rays from the Swift-XRT and Fermi observations are modeled using a one-zone leptonic model considering synchrotron, SSC, and EC processes (Section 1.3.6) (Shah et al., 2017; Sahayanathan et al., 2018). The emissivity functions corresponding to these radiative processes are solved numerically and the routines developed are incorporated as a local model in the spectral fitting package *XSPEC* (Arnaud, 1996). The energy density of the target photon field involved in the external Compton scattering process is expressed as a fraction (f) of the corresponding black-body energy density.

$$U_{\rm target} = f \times U_{\rm BB} \tag{4.6}$$

where, $U_{\rm BB} = \dfrac{4\sigma_B}{c} T^4$ is the black-body energy density. The temperature for BLR emission was taken as 42000 K and that for Torus was set at 1000 K. The total number of parameters governing the broadband spectrum exceeds

Table 4.6: Best-fit values of the source parameters from broadband SED fitting. Description of symbols in column1: p - Low energy particle index, q - High energy particle index, γ_b - Break Lorentz factor, B - Magnetic Field (G), Γ - Bulk Lorentz factor, δ - Doppler Factor, η - Equipartition, f - External Compton fraction f, and $U_{\rm target}$ - External photon energy density (erg cm^{-3})

Parameter	Flare 1	Flare 2	Quiescent
p	2.32±0.04	1.78±0.05	1.63±0.13
q	4.4±0.1	4.8±0.2	4.2±0.1
γ_b	4542±508	2617±257	1230± 69
B	0.86±0.03	0.80±0.01	0.68±0.02
Γ	28	16	13
δ	28.6	24.4	21.5
η	3.0	3.0	3.0
f	0.048±0.004	0.029±0.005	0.008±0.002
$U_{\rm target}$	3.6×10^{-4}	2.2×10^{-4}	6.1×10^{-5}

the information available from the optical, X-ray, and γ-ray energies, and hence, certain constraints were imposed. The emission region size was optimized at 2×10^{16} cm after freeing initially, and was then kept fixed in further steps. In addition to these, we also fixed the parameters: $\gamma_{\rm min}$=10, $\gamma_{\rm max}$=2×10^6, and viewing angle, θ=2°.

The spectral fit to the different activity states using these emission processes was first performed by setting all parameters free except the ones mentioned above. However, the confidence intervals were obtained only for the parameters p, q, γ_b, B, and the external Compton fraction f, since the iterations were unable to converge due to plausible degeneracies. In Table 4.6, we provide the details of the best-fit parameters, and the spectrum corresponding to these best-fit parameters are shown in Figure 4.9 with the right panels showing the output from *XSPEC*.

The observed fluxes at the three selected epochs were reasonably reproduced by the model using synchrotron, SSC and EC-IR emission

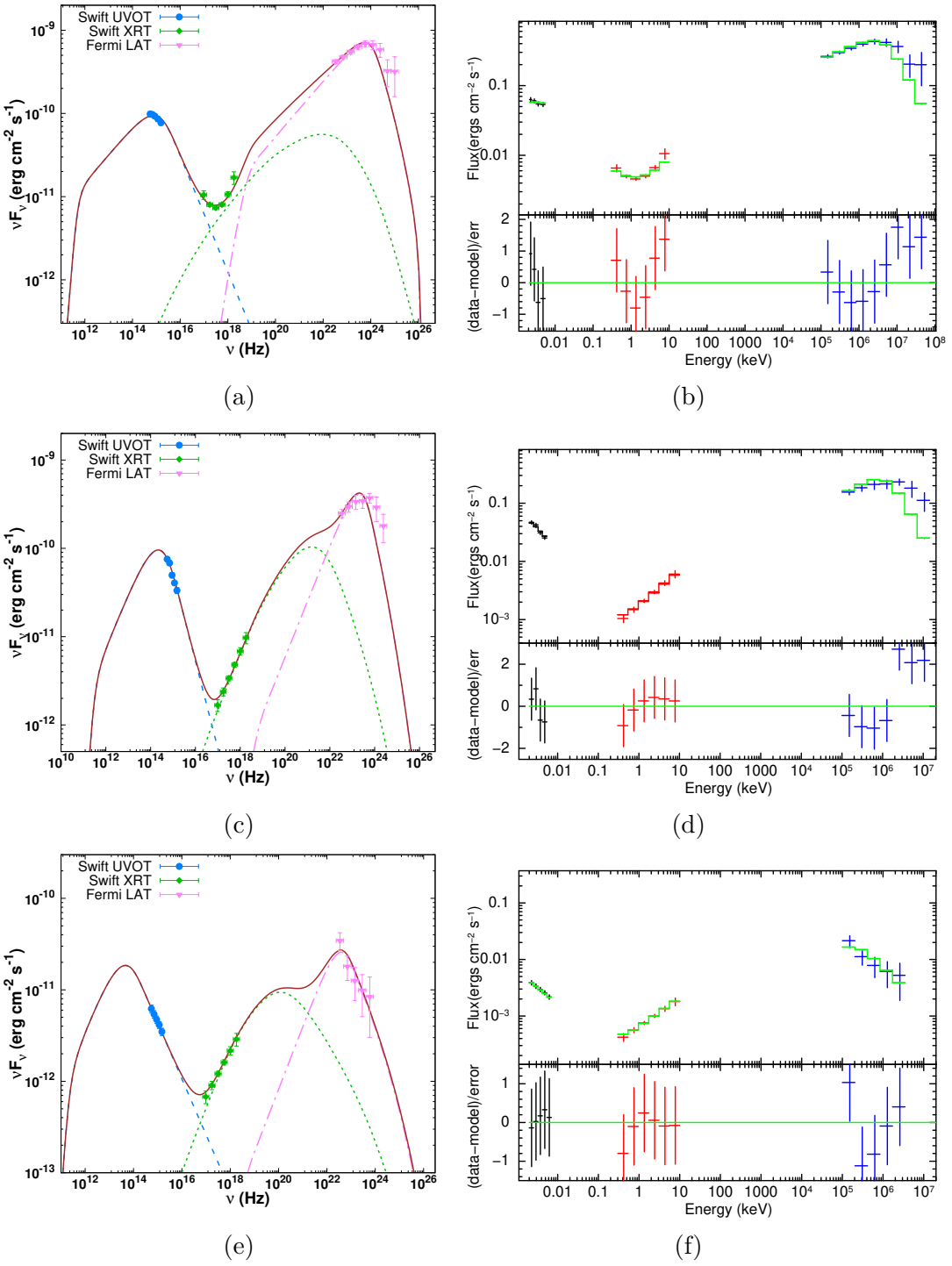

Figure 4.9: Left) The selected SEDs with best-fit models. The dashed line represents the synchrotron, dotted line SSC, and dotted dashed line EC process respectively. The solid curve shows the total best-fit model. Right) Corresponding plot of unfolded spectrum with residuals generated from *XSPEC*. From top to bottom: Flare 1, 2, and quiescent state.

processes. Comparing the SEDs in the Figure 4.8, one can note that the flux has substantially increased across all the wavebands during flares. The results of our SED fit suggest that this transition is associated with significant variations in most of the source parameters, including low and high energy particle indices, bulk Lorentz factor, γ_b, magnetic field B, and the target photon energy density $U_{\rm target}$. The variation in $U_{\rm target}$ across the activity states can be associated with the location of the emission region from the central black-hole (Ghisellini & Tavecchio, 2009b). The target photon energy density is higher for the flaring states compared to quiescent period, and this implies that during the flares, the emission region is more closer to central black-hole than in the case of quiescent state. Similarly, the target photon field energy density for flare 1 is larger than that of flare 2, suggesting that the location of the emission region can be closer to the central black hole for Flare 1. The SEDs also exhibit a significant difference in the spectral shape. For example, the X-ray spectrum during flare 1 has the contribution from synchrotron and SSC processes and shows a negative curvature, while for the other epochs the X-ray emission is predominantly due to SSC process following a power-law.

Our broadband analysis suggests that the γ-ray emission from 4C 31.03 can be due to the inverse Compton scattering of IR photons from the torus. This is consistent with our findings from the γ-ray observational results mentioned in previous sections. Further, the observed cooling time scale of the underlying electron distribution for the EC emission can be calculated as (Tavecchio et al., 2010; Saito et al., 2013),

$$t_c^{\rm obs} = \frac{3\, m_e\, c}{4\, \sigma_T\, U'} \left(\frac{\nu_{\rm seed}^{\rm obs}\, \Gamma\, (1+z)}{\nu_{\rm IC}^{\rm obs}\, \delta} \right)^{\frac{1}{2}} \tag{4.7}$$

where, $U' = U_{\rm target}\, \Gamma^2$ is the target photon field energy density in the

co-moving frame, $\nu_{\rm seed}^{\rm obs}$ (2×10^{13}Hz) is the observed seed photon frequency (for torus IR as the target photon field) and $\nu_{\rm IC}^{\rm obs}$ is the observed EC peak frequency. The peak EC frequency is obtained from the best-fit values of the log-parabola spectral fit to the γ-ray observations (Massaro et al., 2006). In the case of flare 1, $\nu_{\rm IC}^{\rm obs}$ is equal to 1.2×10^{23} Hz. Using the best-fit values provided in Table 4.6, we obtained $t_c^{\rm obs}$ to be 7.3 hours. This is in close agreement with the decay time scales obtained from the temporal analysis of the source (Section 4.3.1).

4.4 Summary

The blazar 4C 31.03 has recently been reported by *Fermi*-LAT for exhibiting an exceptionally high γ-ray activity for the first time. In this paper, we performed a detailed study of this major outburst through temporal and spectral analysis. We used publicly available observations by *Fermi*-LAT, *Swift*-XRT, and UVOT instruments for this study.

We performed a detailed temporal study of the γ-ray emission from 4C 31.03 using lightcurves with 7, 1, and 0.5 day binning. Through the statistical analysis of lightcurves using Bayesian blocks, we identified 3 epochs featuring prominent flares. The shortest variability timescale of $5.5\pm$ 0.7 hours was observed from the variability analysis performed using 0.5 day binned lightcurve. The comparison of fluxes in the energy ranges 0.1-1 GeV and 1-500 GeV indicates that this outburst is predominantly caused by the low-energy electrons in the particle distribution. The γ-ray SEDs corresponding to flaring and quiescent states were studied using various models, revealing that the spectra during the flares exhibit significant curvature/break.

The maximum photon energy, detected positionally consistent with the

source, is $\sim$ 82 GeV, and this implies that the emission region may be situated outside the BLR. Using the pair production opacity argument and considering variability time scale, we obtained the value of minimum jet Doppler factor corresponding to the flaring state as 17 and 13 for the quiescent state.

Further, we performed a detailed statistical broadband SED study of 3 multi-wavelength spectra representing flaring and quiescent activities. Using a one-zone leptonic model that incorporates synchrotron, SSC, and EC emission processes, the observed fluxes at considered energy bands were successfully reproduced. Interestingly, the observed γ-ray fluxes are well accounted by attributing with the external Compton process involving IR photons from the torus. Further the value of the observed cooling timescale, $t_c^{\rm obs}$ estimated from the broadband SED results, closely aligns with the values of time scales obtained from the variability analysis. Our study supports the idea that the γ-ray production in 4C 31.03 happens beyond the BLR, but within the molecular torus.

Chapter 5

Study of the long-term flux distribution of 3C 279 and 4C 31.03

5.1 Introduction

Studying the probability density functions (PDF) associated with the long-term flux distribution can provide valuable insights into the underlying processes driving the variability. In general, a Gaussian PDF for the longtime flux distribution indicates that random or additive processes are responsible for the flux variations. However, longterm flux distributions of blazars were known to follow a log-normal PDF (Sinha et al., 2018; Romoli et al., 2018; Shah et al., 2018). In a lognormal process, the fluctuations in an observable are correlated to the actual value. ie, for a stochastic phenomenon X originating from random multiplicative disturbances, x_i, such that $X = \Pi\, x_i$. The logarithm of X will be additive in $\log x_i$ and by central limit theorem, the sum of $\log x_i$'s must approach a normal distribution as $N \to \infty$. Hence, a log-normal flux distribution (normal in logarithm) hints multiplicative origin for the variability and rules out the possibility of additive processes involved with the flux variations.

Log-normal flux variability was initially observed for X-ray binaries

(McHardy, 2010; Uttley et al., 2005). Later, several studies reported log-normal signatures in the long-term flux distributions of blazars (Shah et al., 2018; Pian et al., 1999; Romoli et al., 2018; Rieger, 2019b; Vaughan et al., 2003). A linear trend in rms–flux relation is also observed for blazars, that supports the log-normal flux variability (Uttley et al., 2005; Shah et al., 2018). The log-normal flux distributions found in X-ray binaries can be connected to the multiplicative phenomena associated with accretion disc. The viscous density fluctuations in the disk can propagate inward and make a power-law multiplicative noise. This signals when transmitted to the jet can modulate the jet emission (Arévalo & Uttley, 2006; Lyubarskii, 1997; Uttley et al., 2005; Narayan & Piran, 2012). However, in the case of blazars, the observed rapid variability within timescales in the order of hours or even less than that demands the origin of variability within the jet, since it is difficult for the signals from the disc to propogate in such short time periods (Narayan & Piran, 2012; Shukla et al., 2018). On the other hand, log-normal variability associated with the blazar emission can be intrinsic, and caused by random variations in the spectral index. In a narrow-band photon spectrum approximated with a power-law, any Gaussian variation in the spectral index can cause a log-normal flux distribution (Sinha et al., 2018; Khatoon et al., 2020) as,

$$\begin{aligned} F_\nu &\propto \nu^{-\alpha} \\ \log F_\nu &\propto -\alpha \log \nu \\ \Delta \log F_\nu &\propto -\alpha\, \Delta \log \nu - \Delta\alpha\, \log \nu \end{aligned} \tag{5.1}$$

where α is the spectral index. The Gaussian variation in α indicate similar type of fluctuations in particle distribution index p as $p = (\alpha - 1)/2$.

Considering a particle distribution represented by a power-law as, $N(\gamma) \propto \gamma^{-p}$, the index p is given by $\left(1 + \frac{t_{acc}}{t_{esc}}\right)$, where t_{acc}/t_{esc} is the the particle acceleration/escape time scale. Hence a random variation in α implies a perturbation in the particle acceleration/escape time scale. In this scenario, the fractional variability $\Delta N(\gamma)/N(\gamma)$ or $\Delta \log(N(\gamma))$ will be a linear sum of a Gaussian and $\log \gamma$ terms. The synchrotron and inverse Compton fluxes carries the signatures of log-normality from the particle distribution. The log-normal imprints in this case, is energy dependent and becomes weaker towards lower energies (Rieger, 2019b).

As a continuation to the studies in chapters 3 and 4, we present a detailed analysis of the long-term flux distributions of the sources 3C 279 and 4C 31.03 in this chapter. In the first section, the analysis and results of the flux distribution study of optical, X-ray and γ -ray lightcurves of 3C 279 is presented in detail. The second section elaborates the details of γ-ray flux distributions associated with the quiescent and active phases of 4C 31.03. We summarize our findings in the last section.

5.2 Data selection

To perform the flux distribution study of 3C 279, we took the power-law modeled fluxes and indices from the multi-wavelength data described in the Section 3.2 of chapter 3. These lightcurves in optical, X-ray and γ-ray bands have been obtained using observations spanning 14 years of Swift-UVOT, XRT and Fermi-LAT instruments. For investigating the γ-ray flux distribution of 4C 31.03, we used 7 and 0.5 day binned γ-ray lightcurves obtained from the Fermi observations during the period 54832-60152 MJD, which has been already used in the variability studies presented in chapter 4.

5.3 Multi-wavelength flux distribution study of 3C 279

In general, the flux distribution of 3C 279 supports a log normal behavior, suggesting the physical process responsible for the variability to be multiplicative (Romoli et al., 2018; Goyal et al., 2022; Sahakyan, 2021). This can possibly indicate the coupling of the blazar jet with the accretion disk where the variable emission from the latter is well understood to be log-normal (McHardy, 2010). However, one of the striking features of 3C 279 is its flux variability measured even up to minute timescales (Ackermann et al., 2016; Paliya, 2015). Such rapid variability demands a very compact emission region along with the origin of variability within the jet. A detailed study of the PDF associated with long-term flux distribution can provide insights into this.

3C 279 exhibits prominent flares in various energy bands with significant spectral variations. There are epochs when these flares are correlated over all the energy bands and also for the peculiar orphan ones. For example, the GeV flares at epochs 56646, 56720, 56750, and 57188 have previously been reported as orphan γ-ray flares (MacDonald et al., 2017; Lewis et al., 2019a; Wang et al., 2022; Patel et al., 2021). The spectral property of the source within orphan and multi-wavelength flares differ considerably (Rajput et al., 2020). Besides, the frequent flaring episodes encountered from this source also raise the question of whether the source posses two definite flux states. Studying the long term flux distribution also has the potential to identify whether these flux variations are associated with a single statistical process or the source behavior changes during different flux states (Shah et al., 2018). Such studies on blazar lightcurve (including 3C 279) at different energy bands have already been done and they suggest a log-normal flux

variability (Narayan & Piran, 2012; Shah et al., 2018; Vaughan et al., 2003; Romoli et al., 2018; Sobolewska et al., 2014). Further, the γ-ray flux distribution of 3C 279 shows a double-Gaussian nature suggesting two definite flux states (Shah et al., 2018). We repeated this by including the optical/UV, X-ray, and γ-ray light curves, and also studied the distribution of the spectral indices.

To study whether the flux and index variations are consistent with a normal distribution, we first performed the Anderson-Darling (AD) test on these quantities. Depending on the value of the test statistics, one can reject the normality of the distribution when it is greater than the critical value. The test was performed on the fluxes, logarithm of fluxes, and spectral indices. In Table 5.1, we provide the results of the AD test with the critical values estimated at 5% significance of the null hypothesis. We find that the distributions of the logarithm of the optical/UV fluxes, optical/UV spectral indices and the X-ray spectral indices favour a Gaussian distribution (in bold); while the other distributions are inconclusive. This behaviour of the optical/UV flux is consistent with the earlier studies where the blazar flux variations are log-normal in nature. We repeated this analysis by performing the fitting of histograms of logarithm of fluxes and the spectral indices with Gaussian and double Gaussian PDFs A Gaussian PDF is defined as

$$f(x) = \frac{\mathrm{a}}{\sqrt{2\pi\sigma^2}}\, e^{\frac{-(x-\mu)^2}{2\sigma^2}} \tag{5.2}$$

where, μ and σ are the mean and standard deviation of the distribution respectively; while a double Gaussian PDF is defined as

$$\mathrm{d(x)} = \frac{\mathrm{a}}{\sqrt{2\pi\sigma_1^2}}\, \mathrm{e}^{\frac{-(\mathrm{x}-\mu_1)^2}{2\sigma_1^2}} + \frac{1-\mathrm{a}}{\sqrt{2\pi\sigma_2^2}}\, \mathrm{e}^{\frac{-(\mathrm{x}-\mu_2)^2}{2\sigma_2^2}} \tag{5.3}$$

where μ_1 and μ_2 are the means, and σ_1 and σ_2 are the standard deviations

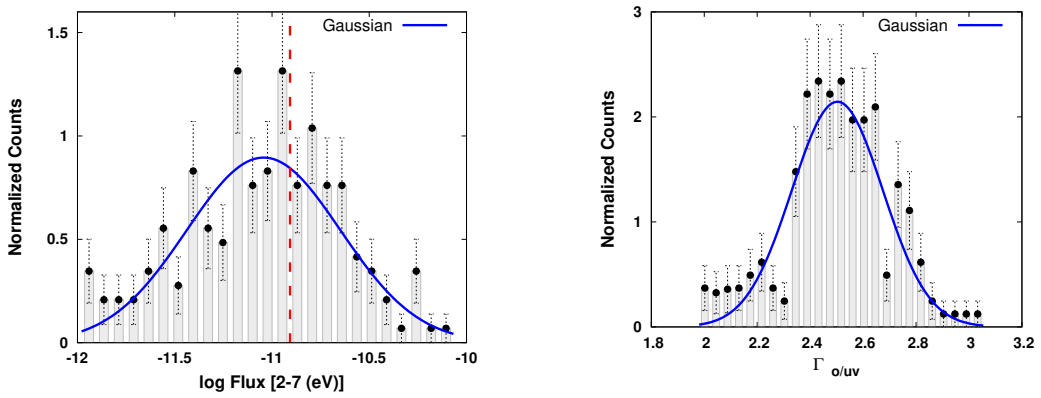

(a) (b)

Figure 5.1: Plots showing the histograms with best-fit PDFs obtained in the case of 3C 279: a) Optical/UV flux, b) Index. The dotted vertical line in the left panel gives the mean value of corresponding flux.

of the two Gaussian PDFs. Consistent with the AD test, histograms of the logarithm of optical/UV fluxes and the corresponding spectral indices can be well fitted by a Gaussian PDF (with reduced chi-squares $\chi^2_{\rm red}$, 1.08 and 1.28 respectively). In Figure 5.1, we show these histograms with the best fit Gaussian PDF. For X-rays, the fit by a double Gaussian PDF to the histogram of the logarithm of X-ray fluxes provided better statistics ($\chi^2_{\rm red} = 0.86$) compared to the Gaussian PDF ($\chi^2_{\rm red} = 1.99$); whereas, a single Gaussian PDF was able to fit the histogram of X-ray spectral index. Though the logarithm of X-ray fluxes favoured a double Gaussian PDF, the distributions are too close to be differentiated. In Figure 5.2, we show that these distributions with the best-fit Gaussian (logarithm of fluxes and indices) and the double Gaussian (logarithm of fluxes) PDFs. The histogram of the logarithm of γ-ray fluxes constructed from the adaptively binned light curve clearly showed two distinct peaks and is well fitted by a double Gaussian PDF ($\chi^2_{\rm red} = 0.824$). A similar feature is also observed in 3-day binned fluxes and the best fit double Gaussian PDF resulted in similar statistical moments (means and the standard deviations). The results are

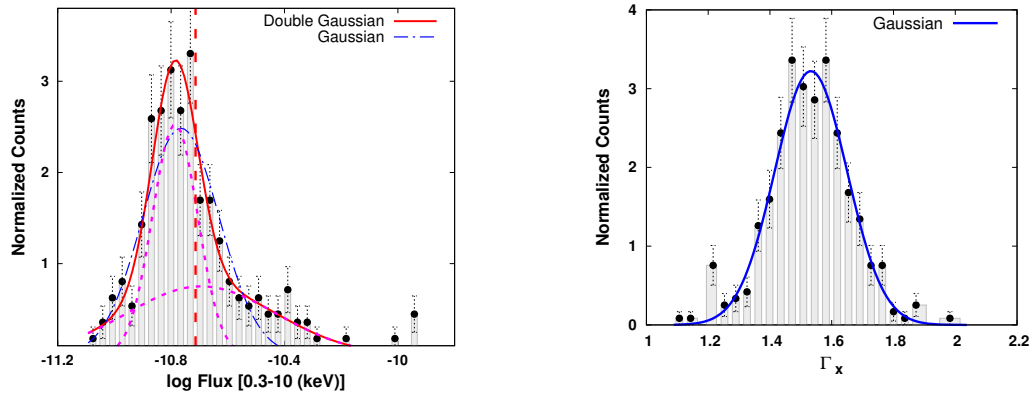

Figure 5.2: Plots showing the histograms with best-fit PDFs obtained in the case of 3C 279: a) X-ray flux – The solid curve represents the best-fit double Gaussian, dotted curves the two components of double Gaussian, dotted dashed curve the best-fit single Gaussian, and dashed vertical line the logarithm of average flux value respectively. b) X-ray index.

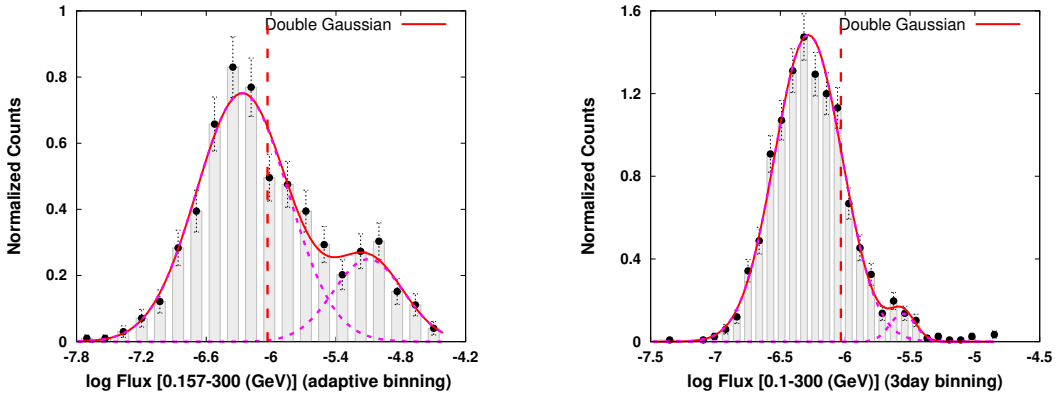

Figure 5.3: Plots showing histograms of γ-ray fluxes of 3C 279: a) adaptively binned, b) 3 day binned. The red solid curves show the best-fit double Gaussian, the dotted curves the two individual components of the double Gaussian, dotted dashed curves the best-fit Gaussian, and the vertical dashed line represents the logarithm of average flux value.

given in Table 5.2 and the histograms with best-fit double Gaussian PDFs are shown in Figure 5.3. In both cases, the index distribution also favoured double Gaussian PDFs and the fit statistics are given in Table 5.2. In Figure 5.4, we show the corresponding histograms and the best fit Gaussian and double Gaussian PDFs. Though the distribution of two Gaussians of the

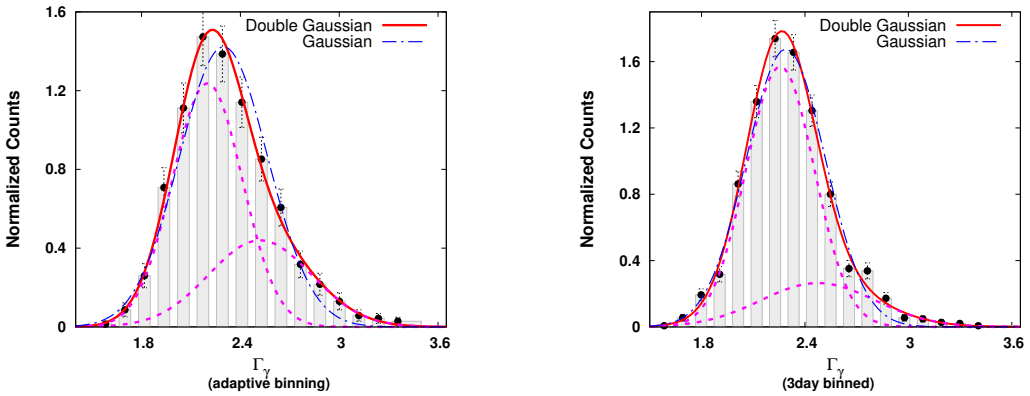

Figure 5.4: Plots showing histograms of γ-ray indices of 3C 279: a) adaptively binned, b) 3 day binned. The red solid curves show the best-fit double Gaussian, the dotted curves the two individual components of the double Gaussian, and the dotted dashed curves the best-fit Gaussian respectively.

double Gaussian PDF is not very distinct in the histogram of indices, they supplement the double Gaussian flux distribution with the fact that the plausible log-normal γ-ray flux variability can be associated with the Gaussian variability in indices. However, to affirm this claim more rigorous statistical treatment is required. In the histogram of logarithm of fluxes, we show the mean γ-ray flux by vertical dashed lines. Based on these histograms, the average flux may not actually differentiate between the high and low states instead one can use the flux value at which the two Gaussian functions intersect (dotted dashed vertical line in Figures 5.3 (a) and (b)). However, this value (3.3×10^{-6} phs cm^{-2} s^{-1}) is not used to demarcate the high and low states in the correlation study described in chapter 3, as we could find very few observations during which the fluxes are higher than this value and hence did not use in the correlation study described in chapter 3.

Table 5.1: Results of the Anderson Darling test done for the flux/index distributions in γ-ray, X-ray and optical/UV bands of 3C 279.

	Number of data points	Normal (Flux) AD(critical value)	Normal (log Flux) AD(critical value)	Normal (Spectral index) AD(critical value)
Fermi-3 day binned	1354	219 (0.785)	2.94 (0.785)	30.7 (0.785)
Fermi adaptive binned	5850	916 (0.786)	57.98 (0.786)	31.80 (0.786)
X-ray	326	39.20 (0.778)	9.76 (0.778)	**0.65** (0.778)
optical/UV	189	11.30 (0.771)	**0.45** (0.771)	**0.54** (0.771)

Table 5.2: Best-fit parameter values of the PDFs fitted to the logarithm of flux and index histograms for X-ray, optical/U and γ-ray light curves. G1 represents single Gaussian PDF and G2 gives double Gaussian PDF.

	Histogram	PDF	μ_1	σ_1	μ_2	σ_2	a_1	dof	χ^2/dof
optical/UV	log10(Flux)	G1	-11.04 ± 0.03	0.39±0.03			0.90 ± 0.07	22	1.08
	Index	G1	2.50±0.01	0.17±0.01			0.92± 0.08	18	1.28
X-ray	log10(Flux)	G2	-10.79 ± 0.01	0.08±0.01	-10.69±0.03	0.26±0.03	0.50±0.07	25	0.86
		G1	-10.76 ± 0.01	0.13 ± 0.01			0.84 ± 0.07	27	1.99
	Index	G1	1.53±0.01	0.12±0.01			0.94± 0.05	19	0.97
3 day binned	log10(Flux)	G2	-6.28±0.01	0.26±0.01	-5.56±0.02	0.10±0.02	0.97±0.01	22	1.14
	Index	G2	2.26±0.01	0.20±0.01	2.48±0.10	0.33±0.03	0.78±0.11	14	1.31
		G1	2.29 ± 0.01	0.23±0.01			0.96±0.05	16	3.25
Adaptive binning	log10(Flux)	G2	-6.27±0.03	0.42±0.02	-5.10±0.06	0.32±0.05	0.78±0.04	14	0.82
	Index	G2	2.199±0.02	0.211±0.03	2.519±0.28	0.310±0.08	0.657±0.35	48	1.42
		G1	2.297±0.01	0.268±0.01			0.956±0.05	14	1.90

5.4 γ-ray flux distribution of 4C 31.03

Being a bright γ-ray source after the prolonged low activity phase, 4C 31.03 forms an ideal blazar to study the log-normal flux and spectral variations. We obtained the histograms for the logarithm of fluxes and indices from the 7 day binned long-term lightcurve. To identify whether the source displays two flux states, we first performed the histogram study using only the prolonged quiescent phase (54832–59940 MJD) and then repeated with the inclusion of the recent active period (59940–60152 MJD). The histogram analysis reveals that the long-term quiescent phase flux alone can reasonably be reproduced by a single log-normal function. Conversely, a double log-normal function gives better representation for the total flux distribution after including the active phase. However, in the double log-normal distribution, the Gaussian component corresponding to the high flux state is significantly suppressed due to the prolonged quiescent activity. Hence, we further explored the flux distribution of the active state using histogram obtained from 12 hour binned lightcurve (to improve statistics). The histogram of the logarithmic fluxes corresponding to the active phase is again well fitted by a single Gaussian PDF reflecting a log-normal flux distribution. The histogram study, therefore supports that the blazar 4C 31.03 is characterized by two definite flux states corresponding to its quiescent and active phases. The results of this study are given in Table 5.3 and the histograms with the best-fit models are shown in Figure 5.5.

We extended our study to understand the index variability by constructing their histograms. Interestingly, the index distributions demanded a double Gaussian shape irrespective of the flux states (Figure 5.5 (d)). A possible reason for this could be that the observed γ-ray

spectrum falls around the peak of the Compton component and hence the spectrum is not represented by a simple power-law. During the different flux states the γ-ray peak shifts significantly and the integrated flux can be either governed by the low or high-energy index.

The observed log-normal flux variability can be attributed to the normal variation in the spectral index. However, we find the index distributions during the flaring and quiescent states are better represented by a double Gaussian function while the flux distributions during these states suggest a single log-normal variability. Alternatively, the observed log-normality in blazars can also be attributed to the Fermi acceleration processes in the jet (Rieger, 2019b; Xu et al., 2019; H. E. S. S. Collaboration et al., 2017). For instance, the quiescent period of the blazar may be dominated by one type of Fermi acceleration (turbulent/shock) and at the flaring period, both could be at play (Dmytriiev et al., 2021; Lewis et al., 2019b). Consistently, the flux distribution of the total period reflects a double log-normal behavior.

To scrutinize our inference drawn from the histograms, we tested the hypothesis of normality for the distributions of γ-ray fluxes and indices using Anderson-Darling (AD) statistics. The test results are provided in Table 5.4. According to the AD test performed, the logarithmic flux distribution of the total lightcurve deviates significantly from a single Gaussian behavior. This result is consistent with conclusions drawn from the histogram study which supports a double log-normal variability. The AD test performed on the active phase fluxes alone supports a log-normal variability in agreement with the corresponding histogram analysis. Interestingly, the AD test for the quiescent phase suggests a slight deviation from the log-normal behavior which is contrary to the conclusion drawn from the histogram study. A plausible reason could be,

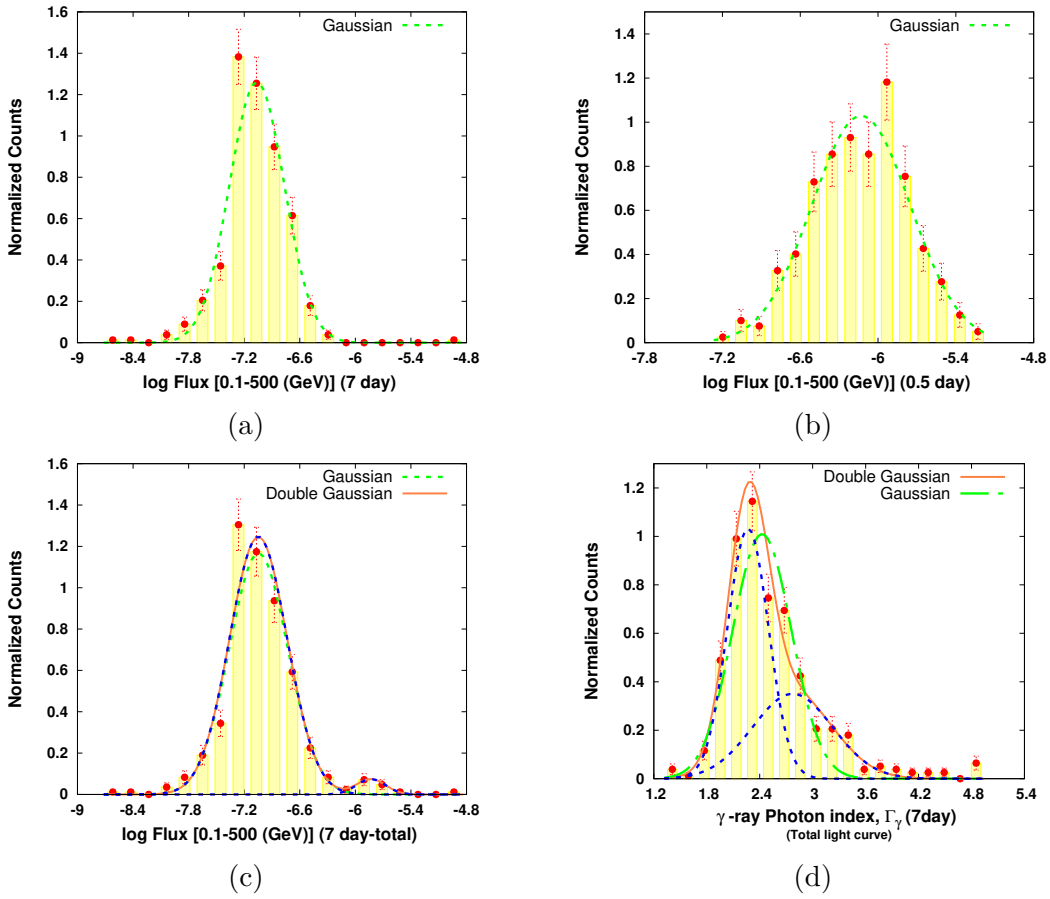

Figure 5.5: Plots showing the histogram fitting of logarithm flux distributions obtained for a) Quiescent state, b) Active state, c) Total lightcurve, and d) The index distribution obtained from the total 7 day binned lightcurve.

the quiescent period may also contain minor flares associated with different physical processes. The presence of such flares deviate the variability behavior from log-normal in case of AD test. However, in case of histogram study, these minor flares may be over shadowed by the prolonged quiescent phase and hence showed a log-normal distribution.

Table 5.3: Best fit parameter values of the PDFs fitted to the logarithm of fluxes and indices . (PDF: GI stands for Gaussian and GII for double Gaussian)

	Histogram	PDF	μ_1	σ_1	μ_2	σ_2	a_1	χ^2/dof
7 day binned	log10(Flux)	GI	-7.06±0.02	0.30±0.01			0.93±0.07	2.2
(Quiescent state)	Index	GI	2.40±0.03	0.30±0.02			0.84± 0.08	3.9
		GII	2.31 ± 0.03	0.23±0.04	2.80±0.20	0.45±0.08	0.60±0.20	1.8
12 hour binned	log10(Flux)	GI	-6.13±0.01	0.38±0.01			0.98±0.04	0.8
(Active)	Index	GI	2.1±0.03	0.24±0.02			0.83±0.1	4.5
		GII	1.98±0.01	0.20±0.01	2.50±0.1	0.40±0.05	0.64±0.09	0.7
7 day binned	log10(Flux)	GI	-7.05±0.02	0.31±0.02			0.92±0.07	2.8
(Total)		GII	-7.0±0.02	0.31±0.01	-5.83± 0.07	0.16± 0.06	0.97±0.02	2.2
	Index	GI	2.41±0.04	0.37±0.03			0.89±0.09	3.9
		GII	2.28±0.04	0.21±0.04	2.60±0.08	0.50±0.04	0.45±0.10	1.8

Table 5.4: Results of the Anderson-Darling test for flux/index distributions, indicating normality when the test statistic is below the critical value.

	Number of data points	Normal (Flux) AD(critical value)	Normal (log Flux) AD(critical value)	Normal (Spectral index) AD(critical value)
7 day binned Quiescent state	1354	124 (0.779)	2.44 (0.779)	12.8 (0.779)
12 hour binned active state	326	15.2 (0.776)	0.48 (0.776)	10.9 (0.776)
7 day binned total	5850	118 (0.78)	5.9 (0.78)	13.3 (0.78)

5.5 Summary

The long-term flux and index distribution of the sources 3C 279 and 4C 31.03 were studied to identify the nature of variability. In the case of 3C 279, a long-term distribution study was performed in optical, X-ray and γ-ray wavelengths. We used observations of Swift-XRT, UVOT, and Fermi-LAT spanning 14 years. The Anderson-Darling test conducted over all the flux and index distributions suggests a log-normal variability for the optical flux and a normal behavior for the optical and X-ray index distributions. To leverage this, we also performed the fitting of the corresponding histograms with single Gaussian and double Gaussian functions. In this study, the X-ray and γ-ray flux distributions are found to be deviating from a single log-normal feature and is better explained by a double Gaussian. However, the double log-normal variability is only evident in the γ-ray flux distribution and in X-ray, the two individual Gaussian are not well resolved. The double log-normal behavior in γ-ray emission is further asserted by the double normal distribution observed for γ-ray index distribution. The log-normal variability observed in the broadband emission of 3C 279 can be associated with the Gaussian perturbations in the index which in turn connect the origin of variability to the perturbations in the particle acceleration/escape time scale.

The comprehensive study seeking the origin of variability in the γ-ray emission of 4C 31.03 was performed using flux and index distributions. The γ-ray emission from 4C 31.03 exhibits log-normal variability and showcase a double flux state corresponding to the prolonged quiescent and the recent active phases. The index distributions corresponding to quiescent, active and total periods show case a double normal variation indicating that the γ-ray spectrum is characterized by two spectral indices. The observed

double log-normal variability in the γ-ray flux cannot be attributed to the Gaussian variation in the index, nevertheless, can be associated with changes in the dominant acceleration processes themselves during different activity phases of the source.

Chapter 6

Summary

This thesis investigates the multi-wavelength variability of blazars, focusing on two prominent Fermi-bright sources: 3C 279 and 4C 31.03. Blazars, a subset of active galactic nuclei (AGN), are distinguished by relativistic jets that are directed towards the earth. Chapter 1 provides a foundational overview of blazars, detailing their distinctive characteristics and offering a discussion on the particle acceleration mechanisms and radiative processes that contribute to their broad-band emissions. Chapter 2 introduces the space telescopes Fermi-LAT, Swift-XRT, and UVOT, alongside an explanation of standard data reduction and analysis procedures.

Chapter 3 focuses on a detailed correlation and regression analysis of various spectral parameters within the narrow band spectra of the blazar 3C 279, which is examined as a case study. We used the Swift-UVOT, XRT, and Fermi-LAT observations of 3C 279 spanning 14 years in this study. Our multi-wavelength sample used in the correlation analysis consists of simultaneous 170 optical and X-ray spectra, 260 X-ray and γ-ray spectra, and 164 optical and γ-ray spectra. Additionally, we included all the available γ-ray, X-ray and optical/UV spectra of 3C 279 for performing

correlation analysis in each individual energy band. The major findings of this study are

- Blazars are known for exhibiting positive/negative correlation between flux and indices during the flares in the narrow band emissions. However, this trend may or may not be present on a long-term basis.

- In the case of FSRQs, particularly 3C 279, the optical emission can be considered to be from the high energy particles and X-ray emission is from the low energy particles in the distribution. Further, under the radiative cooling interpretation, a strong positive correlation is expected between X-ray and optical indices with an index difference of 0.5. The detailed correlation study does not support such a trend and the index difference strongly deviate from 0.5.

- The correlation study perfomed on transition energy shows a strong positive correlation with the optical/UV flux and a notable anticorrelation with X-ray index.

- The results of the correlation/regression analysis suggest that flux changes in the optical band are primarily driven by normalization variations, while flux variability in the X-ray band is largely influenced by changes in the index.

- Extending these results to the underlying particle distribution with a break energy E_b, one can say that at low energy ($E < E_b$) the spectral variations are mainly caused by the index, whereas at high energy ($E > E_b$) the variations can be due to the changes in E_b.

- Broadband SED modeling of 3C 279 reveals substantial shifts in the EC peak energy, which can be attributed to changes in the break

energy. The SED analysis also suggests that EC peak energy shifts may occur when the target photon field is altered.

4C 31.03 is a sparsely studied object due to its prolonged quiescent activity. In January 2023, it underwent its first γ-ray outburst, during which the flux level rose to 60 times its previous average. The thesis explores γ-ray variability and presents a multi-wavelength study of this source in Chapter 4. In this work, we conducted an in-depth study on the temporal variability of the active γ-ray phase of 4C 31.03 and explored its multi-wavelength implications. The main findings of this study are summarized.

- The study of 12 hour binned lightcurve using Bayesian blocks and HOP algorithm shows three prominent flaring epochs
- The short-term variability times obtained scales from 5-18 hours with the fastest variability observed at 5.5 hours.
- The maximum photon energy for the γ-ray photon detected with more than 99% association probability is 82 GeV, and these γ-ray observations indicate that the γ-ray emission region may lie beyond the BLR.
- A systematic SED modeling using one zone leptonic model was performed for the selected 3 SEDs. The observed gamma-ray fluxes were well accounted for by assigning EC-IR process as the likely gamma-ray production mechanism at all the selected epochs.
- The observed gamma-ray fluxes were well accounted for by assigning EC-IR process as the likely gamma-ray production mechanism at all the selected epochs.

- Results of SED analysis show notable variations in the parameters B, Γ, δ, γ_b, and $U_{\rm target}$ during the transition of the source from quiescent to active phase.

- The observed cooling time of the emitting particle spectrum estimated using best-fit parameters of SED modeling is 7.3 hours. This value aligns perfectly with the variability time scales measured from the timing analysis.

- SED modeling also revealed a significant change in the spectral shape of the source, particularly in the X-ray energies. The X-ray spectrum shifts from a power-law form during the quiescent phase to a negatively curved spectrum during the flaring epoch. During this flaring period, there is a soft X-ray excess in the synchrotron emission component, indicating that particles are accelerated to much high energies.

The long-term flux distribution study possesses the potential to probe the nature of physical processes that drives the variability. We performed a detailed study to understand the nature of flux distributions in 3C 279 and 4C 31.03 and is presented in Chapter 5. The study on 3C 279 covers the optical, X-ray, and γ-ray emission, while the flux distribution study for 4C 31.03 was limited to γ-ray spectrum. We tested the normality of flux and index distributions using Anderson-Darling test and also performed the histogram fitting with Gaussian and double Gaussian PDFs to identify the nature of distributions.

- A clear log-normal variability behavior is observed for 3C 279 (in optical, X-ray, and γ-ray spectra) and 4C 31.03 (for the γ-ray emission).

- The γ-ray flux distribution in 3C 279 and 4C 31.03 displays a double

flux state.

- The double flux state in 4C 31.03 clearly corresponds to the overlong quiescent phase and the recently observed high activity state.
- The log-normal variability observed in 3C 279 can be attributed to the random fluctuations in the particle acceleration/escape time scales that can cause a Gaussian variation in the index.
- However, the double log-normal variability observed for 4C 31.03 cannot be attributed to the above mentioned phenomenon. In this case, the γ-ray index distribution displays a double normal behavior irrespective of the flux state. Hence, the double log-normal flux distribution of 4C 31.03 may be an outcome of the variations in the dominant particle acceleration process corresponding to quiescent and flaring periods.

Chapter 7

Recommendations for future study

- *Searching for the lower-energy counterpart of the galactic plane transient source 4FGL J0133.0+5930*: This is a galactic plane γ-ray source for which the lower-energy counterpart is unknown. Martí et al. (2017), considered two objects as the possible candidates for the low-energy counter part of this source. One is an eclipsing binary star TYC 3683-985-1, and the other is a Swift X-ray source SWIFT J0132.9+5932. However, according to the latest 4FGL-DR3 catalog, the 95% confidence Fermi ellipse does not include the position of TYC 3683-985-1. This indicate SWIFT J0132.9+5932 as a promising candidate and we observed an enhanced X-ray and optical activity simultaneous to the detection of γ-ray emission by Fermi-LAT (Angioni et al., 2021). We aim to explore SWIFT J0132.9+5932 to identify the nature of the astronomical object that is responsible for the γ-ray emission.

- *Study of the unknown/unassociated γ-ray sources*: Many sources have shown γ-ray activity detected by Fermi telescope, but not included in any γ-ray source catalogs (Benke et al., 2024; Cheung & Kocevski, 2023). The spatial templates of such sources are not designated as

a point source or an extended one. The emission from such sources is below the Fermi detection threshold most of the time. Studying the properties of such sources offers potential data analysis challenges. Besides this, recently there are several detections of TeV emission by LHAASO and HAWC for which the lower energy/GeV counterpart is unknown (Horan & Wakely, 2008). It is interesting to explore the exact origin of such powerful emissions from the unidentified positions in the universe.

- *Exploring X-ray and MeV polarization*: Polarization is an efficient tool to probe the radiation mechanism and the physical environments within the jet. The polarization angle shows drastic variability correlated with flares at optical and X-ray wavelengths and this parameter can point out the orientation of the magnetic field in the jet (Pavlidou et al., 2014). The Imaging X-ray Polarimetry Explorer (IXPE) onboard since 2021 December, provides polarization data for blazars at X-ray energies. The MeV polarization can probe the radiative mechanism in blazars since a high degree of MeV polarization confirms hadronic processes. Studying the data from The Compton Spectrometer and Imager (COSI) can unveil the *gamma*-ray polarization in blazars and constrain the high energy emission mechanism.

- *The study of the nature of γ-ray variability for a sample of southern sky blazars detected by TESS*: If FSRQs and BLLs are physically distinct classes, then they should manifest statistically different variability properties. The same scenario is true if there is a clear balance between disk driven and jet driven emission. A recent study on the optical variability of a sample of southern sky blazars reveals

no significant distinction between the variability properties of FSRQs and BLLs (Dingler & Smith, 2024). However, the γ-ray emission from these classes has distinct origin and FSRQs are more luminous in γ-ray energies with higher Compton dominance than BLLs. Moreover, the long-term γ-ray flux distribution of blazars is characterized by double log-normal feature (Thekkoth et al., 2024, 2023). A study exploring the nature of variability of γ-ray emission using Fermi-LAT observations is crucial in understanding the connection or distinction between FSRQs and BLLS. A further comparison of the results with the optical study can also provide better understanding of the difference in the statistical processes driving variability in low and high energies.

Bibliography

Abdo, A. A., Ackermann, M., Ajello, M., et al. 2010a, ApJ, 722, 520

—. 2010b, ApJ, 716, 835

—. 2010c, ApJ, 715, 429

Abdo, A. A., Ackermann, M., Agudo, I., et al. 2010d, ApJ, 716, 30

Abdollahi, S., Acero, F., Ackermann, M., et al. 2020, ApJS, 247, 33

Abdollahi, S., Acero, F., Baldini, L., et al. 2022, ApJS, 260, 53

Acciari, V. A., Aliu, E., Arlen, T., et al. 2011, ApJ, 738, 25

Ackermann, M., Ajello, M., Albert, A., et al. 2012, ApJS, 203, 4

Ackermann, M., Anantua, R., Asano, K., et al. 2016, ApJ, 824, L20

Aharonian, F., Akhperjanian, A., Beilicke, M., et al. 2003, A&A, 410, 813

Aharonian, F., Akhperjanian, A. G., Bazer-Bachi, A. R., et al. 2007, ApJ, 664, L71

Aharonian, F. A. 2000, New A, 5, 377

Ajello, M., Atwood, W. B., Baldini, L., et al. 2017, ApJS, 232, 18

Albert, J., Aliu, E., Anderhub, H., et al. 2007, ApJ, 669, 862

Angel, J. R. P., & Stockman, H. S. 1980, ARA&A, 18, 321

Angioni, R., Buson, S., & Cheung, C. C. 2021, The Astronomer's Telegram, 14299, 1

Antonucci, R. 1993, ARA&A, 31, 473

Arnaud, K. A. 1996, in Astronomical Society of the Pacific Conference Series, Vol. 101, Astronomical Data Analysis Software and Systems V, ed. G. H. Jacoby & J. Barnes, 17

Arévalo, P., & Uttley, P. 2006, Monthly Notices of the Royal Astronomical Society, 367, 801

Atwood, W., Albert, A., Baldini, L., et al. 2013, arXiv e-prints, arXiv:1303.3514

Atwood, W. B., Abdo, A. A., Ackermann, M., et al. 2009, ApJ, 697, 1071

Baheeja, C., Sahayanathan, S., Rieger, F. M., Jagan, S. K., & Ravikumar, C. D. 2022, MNRAS, 514, 3074

Beasley, A. J., Gordon, D., Peck, A. B., et al. 2002, ApJS, 141, 13

Beckmann, V., & Shrader, C. R. 2012, Active Galactic Nuclei

Begelman, M. C., Blandford, R. D., & Rees, M. J. 1984, Rev. Mod. Phys., 56, 255

Begelman, M. C., Rudak, B., & Sikora, M. 1990, ApJ, 362, 38

Bell, A. R. 1978, MNRAS, 182, 147

Benke, P., Valverde, J., & Mereu, I. 2024, The Astronomer's Telegram, 16710, 1

Bhagwan, J., Gupta, A., Papadakis, I., & Wiita, P. 2015, New Astronomy, 44

Bhatta, G. 2017, ApJ, 847, 7

Bhatta, G., & Dhital, N. 2020, ApJ, 891, 120

Bhatta, G., Mohorian, M., & Bilinsky, I. 2018, A&A, 619, A93

Blandford, R., Meier, D., & Readhead, A. 2019, ARA&A, 57, 467

Blandford, R. D., & Levinson, A. 1995, ApJ, 441, 79

Blandford, R. D., & Ostriker, J. P. 1978, ApJ, 221, L29

Błażejowski, M., Sikora, M., Moderski, R., & Madejski, G. M. 2000, ApJ, 545, 107

Błażejowski, M., Blaylock, G., Bond, I. H., et al. 2005, ApJ, 630, 130

Blumenthal, G. R., & Gould, R. J. 1970, Rev. Mod. Phys., 42, 237

Boccardi, B., Krichbaum, T. P., Ros, E., & Zensus, J. A. 2017, A&A Rev., 25, 4

Boettcher, M. 2010, arXiv e-prints, arXiv:1006.5048

Bonnoli, G., Ghisellini, G., Foschini, L., Tavecchio, F., & Ghirlanda, G. 2010, Monthly Notices of the Royal Astronomical Society, 410, 368

Böttcher, M., & Bloom, S. D. 2000, AJ, 119, 469

Böttcher, M., Reimer, A., Sweeney, K., & Prakash, A. 2013, ApJ, 768, 54

Burbidge, G. R. 1959, ApJ, 129, 849

Burrows, D. N., Hill, J. E., Nousek, J. A., et al. 2005, Space Sci. Rev., 120, 165

Campbell, W. W. 1908, PASP, 20, 293

Caprioli, D. 2023, arXiv e-prints, arXiv:2307.00284

Cash, W. 1979, ApJ, 228, 939

Celotti, A., Padovani, P., & Ghisellini, G. 1997, MNRAS, 286, 415

Cerruti, M. 2020, arXiv e-prints, arXiv:2012.13302

Cerruti, M., Dermer, C. D., Lott, B., Boisson, C., & Zech, A. 2013, ApJ, 771, L4

Cerruti, M., Zech, A., Boisson, C., & Inoue, S. 2011, in SF2A-2011: Proceedings of the Annual meeting of the French Society of Astronomy and Astrophysics, ed. G. Alecian, K. Belkacem, R. Samadi, & D. Valls-Gabaud, 555–558

Cerruti, M., Zech, A., Boisson, C., & Inoue, S. 2011, in Week of French Astrophysics/Semaine de l'Astrophysique Francaise, 555–558

Chang, Y.-L., Arsioli, B., Li, W., Xu, D., & Chen, L. 2022, ApJ, 939, 123

Cheung, C. C., & Kocevski, D. 2023, The Astronomer's Telegram, 16389, 1

Ciprini, S., & Garrappa, S. 2023, The Astronomer's Telegram, 15841, 1

Citterio, O., Campana, S., Conconi, P., et al. 1996, in Multilayer and Grazing Incidence X-Ray/EUV Optics III, ed. R. B. Hoover & A. B. C. W. II, Vol. 2805, International Society for Optics and Photonics (SPIE), 56 – 65

Compton, A. H. 1923, Physical Review, 21, 483

Condon, J. J., & Ransom, S. M. 2016, Essential Radio Astronomy

Cortina, J., & LST collaboration. 2023, The Astronomer's Telegram, 16381, 1

Costamante, L., Cutini, S., Tosti, G., Antolini, E., & Tramacere, A. 2018, MNRAS, 477, 4749

Cutini, S. 2023, The Astronomer's Telegram, 16068, 1

Dermer, C. D. 1995, ApJ, 446, L63

Dermer, C. D., Finke, J. D., Krug, H., & Böttcher, M. 2009, ApJ, 692, 32

Dermer, C. D., & Schlickeiser, R. 1994a, ApJS, 90, 945

—. 1994b, ApJS, 90, 945

Dingler, R., & Smith, K. L. 2024, ApJ, 973, 10

Dmytriiev, A., Sol, H., & Zech, A. 2021, MNRAS, 505, 2712

Dondi, L., & Ghisellini, G. 1995a, MNRAS, 273, 583

—. 1995b, MNRAS, 273, 583

Edelson, R. A., & Krolik, J. H. 1988, ApJ, 333, 646

Eisenstein, D. J., & Hut, P. 1998, ApJ, 498, 137

Evans, P. A., Beardmore, A. P., Page, K. L., et al. 2009, MNRAS, 397, 1177

Fermi, E. 1949, Physical Review, 75, 1169

—. 1954, ApJ, 119, 1

Finke, J. D., & Dermer, C. D. 2010, ApJ, 714, L303

Foschini, L., Bonnoli, G., Ghisellini, G., et al. 2013, A&A, 555, A138

Foschini, L., Ghisellini, G., Tavecchio, F., Bonnoli, G., & Stamerra, A. 2011, A&A, 530, A77

Fossati, G., Maraschi, L., Celotti, A., Comastri, A., & Ghisellini, G. 1998, MNRAS, 299, 433

Geng, X., Zeng, W., Rani, B., et al. 2020, ApJ, 904, 67

Ghisellini, G. 2013, Radiative Processes in High Energy Astrophysics, Vol. 873

Ghisellini, G., Celotti, A., Fossati, G., Maraschi, L., & Comastri, A. 1998, MNRAS, 301, 451

Ghisellini, G., Righi, C., Costamante, L., & Tavecchio, F. 2017, MNRAS, 469, 255

Ghisellini, G., & Tavecchio, F. 2009a, MNRAS, 397, 985

—. 2009b, MNRAS, 397, 985

Ghisellini, G., Tavecchio, F., Foschini, L., & Ghirlanda, G. 2011, MNRAS, 414, 2674

Goad, M. R., Tyler, L. G., Beardmore, A. P., et al. 2007, A&A, 476, 1401

González, M. M., Patricelli, B., Fraija, N., & García-González, J. A. 2019, MNRAS, 484, 2944

Goswami, P., Sahayanathan, S., Sinha, A., & Gogoi, R. 2020, MNRAS, 499, 2094

Goyal, A., Soida, M., Stawarz, Ł., et al. 2022, ApJ, 927, 214

Gupta, A. C., Krichbaum, T. P., Wiita, P. J., et al. 2012, MNRAS, 425, 1357

H. E. S. S. Collaboration, Abdalla, H., Abramowski, A., et al. 2017, A&A, 598, A39

H. E. S. S. Collaboration, Abdalla, H., Adam, R., et al. 2021, A&A, 648, A23

Hahn, J. 2016, PoS, ICRC2015, 917

Hartman, R. C., Bertsch, D. L., Bloom, S. D., et al. 1999, ApJS, 123, 79

Hayashida, M., Madejski, G. M., Nalewajko, K., et al. 2012, ApJ, 754, 114

Hayashida, M., Nalewajko, K., Madejski, G. M., et al. 2015, ApJ, 807, 79

Hays, E. 2023, Bulletin of the AAS, 55, https://baas.aas.org/pub/2023n2i141p06

Hill, J. E., Zugger, M. E., Shoemaker, J., et al. 2000, in X-Ray and Gamma-Ray Instrumentation for Astronomy XI, ed. K. A. Flanagan & O. H. W. Siegmund, Vol. 4140, International Society for Optics and Photonics (SPIE), 87 – 98

Horan, D., & Wakely, S. 2008, in AAS/High Energy Astrophysics Division, Vol. 10, AAS/High Energy Astrophysics Division #10, 41.06

Hori, S., & IceCube Collaboration. 2023, The Astronomer's Telegram, 15889, 1

Hoyle, F., & Fowler, W. A. 1963, MNRAS, 125, 169

IceCube Collaboration, Aartsen, M. G., Ackermann, M., et al. 2018, Science, 361, eaat1378

Jagan, S. K., Sahayanathan, S., Rieger, F. M., & Ravikumar, C. D. 2021, MNRAS, 506, 3996

Joshi, M., Marscher, A., & Böttcher, M. 2013, in European Physical Journal Web of Conferences, Vol. 61, European Physical Journal Web of Conferences, 05004

Kalberla, P. M. W., Burton, W. B., Hartmann, D., et al. 2005, A&A, 440, 775

Kang, S.-J., Zheng, Y.-G., Wu, Q., Chen, L., & Yin, Y. 2021, MNRAS, 502, 5875

Kapanadze, B., Vercellone, S., Romano, P., et al. 2018, ApJ, 854, 66

Kapanadze, B., Gurchumelia, A., Dorner, D., et al. 2020, ApJS, 247, 27

Kardashev, N. S. 1962, Soviet Ast., 6, 317

Kellermann, K. I., Vermeulen, R. C., Zensus, J. A., & Cohen, M. H. 1998, AJ, 115, 1295

Kembhavi, A. K., & Narlikar, J. V. 1999, Quasars and active galactic nuclei : an introduction

Khatoon, R., Shah, Z., Misra, R., & Gogoi, R. 2020, MNRAS, 491, 1934

Klein, O., & Nishina, Y. 1928, Nature, 122, 398

Krymskii, G. F. 1977, Akademiia Nauk SSSR Doklady, 234, 1306

Kuin, N. P. M., Landsman, W., Breeveld, A. A., et al. 2015, MNRAS, 449, 2514

Larionov, V. M., Jorstad, S. G., Marscher, A. P., et al. 2020, MNRAS, 492, 3829

Lefa, E., Kelner, S. R., & Aharonian, F. A. 2012, ApJ, 753, 176

Lewis, T., Finke, J., & Becker, P. A. 2019a, in High Energy Phenomena in Relativistic Outflows VII, 75

Lewis, T. R., Finke, J. D., & Becker, P. A. 2019b, ApJ, 884, 116

Liodakis, I., & Petropoulou, M. 2020, ApJ, 893, L20

Liodakis, I., Romani, R. W., Filippenko, A. V., Kocevski, D., & Zheng, W. 2019, ApJ, 880, 32

Lister, M. L., Aller, M., Aller, H., et al. 2011, ApJ, 742, 27

Lister, M. L., Aller, M. F., Aller, H. D., et al. 2013, AJ, 146, 120

—. 2016, AJ, 152, 12

Liu, H. T., & Bai, J. M. 2006, ApJ, 653, 1089

Lott, B., Escande, L., Larsson, S., & Ballet, J. 2012, A&A, 544, A6

Lynden-Bell, D. 1969, Nature, 223, 690

Lynds, C. R., Stockton, A. N., & Livingston, W. C. 1965, ApJ, 142, 1667

Lyubarskii, Y. E. 1997, Monthly Notices of the Royal Astronomical Society, 292, 679

MacDonald, N. R., Jorstad, S. G., & Marscher, A. P. 2017, ApJ, 850, 87

Madejski, G. M., Sikora, M., Jaffe, T., et al. 1999, ApJ, 521, 145

Martí, J., Luque-Escamilla, P. L., Paredes, J. M., et al. 2017, A&A, 598, A81

Massaro, E., Perri, M., Giommi, P., & Nesci, R. 2004, A&A, 413, 489

Massaro, E., Tramacere, A., Perri, M., Giommi, P., & Tosti, G. 2006, A&A, 448, 861

Mastichiadis, A., & Kirk, J. G. 1997, A&A, 320, 19

Mattox, J. R., Bertsch, D. L., Chiang, J., et al. 1996, ApJ, 461, 396

McHardy, I. 2010, in Lecture Notes in Physics, Berlin Springer Verlag, ed. T. Belloni, Vol. 794, 203

Meyer, M., Scargle, J. D., & Blandford, R. D. 2019, ApJ, 877, 39

Mücke, A., & Protheroe, R. J. 2001, Astroparticle Physics, 15, 121

Narayan, R., & Piran, T. 2012, MNRAS, 420, 604

Nigro, C., Sitarek, J., Gliwny, P., et al. 2022, A&A, 660, A18

Pacholczyk, A. G. 1970, Radio astrophysics. Nonthermal processes in galactic and extragalactic sources

Paliya, V. S. 2015, ApJ, 808, L48

Paliya, V. S., Böttcher, M., Gurwell, M., & Stalin, C. S. 2021, ApJS, 257, 37

Paliya, V. S., Diltz, C., Böttcher, M., Stalin, C. S., & Buckley, D. 2016, ApJ, 817, 61

Pandey, A., Gupta, A. C., & Wiita, P. J. 2017, ApJ, 841, 123

Patel, S. R., Bose, D., Gupta, N., & Zuberi, M. 2021, Journal of High Energy Astrophysics, 29, 31

Patiño-Álvarez, V. M., Fernandes, S., Chavushyan, V., et al. 2018, MNRAS, 479, 2037

Pavlidou, V., Angelakis, E., Myserlis, I., et al. 2014, MNRAS, 442, 1693

Petropoulou, M., & Mastichiadis, A. 2012, MNRAS, 426, 462

Pian, E., Urry, C. M., Maraschi, L., et al. 1999, The Astrophysical Journal, 521, 112–120

Poutanen, J., & Stern, B. 2010, ApJ, 717, L118

Prince, R. 2020a, ApJ, 890, 164

—. 2020b, ApJ, 890, 164

Prince, R., Khatoon, R., & Stalin, C. S. 2021, MNRAS, 502, 5245

Rajput, B., Stalin, C. S., & Sahayanathan, S. 2020, MNRAS, 498, 5128

Rani, B., Lott, B., Krichbaum, T. P., Fuhrmann, L., & Zensus, J. A. 2013, A&A, 557, A71

Rieger, F. M. 2019a, Galaxies, 7, 78

—. 2019b, Galaxies, 7, 28

Rieger, F. M., Bosch-Ramon, V., & Duffy, P. 2007, Ap&SS, 309, 119

Roming, P. W. A., Kennedy, T. E., Mason, K. O., et al. 2005, Space Sci. Rev., 120, 95

Romoli, C., Chakraborty, N., Dorner, D., Taylor, A., & Blank, M. 2018, Galaxies, 6, 135

Roy, A., Patel, S. R., Sarkar, A., Chatterjee, A., & Chitnis, V. R. 2021, MNRAS, 504, 1103

Rybicki, G. B., & Lightman, A. P. 1986, Radiative Processes in Astrophysics

Sahakyan, N. 2021, MNRAS, 504, 5074

Sahakyan, N., Israyelyan, D., Harutyunyan, G., et al. 2022, MNRAS, 517, 2757

Sahayanathan, S. 2008, MNRAS, 388, L49

Sahayanathan, S., & Godambe, S. 2012, MNRAS, 419, 1660

Sahayanathan, S., Sinha, A., & Misra, R. 2018, Research in Astronomy and Astrophysics, 18, 035

Saito, S., Stawarz, Ł., Tanaka, Y. T., et al. 2013, ApJ, 766, L11

Salpeter, E. E. 1964, ApJ, 140, 796

Schlafly, E. F., & Finkbeiner, D. P. 2011a, ApJ, 737, 103

—. 2011b, ApJ, 737, 103

Schmidt, M. 1963, Nature, 197, 1040

Seyfert, C. K. 1943, ApJ, 97, 28

Shah, Z., Jithesh, V., Sahayanathan, S., Misra, R., & Iqbal, N. 2019, Mon. Not. Roy. Astron. Soc., 484, 3168

Shah, Z., Mankuzhiyil, N., Sinha, A., et al. 2018, Research in Astronomy and Astrophysics, 18, 141

Shah, Z., Sahayanathan, S., Mankuzhiyil, N., et al. 2017, MNRAS, 470, 3283

Shastri, P., Wilkes, B. J., Elvis, M., & McDowell, J. 1993, ApJ, 410, 29

Shukla, A., Mannheim, K., Patel, S. R., et al. 2018, ApJ, 854, L26

Sikora, M., Begelman, M. C., & Rees, M. J. 1994, ApJ, 421, 153

Sikora, M., Stawarz, Ł., Moderski, R., Nalewajko, K., & Madejski, G. M. 2009, ApJ, 704, 38

Singh, K. P. 2013, Bulletin of the Astronomical Society of India, 41, 137

Sinha, A., Khatoon, R., Misra, R., et al. 2018, MNRAS, 480, L116

Sobolewska, M. A., Siemiginowska, A., Kelly, B. C., & Nalewajko, K. 2014, ApJ, 786, 143

Sunanda, & Moharana, R. 2023, PoS, ICRC2023, 1580

Sunanda, Moharana, R., & Majumdar, P. 2022, Phys. Rev. D, 106, 123005

Tavecchio, F., Ghisellini, G., Bonnoli, G., & Ghirlanda, G. 2010, MNRAS, 405, L94

Thekkoth, A., Baheeja, C., Sahayanathan, S., & C. D., R. 2024, Journal of High Energy Astrophysics, 42, 115

Thekkoth, A., Sahayanathan, S., Shah, Z., Paliya, V. S., & Ravikumar, C. D. 2023, MNRAS, 526, 6364

Thompson, D. J., & Wilson-Hodge, C. A. 2022, in Handbook of X-ray and Gamma-ray Astrophysics, 29

Tramacere, A. 2020, JetSeT: Numerical modeling and SED fitting tool for relativistic jets, Astrophysics Source Code Library, record ascl:2009.001

Tripathi, T., Gupta, A. C., Takey, A., et al. 2024, MNRAS, 527, 5220

Urry, C. M., & Padovani, P. 1995, PASP, 107, 803

Uttley, P., McHardy, I. M., & Vaughan, S. 2005, MNRAS, 359, 345

Vaughan, S., Edelson, R., Warwick, R. S., & Uttley, P. 2003, MNRAS, 345, 1271

Wagner, S. M., Burd, P., Dorner, D., et al. 2022, in 37th International Cosmic Ray Conference, 868

Wang, Z.-R., Liu, R.-Y., Petropoulou, M., et al. 2022, Phys. Rev. D, 105, 023005

Wills, D., & Wills, B. J. 1976, ApJS, 31, 143

Wilson, A. S., & Colbert, E. J. M. 1995, ApJ, 438, 62

Xu, J., Hu, S., Webb, J. R., et al. 2019, ApJ, 884, 92

Yoo, S., & An, H. 2020, ApJ, 902, 2

Zhang, B. K., Dai, B. Z., Wang, L. P., et al. 2012, MNRAS, 421, 3111

Zhang, B.-K., Jin, M., Zhao, X.-Y., Zhang, L., & Dai, B.-Z. 2021, arXiv e-prints, arXiv:2103.11149

Appendix A

Tables

Table A.1: Table showing results of power-law fitting of Swift-XRT observations. From left to right: Observation id, time in MJD, un-absorbed flux in the energy range 0.2–10 keV, spectral index, chi-square, and degrees of freedom.

Obs.Id	**Time in MJD**	**Flux in 0.3-10 keV** 10^{-11} **ergs cm**$^{-2}$ **s**$^{-1}$	**Photon index,** Γ_x	χ^2	**Dof**
000 35019001	53748.0	1.498 ± 0.057	1.517 ± 0.04	111.22	132.0
000 35019002	53749.0	1.414 ± 0.066	1.579 ± 0.052	70.27	96.0
000 35019003	53751.2	1.636 ± 0.202	1.397 ± 0.13	16.06	15.0
000 35019004	53752.0	1.592 ± 0.051	1.521 ± 0.033	178.63	179.0
000 35019005	53753.1	1.766 ± 0.061	1.545 ± 0.037	160.48	148.0
000 35019006	53754.1	1.685 ± 0.118	1.529 ± 0.074	47.22	45.0
000 53516002	53926.2	2.356 ± 0.467	1.533 ± 0.213	5.1	7.0
000 53517002	53926.3	2.218 ± 0.38	1.492 ± 0.178	5.13	7.0
000 53519002	53926.4	1.728 ± 0.439	1.624 ± 0.283	5.04	4.0
000 53521002	53928.0	1.815 ± 0.493	1.742 ± 0.294	2.8	4.0
000 53522002	53928.1	1.96 ± 0.347	1.612 ± 0.193	5.48	7.0
000 53523002	53928.2	1.68 ± 0.394	1.755 ± 0.281	3.2	4.0
000 53524002	53928.2	2.222 ± 0.353	1.606 ± 0.167	5.29	8.0
000 53526002	53928.4	1.878 ± 0.471	1.486 ± 0.28	5.27	4.0
000 53502004	53930.5	2.421 ± 0.466	1.459 ± 0.201	3.9	6.0
000 53503004	53930.6	1.803 ± 0.425	1.628 ± 0.277	2.59	4.0
000 30867001	54113.0	2.396 ± 0.091	1.587 ± 0.042	141.59	134.0
000 30867002	54117.2	3.369 ± 0.386	1.403 ± 0.122	13.26	19.0
000 30867003	54118.2	2.077 ± 0.212	1.597 ± 0.115	22.39	23.0
000 30867004	54119.2	1.859 ± 0.187	1.571 ± 0.109	23.46	21.0
000 30867005	54120.2	2.218 ± 0.223	1.538 ± 0.109	21.64	24.0
000 30867006	54121.2	2.103 ± 0.155	1.583 ± 0.082	27.2	41.0
000 30867008	54265.8	1.71 ± 0.122	1.613 ± 0.076	49.55	41.0
000 30867009	54266.8	1.542 ± 0.105	1.489 ± 0.07	35.63	44.0
000 30867010	54289.5	1.455 ± 0.073	1.458 ± 0.051	83.63	83.0
000 30867011	54291.2	1.778 ± 0.11	1.372 ± 0.062	48.95	59.0
000 30867012	54292.7	1.752 ± 0.155	1.469 ± 0.095	30.44	34.0

Obs.Id	**Time in MJD**	**Flux in 0.3-10 keV** 10^{-11} **ergs cm**$^{-2}$ **s**$^{-1}$	**Photon index,** Γ_x	χ^2	**Dof**
000 30867013	54293.4	1.497 ± 0.103	1.429 ± 0.072	42.51	49.0
000 30867014	54294.4	1.663 ± 0.122	1.416 ± 0.075	30.1	42.0
000 30867015	54295.3	1.744 ± 0.112	1.496 ± 0.068	55.84	54.0
000 53652001	54487.2	1.878 ± 0.471	1.486 ± 0.28	5.27	4.0
000 53652002	54487.2	1.878 ± 0.471	1.486 ± 0.28	5.27	4.0
000 53651001	54487.4	1.878 ± 0.471	1.486 ± 0.28	5.27	4.0
000 53651002	54487.4	1.878 ± 0.471	1.486 ± 0.28	5.27	4.0
000 53650001	54487.5	1.878 ± 0.471	1.486 ± 0.28	5.27	4.0
000 53650002	54487.5	1.878 ± 0.471	1.486 ± 0.28	5.27	4.0
000 53656002	54489.0	1.447 ± 0.255	1.685 ± 0.204	3.66	6.0
000 53675002	54496.9	1.44 ± 0.305	1.627 ± 0.247	4.39	5.0
000 53660002	54512.5	1.49 ± 0.334	1.681 ± 0.262	6.48	7.0
000 53665002	54514.5	1.628 ± 0.26	1.584 ± 0.183	12.53	11.0
000 53666002	54517.0	1.628 ± 0.304	1.656 ± 0.201	7.25	5.0
000 53654006	54518.0	1.826 ± 0.269	1.563 ± 0.158	7.08	9.0
000 53667002	54523.0	1.011 ± 0.177	1.667 ± 0.207	7.79	7.0
000 53668002	54523.1	1.818 ± 0.324	1.572 ± 0.183	8.66	9.0
000 53669002	54524.0	1.052 ± 0.204	1.711 ± 0.229	6.68	5.0
000 53670002	54525.4	1.373 ± 0.239	1.491 ± 0.189	6.21	8.0
000 53671002	54526.4	1.226 ± 0.239	1.67 ± 0.21	3.9	6.0
000 53671002	54526.4	1.226 ± 0.239	1.67 ± 0.21	3.9	6.0
000 53673002	54528.7	1.264 ± 0.256	1.826 ± 0.257	5.9	4.0
000 53674002	54529.5	1.288 ± 0.239	1.662 ± 0.215	6.5	8.0
000 53662004	54531.3	1.529 ± 0.243	1.471 ± 0.172	6.89	10.0
000 53661006	54539.1	1.767 ± 0.362	1.522 ± 0.228	6.64	8.0
000 53663004	54540.1	1.611 ± 0.304	1.462 ± 0.2	3.83	6.0
000 53672004	54542.4	1.544 ± 0.403	1.471 ± 0.276	8.52	6.0
000 30867016	54678.6	1.049 ± 0.128	1.652 ± 0.144	8.56	15.0
000 30867018	54688.4	1.078 ± 0.108	1.599 ± 0.109	23.28	23.0
000 30867019	54690.8	1.001 ± 0.126	1.745 ± 0.152	20.78	16.0
000 30867021	54694.3	1.026 ± 0.135	1.618 ± 0.153	10.18	13.0
000 30867022	54695.6	0.912 ± 0.13	1.599 ± 0.159	17.33	13.0

Obs.Id	**Time in MJD**	**Flux in 0.3-10 keV** $10^{-11}\,\mathbf{ergs\,cm^{-2}\,s^{-1}}$	**Photon index,** Γ_x	χ^2	**Dof**
000 30867023	54696.3	0.82 ± 0.115	1.709 ± 0.163	8.23	12.0
000 30867024	54698.0	1.194 ± 0.135	1.86 ± 0.135	18.51	15.0
000 35019007	54795.4	1.478 ± 0.075	1.532 ± 0.053	70.41	81.0
000 35019008	54795.9	1.39 ± 0.129	1.603 ± 0.101	24.58	26.0
000 35019009	54796.1	1.497 ± 0.048	1.563 ± 0.034	130.3	175.0
000 35019010	54799.0	1.586 ± 0.052	1.571 ± 0.035	191.39	178.0
000 35019011	54800.0	1.502 ± 0.06	1.573 ± 0.042	123.39	117.0
000 35019012	54816.0	1.381 ± 0.149	1.579 ± 0.12	15.88	20.0
000 30867026	54824.2	1.645 ± 0.251	1.511 ± 0.163	15.28	12.0
000 30867028	54828.2	1.529 ± 0.186	1.55 ± 0.13	9.65	17.0
000 30867029	54830.2	1.507 ± 0.163	1.683 ± 0.122	25.39	20.0
000 30867030	54832.2	1.278 ± 0.161	1.533 ± 0.133	13.66	16.0
000 30867031	54834.2	1.417 ± 0.192	1.587 ± 0.151	10.35	12.0
000 30867032	54836.2	1.235 ± 0.193	1.43 ± 0.157	9.62	12.0
000 30867033	54838.2	1.4 ± 0.191	1.544 ± 0.143	12.37	13.0
000 35019013	54864.0	1.48 ± 0.098	1.537 ± 0.07	41.1	49.0
000 35019014	54866.0	1.327 ± 0.178	1.676 ± 0.145	17.48	11.0
000 35019015	54880.0	1.904 ± 0.308	1.402 ± 0.156	14.28	9.0
000 35019016	54887.0	1.54 ± 0.214	1.542 ± 0.151	14.83	12.0
000 90022001	54893.5	1.353 ± 0.273	1.417 ± 0.198	4.46	6.0
000 90022003	54896.5	1.189 ± 0.186	1.531 ± 0.17	7.61	9.0
000 90022004	54897.1	1.428 ± 0.242	1.398 ± 0.18	8.02	10.0
000 90022007	54900.8	1.267 ± 0.25	1.605 ± 0.205	3.52	6.0
000 90022009	54905.1	1.178 ± 0.299	1.312 ± 0.246	3.17	5.0
000 90022010	54906.6	1.003 ± 0.231	1.489 ± 0.241	3.63	5.0
000 35019018	54915.0	0.808 ± 0.197	1.885 ± 0.341	5.91	4.0
000 90109001	54936.6	1.31 ± 0.192	1.49 ± 0.162	9.86	12.0
000 90109002	54937.7	1.355 ± 0.14	1.586 ± 0.11	19.42	20.0
000 90109004	54939.9	1.635 ± 0.191	1.449 ± 0.123	21.13	19.0
000 90109006	54941.7	1.708 ± 0.247	1.451 ± 0.153	12.76	11.0
000 90109007	54942.7	1.348 ± 0.164	1.565 ± 0.13	9.41	14.0

Obs.Id	**Time in MJD**	**Flux in 0.3-10 keV** $10^{-11}\,\mathbf{ergs\,cm^{-2}\,s^{-1}}$	**Photon index,** Γ_x	χ^2	**Dof**
000 90109009	54944.6	1.914 ± 0.187	1.534 ± 0.103	24.48	24.0
000 90109010	54945.7	1.997 ± 0.193	1.402 ± 0.101	31.13	27.0
000 90109011	54946.7	1.81 ± 0.162	1.468 ± 0.088	33.06	27.0
000 90109013	54948.3	2.507 ± 0.217	1.456 ± 0.092	44.93	35.0
000 90109014	54949.9	1.801 ± 0.176	1.532 ± 0.104	22.02	24.0
000 90109015	54950.6	2.329 ± 0.259	1.46 ± 0.111	23.39	20.0
000 90109017	54953.4	2.113 ± 0.234	1.473 ± 0.114	20.67	19.0
000 90109018	54954.6	2.237 ± 0.237	1.493 ± 0.108	23.71	20.0
000 90109019	54955.6	2.981 ± 0.313	1.35 ± 0.104	21.94	23.0
000 90109020	54959.6	1.95 ± 0.205	1.446 ± 0.11	24.9	24.0
000 90109021	54960.5	1.919 ± 0.179	1.595 ± 0.099	27.75	26.0
000 90109022	54961.1	1.945 ± 0.281	1.461 ± 0.148	17.0	13.0
000 90109024	54963.9	1.712 ± 0.2	1.684 ± 0.136	19.73	16.0
000 90109025	54964.8	1.277 ± 0.167	1.62 ± 0.136	16.26	15.0
000 90109026	54965.0	1.456 ± 0.157	1.586 ± 0.115	14.73	18.0
000 90109027	54966.1	1.723 ± 0.254	1.593 ± 0.168	20.67	15.0
000 90109028	54967.0	1.318 ± 0.141	1.626 ± 0.116	21.98	19.0
000 90109031	54970.3	1.496 ± 0.183	1.552 ± 0.129	15.27	17.0
000 90109032	54971.4	1.345 ± 0.183	1.546 ± 0.154	7.83	14.0
000 90109033	54972.8	1.328 ± 0.139	1.514 ± 0.108	25.68	21.0
000 90109034	54973.4	1.051 ± 0.123	1.567 ± 0.123	15.14	15.0
000 90109035	54974.7	1.061 ± 0.123	1.677 ± 0.132	11.81	16.0
000 90109036	54975.7	0.967 ± 0.097	1.669 ± 0.107	15.74	20.0
000 90109037	54976.1	0.984 ± 0.112	1.576 ± 0.123	12.84	18.0
000 90109038	54977.7	0.99 ± 0.128	1.552 ± 0.138	10.9	14.0
000 90109039	54978.3	0.877 ± 0.084	1.719 ± 0.108	17.56	21.0
000 90109041	54980.1	0.903 ± 0.118	1.686 ± 0.152	7.49	13.0
000 90109043	54982.1	1.048 ± 0.115	1.563 ± 0.114	30.9	19.0
000 30867034	55041.1	2.314 ± 0.154	1.357 ± 0.067	40.48	58.0
000 30867035	55042.7	2.322 ± 0.144	1.433 ± 0.064	49.54	58.0
000 30867036	55043.5	2.73 ± 0.206	1.329 ± 0.077	46.15	45.0

Obs.Id	**Time in MJD**	**Flux in 0.3-10 keV** 10^{-11} **ergs cm**$^{-2}$ **s**$^{-1}$	**Photon index,** Γ_x	χ^2	**Dof**
000 30867037	55044.5	2.394 ± 0.13	1.383 ± 0.055	80.33	77.0
000 30867038	55045.2	2.163 ± 0.151	1.403 ± 0.07	75.51	50.0
000 35019020	55170.5	1.524 ± 0.099	1.555 ± 0.068	59.36	50.0
000 35019021	55211.5	1.313 ± 0.108	1.506 ± 0.085	38.16	34.0
000 35019023	55225.8	1.331 ± 0.175	1.484 ± 0.136	14.94	13.0
000 35019024	55237.9	1.629 ± 0.313	1.432 ± 0.188	6.37	8.0
000 35019025	55244.4	1.68 ± 0.281	1.634 ± 0.18	8.54	9.0
000 35019026	55251.6	1.384 ± 0.183	1.607 ± 0.146	9.1	12.0
000 35019029	55272.0	1.467 ± 0.186	1.661 ± 0.136	8.56	12.0
000 35019030	55280.0	1.322 ± 0.242	1.456 ± 0.188	5.79	8.0
000 35019031	55288.8	1.865 ± 0.556	1.572 ± 0.312	3.69	4.0
000 35019033	55300.7	1.383 ± 0.177	1.612 ± 0.146	10.22	14.0
000 35019037	55374.1	0.917 ± 0.134	1.555 ± 0.15	6.58	9.0
000 35019039	55567.9	1.751 ± 0.167	1.527 ± 0.103	24.67	26.0
000 35019040	55588.1	1.498 ± 0.153	1.452 ± 0.103	29.05	24.0
000 35019041	55593.4	1.504 ± 0.221	1.389 ± 0.147	7.8	10.0
000 35019043	55615.0	1.572 ± 0.205	1.615 ± 0.146	8.1	13.0
000 35019044	55621.1	1.345 ± 0.25	1.591 ± 0.193	5.98	6.0
000 35019045	55629.2	1.525 ± 0.224	1.517 ± 0.153	6.07	9.0
000 35019046	55634.2	1.602 ± 0.14	1.482 ± 0.088	24.07	28.0
000 35019047	55642.5	1.892 ± 0.215	1.531 ± 0.118	9.39	16.0
000 35019048	55649.1	1.258 ± 0.232	1.664 ± 0.205	7.18	6.0
000 35019049	55665.7	2.072 ± 0.192	1.451 ± 0.093	28.24	26.0
000 35019052	55684.3	2.251 ± 0.18	1.52 ± 0.083	32.92	35.0
000 35019053	55691.5	1.771 ± 0.245	1.517 ± 0.151	7.43	12.0
000 35019054	55698.3	2.235 ± 0.436	1.401 ± 0.199	10.66	8.0
000 35019055	55705.3	1.81 ± 0.226	1.459 ± 0.135	13.66	17.0
000 35019057	55710.3	1.867 ± 0.176	1.447 ± 0.1	22.57	30.0
000 35019056	55712.1	1.834 ± 0.281	1.495 ± 0.157	12.34	11.0
000 91020001	55725.1	1.846 ± 0.268	1.651 ± 0.168	8.93	11.0
000 91020002	55727.6	1.808 ± 0.258	1.587 ± 0.153	7.68	13.0

Obs.Id	**Time in MJD**	**Flux in 0.3-10 keV** 10^{-11} **ergs cm**$^{-2}$ **s**$^{-1}$	**Photon index,** Γ_x	χ^2	**Dof**
000 91020003	55729.0	1.934 ± 0.43	1.441 ± 0.229	4.75	7.0
000 35019058	55729.8	1.602 ± 0.153	1.596 ± 0.101	26.08	27.0
000 91020005	55733.6	1.305 ± 0.23	1.561 ± 0.185	7.63	7.0
000 91020007	55737.5	1.536 ± 0.232	1.52 ± 0.165	9.88	11.0
000 91020009	55741.6	1.527 ± 0.247	1.569 ± 0.187	11.42	9.0
000 91020011	55745.5	1.385 ± 0.245	1.647 ± 0.193	4.11	7.0
000 91020014	55755.3	1.26 ± 0.176	1.792 ± 0.16	16.95	11.0
000 35019060	55755.4	1.596 ± 0.18	1.554 ± 0.122	11.08	19.0
000 91020017	55761.9	1.427 ± 0.217	1.789 ± 0.171	7.23	8.0
000 91020018	55763.7	1.596 ± 0.257	1.439 ± 0.163	9.13	9.0
000 91020019	55765.9	1.907 ± 0.363	1.292 ± 0.181	5.72	8.0
000 91020020	55768.0	1.248 ± 0.152	1.756 ± 0.133	9.88	12.0
000 91020021	55770.0	1.573 ± 0.284	1.505 ± 0.181	12.28	9.0
000 91020023	55773.3	1.704 ± 0.327	1.497 ± 0.203	5.69	6.0
000 35019061	55774.8	1.629 ± 0.226	1.687 ± 0.162	7.15	11.0
000 35019062	55775.0	1.399 ± 0.216	1.591 ± 0.168	5.59	10.0
000 91020024	55780.0	1.315 ± 0.294	1.642 ± 0.27	3.48	4.0
000 91020025	55782.3	1.484 ± 0.243	1.74 ± 0.197	6.04	8.0
000 35019063	55794.6	1.3 ± 0.131	1.607 ± 0.108	35.48	23.0
000 35019064	55894.7	1.272 ± 0.26	1.626 ± 0.246	8.28	5.0
000 35019065	55931.3	1.771 ± 0.149	1.532 ± 0.09	33.75	32.0
000 35019066	55952.5	1.824 ± 0.168	1.61 ± 0.098	30.87	28.0
000 35019069	55975.0	1.751 ± 0.282	1.491 ± 0.172	6.11	10.0
000 35019069	55975.0	1.751 ± 0.282	1.491 ± 0.172	6.11	10.0
000 35019074	56011.0	1.682 ± 0.284	1.463 ± 0.168	7.38	7.0
000 35019078	56044.3	1.443 ± 0.205	1.754 ± 0.177	11.71	10.0
000 35019079	56052.7	2.078 ± 0.277	1.662 ± 0.15	7.24	11.0
000 35019080	56059.6	1.992 ± 0.293	1.706 ± 0.162	12.73	11.0
000 35019083	56137.9	1.307 ± 0.155	1.564 ± 0.122	20.04	15.0
000 35019084	56151.0	1.196 ± 0.157	1.689 ± 0.141	17.96	12.0

Obs.Id	**Time in MJD**	**Flux in 0.3-10 keV** $10^{-11}\,\mathbf{ergs\,cm^{-2}\,s^{-1}}$	**Photon index,** Γ_x	χ^2	**Dof**
000 35019086	56332.7	1.372 ± 0.183	1.762 ± 0.15	11.41	10.0
000 35019087	56339.5	1.59 ± 0.204	1.668 ± 0.141	17.23	12.0
000 35019088	56346.4	1.961 ± 0.361	1.641 ± 0.209	8.93	7.0
000 35019089	56353.4	2.624 ± 0.461	1.505 ± 0.172	13.46	10.0
000 35019092	56374.9	1.348 ± 0.2	1.886 ± 0.181	9.95	8.0
000 35019093	56383.6	1.372 ± 0.26	1.52 ± 0.19	7.37	5.0
000 35019094	56388.9	1.527 ± 0.337	1.778 ± 0.276	2.51	3.0
000 35019095	56395.6	1.084 ± 0.176	1.714 ± 0.184	10.57	9.0
000 35019096	56401.5	1.115 ± 0.166	1.72 ± 0.16	6.36	8.0
000 35019097	56409.3	1.134 ± 0.235	1.584 ± 0.228	4.26	4.0
000 35019098	56423.2	1.628 ± 0.367	1.523 ± 0.229	3.37	6.0
000 35019099	56437.4	3.313 ± 0.453	1.584 ± 0.145	13.2	11.0
000 33052001	56633.6	2.891 ± 0.184	1.376 ± 0.065	66.46	60.0
000 33052002	56635.7	3.345 ± 0.198	1.503 ± 0.061	59.35	59.0
000 35019100	56638.0	2.309 ± 0.092	1.542 ± 0.042	107.13	120.0
000 80090001	56643.9	1.743 ± 0.206	1.569 ± 0.124	18.74	15.0
000 33059001	56648.3	3.276 ± 0.2	1.392 ± 0.06	50.01	62.0
000 33059002	56650.0	4.778 ± 0.371	1.236 ± 0.075	60.48	41.0
000 35019101	56655.1	3.281 ± 0.613	1.353 ± 0.181	10.77	8.0
000 35019103	56655.2	3.838 ± 0.578	1.452 ± 0.154	12.0	10.0
000 35019104	56655.3	4.976 ± 0.71	1.37 ± 0.142	12.88	12.0
000 35019108	56655.5	4.175 ± 0.67	1.362 ± 0.165	6.3	10.0
000 35019111	56655.7	4.92 ± 0.871	1.4 ± 0.169	9.75	9.0
000 35019112	56655.8	4.386 ± 0.718	1.314 ± 0.162	7.97	8.0
000 35019113	56655.9	4.386 ± 0.724	1.438 ± 0.16	6.68	8.0
000 35019114	56655.9	3.694 ± 0.584	1.542 ± 0.171	8.43	8.0
000 35019117	56656.2	3.31 ± 0.532	1.425 ± 0.166	9.53	8.0
000 35019118	56656.2	3.281 ± 0.657	1.555 ± 0.217	6.11	6.0
000 35019126	56656.7	3.671 ± 0.592	1.441 ± 0.162	10.36	9.0
000 35019127	56656.8	4.462 ± 0.878	1.347 ± 0.191	4.59	6.0
000 35019128	56656.9	4.173 ± 0.827	1.38 ± 0.212	3.54	6.0

Obs.Id	Time in MJD	Flux in 0.3-10 keV	Photon index, Γ_x	χ^2	Dof
		10^{-11} ergs cm^{-2} s^{-1}			
000 35019129	56656.9	4.021 ± 0.728	1.452 ± 0.184	5.97	8.0
000 35019131	56657.0	4.36 ± 0.197	1.389 ± 0.046	99.62	105.0
000 35019132	56658.0	4.158 ± 0.199	1.352 ± 0.049	97.43	101.0
000 35019133	56659.0	3.936 ± 0.181	1.456 ± 0.047	95.31	101.0
000 35019134	56666.9	3.936 ± 0.181	1.456 ± 0.047	95.31	101.0
000 35019135	56673.5	1.878 ± 0.389	1.494 ± 0.226	4.71	4.0
000 35019136	56681.9	2.745 ± 0.48	1.346 ± 0.172	10.57	7.0
000 35019138	56688.9	1.993 ± 0.3	1.506 ± 0.15	16.69	10.0
000 35019140	56701.6	2.238 ± 0.366	1.553 ± 0.177	10.82	8.0
000 35019141	56703.0	1.875 ± 0.284	1.664 ± 0.167	6.08	9.0
000 35019144	56729.2	1.447 ± 0.255	1.602 ± 0.186	4.79	6.0
000 35019148	56745.8	4.105 ± 0.455	1.297 ± 0.106	32.01	20.0
000 35019149	56748.0	1.692 ± 0.208	1.631 ± 0.14	16.06	15.0
000 35019150	56749.1	1.92 ± 0.317	1.454 ± 0.176	9.61	11.0
000 35019151	56749.3	1.834 ± 0.429	1.525 ± 0.26	5.05	5.0
000 35019152	56750.0	2.637 ± 0.296	1.462 ± 0.118	16.62	18.0
000 35019155	56750.3	4.987 ± 0.521	1.214 ± 0.107	13.82	24.0
000 35019157	56751.3	3.052 ± 0.325	1.605 ± 0.115	14.58	18.0
000 35019159	56752.3	5.627 ± 0.818	1.234 ± 0.142	8.04	12.0
000 35019161	56753.3	3.5 ± 0.387	1.416 ± 0.114	12.01	18.0
000 35019162	56754.4	2.869 ± 0.34	1.431 ± 0.12	17.69	18.0
000 35019164	56766.7	1.732 ± 0.21	1.7 ± 0.135	14.84	13.0
000 35019165	56780.5	1.58 ± 0.286	1.756 ± 0.207	3.07	5.0
000 35019166	56786.9	2.202 ± 0.417	1.375 ± 0.186	6.44	8.0
000 35019167	56790.7	1.76 ± 0.179	1.499 ± 0.113	43.56	27.0
000 35019168	56793.2	1.527 ± 0.199	1.542 ± 0.142	10.11	13.0
000 35019169	56797.4	2.017 ± 0.178	1.51 ± 0.095	28.67	31.0
000 35019171	57053.8	1.909 ± 0.323	1.511 ± 0.173	6.99	8.0
000 35019174	57155.2	3.531 ± 0.344	1.373 ± 0.101	35.1	28.0
000 92194001	57156.5	1.583 ± 0.182	1.622 ± 0.131	13.7	17.0
000 92194002	57157.7	1.603 ± 0.222	1.446 ± 0.141	12.4	12.0
000 92194005	57160.7	1.863 ± 0.332	1.37 ± 0.189	6.01	7.0

Obs.Id	**Time in MJD**	**Flux in 0.3-10 keV** 10^{-11} **ergs cm**$^{-2}$ **s**$^{-1}$	**Photon index,** Γ_x	χ^2	**Dof**
000 92194006	57161.5	1.275 ± 0.208	1.612 ± 0.188	8.0	10.0
000 35019176	57188.6	6.565 ± 0.461	1.224 ± 0.067	59.41	48.0
000 35019180	57189.1	12.868 ± 1.327	1.088 ± 0.099	27.27	26.0
000 35019181	57189.7	4.173 ± 0.508	1.354 ± 0.127	22.88	19.0
000 35019185	57190.2	3.588 ± 0.494	1.289 ± 0.135	12.42	15.0
000 35019187	57190.9	2.452 ± 0.591	1.291 ± 0.239	3.33	5.0
000 92194012	57457.2	1.507 ± 0.29	1.457 ± 0.214	5.84	7.0
000 92194013	57458.1	1.026 ± 0.176	1.627 ± 0.205	5.8	7.0
000 92194014	57459.6	2.477 ± 0.425	1.648 ± 0.198	12.83	8.0
000 92194015	57460.5	1.281 ± 0.229	1.566 ± 0.197	7.85	6.0
000 35019190	57465.3	1.271 ± 0.278	1.529 ± 0.219	5.04	5.0
000 35019193	57522.6	0.98 ± 0.254	1.643 ± 0.275	2.33	3.0
000 30867041	57821.1	2.733 ± 0.383	1.401 ± 0.145	11.18	12.0
000 30867042	57822.1	2.328 ± 0.309	1.526 ± 0.141	13.24	14.0
000 30867043	57837.0	3.508 ± 0.437	1.428 ± 0.128	16.49	14.0
000 30867048	57851.8	1.931 ± 0.393	1.438 ± 0.2	3.37	6.0
000 30867049	57855.6	1.423 ± 0.224	1.571 ± 0.171	5.78	10.0
000 30867050	57856.6	1.954 ± 0.356	1.451 ± 0.199	10.06	9.0
000 30867051	57857.3	2.346 ± 0.345	1.622 ± 0.157	12.08	10.0
000 35019194	57894.7	2.601 ± 0.316	1.471 ± 0.123	16.18	18.0
000 35019198	57899.3	2.258 ± 0.279	1.493 ± 0.127	8.69	15.0
000 35019199	57930.3	3.769 ± 0.436	1.417 ± 0.123	22.94	20.0
000 35019200	57932.3	2.38 ± 0.311	1.564 ± 0.145	20.14	14.0
000 35019201	58081.3	1.578 ± 0.234	1.578 ± 0.159	11.77	13.0
000 35019203	58083.7	1.443 ± 0.182	1.573 ± 0.14	14.87	14.0
000 35019204	58085.4	1.972 ± 0.236	1.738 ± 0.137	16.14	16.0
000 35019206	58134.2	9.594 ± 1.304	1.15 ± 0.133	10.93	13.0
000 35019210	58135.1	9.79 ± 0.954	1.309 ± 0.098	38.39	28.0
000 35019211	58136.1	11.356 ± 1.426	1.222 ± 0.127	14.0	18.0
000 35019213	58137.1	11.356 ± 1.426	1.222 ± 0.127	14.0	18.0
000 35019214	58139.1	11.356 ± 1.426	1.222 ± 0.127	14.0	18.0

Obs.Id	**Time in MJD**	**Flux in 0.3-10 keV** 10^{-11} **ergs cm**$^{-2}$ **s**$^{-1}$	**Photon index,** Γ_x	χ^2	**Dof**
000 35019218	58141.2	11.356 ± 1.426	1.222 ± 0.127	14.0	18.0
000 35019219	58143.1	11.356 ± 1.426	1.222 ± 0.127	14.0	18.0
000 35019220	58144.2	2.851 ± 0.327	1.556 ± 0.125	13.85	17.0
000 35019221	58147.7	2.769 ± 0.274	1.418 ± 0.107	16.34	28.0
000 35019222	58150.5	2.184 ± 0.223	1.558 ± 0.11	18.73	23.0
000 35019224	58158.1	3.029 ± 0.305	1.523 ± 0.107	18.57	24.0
000 35019225	58165.3	2.502 ± 0.276	1.432 ± 0.12	23.56	21.0
000 35019227	58173.7	2.502 ± 0.276	1.432 ± 0.12	23.56	21.0
000 35019229	58184.2	1.945 ± 0.317	1.485 ± 0.166	5.73	7.0
000 35019230	58201.5	2.239 ± 0.254	1.401 ± 0.121	13.32	21.0
000 35019231	58202.8	1.672 ± 0.19	1.572 ± 0.129	28.19	19.0
000 35019232	58203.9	2.132 ± 0.334	1.438 ± 0.166	9.35	9.0
000 35019233	58205.7	2.319 ± 0.247	1.488 ± 0.12	17.96	22.0
000 35019234	58225.9	6.001 ± 0.529	1.249 ± 0.085	36.6	32.0
000 35019236	58227.7	4.746 ± 0.436	1.341 ± 0.094	32.09	30.0
000 35019237	58228.4	6.814 ± 1.008	1.265 ± 0.15	17.46	12.0
000 35019238	58240.4	2.649 ± 0.297	1.432 ± 0.121	21.68	21.0
000 35019239	58241.3	3.176 ± 0.329	1.455 ± 0.109	33.14	26.0
000 35019240	58242.5	2.249 ± 0.246	1.607 ± 0.123	16.46	20.0
000 35019241	58249.9	1.688 ± 0.238	1.5 ± 0.151	12.76	13.0
000 35019242	58253.9	2.24 ± 0.355	1.549 ± 0.172	13.38	10.0
000 30867052	58270.3	5.135 ± 0.576	1.226 ± 0.116	29.71	23.0
000 30867054	58276.1	2.615 ± 0.277	1.491 ± 0.117	14.23	22.0
000 30867056	58279.9	1.856 ± 0.326	1.465 ± 0.18	10.15	9.0
000 30867057	58282.0	1.584 ± 0.33	1.681 ± 0.258	4.91	6.0
000 30867058	58284.8	1.513 ± 0.276	1.781 ± 0.236	9.8	8.0
000 30867059	58286.1	2.047 ± 0.318	1.478 ± 0.158	11.05	10.0
000 30867060	58288.6	2.417 ± 0.334	1.489 ± 0.147	12.46	13.0
000 30867061	58292.6	3.731 ± 0.66	1.405 ± 0.184	6.25	9.0
000 30867062	58294.2	2.384 ± 0.298	1.455 ± 0.135	15.1	15.0
000 30867063	58296.3	2.115 ± 0.387	1.417 ± 0.183	7.12	7.0

Obs.Id	**Time in MJD**	**Flux in 0.3-10 keV** 10^{-11} **ergs cm**$^{-2}$ **s**$^{-1}$	**Photon index,** Γ_x	χ^2	**Dof**
000 30867064	58298.9	1.656 ± 0.25	1.602 ± 0.17	11.83	10.0
000 35019243	58927.7	1.281 ± 0.172	1.675 ± 0.153	12.6	13.0
000 30867068	59228.1	1.443 ± 0.253	1.566 ± 0.197	6.03	8.0
000 30867070	59234.4	1.4 ± 0.163	1.703 ± 0.134	14.6	15.0
000 96563001	59736.4	3.054 ± 0.463	1.732 ± 0.188	8.83	9.0
000 96564004	59738.0	1.45 ± 0.26	1.614 ± 0.197	7.54	9.0
000 96564005	59741.5	2.06 ± 0.337	1.487 ± 0.172	7.35	10.0
000 96564006	59742.4	2.121 ± 0.348	1.553 ± 0.181	12.93	9.0
000 96564007	59743.4	1.852 ± 0.231	1.647 ± 0.139	10.08	13.0
000 96564008	59744.3	2.752 ± 0.576	1.385 ± 0.226	5.23	6.0
000 96564009	59745.3	1.484 ± 0.29	1.702 ± 0.215	3.56	6.0
000 96564011	59747.4	1.352 ± 0.253	1.597 ± 0.202	5.52	7.0
000 96564012	59748.5	1.653 ± 0.252	1.52 ± 0.154	13.73	9.0
000 96564013	59749.3	1.75 ± 0.263	1.632 ± 0.163	7.11	10.0
000 96564015	59753.2	1.845 ± 0.393	1.491 ± 0.216	2.87	5.0

Table A.2: Table showing results of power-law fitting of Swift-UVOT observations. From left to right: Observation id, time in MJD, un-absorbed flux in the energy range 2–7 eV, spectral index, chi-square, and degrees of freedom.

Obs.Id	**Time in MJD**	**Flux in 2-7 eV**	**Photon index,** $\Gamma_{o/uv}$	χ^2	**Dof**
		10^{-11} **ergs cm**$^{-2}$ **s**$^{-1}$			
000 30867007	54157.27	2.23 ± 0.04	2.777 ± 0.049	2.04	4.0
000 30867009	54266.79	1.07 ± 0.02	2.665 ± 0.046	5.12	4.0
000 30867017	54686.49	0.38 ± 0.02	2.149 ± 0.135	3.13	4.0
000 30867022	54695.6	0.45 ± 0.02	2.14 ± 0.114	4.65	4.0
000 30867024	54698.01	0.75 ± 0.02	2.164 ± 0.081	3.65	4.0
000 30867025	54823.23	1.26 ± 0.03	2.605 ± 0.058	4.63	4.0
000 30867028	54828.2	1.08 ± 0.03	2.623 ± 0.06	4.87	4.0
000 30867031	54834.23	0.98 ± 0.03	2.654 ± 0.067	4.42	4.0
000 30867032	54836.24	1.01 ± 0.03	2.78 ± 0.066	5.88	4.0
000 30867035	55042.65	0.95 ± 0.02	2.556 ± 0.049	5.22	4.0
000 30867036	55043.52	1.25 ± 0.02	2.393 ± 0.048	7.13	4.0
000 30867044	57838.0	1.46 ± 0.04	2.633 ± 0.075	3.98	4.0
000 30867050	57856.61	0.67 ± 0.03	2.517 ± 0.102	4.12	4.0
000 30867054	58276.07	1.92 ± 0.04	2.434 ± 0.056	6.75	4.0
000 30867056	58279.93	0.84 ± 0.03	2.617 ± 0.09	4.11	4.0
000 30867058	58284.83	1.39 ± 0.04	2.466 ± 0.074	4.74	4.0
000 30867060	58288.63	1.68 ± 0.04	2.342 ± 0.065	5.65	4.0
000 30867061	58292.61	2.32 ± 0.07	2.633 ± 0.075	2.49	4.0
000 30867062	58294.2	1.51 ± 0.04	2.468 ± 0.067	4.89	4.0
000 30867064	58298.85	1.28 ± 0.04	2.575 ± 0.073	6.19	4.0
000 30867068	59228.11	3.78 ± 0.07	2.572 ± 0.048	4.26	4.0
000 33052001	56633.59	0.6 ± 0.01	2.523 ± 0.063	2.71	4.0
000 35019006	53754.05	0.87 ± 0.02	2.775 ± 0.051	4.19	4.0
000 35019023	55225.77	0.28 ± 0.02	2.83 ± 0.148	2.03	4.0
000 35019024	55237.94	0.18 ± 0.02	2.627 ± 0.211	4.79	4.0
000 35019025	55244.42	0.14 ± 0.01	2.238 ± 0.263	3.64	4.0
000 35019026	55251.6	0.13 ± 0.01	2.362 ± 0.29	4.96	4.0
000 35019028	55265.31	0.15 ± 0.02	2.434 ± 0.309	6.82	4.0
000 35019029	55272.0	0.14 ± 0.01	2.357 ± 0.251	4.14	4.0
000 35019032	55293.35	0.16 ± 0.02	2.562 ± 0.264	6.03	4.0
000 35019033	55300.65	0.12 ± 0.01	2.186 ± 0.278	5.05	4.0

Obs.Id	**Time in MJD**	**Flux in 2-7 eV** 10^{-11} **ergs cm**$^{-2}$ **s**$^{-1}$	**Photon index,** $\Gamma_{o/uv}$	χ^2	**Dof**
000 35019034	55314.98	0.11 ± 0.01	2.015 ± 0.331	6.36	4.0
000 35019036	55335.92	0.14 ± 0.01	2.335 ± 0.249	6.06	4.0
000 35019037	55374.07	0.12 ± 0.01	2.227 ± 0.281	4.94	4.0
000 35019038	55547.71	0.46 ± 0.01	2.722 ± 0.086	5.77	4.0
000 35019043	55615.03	0.61 ± 0.02	2.708 ± 0.099	4.68	4.0
000 35019044	55621.12	0.46 ± 0.02	2.806 ± 0.137	4.27	4.0
000 35019045	55629.15	0.45 ± 0.02	2.749 ± 0.123	4.48	4.0
000 35019046	55634.17	0.45 ± 0.01	2.753 ± 0.074	2.08	4.0
000 35019047	55642.52	0.42 ± 0.02	2.78 ± 0.106	6.32	4.0
000 35019050	55671.76	0.96 ± 0.03	2.744 ± 0.077	4.84	4.0
000 35019052	55684.26	0.64 ± 0.02	2.734 ± 0.062	4.06	4.0
000 35019053	55691.5	0.72 ± 0.03	2.8 ± 0.094	2.65	4.0
000 35019064	55894.65	1.2 ± 0.05	2.655 ± 0.107	3.57	4.0
000 35019066	55952.46	1.52 ± 0.03	2.584 ± 0.048	3.3	4.0
000 35019067	55961.16	1.16 ± 0.03	2.575 ± 0.078	2.07	4.0
000 35019068	55967.05	1.23 ± 0.03	2.473 ± 0.073	2.47	4.0
000 35019069	55975.0	1.5 ± 0.04	2.544 ± 0.066	3.7	4.0
000 35019072	55998.19	1.05 ± 0.03	2.472 ± 0.072	4.37	4.0
000 35019073	56003.08	0.93 ± 0.03	2.537 ± 0.081	3.08	4.0
000 35019075	56017.99	0.82 ± 0.03	2.493 ± 0.094	5.02	4.0
000 35019083	56137.93	0.59 ± 0.02	2.341 ± 0.097	4.55	4.0
000 35019084	56151.03	0.83 ± 0.04	2.402 ± 0.112	4.59	4.0
000 35019085	56326.32	1.0 ± 0.03	2.353 ± 0.074	3.9	4.0
000 35019087	56339.48	0.81 ± 0.03	2.288 ± 0.089	6.21	4.0
000 35019092	56374.94	1.16 ± 0.03	2.288 ± 0.073	3.13	4.0
000 35019095	56395.64	0.81 ± 0.03	2.453 ± 0.088	5.36	4.0
000 35019099	56437.38	0.86 ± 0.03	2.366 ± 0.086	2.66	4.0
000 35019100	56638.0	0.6 ± 0.01	2.594 ± 0.049	2.82	4.0
000 35019138	56688.92	1.57 ± 0.04	2.53 ± 0.073	4.8	4.0
000 35019141	56702.98	1.77 ± 0.04	2.428 ± 0.065	4.7	4.0
000 35019157	56751.32	2.01 ± 0.05	2.448 ± 0.06	6.78	4.0

Obs.Id	Time in MJD	Flux in 2-7 eV	Photon index, $\Gamma_{o/uv}$	χ^2	Dof
		10^{-11} **ergs cm^{-2} s^{-1}**			
000 35019159	56752.32	1.93 ± 0.05	2.464 ± 0.062	2.76	4.0
000 35019165	56780.52	1.62 ± 0.04	2.387 ± 0.069	3.36	4.0
000 35019166	56786.92	1.68 ± 0.05	2.526 ± 0.071	3.05	4.0
000 35019167	56790.73	1.96 ± 0.04	2.373 ± 0.051	4.03	4.0
000 35019168	56793.19	1.96 ± 0.04	2.35 ± 0.054	2.77	4.0
000 35019171	57053.79	0.92 ± 0.03	2.57 ± 0.084	4.42	4.0
000 35019175	57165.98	0.71 ± 0.03	2.39 ± 0.114	5.65	4.0
000 35019190	57465.28	1.55 ± 0.05	2.409 ± 0.079	4.21	4.0
000 35019192	57515.93	0.67 ± 0.03	2.387 ± 0.136	3.44	4.0
000 35019193	57522.64	0.78 ± 0.03	2.604 ± 0.121	2.52	4.0
000 35019211	58136.13	3.84 ± 0.07	2.44 ± 0.05	2.79	4.0
000 35019213	58137.07	3.63 ± 0.08	2.521 ± 0.062	5.01	4.0
000 35019214	58139.12	3.23 ± 0.07	2.442 ± 0.053	6.22	4.0
000 35019218	58141.24	3.15 ± 0.06	2.465 ± 0.052	4.12	4.0
000 35019219	58143.1	3.05 ± 0.06	2.475 ± 0.054	2.04	4.0
000 35019224	58158.12	1.08 ± 0.03	2.502 ± 0.065	4.51	4.0
000 35019225	58165.28	1.46 ± 0.03	2.445 ± 0.06	6.86	4.0
000 35019229	58184.22	1.8 ± 0.05	2.591 ± 0.078	6.96	4.0
000 35019238	58240.4	2.96 ± 0.05	2.259 ± 0.048	4.39	4.0
000 35019244	58928.69	2.27 ± 0.05	2.611 ± 0.061	2.95	4.0
000 90022002	54894.79	0.71 ± 0.03	2.792 ± 0.097	2.78	4.0
000 90022009	54905.09	0.55 ± 0.02	2.644 ± 0.104	2.56	4.0
000 90022010	54906.63	0.5 ± 0.02	2.593 ± 0.113	3.42	4.0
000 90109001	54936.64	0.32 ± 0.01	2.561 ± 0.131	2.82	4.0
000 90109004	54939.85	0.36 ± 0.01	2.444 ± 0.097	2.23	4.0
000 90109010	54945.67	0.41 ± 0.01	2.491 ± 0.088	5.57	4.0
000 90109011	54946.66	0.4 ± 0.01	2.698 ± 0.09	2.84	4.0
000 90109013	54948.28	0.38 ± 0.01	2.709 ± 0.097	4.86	4.0
000 90109014	54949.88	0.34 ± 0.01	2.626 ± 0.104	6.19	4.0
000 90109017	54953.43	0.54 ± 0.02	2.478 ± 0.082	4.28	4.0
000 90109018	54954.64	0.4 ± 0.02	2.443 ± 0.122	2.9	4.0

Obs.Id	Time in MJD	Flux in 2-7 eV	Photon index, $\Gamma_{o/uv}$	χ^2	Dof
		10^{-11} ergs cm^{-2} s^{-1}			
000 90109019	54955.58	0.32 ± 0.01	2.413 ± 0.111	2.71	4.0
000 90109022	54961.07	0.29 ± 0.01	2.436 ± 0.118	6.5	4.0
000 90109025	54964.81	0.23 ± 0.01	2.457 ± 0.137	5.16	4.0
000 90109026	54965.01	0.26 ± 0.01	2.546 ± 0.127	2.23	4.0
000 90109028	54967.02	0.23 ± 0.01	2.376 ± 0.129	3.75	4.0
000 90109032	54971.38	0.27 ± 0.01	2.362 ± 0.132	3.66	4.0
000 90109033	54972.78	0.45 ± 0.02	2.388 ± 0.107	2.55	4.0
000 90109035	54974.66	0.29 ± 0.01	2.395 ± 0.123	2.52	4.0
000 90109036	54975.71	0.24 ± 0.01	2.339 ± 0.118	4.82	4.0
000 90109037	54976.12	0.23 ± 0.01	2.462 ± 0.122	6.41	4.0
000 90109039	54978.25	0.22 ± 0.01	2.336 ± 0.12	2.37	4.0
000 90109040	54979.05	0.19 ± 0.01	2.463 ± 0.172	2.26	4.0
000 90109041	54980.12	0.16 ± 0.01	2.429 ± 0.186	6.51	4.0
000 96564004	59738.04	0.71 ± 0.03	2.553 ± 0.102	3.19	4.0
000 96564005	59741.49	0.62 ± 0.03	2.447 ± 0.123	2.04	4.0
000 96564007	59743.35	0.66 ± 0.03	2.545 ± 0.105	6.02	4.0
000 96564009	59745.34	0.66 ± 0.03	2.496 ± 0.114	3.26	4.0
000 96564010	59746.41	0.64 ± 0.03	2.497 ± 0.114	2.91	4.0
000 96564012	59748.53	0.72 ± 0.03	2.362 ± 0.109	2.81	4.0
000 96564013	59749.32	0.74 ± 0.03	2.559 ± 0.106	2.88	4.0
000 30867003	54118.22	5.65 ± 0.15	2.63 ± 0.072	2.7	4.0
000 30867004	54119.22	5.6 ± 0.15	2.628 ± 0.071	3.63	4.0
000 30867005	54120.18	5.29 ± 0.14	2.642 ± 0.07	3.58	4.0
000 30867008	54265.78	1.17 ± 0.04	2.737 ± 0.08	3.57	4.0
000 30867018	54688.43	0.36 ± 0.02	1.992 ± 0.169	3.99	4.0
000 30867019	54690.77	0.43 ± 0.03	2.226 ± 0.186	4.73	4.0
000 30867021	54694.32	0.41 ± 0.03	2.225 ± 0.207	3.01	4.0
000 30867023	54696.33	0.56 ± 0.03	2.115 ± 0.163	3.27	4.0
000 30867029	54830.21	1.04 ± 0.04	2.583 ± 0.1	3.25	4.0
000 30867034	55041.1	0.82 ± 0.03	2.585 ± 0.097	3.22	4.0
000 30867037	55044.45	1.08 ± 0.04	2.439 ± 0.089	2.94	4.0

Obs.Id	**Time in MJD**	**Flux in 2-7 eV**	**Photon index,** $\Gamma_{o/uv}$	χ^2	**Dof**
		10^{-11} **ergs cm**$^{-2}$ **s**$^{-1}$			
000 30867038	55045.18	0.72 ± 0.03	2.508 ± 0.103	2.92	4.0
000 30867040	57820.47	6.75 ± 0.21	2.783 ± 0.08	4.58	4.0
000 30867041	57821.12	5.1 ± 0.15	2.745 ± 0.076	3.42	4.0
000 30867063	58296.25	1.14 ± 0.05	2.5 ± 0.12	6.77	4.0
000 30867067	59003.45	1.31 ± 0.05	2.514 ± 0.102	6.0	4.0
000 30867070	59234.42	2.24 ± 0.07	2.725 ± 0.079	3.59	4.0
000 33059001	56648.27	0.71 ± 0.03	2.464 ± 0.106	3.86	4.0
000 35019001	53748.03	1.38 ± 0.04	2.74 ± 0.076	2.72	4.0
000 35019002	53749.03	1.22 ± 0.04	2.747 ± 0.077	2.25	4.0
000 35019004	53752.04	1.03 ± 0.03	2.745 ± 0.077	2.26	4.0
000 35019021	55211.45	0.26 ± 0.01	2.846 ± 0.142	4.76	4.0
000 35019021	55211.45	0.26 ± 0.01	2.854 ± 0.141	3.79	4.0
000 35019034	55314.98	0.11 ± 0.01	1.981 ± 0.371	5.93	4.0
000 35019041	55593.35	0.39 ± 0.02	2.667 ± 0.161	6.62	4.0
000 35019047	55642.52	0.41 ± 0.02	2.773 ± 0.135	4.7	4.0
000 35019057	55710.29	1.37 ± 0.05	2.822 ± 0.086	2.76	4.0
000 35019060	55755.39	1.43 ± 0.05	2.623 ± 0.086	3.98	4.0
000 35019061	55774.84	1.08 ± 0.05	2.782 ± 0.102	5.78	4.0
000 35019071	55989.52	1.56 ± 0.05	2.367 ± 0.094	4.07	4.0
000 35019080	56059.55	1.23 ± 0.05	2.484 ± 0.097	4.84	4.0
000 35019082	56123.1	0.7 ± 0.03	2.409 ± 0.113	3.84	4.0
000 35019091	56367.26	1.06 ± 0.04	2.171 ± 0.097	4.59	4.0
000 35019096	56401.53	1.06 ± 0.04	2.171 ± 0.097	4.59	4.0
000 35019146	56738.85	1.69 ± 0.07	2.432 ± 0.111	6.29	4.0
000 35019148	56745.79	1.87 ± 0.06	2.55 ± 0.089	7.07	4.0
000 35019152	56749.98	2.26 ± 0.07	2.382 ± 0.086	5.01	4.0
000 35019155	56750.32	2.19 ± 0.07	2.391 ± 0.086	3.05	4.0
000 35019163	56759.25	1.71 ± 0.06	2.427 ± 0.093	4.51	4.0
000 35019191	57474.19	2.18 ± 0.08	2.394 ± 0.104	3.46	4.0
000 35019201	58081.28	1.57 ± 0.06	2.198 ± 0.116	4.13	4.0
000 35019204	58085.38	5.87 ± 0.16	2.244 ± 0.074	3.35	4.0

Obs.Id	**Time in MJD**	**Flux in 2-7 eV** 10^{-11} **ergs cm**$^{-2}$ **s**$^{-1}$	**Photon index,** $\Gamma_{o/uv}$	χ^2	**Dof**
000 35019210	58135.13	3.3 ± 0.1	2.398 ± 0.081	3.84	4.0
000 35019220	58144.23	2.79 ± 0.08	2.524 ± 0.081	5.31	4.0
000 35019221	58147.68	2.34 ± 0.07	2.504 ± 0.077	4.25	4.0
000 35019239	58241.26	3.3 ± 0.09	2.268 ± 0.077	4.34	4.0
000 35019243	58927.69	2.35 ± 0.08	2.575 ± 0.084	3.18	4.0
000 90109015	54950.63	0.4 ± 0.02	2.619 ± 0.139	5.85	4.0
000 90109021	54960.53	0.29 ± 0.02	2.551 ± 0.146	6.26	4.0
000 90109043	54982.07	0.2 ± 0.01	2.388 ± 0.18	5.7	4.0
000 96564008	59744.28	0.61 ± 0.04	2.757 ± 0.144	5.77	4.0
000 30867055	58278.06	1.01 ± 0.05	2.527 ± 0.148	6.09	4.0
000 35019074	56010.96	0.76 ± 0.04	2.518 ± 0.124	5.1	4.0
000 35019082	56123.1	0.69 ± 0.03	2.392 ± 0.113	3.82	4.0
000 35019071	55997.0	1.73 ± 0.05	2.57 ± 0.086	4.47	4.0
000 35019164	56766.67	1.53 ± 0.05	2.469 ± 0.093	3.94	4.0
000 35019169	56797.39	1.99 ± 0.06	2.414 ± 0.079	2.66	4.0
000 35019170	56808.64	1.19 ± 0.06	2.458 ± 0.126	5.43	4.0
000 30867001	54113.0	8.57 ± 0.33	2.586 ± 0.104	1.93	4.0
000 30867010	54289.48	2.29 ± 0.1	2.666 ± 0.111	1.96	4.0
000 30867011	54291.22	2.35 ± 0.1	2.66 ± 0.111	2.16	4.0
000 30867012	54292.69	2.71 ± 0.12	2.622 ± 0.111	2.13	4.0
000 30867013	54293.35	2.76 ± 0.12	2.593 ± 0.11	1.8	4.0
000 30867014	54294.36	2.91 ± 0.12	2.652 ± 0.11	2.1	4.0
000 30867015	54295.3	2.86 ± 0.12	2.638 ± 0.11	1.77	4.0
000 30867052	58270.3	4.3 ± 0.18	2.498 ± 0.108	3.24	4.0
000 35019063	55794.58	2.07 ± 0.11	2.533 ± 0.134	2.49	4.0
000 35019048	55649.14	0.43 ± 0.03	3.054 ± 0.18	4.49	4.0
000 35019058	55729.84	1.48 ± 0.07	2.892 ± 0.118	1.74	4.0
000 35019093	56383.61	0.88 ± 0.05	2.445 ± 0.144	4.7	4.0
000 35019055	55705.34	1.24 ± 0.06	2.838 ± 0.125	5.01	4.0
000 35019063	55794.58	2.06 ± 0.11	2.533 ± 0.134	2.68	4.0
000 96564002	59731.48	1.1 ± 0.05	2.952 ± 0.135	5.35	4.0

Obs.Id	**Time in MJD**	**Flux in 2-7 eV** 10^{-11} **ergs cm**$^{-2}$ **s**$^{-1}$	**Photon index,** $\Gamma_{o/uv}$	χ^2	**Dof**
000 35019078	56044.26	1.03 ± 0.06	2.417 ± 0.133	4.48	4.0
000 35019097	56409.26	0.69 ± 0.05	2.681 ± 0.168	4.89	4.0
000 35019173	57150.17	0.65 ± 0.05	2.63 ± 0.182	5.41	4.0

Table A.3: Table showing Details of best fit parameter values of power-law fit of selected γ-ray observations (adaptive time bins) simultanoeus to Swift observtaions. From left to right: column 1–Tstart in MJD, column 2–Tstop, column 3–integrated flux in the energy 0.157-300 GeV, column 4–spectral index, column 5– TS of power-law function, column 6: TS of log-parabola model, and column 8: TS(Curvature).

Tstart MJD	Tstop MJD	Flux [0.1-300 GeV] 10^{-7}phs cm^{-2} s^{-1}	PL Index Γ_γ	TS(PL)	TS(LP)	TS(Curvature)
54693.0	54696.0271	1.048 ± 0.52	2.006 ± 0.302	34.58	34.59	0.02
54693.0	54696.0271	1.048 ± 0.52	2.006 ± 0.302	34.58	34.59	0.02
54696.0271	54697.0139	6.201 ± 1.743	2.391 ± 0.273	57.42	57.42	0.0
54697.8665	54698.2684	8.895 ± 2.604	2.13 ± 0.235	72.46	72.46	0.0
54795.0751	54795.6055	15.33 ± 3.844	2.199 ± 0.208	110.21	110.21	0.0
54795.6055	54795.8768	16.22 ± 4.402	2.14 ± 0.215	73.69	73.69	0.01
54796.1294	54796.6023	15.31 ± 4.241	2.306 ± 0.247	73.41	74.42	1.01
54798.9292	54799.1258	19.0 ± 5.224	2.387 ± 0.26	86.59	86.87	0.28
54799.8488	54800.0567	15.07 ± 3.945	2.294 ± 0.237	85.34	86.82	1.47
54815.7986	54816.1867	11.25 ± 2.847	2.322 ± 0.231	68.75	71.6	2.85
54824.1679	54824.5548	10.78 ± 2.786	2.158 ± 0.208	75.08	75.46	0.38
54827.8209	54828.2106	10.45 ± 2.754	2.284 ± 0.229	62.21	64.4	2.19

Tstart MJD	Tstop MJD	Flux [0.1-300 GeV] 10^{-7}phs cm^{-2} s^{-1}	PL Index Γ_γ	TS(PL)	TS(LP)	TS(Curvature)
54829.8017	54830.6031	3.939 ± 1.312	2.209 ± 0.253	54.93	55.33	0.4
54831.9298	54832.5894	6.653 ± 1.935	2.298 ± 0.239	61.27	62.97	1.7
54833.8503	54834.3066	9.214 ± 2.389	2.433 ± 0.25	64.09	64.69	0.6
54835.7782	54836.4362	6.559 ± 1.936	2.34 ± 0.25	53.44	53.69	0.25
54838.1632	54838.8986	6.15 ± 1.954	2.273 ± 0.277	36.82	39.72	2.9
54863.9278	54864.3817	9.212 ± 2.444	2.208 ± 0.23	60.04	60.58	0.54
54865.5799	54866.1196	8.374 ± 2.155	2.222 ± 0.212	79.42	79.57	0.15
54879.8545	54880.0624	20.17 ± 4.394	2.36 ± 0.209	103.61	104.29	0.68
54886.9723	54887.4289	15.24 ± 3.503	2.839 ± 0.292	78.93	79.15	0.22
54893.0061	54893.5393	8.738 ± 2.791	1.933 ± 0.207	65.8	66.18	0.38
54896.3141	54896.7824	8.08 ± 2.434	2.309 ± 0.255	54.33	55.89	1.57
54896.7824	54897.8504	8.111 ± 2.075	2.753 ± 0.265	56.55	60.51	3.95
54900.435	54906.6066	2.525 ± 1.034	1.846 ± 0.235	44.35	45.02	0.67
54900.435	54906.6066	2.525 ± 1.034	1.846 ± 0.235	44.35	45.02	0.67
54906.6066	54908.8049	2.787 ± 0.935	2.491 ± 0.29	30.95	31.44	0.5
54914.4469	54917.0375	2.265 ± 0.779	2.72 ± 0.335	19.76	21.33	1.57
54935.0939	54937.1485	2.051 ± 0.765	2.433 ± 0.304	25.39	26.24	0.85
54937.1485	54938.69	3.183 ± 1.041	2.543 ± 0.315	33.02	33.02	0.0
54938.69	54940.9354	1.488 ± 0.694	2.536 ± 0.381	12.24	16.01	3.76
54940.9354	54942.3323	2.065 ± 0.974	1.988 ± 0.298	38.31	36.94	-1.37
54942.3323	54944.1149	2.924 ± 0.962	2.594 ± 0.309	31.32	31.32	0.0
54944.1149	54946.3841	1.585 ± 0.625	2.063 ± 0.248	38.87	39.41	0.54
54944.1149	54946.3841	1.585 ± 0.625	2.063 ± 0.248	38.87	39.41	0.54
54946.3841	54947.7007	5.015 ± 1.265	2.711 ± 0.299	53.52	53.82	0.3
54947.7007	54949.3076	2.232 ± 0.97	2.068 ± 0.284	36.1	36.1	0.0
54949.3076	54951.3626	4.293 ± 1.186	2.813 ± 0.302	37.15	40.84	3.69
54949.3076	54951.3626	4.293 ± 1.186	2.813 ± 0.302	37.15	40.84	3.69
54952.6791	54954.6765	4.145 ± 1.287	2.411 ± 0.3	39.15	39.15	0.0
54952.6791	54954.6765	4.145 ± 1.287	2.411 ± 0.3	39.15	39.15	0.0
54954.6765	54957.6083	3.383 ± 0.969	3.112 ± 0.38	28.98	29.03	0.05
54957.6083	54959.7373	1.965 ± 0.978	2.158 ± 0.322	22.14	22.99	0.85

Tstart MJD	Tstop MJD	Flux [0.1-300 GeV] 10^{-7}phs cm^{-2} s^{-1}	PL Index Γ_γ	Ts(PL)	Ts(LP)	Ts(Curvature)
54959.7373	54961.6665	4.83 ± 1.382	2.685 ± 0.32	33.68	33.68	0.0
54959.7373	54961.6665	4.83 ± 1.382	2.685 ± 0.32	33.68	33.68	0.0
54961.6665	54965.4441	2.158 ± 0.744	2.813 ± 0.382	20.72	20.72	0.0
54961.6665	54965.4441	2.158 ± 0.744	2.813 ± 0.382	20.72	20.72	0.0
54961.6665	54965.4441	2.158 ± 0.744	2.813 ± 0.382	20.72	20.72	0.0
54965.4441	54968.699	1.555 ± 0.642	2.43 ± 0.316	21.86	22.48	0.62
54965.4441	54968.699	1.555 ± 0.642	2.43 ± 0.316	21.86	22.48	0.62
54968.699	54970.8815	3.569 ± 0.92	2.699 ± 0.274	41.61	42.87	1.27
54970.8815	54971.7455	4.075 ± 1.595	2.321 ± 0.312	28.42	28.42	0.0
54972.6865	54973.6725	4.897 ± 1.228	2.307 ± 0.214	67.65	75.36	7.7
54972.6865	54973.6725	4.897 ± 1.228	2.307 ± 0.214	67.65	75.36	7.7
54973.6725	54975.3231	3.331 ± 0.909	2.622 ± 0.286	40.77	41.28	0.51
54975.3231	54977.1851	3.505 ± 0.978	2.73 ± 0.306	47.77	47.77	0.0
54975.3231	54977.1851	3.505 ± 0.978	2.73 ± 0.306	47.77	47.77	0.0
54977.1851	54978.9226	2.021 ± 0.714	2.242 ± 0.262	28.89	30.76	1.86
54977.1851	54978.9226	2.021 ± 0.714	2.242 ± 0.262	28.89	30.76	1.86
54978.9226	54980.9071	1.769 ± 0.687	2.495 ± 0.367	16.62	17.4	0.79
54980.9071	54982.2447	2.987 ± 0.892	2.206 ± 0.233	53.26	53.67	0.4
55040.8613	55041.2518	16.58 ± 4.042	2.456 ± 0.264	85.72	85.72	0.0
55042.575	55042.8466	14.26 ± 3.571	2.378 ± 0.238	86.11	86.11	0.0
55043.5158	55043.7171	29.14 ± 6.865	2.709 ± 0.263	95.94	95.95	0.01
55044.4476	55044.7829	13.08 ± 3.53	2.379 ± 0.239	74.74	74.8	0.05
55044.9776	55045.3029	13.04 ± 3.259	2.083 ± 0.197	96.98	98.16	1.18
55169.7179	55170.9057	7.68 ± 2.177	2.537 ± 0.274	54.72	54.72	0.0
55210.9443	55212.1963	7.135 ± 1.904	2.454 ± 0.238	59.96	61.94	1.98
55222.422	55225.8774	1.939 ± 0.754	2.276 ± 0.31	22.19	22.81	0.63
55236.9673	55238.8149	4.862 ± 1.456	2.81 ± 0.353	33.52	33.52	0.0
55242.8126	55244.8029	3.203 ± 0.91	2.629 ± 0.303	33.41	34.95	1.54
55248.2537	55251.7076	1.881 ± 0.552	2.666 ± 0.297	26.73	29.28	2.55
55268.4989	55272.5938	3.764 ± 1.06	3.407 ± 0.471	27.39	28.96	1.57
55278.6015	55281.7848	1.69 ± 0.773	2.283 ± 0.339	17.89	18.81	0.91

Tstart MJD	Tstop MJD	Flux [0.1-300 GeV] 10^{-7}phs cm^{-2} s^{-1}	PL Index Γ_γ	Ts(PL)	Ts(LP)	Ts(Curvature)
55286.6305	55289.8737	6.422 ± 1.372	3.376 ± 0.316	61.74	61.76	0.02
55300.4288	55303.2114	1.314 ± 0.513	2.195 ± 0.277	27.58	27.81	0.23
55369.1367	55374.319	1.166 ± 0.464	2.323 ± 0.278	19.24	23.77	4.52
55566.6293	55568.0271	4.371 ± 1.105	2.566 ± 0.275	49.6	50.71	1.11
55586.4739	55588.7916	2.363 ± 1.025	2.138 ± 0.297	32.45	34.73	2.29
55591.7113	55594.901	2.011 ± 0.846	2.202 ± 0.29	40.54	40.54	0.0
55614.6308	55616.3438	4.771 ± 1.249	2.605 ± 0.28	49.41	49.41	0.0
55619.7917	55621.1282	2.655 ± 0.917	2.146 ± 0.249	28.55	33.09	4.54
55627.89	55630.5541	2.834 ± 0.863	2.643 ± 0.315	28.2	28.66	0.47
55632.1454	55635.3173	2.743 ± 0.906	2.536 ± 0.307	32.97	33.05	0.08
55641.5031	55643.8946	3.003 ± 0.964	2.273 ± 0.256	40.13	41.45	1.33
55643.8946	55649.7986	2.015 ± 0.799	2.476 ± 0.313	27.02	27.02	0.0
55663.6583	55667.5305	11.5 ± 3.082	2.164 ± 0.208	76.1	79.55	3.45
55682.9078	55684.5087	4.645 ± 1.189	2.513 ± 0.241	50.36	52.97	2.61
55690.6179	55691.8107	4.242 ± 1.455	2.005 ± 0.214	50.49	48.41	-2.08
55698.1068	55698.393	22.12 ± 5.246	2.421 ± 0.235	101.5	102.89	1.39
55704.6826	55705.4084	12.69 ± 3.541	2.252 ± 0.23	74.71	74.71	0.0
55709.4635	55710.3224	10.4 ± 2.709	2.101 ± 0.195	87.91	90.14	2.23
55711.3274	55712.3939	7.194 ± 2.003	2.307 ± 0.237	56.54	57.35	0.8
55724.7273	55725.2714	10.05 ± 2.354	2.471 ± 0.236	81.14	81.79	0.65
55726.9882	55727.6401	12.34 ± 2.332	2.642 ± 0.227	115.47	119.65	4.17
55728.9779	55729.5252	7.251 ± 1.977	2.185 ± 0.222	63.52	63.92	0.4
55729.5252	55730.7006	4.093 ± 1.125	2.184 ± 0.214	53.06	57.52	4.46
55732.5621	55733.878	4.918 ± 1.269	2.611 ± 0.279	52.08	52.08	0.0
55736.5536	55738.1341	2.994 ± 1.041	2.184 ± 0.258	43.37	43.54	0.17
55741.0485	55741.602	7.554 ± 2.292	1.99 ± 0.197	68.0	72.58	4.58
55744.7087	55745.6439	5.095 ± 2.09	2.164 ± 0.286	33.92	33.95	0.03
55753.1928	55756.6606	2.477 ± 0.819	2.394 ± 0.269	41.37	41.4	0.03
55759.4454	55762.6283	2.393 ± 0.749	2.111 ± 0.218	41.73	47.27	5.54
55762.6283	55767.2122	2.668 ± 0.851	2.709 ± 0.283	25.32	30.77	5.45
55762.6283	55767.2122	2.668 ± 0.851	2.709 ± 0.283	25.32	30.77	5.45

Tstart MJD	Tstop MJD	Flux [0.1-300 GeV] 10^{-7}phs cm^{-2} s^{-1}	PL Index Γ_γ	Ts(PL)	Ts(LP)	Ts(Curvature)
55767.2122	55769.7993	2.798 ± 1.018	2.215 ± 0.295	35.44	35.44	0.0
55769.7993	55772.9052	2.26 ± 0.7	2.199 ± 0.215	45.42	51.9	6.49
55772.9052	55775.1686	2.291 ± 0.736	2.162 ± 0.228	43.54	44.22	0.69
55772.9052	55775.1686	2.291 ± 0.736	2.162 ± 0.228	43.54	44.22	0.69
55772.9052	55775.1686	2.291 ± 0.736	2.162 ± 0.228	43.54	44.22	0.69
55779.9588	55781.2674	4.117 ± 1.174	2.398 ± 0.256	52.78	53.89	1.11
55781.2674	55782.5994	2.298 ± 0.767	1.896 ± 0.211	50.63	56.57	5.95
55793.1003	55795.3459	5.406 ± 1.3	2.763 ± 0.261	52.87	55.22	2.35
55893.621	55895.1657	3.297 ± 0.982	2.477 ± 0.269	40.44	42.06	1.62
55929.191	55931.7078	1.805 ± 0.737	2.12 ± 0.268	36.59	36.59	0.0
55951.1632	55952.6116	2.324 ± 1.008	1.993 ± 0.273	38.23	38.23	0.0
55972.9153	55976.9009	1.459 ± 0.551	2.204 ± 0.259	25.01	27.74	2.73
55972.9153	55976.9009	1.459 ± 0.551	2.204 ± 0.259	25.01	27.74	2.73
56008.9257	56013.5023	3.28 ± 1.03	3.156 ± 0.486	29.45	29.45	0.0
56041.7166	56045.283	1.722 ± 0.642	2.493 ± 0.3	23.71	23.79	0.08
56052.716	56054.0554	3.749 ± 1.136	2.399 ± 0.277	36.59	36.67	0.09
56058.4913	56061.6114	3.356 ± 0.964	2.882 ± 0.322	33.09	33.26	0.17
56131.6578	56141.4105	0.64 ± 0.351	2.331 ± 0.354	16.05	16.5	0.45
56150.3679	56151.6964	1.896 ± 0.813	1.74 ± 0.222	45.35	45.76	0.41
56329.1525	56334.003	1.704 ± 0.652	2.638 ± 0.418	21.96	21.96	0.0
56334.003	56341.0243	0.996 ± 0.448	2.428 ± 0.395	13.13	16.8	3.68
56341.0243	56346.5995	0.628 ± 0.362	1.819 ± 0.299	35.67	37.7	2.02
56349.6431	56354.9435	1.383 ± 0.619	2.424 ± 0.315	24.3	25.44	1.14
56374.4727	56376.3572	2.605 ± 0.986	2.375 ± 0.311	31.17	31.28	0.11
56382.6592	56388.7545	1.228 ± 0.612	2.345 ± 0.334	17.13	17.13	0.0
56388.7545	56394.8608	1.796 ± 0.699	2.938 ± 0.593	14.85	14.85	0.0
56394.8608	56402.6172	1.084 ± 0.449	2.427 ± 0.304	16.34	17.59	1.25
56394.8608	56402.6172	1.084 ± 0.449	2.427 ± 0.304	16.34	17.59	1.25
56402.6172	56409.5833	0.389 ± 0.283	1.731 ± 0.324	20.11	21.28	1.17
56419.9871	56424.4959	1.35 ± 0.479	2.639 ± 0.362	22.86	23.42	0.56
56436.494	56438.8252	3.699 ± 0.969	2.625 ± 0.254	43.25	46.96	3.71

Tstart MJD	Tstop MJD	Flux [0.1-300 GeV] 10^{-7}phs cm^{-2} s^{-1}	PL Index Γ_γ	Ts(PL)	Ts(LP)	Ts(Curvature)
56633.5033	56633.6359	21.74 ± 4.712	2.481 ± 0.232	109.29	113.41	4.11
56635.6146	56635.694	16.96 ± 5.089	2.073 ± 0.231	82.21	82.24	0.03
56637.9445	56638.5968	18.5 ± 3.695	2.614 ± 0.252	106.28	106.28	0.0
56643.4578	56644.1637	7.191 ± 1.608	2.666 ± 0.253	70.77	71.32	0.55
56648.2111	56648.606	22.02 ± 6.086	2.109 ± 0.203	91.24	93.57	2.32
56649.7981	56650.1374	24.56 ± 5.69	2.623 ± 0.249	75.19	78.45	3.26
56654.7608	56655.1128	12.75 ± 3.37	2.037 ± 0.195	90.7	91.77	1.07
56655.1128	56655.7743	13.38 ± 3.697	2.111 ± 0.203	74.1	75.71	1.6
56655.1128	56655.7743	13.38 ± 3.697	2.111 ± 0.203	74.1	75.71	1.6
56655.1128	56655.7743	13.38 ± 3.697	2.111 ± 0.203	74.1	75.71	1.6
56655.1128	56655.7743	13.38 ± 3.697	2.111 ± 0.203	74.1	75.71	1.6
56655.7743	56656.6258	10.46 ± 3.299	2.517 ± 0.282	46.54	46.54	0.0
56655.7743	56656.6258	10.46 ± 3.299	2.517 ± 0.282	46.54	46.54	0.0
56655.7743	56656.6258	10.46 ± 3.299	2.517 ± 0.282	46.54	46.54	0.0
56655.7743	56656.6258	10.46 ± 3.299	2.517 ± 0.282	46.54	46.54	0.0
56655.7743	56656.6258	10.46 ± 3.299	2.517 ± 0.282	46.54	46.54	0.0
56656.6258	56656.8876	24.69 ± 6.818	2.418 ± 0.254	57.62	58.6	0.98
56656.8876	56657.1054	23.72 ± 6.585	2.287 ± 0.228	76.48	76.48	0.0
56656.8876	56657.1054	23.72 ± 6.585	2.287 ± 0.228	76.48	76.48	0.0
56657.8092	56658.0821	21.45 ± 5.295	2.418 ± 0.233	86.52	90.24	3.72
56658.6927	56659.0148	17.4 ± 4.945	2.502 ± 0.268	58.5	58.51	0.01
56666.1743	56666.9018	5.522 ± 1.819	2.05 ± 0.244	56.87	56.98	0.11
56673.4079	56673.6023	18.93 ± 5.497	2.141 ± 0.219	79.77	79.8	0.03
56680.415	56693.1574	10.94 ± 2.873	2.441 ± 0.241	60.98	68.3	7.33
56680.415	56693.1574	10.94 ± 2.873	2.441 ± 0.241	60.98	68.3	7.33
56700.5589	56701.9529	7.17 ± 2.032	2.436 ± 0.258	54.1	54.17	0.07
56701.9529	56703.0881	6.116 ± 1.714	2.085 ± 0.197	84.55	88.0	3.45
56727.3461	56729.7185	5.584 ± 1.495	2.501 ± 0.238	52.68	54.05	1.37
56745.6847	56745.8187	41.23 ± 10.76	2.294 ± 0.238	105.01	106.52	1.51
56747.9487	56748.0766	5.872 ± 1.995	1.767 ± 0.21	48.24	49.81	1.56
56749.0021	56749.3218	5.823 ± 1.561	2.315 ± 0.256	56.95	57.42	0.47

Tstart MJD	Tstop MJD	Flux [0.1-300 GeV] 10^{-7}phs cm^{-2} s^{-1}	PL Index Γ_γ	Ts(PL)	Ts(LP)	Ts(Curvature)
56749.0021	56749.3218	5.823 ± 1.561	2.315 ± 0.256	56.95	57.42	0.47
56749.8656	56749.9894	15.89 ± 3.903	2.587 ± 0.277	75.02	75.02	0.0
56750.3168	56750.3219	136.2 ± 28.01	2.347 ± 0.226	184.05	185.53	1.48
56751.312	56751.3673	57.78 ± 13.41	1.98 ± 0.19	127.39	127.73	0.34
56752.3	56752.3731	66.33 ± 16.33	2.027 ± 0.193	159.66	160.11	0.46
56753.037	56753.3658	21.84 ± 5.888	2.142 ± 0.215	89.81	93.16	3.35
56754.0308	56754.4213	20.68 ± 5.461	1.954 ± 0.18	97.26	98.26	1.0
56765.621	56766.8144	5.747 ± 1.697	2.285 ± 0.24	59.37	63.19	3.82
56779.3413	56780.9353	5.422 ± 1.548	2.667 ± 0.337	38.23	38.23	0.0
56786.2223	56787.0276	6.438 ± 1.868	2.408 ± 0.261	46.74	46.76	0.02
56790.6094	56791.3946	4.436 ± 1.295	1.761 ± 0.172	109.67	109.7	0.03
56793.1224	56794.1836	2.986 ± 0.849	1.654 ± 0.148	109.25	111.5	2.25
56797.3579	56797.8795	8.451 ± 2.292	2.132 ± 0.207	66.6	69.0	2.4
57052.4998	57054.7483	3.16 ± 0.986	2.72 ± 0.363	26.21	26.22	0.01
57155.0789	57155.2219	26.69 ± 6.641	2.344 ± 0.243	80.71	89.4	8.7
57156.021	57157.1986	6.441 ± 1.756	2.694 ± 0.318	43.56	43.56	0.0
57157.1986	57159.4448	3.422 ± 0.98	2.62 ± 0.295	35.01	35.01	0.0
57159.4448	57161.5699	4.913 ± 1.017	2.869 ± 0.262	66.37	68.55	2.18
57159.4448	57161.5699	4.913 ± 1.017	2.869 ± 0.262	66.37	68.55	2.18
57188.5163	57188.6187	357.6 ± 93.13	2.324 ± 0.223	150.79	151.17	0.38
57189.0993	57189.1481	506.1 ± 83.75	2.329 ± 0.185	402.82	403.1	0.28
57189.6412	57189.6942	105.1 ± 25.77	2.027 ± 0.197	171.32	173.55	2.23
57190.1578	57190.2315	45.69 ± 7.679	2.522 ± 0.2	200.66	204.98	4.31
57190.7651	57191.0762	14.55 ± 3.296	2.323 ± 0.224	98.83	100.27	1.44
57456.769	57459.5534	3.669 ± 1.121	2.518 ± 0.28	41.23	41.23	0.0
57456.769	57459.5534	3.669 ± 1.121	2.518 ± 0.28	41.23	41.23	0.0
57459.5534	57463.6578	2.327 ± 0.726	2.306 ± 0.244	33.66	34.87	1.21
57459.5534	57463.6578	2.327 ± 0.726	2.306 ± 0.244	33.66	34.87	1.21
57463.6578	57465.6387	4.372 ± 1.307	2.388 ± 0.249	40.21	41.2	0.99
57522.1183	57522.855	8.465 ± 2.434	2.116 ± 0.213	100.75	100.75	0.0
57820.4557	57821.4549	8.702 ± 2.598	2.507 ± 0.261	47.48	48.97	1.5

Tstart MJD	Tstop MJD	Flux [0.1-300 GeV] 10^{-7}phs cm^{-2} s^{-1}	PL Index Γ_γ	Ts(PL)	Ts(LP)	Ts(Curvature)
57821.9972	57822.8984	8.331 ± 2.063	1.843 ± 0.154	85.25	94.13	8.88
57836.7351	57837.1342	19.13 ± 5.013	2.006 ± 0.187	134.66	134.66	0.0
57851.742	57851.8143	19.85 ± 4.802	2.126 ± 0.208	103.65	104.86	1.21
57854.7262	57855.6452	4.243 ± 1.313	2.081 ± 0.228	58.38	58.89	0.51
57856.4338	57856.839	13.64 ± 3.121	2.457 ± 0.24	74.89	74.95	0.06
57857.225	57857.7547	14.43 ± 2.904	2.81 ± 0.257	100.6	100.6	0.0
57894.6634	57895.1831	15.23 ± 4.172	2.441 ± 0.264	64.51	65.1	0.59
57898.7717	57899.5663	8.832 ± 2.472	2.467 ± 0.257	72.23	72.23	0.0
57930.0376	57930.4246	20.78 ± 4.97	2.447 ± 0.238	92.67	94.32	1.65
57932.2822	57933.6063	10.8 ± 2.638	2.603 ± 0.261	73.46	73.46	0.0
58081.0711	58081.9889	4.3 ± 1.434	1.876 ± 0.203	53.6	53.77	0.17
58083.2389	58084.6355	4.547 ± 1.375	2.022 ± 0.204	55.8	58.33	2.53
58085.0327	58085.4883	12.76 ± 3.361	1.945 ± 0.181	81.11	81.71	0.6
58134.1082	58134.1622	178.6 ± 43.4	2.145 ± 0.196	221.68	222.98	1.3
58135.1038	58135.1488	169.0 ± 48.92	1.968 ± 0.207	116.19	117.02	0.83
58136.0948	58136.1374	214.0 ± 54.47	2.166 ± 0.217	151.63	151.69	0.06
58137.066	58137.0747	176.3 ± 39.47	2.523 ± 0.247	167.09	167.12	0.03
58139.0479	58139.1283	43.26 ± 11.05	2.347 ± 0.252	80.55	80.55	0.0
58141.1883	58141.296	62.79 ± 16.48	2.068 ± 0.205	113.77	113.77	0.0
58143.0975	58143.5427	27.36 ± 7.492	2.131 ± 0.218	95.41	95.41	0.0
58144.0212	58144.4733	26.97 ± 7.004	2.438 ± 0.249	95.29	97.59	2.31
58147.6532	58147.7906	27.01 ± 6.48	2.21 ± 0.206	108.15	112.67	4.52
58150.4283	58150.643	18.33 ± 4.285	2.091 ± 0.184	119.7	122.71	3.0
58157.9741	58158.6821	15.27 ± 3.484	2.89 ± 0.281	65.43	66.31	0.87
58165.1849	58165.4312	34.17 ± 7.388	2.441 ± 0.221	123.7	124.3	0.6
58173.649	58173.7801	28.94 ± 6.238	1.9 ± 0.16	157.61	159.28	1.67
58184.0945	58184.6719	14.55 ± 3.904	2.346 ± 0.237	87.75	87.75	0.0
58191.8281	58216.5537	8.389 ± 2.502	2.291 ± 0.249	60.06	60.11	0.04
58225.8856	58225.9321	110.1 ± 26.98	2.217 ± 0.215	124.97	125.1	0.13
58227.7147	58227.7226	110.2 ± 27.66	2.198 ± 0.223	101.57	104.46	2.89
58228.3791	58228.3826	250.2 ± 48.97	1.754 ± 0.133	406.33	413.53	7.2

Tstart MJD	Tstop MJD	Flux [0.1-300 GeV] 10^{-7}phs cm^{-2} s^{-1}	PL Index Γ_γ	Ts(PL)	Ts(LP)	Ts(Curvature)
58240.3607	58240.4844	33.51 ± 7.849	1.908 ± 0.168	156.95	159.79	2.85
58241.1466	58241.272	70.83 ± 14.87	1.819 ± 0.143	205.12	206.48	1.35
58242.5268	58242.5922	37.88 ± 9.795	1.746 ± 0.161	156.78	156.83	0.05
58249.6861	58250.2632	9.979 ± 2.589	2.081 ± 0.195	93.38	95.13	1.76
58251.6761	58256.6869	8.74 ± 2.238	2.041 ± 0.171	112.32	116.42	4.11
58270.2987	58270.3611	136.3 ± 33.23	2.258 ± 0.216	154.81	159.23	4.42
58275.9203	58276.1171	21.99 ± 6.162	1.957 ± 0.198	86.12	86.12	0.0
58279.8954	58280.1459	10.3 ± 2.631	2.215 ± 0.222	87.25	87.25	0.0
58281.6797	58282.0662	10.19 ± 2.352	2.715 ± 0.272	68.12	68.55	0.43
58284.644	58285.0532	6.432 ± 1.919	2.173 ± 0.234	63.44	63.58	0.14
58285.7808	58286.293	5.703 ± 1.921	2.114 ± 0.245	53.29	53.29	0.0
58288.5453	58289.0837	13.45 ± 4.221	2.11 ± 0.233	61.93	61.93	0.0
58292.5846	58292.655	48.24 ± 11.66	2.079 ± 0.193	125.06	126.29	1.23
58293.8385	58294.2415	22.39 ± 5.366	2.437 ± 0.225	90.35	100.46	10.11
58295.5701	58297.352	17.82 ± 4.198	2.491 ± 0.213	95.63	99.5	3.88
58297.352	58304.7658	8.368 ± 2.382	2.404 ± 0.229	50.13	51.54	1.41
58926.7	58927.7474	5.728 ± 1.769	2.003 ± 0.205	50.88	51.35	0.47
59227.5572	59228.1363	9.624 ± 2.162	2.456 ± 0.22	82.43	94.91	12.48
59234.3518	59235.1444	5.955 ± 1.541	2.08 ± 0.197	75.61	76.47	0.86

Table A.4: Table showing results of combined spectral fitting of XRT and UVOT spectra with the Broken power-law model. column 1 – observation id, column 2 – time in MJD, column 3 – optical index, column 4 – break energy, ϵ_b, column 5 – X-ray index, column 6 – chisquare, and column 7 – Dof.

Obs Id	**Time**	$\Gamma_{o/uv}$	**Break energy,ϵ_b**	Γ_x	χ^2	**Dof**
	MJD		keV			
000 30867009	54266.79	2.6645 ± 0.0459	0.1029 ± 0.0049	1.4886 ± 0.0697	40.09	50.0
000 30867022	54695.6	2.1404 ± 0.1136	0.757 ± 0.1657	1.5987 ± 0.1587	21.44	19.0
000 30867024	54698.01	2.1636 ± 0.0809	0.4083 ± 0.1346	1.8595 ± 0.1346	21.53	21.0
000 30867028	54828.2	2.6226 ± 0.0603	0.0987 ± 0.008	1.5496 ± 0.1304	13.62	23.0
000 30867031	54834.23	2.6541 ± 0.0674	0.0787 ± 0.0076	1.5867 ± 0.151	13.82	18.0
000 30867032	54836.24	2.7798 ± 0.0662	0.1001 ± 0.0076	1.4299 ± 0.1572	14.42	18.0
000 30867035	55042.65	2.5564 ± 0.049	0.1048 ± 0.0046	1.433 ± 0.064	55.36	64.0
000 30867036	55043.52	2.3926 ± 0.0481	0.2756 ± 0.0144	1.3288 ± 0.077	52.33	51.0
000 30867050	57856.61	2.5174 ± 0.1015	0.095 ± 0.0106	1.4513 ± 0.199	13.89	15.0
000 30867054	58276.07	2.4337 ± 0.0561	0.2488 ± 0.0207	1.4907 ± 0.1165	20.4	28.0
000 30867056	58279.93	2.617 ± 0.0897	0.0873 ± 0.009	1.4645 ± 0.1803	14.49	15.0
000 30867058	58284.83	2.4664 ± 0.0739	0.1062 ± 0.0193	1.7808 ± 0.2363	14.88	14.0
000 30867060	58288.63	2.3415 ± 0.0649	0.3707 ± 0.0435	1.4886 ± 0.1466	17.54	19.0
000 30867061	58292.61	2.6331 ± 0.0752	0.1292 ± 0.0121	1.4046 ± 0.184	8.26	15.0
000 30867062	58294.2	2.4681 ± 0.0667	0.2025 ± 0.0187	1.4546 ± 0.1351	19.66	21.0
000 30867064	58298.85	2.5753 ± 0.0727	0.1068 ± 0.0124	1.6017 ± 0.1704	17.81	16.0
000 30867068	59228.11	2.5722 ± 0.0476	0.4109 ± 0.0517	1.5663 ± 0.1967	9.2	14.0
000 33052001	56633.59	2.5226 ± 0.0628	0.0762 ± 0.0033	1.3762 ± 0.0654	69.12	66.0
000 35019006	53754.05	2.7746 ± 0.0506	0.0541 ± 0.0024	1.5286 ± 0.0744	50.32	51.0
000 35019023	55225.77	2.8299 ± 0.148	0.0284 ± 0.0022	1.4841 ± 0.1362	17.4	19.0
000 35019024	55237.94	2.6274 ± 0.2112	0.0298 ± 0.0034	1.432 ± 0.1875	10.46	14.0
000 35019025	55244.42	2.2377 ± 0.2626	0.0146 ± 0.0033	1.6341 ± 0.1804	12.36	15.0
000 35019026	55251.6	2.3622 ± 0.2899	0.016 ± 0.0027	1.6066 ± 0.1458	14.19	18.0
000 35019029	55272.0	2.3569 ± 0.2509	0.0123 ± 0.0022	1.6614 ± 0.1356	11.15	18.0
000 35019033	55300.65	2.1864 ± 0.2778	0.0235 ± 0.0049	1.6116 ± 0.1458	16.48	20.0
000 35019037	55374.07	2.2274 ± 0.2808	0.0584 ± 0.0119	1.5547 ± 0.1504	11.33	15.0
000 35019043	55615.03	2.7078 ± 0.0989	0.0363 ± 0.0034	1.6149 ± 0.1457	12.73	19.0
000 35019044	55621.12	2.8063 ± 0.1365	0.0295 ± 0.0034	1.5905 ± 0.1934	10.86	12.0
000 35019045	55629.15	2.7494 ± 0.1233	0.0376 ± 0.0037	1.5171 ± 0.1532	10.49	15.0
000 35019046	55634.17	2.7531 ± 0.0744	0.0405 ± 0.0023	1.4822 ± 0.0882	26.15	34.0
000 35019047	55642.52	2.7802 ± 0.1064	0.0267 ± 0.002	1.5312 ± 0.1182	14.97	22.0

Obs Id	**Time**	$\Gamma_{\rm o/uv}$	**Break energy,**ϵ_b	Γ_x	χ^2	**Dof**
	MJD		keV			
000 35019052	55684.26	2.7335 ± 0.0623	0.0372 ± 0.0019	1.5197 ± 0.0834	36.36	41.0
000 35019053	55691.5	2.7997 ± 0.0937	0.0441 ± 0.0036	1.5168 ± 0.1513	10.66	18.0
000 35019064	55894.65	2.6553 ± 0.1069	0.0923 ± 0.0135	1.6264 ± 0.2463	11.62	11.0
000 35019066	55952.46	2.5836 ± 0.0478	0.1097 ± 0.0079	1.6098 ± 0.0979	33.68	34.0
000 35019069	55975.0	2.5441 ± 0.0661	0.1835 ± 0.0193	1.4912 ± 0.172	9.89	16.0
000 35019069	55975.0	2.5441 ± 0.0661	0.1835 ± 0.0193	1.4912 ± 0.172	9.89	16.0
000 35019083	56137.93	2.3406 ± 0.0972	0.1761 ± 0.0219	1.5637 ± 0.1222	25.09	21.0
000 35019084	56151.03	2.402 ± 0.1116	0.143 ± 0.0217	1.6888 ± 0.1408	21.89	18.0
000 35019087	56339.48	2.2881 ± 0.0894	0.1879 ± 0.0322	1.6678 ± 0.1406	23.41	18.0
000 35019092	56374.94	2.2879 ± 0.0733	0.1856 ± 0.0578	1.8857 ± 0.181	12.73	14.0
000 35019095	56395.64	2.4533 ± 0.0883	0.1111 ± 0.0179	1.7143 ± 0.1835	15.49	15.0
000 35019099	56437.38	2.3661 ± 0.0862	0.0714 ± 0.01	1.5839 ± 0.1447	15.68	17.0
000 35019100	56638.0	2.5939 ± 0.0487	0.0433 ± 0.0014	1.5415 ± 0.0418	109.07	126.0
000 35019138	56688.92	2.5295 ± 0.0734	0.1715 ± 0.0191	1.5064 ± 0.1496	21.29	16.0
000 35019141	56702.98	2.4283 ± 0.0651	0.2078 ± 0.0317	1.6644 ± 0.1671	10.11	15.0
000 35019157	56751.32	2.4479 ± 0.0603	0.1473 ± 0.0149	1.6046 ± 0.1149	20.2	24.0
000 35019159	56752.32	2.4636 ± 0.0624	0.2051 ± 0.0171	1.2343 ± 0.1421	10.97	18.0
000 35019165	56780.52	2.3871 ± 0.0686	0.2163 ± 0.0502	1.7558 ± 0.2066	5.9	11.0
000 35019166	56786.92	2.5259 ± 0.0706	0.2342 ± 0.0249	1.3754 ± 0.1861	9.18	14.0
000 35019167	56790.73	2.3726 ± 0.0507	0.5419 ± 0.0477	1.4991 ± 0.1126	43.78	33.0
000 35019168	56793.19	2.3495 ± 0.054	0.6707 ± 0.0895	1.5422 ± 0.1424	14.94	19.0
000 35019171	57053.79	2.5697 ± 0.0835	0.0918 ± 0.0107	1.5105 ± 0.1725	11.04	14.0
000 35019190	57465.28	2.4091 ± 0.0787	0.4451 ± 0.0754	1.5285 ± 0.2192	9.34	11.0
000 35019211	58136.13	2.4399 ± 0.0503	0.2263 ± 0.0159	1.2218 ± 0.1269	16.13	24.0
000 35019224	58158.12	2.5024 ± 0.0645	0.0818 ± 0.0063	1.5226 ± 0.107	23.39	30.0
000 35019225	58165.28	2.4449 ± 0.0602	0.2175 ± 0.0175	1.4319 ± 0.1196	29.68	27.0
000 35019229	58184.22	2.5907 ± 0.0778	0.1688 ± 0.0198	1.4854 ± 0.1656	12.22	13.0
000 90022009	54905.09	2.6442 ± 0.104	0.1257 ± 0.0139	1.3117 ± 0.2464	5.66	11.0
000 90022010	54906.63	2.5931 ± 0.1125	0.0949 ± 0.0128	1.4889 ± 0.2406	6.93	11.0
000 90109001	54936.64	2.5612 ± 0.1309	0.0538 ± 0.0054	1.4895 ± 0.1623	13.19	18.0
000 90109004	54939.85	2.4443 ± 0.0968	0.0794 ± 0.007	1.4492 ± 0.1225	23.15	25.0

Obs Id	**Time** MJD	$\Gamma_{o/uv}$	**Break energy,**ϵ_b keV	Γ_x	χ^2	**Dof**
000 90109010	54945.67	2.4907 ± 0.0879	0.0755 ± 0.0051	1.4015 ± 0.1006	36.73	33.0
000 90109011	54946.66	2.6981 ± 0.0895	0.0394 ± 0.0024	1.4681 ± 0.0882	35.1	33.0
000 90109013	54948.28	2.7087 ± 0.0967	0.0295 ± 0.0016	1.4559 ± 0.0916	51.23	41.0
000 90109014	54949.88	2.6258 ± 0.1043	0.0305 ± 0.0022	1.5324 ± 0.1038	28.13	30.0
000 90109017	54953.43	2.4784 ± 0.0818	0.0754 ± 0.0064	1.4731 ± 0.1141	25.28	25.0
000 90109018	54954.64	2.4428 ± 0.1222	0.0532 ± 0.0049	1.4925 ± 0.1082	26.77	26.0
000 90109019	54955.58	2.4133 ± 0.111	0.061 ± 0.0047	1.3499 ± 0.1042	24.6	29.0
000 90109022	54961.07	2.4358 ± 0.1175	0.0534 ± 0.0057	1.4606 ± 0.1483	18.15	19.0
000 90109025	54964.81	2.4567 ± 0.1369	0.0284 ± 0.0034	1.6203 ± 0.1359	21.36	21.0
000 90109026	54965.01	2.5459 ± 0.1266	0.0275 ± 0.0026	1.5862 ± 0.1152	17.36	24.0
000 90109028	54967.02	2.3756 ± 0.1292	0.0331 ± 0.004	1.6263 ± 0.1161	25.45	25.0
000 90109032	54971.38	2.362 ± 0.132	0.0617 ± 0.0077	1.5464 ± 0.1536	12.17	20.0
000 90109033	54972.78	2.3875 ± 0.1069	0.1186 ± 0.0116	1.5141 ± 0.108	27.74	27.0
000 90109035	54974.66	2.3945 ± 0.1233	0.0422 ± 0.0057	1.6773 ± 0.1319	14.41	22.0
000 90109036	54975.71	2.3394 ± 0.1182	0.0479 ± 0.0062	1.6692 ± 0.1065	20.64	26.0
000 90109037	54976.12	2.4615 ± 0.1222	0.0467 ± 0.0048	1.5759 ± 0.1227	19.37	24.0
000 90109039	54978.25	2.3357 ± 0.12	0.0348 ± 0.0048	1.7191 ± 0.1079	20.1	27.0
000 90109041	54980.12	2.4287 ± 0.1863	0.0207 ± 0.0031	1.6856 ± 0.1518	14.52	19.0
000 96564004	59738.04	2.5534 ± 0.1023	0.069 ± 0.0087	1.6135 ± 0.1969	10.26	15.0
000 96564005	59741.49	2.4467 ± 0.123	0.0938 ± 0.0113	1.487 ± 0.1722	9.45	16.0
000 96564007	59743.35	2.5454 ± 0.1054	0.0431 ± 0.005	1.6474 ± 0.1386	15.7	19.0
000 96564009	59745.34	2.4964 ± 0.1137	0.0505 ± 0.0089	1.7019 ± 0.2152	6.55	12.0
000 96564012	59748.53	2.3619 ± 0.1085	0.1771 ± 0.0254	1.5203 ± 0.1537	16.76	15.0
000 96564013	59749.32	2.5585 ± 0.1056	0.0539 ± 0.0067	1.6321 ± 0.163	9.6	16.0
000 30867007	54157.27	2.7769 ± 0.0486	0.133 ± 0.0078	1.3866 ± 0.1085	10.86	25.0
000 30867017	54686.49	2.1492 ± 0.135	0.2441 ± 0.053	1.6716 ± 0.1402	9.14	19.0
000 30867025	54823.23	2.605 ± 0.0582	0.1063 ± 0.0084	1.5499 ± 0.13	38.22	26.0
000 30867044	57838.0	2.6328 ± 0.0754	0.0858 ± 0.008	1.5239 ± 0.2888	9.85	18.0
000 35019032	55293.35	2.5618 ± 0.2635	0.0476 ± 0.0066	1.3122 ± 0.1608	11.16	10.0
000 35019034	55314.98	2.0146 ± 0.3305	0.0842 ± 0.0247	1.5468 ± 0.202	11.66	16.0
000 35019036	55335.92	2.3349 ± 0.2485	0.0654 ± 0.0102	1.3826 ± 0.087	16.99	13.0

Obs Id	**Time** MJD	$\Gamma_{o/uv}$	**Break energy,**ϵ_b keV	Γ_x	χ^2	**Dof**
000 35019038	55547.71	2.7222 ± 0.0864	0.0329 ± 0.0018	1.464 ± 0.1737	22.94	38.0
000 35019050	55671.76	2.7435 ± 0.0771	0.106 ± 0.0096	1.3407 ± 0.1864	7.57	13.0
000 35019067	55961.16	2.5748 ± 0.078	0.0753 ± 0.0105	1.6668 ± 0.1678	5.14	13.0
000 35019072	55998.19	2.4715 ± 0.0718	0.1148 ± 0.0163	1.6578 ± 0.1678	6.98	15.0
000 35019073	56003.08	2.5372 ± 0.0807	0.0997 ± 0.0185	1.6799 ± 0.128	3.61	10.0
000 35019075	56017.99	2.493 ± 0.0941	0.096 ± 0.0127	1.5846 ± 0.1825	6.24	14.0
000 35019082	56123.1	2.409 ± 0.1126	0.2523 ± 0.0264	1.418 ± 0.1527	30.78	19.0
000 35019085	56326.32	2.3529 ± 0.0741	0.125 ± 0.0214	1.7091 ± 0.1579	6.91	16.0
000 35019175	57165.98	2.3896 ± 0.1138	0.2245 ± 0.0425	1.343 ± 0.3591	6.45	8.0
000 35019192	57515.93	2.3866 ± 0.1358	0.3666 ± 0.057	1.1091 ± 0.3873	3.88	8.0
000 35019193	57522.64	2.6042 ± 0.1212	0.087 ± 0.016	1.6427 ± 0.2751	4.64	9.0
000 35019244	58928.69	2.6108 ± 0.0608	0.1674 ± 0.0236	1.7339 ± 0.1822	16.68	14.0
000 30867003	54118.22	2.6297 ± 0.0719	0.3072 ± 0.0233	1.5966 ± 0.1149	24.88	29.0
000 30867004	54119.22	2.6279 ± 0.0714	0.3597 ± 0.0281	1.5714 ± 0.1085	26.55	27.0
000 30867005	54120.18	2.6417 ± 0.0702	0.2914 ± 0.0202	1.5379 ± 0.1091	24.4	30.0
000 30867008	54265.78	2.7369 ± 0.0797	0.0568 ± 0.0031	1.6129 ± 0.0758	52.52	47.0
000 30867019	54690.77	2.2261 ± 0.1858	0.1517 ± 0.032	1.7454 ± 0.1517	25.23	22.0
000 30867021	54694.32	2.2248 ± 0.2072	0.2378 ± 0.0429	1.6176 ± 0.1527	13.64	19.0
000 30867023	54696.33	2.1147 ± 0.1629	1.354 ± 0.7014	1.7091 ± 0.1631	30.42	18.0
000 30867029	54830.21	2.5828 ± 0.1002	0.0693 ± 0.0066	1.6827 ± 0.1219	27.98	26.0
000 30867034	55041.1	2.5852 ± 0.0971	0.1067 ± 0.0048	1.357 ± 0.0674	43.75	64.0
000 30867037	55044.45	2.4385 ± 0.0893	0.1986 ± 0.0093	1.3826 ± 0.0547	83.22	83.0
000 30867038	55045.18	2.5076 ± 0.1034	0.111 ± 0.006	1.4027 ± 0.0698	77.99	56.0
000 30867041	57821.12	2.7453 ± 0.0757	0.218 ± 0.0169	1.4008 ± 0.1447	13.81	18.0
000 30867063	58296.25	2.4995 ± 0.1195	0.1704 ± 0.0208	1.4174 ± 0.183	13.24	13.0
000 30867070	59234.42	2.725 ± 0.0789	0.0965 ± 0.009	1.703 ± 0.134	17.49	21.0
000 33059001	56648.27	2.4638 ± 0.1057	0.0893 ± 0.0046	1.3916 ± 0.0604	53.26	68.0
000 35019001	53748.03	2.74 ± 0.0758	0.0975 ± 0.0031	1.5166 ± 0.0402	113.62	138.0
000 35019002	53749.03	2.747 ± 0.077	0.0757 ± 0.0028	1.5789 ± 0.0516	72.45	102.0
000 35019004	53752.04	2.7453 ± 0.0774	0.0713 ± 0.0021	1.5209 ± 0.0334	180.19	185.0
000 35019021	55211.45	2.8461 ± 0.1421	0.024 ± 0.0013	1.5064 ± 0.0851	42.39	40.0

Obs Id	**Time** MJD	$\Gamma_{o/uv}$	**Break energy,**ϵ_b keV	Γ_x	χ^2	**Dof**
000 35019021	55211.45	2.8544 ± 0.1408	0.0238 ± 0.0013	1.5064 ± 0.0851	42.41	40.0
000 35019041	55593.35	2.6672 ± 0.1611	0.0617 ± 0.0057	1.3891 ± 0.1467	14.66	16.0
000 35019047	55642.52	2.7726 ± 0.135	0.0269 ± 0.0021	1.5312 ± 0.1182	13.58	22.0
000 35019057	55710.29	2.8217 ± 0.0856	0.0802 ± 0.0042	1.4469 ± 0.0996	25.16	36.0
000 35019060	55755.39	2.6225 ± 0.0856	0.1215 ± 0.0098	1.5543 ± 0.122	14.35	25.0
000 35019061	55774.84	2.7823 ± 0.1021	0.0381 ± 0.0038	1.687 ± 0.1618	12.48	17.0
000 35019080	56059.55	2.4839 ± 0.0965	0.079 ± 0.0112	1.7058 ± 0.162	16.75	17.0
000 35019148	56745.79	2.5504 ± 0.0889	0.1684 ± 0.0116	1.2967 ± 0.1058	38.15	26.0
000 35019152	56749.98	2.3816 ± 0.0861	0.4063 ± 0.0406	1.4616 ± 0.1183	20.62	24.0
000 35019155	56750.32	2.3914 ± 0.0861	0.3416 ± 0.0229	1.2135 ± 0.1074	16.66	30.0
000 35019210	58135.13	2.3977 ± 0.0814	0.2128 ± 0.0145	1.3088 ± 0.098	41.95	34.0
000 35019220	58144.23	2.5235 ± 0.0809	0.1906 ± 0.0178	1.5564 ± 0.1251	18.3	23.0
000 35019221	58147.68	2.5036 ± 0.0767	0.2534 ± 0.0169	1.4182 ± 0.1073	20.03	34.0
000 35019243	58927.69	2.5753 ± 0.0842	0.2167 ± 0.0245	1.6751 ± 0.1532	15.11	19.0
000 90109015	54950.63	2.6194 ± 0.1391	0.0386 ± 0.0031	1.4596 ± 0.1113	28.78	26.0
000 90109021	54960.53	2.5513 ± 0.1464	0.0215 ± 0.0019	1.5947 ± 0.099	34.35	32.0
000 90109043	54982.07	2.388 ± 0.1803	0.0507 ± 0.006	1.5631 ± 0.1139	36.49	25.0
000 96564008	59744.28	2.7574 ± 0.1439	0.0459 ± 0.0048	1.3847 ± 0.2263	11.0	12.0
000 35019074	56010.96	2.518 ± 0.1239	0.1186 ± 0.015	1.4627 ± 0.1679	11.81	13.0
000 35019164	56766.67	2.4685 ± 0.0931	0.1377 ± 0.0185	1.7003 ± 0.1354	18.96	19.0
000 35019169	56797.39	2.4137 ± 0.0785	0.3607 ± 0.0282	1.5095 ± 0.0953	31.67	37.0
000 30867067	59003.45	2.514 ± 0.1024	0.0885 ± 0.0103	1.5345 ± 0.1617	10.75	16.0
000 35019091	56367.26	2.1709 ± 0.0972	0.9765 ± 0.3277	1.6981 ± 0.1487	24.05	18.0
000 35019191	57474.19	2.3938 ± 0.104	0.4946 ± 0.1311	1.5766 ± 0.3706	4.41	8.0
000 35019163	56759.25	2.4269 ± 0.0925	0.1295 ± 0.0217	1.7594 ± 0.1673	9.7	16.0
000 30867001	54113.0	2.5856 ± 0.1037	0.5026 ± 0.0247	1.5865 ± 0.0421	149.85	140.0
000 30867010	54289.48	2.6657 ± 0.1111	0.2198 ± 0.0099	1.458 ± 0.0505	84.88	89.0
000 30867011	54291.22	2.6603 ± 0.1108	0.2329 ± 0.0109	1.3716 ± 0.0616	50.96	65.0
000 30867012	54292.69	2.6222 ± 0.1114	0.2476 ± 0.0156	1.4689 ± 0.0954	32.68	40.0
000 30867013	54293.35	2.5933 ± 0.1104	0.3486 ± 0.0193	1.4292 ± 0.072	44.21	55.0
000 30867014	54294.36	2.6516 ± 0.1098	0.2748 ± 0.0149	1.4161 ± 0.0754	31.86	48.0

Obs Id	**Time**	$\Gamma_{\rm o/uv}$	**Break energy,**ϵ_b	Γ_x	χ^2	**Dof**
	MJD		keV			
000 30867015	54295.3	2.6378 ± 0.1098	0.2318 ± 0.0125	1.4957 ± 0.0679	57.59	60.0
000 30867052	58270.3	2.4978 ± 0.1081	0.3795 ± 0.0256	1.2256 ± 0.1158	32.57	29.0
000 35019063	55794.58	2.5332 ± 0.1339	0.2677 ± 0.0252	1.6071 ± 0.108	37.67	29.0
000 35019048	55649.14	3.0542 ± 0.1795	0.0156 ± 0.0017	1.6644 ± 0.2053	11.38	12.0
000 35019058	55729.84	2.8917 ± 0.1179	0.0536 ± 0.0033	1.5962 ± 0.1005	27.22	33.0
000 35019093	56383.61	2.4452 ± 0.1435	0.188 ± 0.0314	1.5198 ± 0.1898	11.53	11.0
000 35019055	55705.34	2.8381 ± 0.1245	0.0711 ± 0.0049	1.4592 ± 0.1345	18.42	23.0
000 35019063	55794.58	2.5325 ± 0.1341	0.2685 ± 0.0253	1.6071 ± 0.108	37.67	29.0
000 35019078	56044.26	2.4165 ± 0.1326	0.1149 ± 0.0207	1.7539 ± 0.177	15.93	16.0
000 35019097	56409.26	2.6811 ± 0.1679	0.0693 ± 0.0106	1.5835 ± 0.2276	8.73	10.0

Table A.5: Table showing Details of Combined spectral fitting of XRT and UVOT specra with the Double power-law model. Column 2 – Photon index $< \epsilon_v$, column 3 – index at $> \epsilon_v$, column 4 – Transition Energy, ϵ_v, column 5 – chi-square, and column 6 – Dof

ObsId	Time MJD	$\Gamma_{\rm syn}$ ($\Gamma_{\rm o/uv}$)	$\Gamma_{\rm com}$ ($\Gamma_{\rm x}$)	Transition energy, E_v keV	χ^2	Dof
000 30867001	54113.0	2.761 ± 0.056	1.415 ± 0.086	0.4272 ± 0.08	154.53	138.0
000 30867003	54118.22	2.606 ± 0.062	1.269 ± 0.205	0.563 ± 0.1282	34.61	27.0
000 30867004	54119.22	2.63 ± 0.059	1.239 ± 0.182	0.5765 ± 0.12	36.05	25.0
000 30867005	54120.18	2.625 ± 0.06	1.282 ± 0.17	0.472 ± 0.104	25.4	28.0
000 30867007	54157.27	2.752 ± 0.039	1.386 ± 0.141	0.172 ± 0.0217	11.07	23.0
000 30867008	54265.78	2.763 ± 0.087	1.613 ± 0.084	0.0954 ± 0.0164	54.0	45.0
000 30867009	54266.79	2.661 ± 0.05	1.488 ± 0.091	0.1348 ± 0.0145	44.72	48.0
000 30867010	54289.48	2.71 ± 0.095	1.364 ± 0.076	0.263 ± 0.0558	97.87	87.0
000 30867011	54291.22	2.749 ± 0.087	1.286 ± 0.063	0.2234 ± 0.0497	62.72	63.0
000 30867012	54292.69	2.618 ± 0.084	1.26 ± 0.164	0.3369 ± 0.1037	33.35	38.0
000 30867013	54293.35	2.639 ± 0.06	1.231 ± 0.117	0.3832 ± 0.0897	52.74	53.0
000 30867014	54294.36	2.664 ± 0.083	1.244 ± 0.116	0.3423 ± 0.0809	38.99	46.0
000 30867015	54295.3	2.651 ± 0.083	1.342 ± 0.108	0.3147 ± 0.0732	64.69	58.0
000 30867025	54823.23	2.608 ± 0.058	1.55 ± 0.14	0.1486 ± 0.0248	41.56	24.0
000 30867028	54828.2	2.62 ± 0.059	1.549 ± 0.165	0.1409 ± 0.0239	14.86	21.0
000 30867031	54834.23	2.658 ± 0.061	1.587 ± 0.174	0.1228 ± 0.0235	14.1	16.0
000 30867032	54836.24	2.76 ± 0.057	1.43 ± 0.173	0.1345 ± 0.0216	15.19	16.0
000 30867034	55041.1	2.606 ± 0.103	1.349 ± 0.09	0.1001 ± 0.0247	46.07	62.0
000 30867035	55042.65	2.535 ± 0.048	1.39 ± 0.077	0.1168 ± 0.017	59.15	62.0
000 30867036	55043.52	2.382 ± 0.045	1.134 ± 0.12	0.2377 ± 0.0463	62.28	49.0
000 30867037	55044.45	2.46 ± 0.076	1.271 ± 0.08	0.173 ± 0.0339	95.22	81.0
000 30867038	55045.18	2.489 ± 0.098	1.326 ± 0.092	0.1136 ± 0.0244	82.7	54.0
000 30867041	57821.12	2.715 ± 0.066	1.262 ± 0.172	0.3112 ± 0.0688	14.79	16.0
000 30867044	57838.0	2.633 ± 0.072	1.524 ± 0.161	0.1141 ± 0.0215	9.79	16.0
000 30867050	57856.61	2.513 ± 0.101	1.451 ± 0.243	0.0945 ± 0.0435	13.42	13.0
000 30867052	58270.3	2.494 ± 0.08	0.94 ± 0.194	0.3685 ± 0.1067	34.21	27.0
000 30867054	58276.07	2.39 ± 0.038	1.173 ± 0.193	0.3386 ± 0.0805	21.68	26.0
000 30867056	58279.93	2.616 ± 0.084	1.464 ± 0.21	0.102 ± 0.0218	14.7	13.0
000 30867060	58288.63	2.321 ± 0.052	1.013 ± 0.312	0.4392 ± 0.1385	22.79	17.0
000 30867061	58292.61	2.615 ± 0.074	1.404 ± 0.226	0.1485 ± 0.0298	8.52	13.0
000 30867062	58294.2	2.444 ± 0.054	1.304 ± 0.19	0.2331 ± 0.0656	19.56	19.0

ObsId	Time MJD	$\Gamma_{\rm syn}$ ($\Gamma_{\rm o/uv}$)	$\Gamma_{\rm com}$ ($\Gamma_{\rm x}$)	Transition energy, E_v keV	χ^2	Dof
000 30867063	58296.25	2.467 ± 0.092	1.28 ± 0.246	0.1969 ± 0.0712	15.44	11.0
000 30867067	59003.45	2.526 ± 0.095	1.534 ± 0.203	0.1 ± 0.0413	11.3	14.0
000 30867068	59228.11	2.552 ± 0.045	1.074 ± 0.25	0.6633 ± 0.1566	17.36	12.0
000 33052001	56633.59	2.528 ± 0.068	1.375 ± 0.077	0.0658 ± 0.0117	69.01	64.0
000 33059001	56648.27	2.51 ± 0.109	1.39 ± 0.078	0.0684 ± 0.0153	56.89	66.0
000 35019001	53748.03	2.76 ± 0.081	1.477 ± 0.052	0.1391 ± 0.0261	115.8	136.0
000 35019002	53749.03	2.754 ± 0.087	1.578 ± 0.068	0.1239 ± 0.0221	71.8	100.0
000 35019004	53752.04	2.776 ± 0.083	1.52 ± 0.041	0.0982 ± 0.0149	184.71	183.0
000 35019006	53754.05	2.786 ± 0.05	1.529 ± 0.079	0.0787 ± 0.0091	51.0	49.0
000 35019021	55211.45	2.958 ± 0.177	1.507 ± 0.09	0.031 ± 0.0072	41.43	38.0
000 35019021	55211.45	2.958 ± 0.177	1.507 ± 0.09	0.031 ± 0.0072	41.43	38.0
000 35019023	55225.77	2.84 ± 0.176	1.484 ± 0.14	0.0381 ± 0.0129	17.06	17.0
000 35019024	55237.94	2.682 ± 0.185	1.432 ± 0.192	0.0295 ± 0.0129	10.66	12.0
000 35019038	55547.71	2.779 ± 0.088	1.464 ± 0.091	0.0382 ± 0.0084	22.92	36.0
000 35019041	55593.35	2.676 ± 0.158	1.389 ± 0.123	0.0655 ± 0.0216	14.58	14.0
000 35019043	55615.03	2.775 ± 0.1	1.615 ± 0.159	0.0547 ± 0.0107	12.39	17.0
000 35019045	55629.15	2.747 ± 0.128	1.517 ± 0.158	0.0518 ± 0.0172	10.49	13.0
000 35019046	55634.17	2.787 ± 0.073	1.482 ± 0.092	0.0511 ± 0.0093	26.42	32.0
000 35019047	55642.52	2.866 ± 0.137	1.531 ± 0.118	0.035 ± 0.0096	16.0	20.0
000 35019047	55642.52	2.859 ± 0.17	1.531 ± 0.12	0.035 ± 0.0106	14.12	20.0
000 35019050	55671.76	2.722 ± 0.066	1.34 ± 0.188	0.1226 ± 0.0217	8.33	11.0
000 35019052	55684.26	2.78 ± 0.064	1.52 ± 0.087	0.0483 ± 0.0076	37.14	39.0
000 35019053	55691.5	2.822 ± 0.093	1.517 ± 0.16	0.0623 ± 0.0114	10.37	16.0
000 35019055	55705.34	2.825 ± 0.109	1.459 ± 0.143	0.1007 ± 0.027	18.35	21.0
000 35019057	55710.29	2.811 ± 0.082	1.446 ± 0.107	0.1104 ± 0.02	25.53	34.0
000 35019058	55729.84	2.904 ± 0.117	1.596 ± 0.106	0.0964 ± 0.0227	27.78	31.0
000 35019060	55755.39	2.63 ± 0.054	1.452 ± 0.161	0.1774 ± 0.0502	15.09	23.0
000 35019063	55794.58	2.585 ± 0.107	1.495 ± 0.201	0.3685 ± 0.1145	42.17	27.0
000 35019063	55794.58	2.585 ± 0.107	1.495 ± 0.201	0.3685 ± 0.1145	42.17	27.0
000 35019066	55952.46	2.582 ± 0.035	1.552 ± 0.123	0.1782 ± 0.0283	35.73	32.0
000 35019069	55975.0	2.531 ± 0.043	1.349 ± 0.245	0.234 ± 0.0585	10.38	14.0

ObsId	Time MJD	$\Gamma_{\rm syn}$ ($\Gamma_{\rm o/uv}$)	$\Gamma_{\rm com}$ ($\Gamma_{\rm x}$)	Transition energy, E_v keV	χ^2	Dof
000 35019069	55975.0	2.531 ± 0.043	1.349 ± 0.245	0.234 ± 0.0585	10.38	14.0
000 35019074	56010.96	2.53 ± 0.095	1.462 ± 0.212	0.1205 ± 0.0532	13.23	11.0
000 35019082	56123.1	2.355 ± 0.075	1.107 ± 0.252	0.304 ± 0.0931	33.53	17.0
000 35019083	56137.93	2.369 ± 0.058	1.484 ± 0.216	0.1609 ± 0.074	29.47	19.0
000 35019099	56437.38	2.39 ± 0.087	1.52 ± 0.191	0.0705 ± 0.0241	16.6	15.0
000 35019100	56638.0	2.648 ± 0.048	1.541 ± 0.046	0.05 ± 0.006	110.04	124.0
000 35019138	56688.92	2.536 ± 0.048	1.389 ± 0.207	0.2087 ± 0.0547	24.75	14.0
000 35019148	56745.79	2.548 ± 0.066	1.254 ± 0.128	0.1551 ± 0.0374	41.94	24.0
000 35019152	56749.98	2.387 ± 0.045	1.1 ± 0.233	0.4325 ± 0.1356	27.11	22.0
000 35019155	56750.32	2.378 ± 0.07	0.951 ± 0.177	0.2848 ± 0.0784	20.52	28.0
000 35019157	56751.32	2.46 ± 0.068	1.555 ± 0.19	0.1935 ± 0.0447	23.24	22.0
000 35019159	56752.32	2.421 ± 0.051	1.045 ± 0.185	0.1947 ± 0.0454	14.19	16.0
000 35019166	56786.92	2.527 ± 0.045	1.306 ± 0.304	0.2362 ± 0.0548	12.28	12.0
000 35019169	56797.39	2.421 ± 0.061	1.159 ± 0.198	0.4227 ± 0.1151	38.22	35.0
000 35019171	57053.79	2.574 ± 0.077	1.51 ± 0.206	0.1098 ± 0.0257	12.15	12.0
000 35019210	58135.13	2.364 ± 0.077	1.139 ± 0.143	0.1839 ± 0.0461	46.32	32.0
000 35019211	58136.13	2.399 ± 0.049	1.021 ± 0.16	0.2049 ± 0.0417	18.22	22.0
000 35019220	58144.23	2.521 ± 0.072	1.416 ± 0.191	0.2665 ± 0.0728	19.04	21.0
000 35019221	58147.68	2.445 ± 0.076	1.109 ± 0.192	0.3512 ± 0.0973	16.77	32.0
000 35019224	58158.12	2.519 ± 0.055	1.522 ± 0.138	0.0867 ± 0.0245	24.27	28.0
000 35019225	58165.28	2.407 ± 0.053	1.208 ± 0.181	0.2546 ± 0.0644	28.58	25.0
000 35019229	58184.22	2.591 ± 0.059	1.376 ± 0.212	0.2152 ± 0.059	14.32	11.0
000 90022009	54905.09	2.623 ± 0.091	1.311 ± 0.243	0.1293 ± 0.0432	5.76	9.0
000 90109001	54936.64	2.589 ± 0.144	1.489 ± 0.185	0.056 ± 0.0246	12.52	16.0
000 90109004	54939.85	2.461 ± 0.112	1.448 ± 0.154	0.0645 ± 0.0218	23.66	23.0
000 90109010	54945.67	2.501 ± 0.1	1.4 ± 0.12	0.0632 ± 0.0161	37.07	31.0
000 90109011	54946.66	2.738 ± 0.096	1.468 ± 0.091	0.0459 ± 0.0096	36.24	31.0
000 90109013	54948.28	2.783 ± 0.124	1.456 ± 0.097	0.0327 ± 0.0079	50.12	39.0
000 90109014	54949.88	2.718 ± 0.116	1.532 ± 0.11	0.0343 ± 0.0099	28.31	28.0
000 90109015	54950.63	2.671 ± 0.144	1.46 ± 0.117	0.04 ± 0.0122	29.48	24.0
000 90109017	54953.43	2.498 ± 0.074	1.473 ± 0.138	0.0682 ± 0.0214	26.05	23.0

ObsId	Time	$\Gamma_{\rm syn}$ ($\Gamma_{\rm o/uv}$)	$\Gamma_{\rm com}$ ($\Gamma_{\rm x}$)	Transition energy, E_{υ}	χ^2	Dof
	MJD			keV		
000 90109018	54954.64	2.497 ± 0.123	1.492 ± 0.126	0.0434 ± 0.0104	27.45	24.0
000 90109019	54955.58	2.441 ± 0.115	1.349 ± 0.118	0.0394 ± 0.0112	25.25	27.0
000 90109021	54960.53	2.76 ± 0.212	1.595 ± 0.112	0.0225 ± 0.0058	33.28	30.0
000 90109022	54961.07	2.496 ± 0.122	1.46 ± 0.167	0.0408 ± 0.0123	18.6	17.0
000 90109025	54964.81	2.616 ± 0.291	1.62 ± 0.153	0.0277 ± 0.0104	21.46	19.0
000 90109026	54965.01	2.688 ± 0.173	1.586 ± 0.128	0.0294 ± 0.0102	16.81	22.0
000 90109028	54967.02	2.514 ± 0.164	1.626 ± 0.135	0.0274 ± 0.0096	26.05	23.0
000 90109032	54971.38	2.414 ± 0.141	1.546 ± 0.214	0.045 ± 0.0158	11.47	18.0
000 90109033	54972.78	2.407 ± 0.079	1.445 ± 0.155	0.1067 ± 0.0348	30.34	25.0
000 90109037	54976.12	2.533 ± 0.121	1.576 ± 0.146	0.0456 ± 0.0155	19.4	22.0
000 90109043	54982.07	2.48 ± 0.181	1.563 ± 0.143	0.04 ± 0.0129	37.06	23.0
000 96564005	59741.49	2.462 ± 0.113	1.486 ± 0.229	0.0839 ± 0.0422	9.5	14.0
000 96564008	59744.28	2.766 ± 0.151	1.384 ± 0.229	0.0523 ± 0.0226	11.1	10.0
000 96564012	59748.53	2.37 ± 0.069	1.386 ± 0.228	0.1655 ± 0.0779	19.32	13.0
000 96564013	59749.32	2.5706 ± 0.052	1.5496 ± 0.19	0.0864 ± 0.0259	10.35	14.0